JNC TJ7410 2001-002

亀裂ネットワークモデルによる解析作業の実施

（核燃料サイクル開発機構　契約業務報告書）

2001年3月

三菱商事株式会社

JNC TJ7410 2001-002
2001 年 3 月

亀裂ネットワークモデルによる解析作業の実施

吉添 誠* William Dershowitz**

要旨

本報告書は、Golder 社により平成 12 年度（2000 年－2001 年）に実施された核燃料サイクル開発機構（JNC）東濃地科学センター殿への支援を取り纏めたものである。平成 12 年度における Golder 社支援活動の主な目的は、エスポ TRUE ブロック・スケール（BS）試験、エスポ Task-5 水理地球化学的解析、及び岐阜県瑞浪市の超深地層研究所（MIU）計画を支援することである。

JNC 殿は、エスポ島にあるスウェーデン硬岩研究所（HRL：Sweden Hard Rock Laboratory）における国際エスポ TRUE-BS 試験にフルパートナーとして参加している。平成 12 年度、Golder 社は、TRUE-BS プロジェクトにおいて、以下のように JNC 殿を支援した：

a) エスポ TRUE-BS プロジェクトにおいて、水理試験及びトレーサー試験の評価、水理構造概念モデルの構築、及び吸着トレーサー移行予測のモデル化を含む、JNC 殿のタスクの遂行。
b) プロジェクト会議に出席することによる、TRUE-BS プロジェクトから JNC 殿スタッフへの技術移転の確実な実施。
c) JNC 殿が TRUE-BS の活動から最大の利益を確実に得られるよう、プロジェクトの戦略策定において、JNC 殿を支援。

エスポ Task-5 は、2 キロ（四方）範囲でのサイト特性に関して、亀裂性岩盤における水理地質学と地球化学を統合する主要なプロジェクトであった。このタスクは、JNC 殿がサイト特性調査及び試験設計の方法を開発及び実証するのに役立つものである。平成 12 年度中に Golder 社は、JNC 殿を以下の 3 つの分野において支援した：

a) 地球化学端成分（end-member）の初期条件について、地球化学／水理学を統合した評価を遂行。
b) これらの最新の評価に基づいたエスポ島水文地球化学的モデルの再調整（re-calibration）。
c) 2 キロ範囲での地下水流動および物質移行の理解に関する当該モデルの利点についての地球化学・水理地質学上の改善効果についての報告。

また MIU 計画の支援では、データの分析、及び同計画における亀裂ネットワーク（DFN）モデル化に関する助言を通じて、JNC を支援した。

Golder 社の平成 12 年度における JNC 殿への支援に関わる技術情報の詳細は、本報告書の補遺に記載されている。

本報告書は、三菱商事（株）が核燃料サイクル開発機構の委託により実施した業務に関するものである。
契約番号：12C1004
機構担当部課室：東濃地科学センター 地質環境特性研究グループ 竹内 真司
* 三菱商事株式会社 石炭・原子燃料事業部
** Golder Associates Inc., Seattle, USA

ABSTRACT

This report describes Golder Associates support for JNC/Tono during the Heisei-12 (2000-2001) fiscal year. The primary objective of the Golder Associates support activities during fiscal year H-12 was in support of the Äspö TRUE-Block Scale Experiment, Äspö Task 5 Hydrogeochemical Analysis, and the MIU underground research facility at Mitsunami, Japan.

JNC participates as a full partner in the international Äspö TRUE-Block Scale experiment at the Äspö, Sweden Hard Rock Laboratory (HRL). During H-12, Golder Associates supported JNC within the TRUE-Block Scale project through:

a) carrying out JNC tasks within the Äspö TRUE-BS Project, including evaluation of hydraulic and tracer tests, development of the hydrostructural conceptual model, and predictive sorbing tracer transport modeling.
b) participating in project meetings, ensuring technology transfer from the TRUE-BS project to JNC staff
c) assisting JNC in developing project strategies to ensure that JNC obtains maximum benefit from TRUE-BS activities.

Äspö Task 5 was a major project for integration of fracture rock hydrogeology and geochemistry for site characterization at the 2 km scale. This task helps JNC to develop and demonstrate improved approaches for site characterization and test design. During H-12, Golder supported JNC in three areas:

a) carrying out an integrated geochemical/hydrogeological assessment of the geochemical end-member initial conditions.
b) Re-calibration of the Äspö Island hydrogeochemical model based on these updated assessments,
c) Reporting on the effect of improved geochemical and hydrogeological assessment on the models usefulness for understanding flow and transport at the 2 km scale.

During H-12, Golder provided support to the MIU Project through review of data, and development of recommendations for DFN modeling of the MIU project.

Technical information about Golder Associates HY-12 support to JNC is provided in the appendices to this report.

概要

（図表に関しては本文をご参照下さい。）

1. はじめに

本報告書は、エスポ島（スウェーデン）における TRUE ブロック・スケール（BS）試験及び Task-5 水理地球化学モデル化に関して、平成 12 年度中に Golder 社が核燃料サイクル開発機構（JNC）東濃地科学センター殿のために実施した支援についての概要を纏めたものである。Golder 社は、亀裂ネットワーク（DFN）及びチャンネル・ネットワーク（CN）における地下水流動・物質移行のモデル化、データ解析、そして原位置試験の設計及び解釈において助力することで、これらの作業に支援を提供した。こうした業務は、JNC が行う深部地質環境の予測評価手法の構築を直接支援することを意図したものである。

2. Task-1：TRUE-BS プロジェクト

平成 12 年度において、Golder 社は、JNC 殿が TRUE-BS プロジェクトに参加するに当たり、以下の事項を通じて支援した：

a) 水理試験、トレーサー試験および構造データのレビュー
b) サイトのリファレンス水理構造モデルの構築
c) JNC／FracMan を用いたサイトのリファレンス DFN モデルの実施
d) フェーズ A とフェーズ B を意図した一連の広範な水理試験との比較をともなう FracMan/PAWorks を用いた地下水流動および物質移行モデルの調整(calibration)
e) 「フェーズ C」トレーサー試験に関する吸着トレーサー移行の「ブラインド」予測

JNC／Golder チームにより開発された DFN モデルは、図 2-2 及び図 2-3 に例示されている。このモデルは、決定論的な亀裂（deterministic discrete features）と現場測定に基づいたバックグラウンドとしての割れ目（background fracturing）を組み合わせたものである。図 2-6、2-7、2-8 は、50～100 メートル四方範囲での原位置での非収着性トレーサー試験に対する JNC／Golder PAWorks CN モデルの調整を示したものである。これらのモデルは全て、亀裂交差ゾーン（FIZ：fracture intersection zone）効果をモデル化するために平成 12 年度中に JNC 殿のために開発された特殊要素を含んでいる。

3. Task-2：エスポ Task-5 地球化学／水文地質学的統合解析

平成 12 年度中、Golder 社は、JNC 殿を以下の 3 つのサブタスクを通じて支援した：
・Task 2.1：BGS 地球化学端成分（end-members）解析
・Task 2.2：端成分空間条件に関する Golder／JNC 再評価
・Task 2.3：水みちの解析と報告

3.1 Task-2-1：BGS 地球化学端成分解析

地球化学端成分解析は、英国地質研究所（BGS）の Mark Cave 氏により実施された。このモデルは、「chemometric」主成分分析手法（Cave and Harmon 1997、Cave and Wragg1997）を使用しており、同手法では現在の端成分の性質についての初期的な仮定を一切行わず、地下水流における化学的変化に寄与するもの全てを考慮するものである。

基本的なアプローチについては、図 3-1 及び 3-2 で例示する。ここで、マトリックス A は地下水データ群で、マトリックス A になるようなマトリックス B と C を見つける必要がある。

図 3-3 は、統計学的に引き出された化学成分から再構築された比較的反応性の高い溶質（Na）の濃度と比較的反応性の低い溶質（Cl、$\delta^{18}O$、δH）の濃度を、実際の濃度と比較したものである。同様の結果は、全ての構成要素で得られる。

表 3-1 及び 3-2 は、「M-3」地球化学的解析と PCA 端成分解析を例示している。PCA 端成分は客観的なもので、従って「実際の」地下水に対してバイアスされるべきではないが、可能な地球化学的測定から直接的な作用を受ける。PCA 解析には、非常に低い残差での端成分特定に利用できるという利点がある。

3.2 Task-2-2：Golder 社／JNC による 端成分空間条件の再調整

平成 12 年度において、地球化学的端成分の初期空間分布を設定するため、解析の更新を実施した。この解析は、亀裂ゾーン毎の地球化学評価に基づいており、そこから岩塊が近似されるが、その際、バックグラウンド割れ目における当初の化学は隣接した主要な亀裂ゾーンの化学と類似していると仮定される。

その結果としての内挿結果は、平成 11 年度で用いた格子近似方式よりも観察点における数値において遥かに適合するものであった。

3.3 Task-2-3：水みち解析と報告

平成 12 年度において、Golder 社は、Task-5 における水みちの解析手法を改善し、グラフ理論の水みち解析よりもむしろ粒子バック・トラッキングの使用に基づくようにした。我々は、Task-5 の端成分移行経路の全ての再計算にこの方式を用いた。端成分、初期条件及び水みち解析の改善により、平成 11 年度の実績に比べて、地球化学／水理地質学的評価におけるエラー及び不確実性は非常に少なくなった。

粒子バック・トラッキング水みち方式により生じた水みちの例は、図 3-4 及び 3-5 に示している。図 3-6 から 3-10 までは、平成 12 年度に策定された方式を用いた、測定された端成分の破過点とシミュレーションされた端成分の破過点間で得られる適合性の向上を例示している。

4. Task-3-1：MIU サイトのデータに関する不連続構造解析

平成 12 年度における MIU 計画の支援では、主に MIU 計画における DFN モデル化及び地下水シミュレーションに関して、現在考慮されている方式に対する助言を行う事に焦点が置かれた。助言には、DFN モデルを構築し、また感度解析を実施する方法論の提案が含まれている。

レビュー文書では、モデル化の結果に大きな影響を及ぼすデータ解析とモデル構築の分野に焦点が当てられており、MIU サイトの有益なモデルを構築するために使用可能な方法論に関わる助言がなされている。

Executive Summary
Support for TRUE Block Scale Experiment,
Äspö Task 5, and MIU Experiments
Golder Associates Inc.
Heisei-12

(Please refer to the main text as to the Figures and Tables.)

1. INTRODUCTION

This report summarizes the Support for the Äspö (Sweden) TRUE Block Scale Experiment and Task 5 Hydrogeochemical Modeling carried out by Golder Associates Inc. for JNC/Tono during the Heisei-12 (2000-2001) fiscal year. Golder provided support to these tasks through assistance in discrete fracture network and channel network flow and transport modeling, data analysis, and design and interpretation of in situ experiments. These efforts are designed to directly support for establishing the methodology for evaluating prediction in deep underground.

2. TASK 1: TRUE-BLOCK SCALE PROJECT

During H-12, Golder Associates supported JNC participation in the TRUE-Block Scale project through:

a) review of hydraulic tests, tracer tests, and structural data
b) development of the site reference hydrostructural model
c) implementation of the site reference discrete fracture network model using JNC/FracMan.
d) Flow and transport model calibration using FracMan/PAWorks with comparison to an extensive series of hydraulic tests designated Phase A and Phase B.
e) "Blind" Prediction of sorbing tracer transport for the "Phase C" tracer experiments

The discrete fracture network model developed by the JNC/Golder team is illustrated in Figures 2-2 and 2-3. This model combines deterministic discrete features, and background fracturing based on field measurements. Figures 2-4 and 2-5 illustrate the hydraulic behavior of the model, when compared to field measurements. Figures 2-6, 2-7, and 2-8 illustrate the calibration of the JNC/Golder PAWorks Channel Network (CN) model against in situ conservative tracer experiments at the 50 to 100 meter scale. These models all include special elements developed for JNC during HY-12 to model fracture intersection zone (FIZ) effects.

3. TASK 2: ÄSPÖ TASK 5 INTEGRATED GEOCHEMICAL/ HYDROGEOLOGICAL ANALYSIS

During H-12, Golder supported JNC through three subtasks:

- Task 2.1: BGS Geochemical End-member Analysis
- Task 2.2: Golder/JNC Re-evaluation of End-member Spatial Conditions
- Task 2.3: Pathways Analysis and Reporting

3.1 Task 2.1: BGS Geochemical End-Member Analysis

Geochemical end-member analysis was carried out by Mark Cave of the British Geological Survey (BGS) under subcontract to Golder. This model used a"chemometric" principal component analysis algorithm (Cave and Harmon 1997, Cave and Wragg 1997), which makes no initial assumptions about the nature of the end-members present, and which considered all the contributions to chemical variability in the groundwaters.
The basic approach is illustrated in Figures 3-1 and 3-2. Here matrix A is the supplied groundwater data matrix and matrices B and C need to be found.

Figure 3-3 compares concentrations of a relatively reactive solute (Na) and a relatively unreactive solutes (Cl, $\delta^{18}O$ and δH) reconstructed from the statistically-derived chemical components, and the actual concentrations. Similar plots were produced for all the constituents.

Tables 3-1 and 3-2 illustrate the"M-3" geochemical and the PCA end-member analyses. The PCA end-member is objective, in that it does not bias toward "real" waters, but works directly from the available geochemical measurements. The PCA analysis has the advantage that it can be used to define end members with very little residual error.

3.2 Task 2.2: Golder/JNC Re-evaluation of End-member Spatial Conditions

During HY-12, Golder carried out updated analyses to establish the initial spatial distribution of geochemical end-members. This analysis works from an assessment of the geochemistry on a fracture-zone by fracture-zone bases, and then extended the approximation to the rock mass assuming that the original chemistry in the background fractures is similar to the chemistry in adjacent major fracture zones.
The resulting interpolation provided a significantly better match to values as observation points than the gridded approximation used during HY-11.

3.3 Task 2.3: Pathways Analysis and Reporting

During HY-12, Golder developed an improved pathways analysis algorithm for Task 5, based on the use of particle back-tracking rather than graph theory pathways analyisis. We used this approach to recalculate all of the Task 5 end-member transport pathways. The combination of improved end-members, improved initial conditions, and improved pathway analysis significantly reduced the error and uncertainty in the geochemical/hydrogeologic assessment when compared to that achieved during HY-11.
Example pathways produced by the particle back-tracking pathway algorithm are shown

in Figures 3-4 and 3-5. Figures 3-6 through 3-10 illustrate the improved matches obtained between measured and simulated end-member breakthroughs using the procedures developed during HY-12.

4. TASK 3.1: DISCRETE FEATURE ANALYSIS OF DATA FROM THE MIU SITE

The main focus of HY-12 support for the MIU project was in preparation of a document providing recommendations for the proposed approach for the DFN modelling and groundwater simulation of the MIU project. Recommendations include a suggested methodology for constructing the discrete fracture network (DFN) model, and running the sensitivity analyses.

The review document highlighted the areas of the data analysis and model construction which have a strong effect on the modelling results, and to discuss, and make recommendations on, the approaches that may be used to achieve a useful model of the MIU site.

Golder Associates, Inc.

18300 Union Hill NE, Suite 200
Redmond, WA 98025
Telephone (425) 883-0777
Fax (425) 882-5498

Golder Associates

Report to:

Japan Nuclear Cycle Development Institute (JNC)
Tono, Japan

Version 1.00

Support for TRUE Block Scale Experiment, Äspö Task 5, and MIU Experiments Heisei-12

Heisei-12 Progress Report

William Dershowitz
Thomas Doe
Dawn Shuttle
Aaron Fox
Kate Klise

February 14, 2001

923-1089.1200

h12 tono version 1.0 rev.doc

ABSTRACT

This report describes Golder Associates support for JNC/Tono during the Heisei-12 (2000-2001) fiscal year. The primary objective of the Golder Associates support activities during fiscal year H-12 was in support of the Äspö TRUE-Block Scale Experiment, Äspö Task 5 Hydrogeochemical Analysis, and the MIU underground research facility at Mizunami, Japan.

JNC participates as a full partner in the international Äspö TRUE-Block Scale experiment at the Äspö, Sweden Hard Rock Laboratory (HRL). During H-12, Golder Associates supported JNC within the TRUE-Block Scale project through:

a) Carrying out JNC tasks within the Äspö TRUE-BS Project, including evaluation of hydraulic and tracer tests, development of the hydrostructural conceptual model, and predictive sorbing tracer transport modeling.

b) Participating in project meetings, ensuring technology transfer from the TRUE-BS project to JNC staff.

c) Assisting JNC in developing project strategies to ensure that JNC obtains maximum benefit from TRUE-BS activities.

Äspö Task 5 was a major project for integration of fracture rock hydrogeology and geochemistry for site characterization at the 2-km scale. This task is directly relevant to the MIU project since it helps JNC to develop and demonstrate improved approaches for site characterization and test design. During H-12, Golder supported JNC for Äspö Task 5 in three areas:

a) Carrying out an integrated geochemical/hydrogeological assessment of the geochemical end-member initial conditions.

b) Re-calibration of the Äspö Island hydrogeochemical model based on these updated assessments.

c) Reporting on the effect of improved geochemical and hydrogeological assessment on the model's usefulness for understanding flow and transport at the 2-km scale.

During H-12, Golder provided support to the MIU Project through review of data, and development of recommendations for DFN modeling of the MIU project.

Technical information about Golder Associates HY-12 support to JNC is provided in the appendices to this report.

TABLE OF CONTENTS

LIST OF TABLES

LIST OF FIGURES

APPENDICES

1. PROJECT OVERVIEW

This report provides an overview of Golder Associates support for JNC/Tono during the Heisei-12 (2000-2001) fiscal year. Support was provided for the Äspö (Sweden) TRUE Block Scale Experiment and Task 5 Hydrogeochemical Modeling carried out by Golder Associates Inc. for. Golder provided support to these tasks through assistance in discrete fracture network and channel network flow and transport modeling, data analysis, and design and interpretation of in situ experiments. These efforts are designed to directly support the development of the MIU underground rock laboratory.

The primary objective of the Golder Associates work scope during fiscal year HY-12 was in support of the Äspö TRUE-Block Scale Experiment, Äspö Task 5 Hydrogeochemical Analysis, and the MIU underground research facility at Mizunami, Japan. HY-12 Tasks and the appendices in which they are reported are summarized in Table 1-1.

No.	Task	Appendix
1	Support to TRUE Block Scale Project	A, B
2	Äspö Task 5 Integrated Geochemical/Hydrogeological Analysis	C
3	Support to MIU Project	D

Table 1-1: HY-11 Task Summary

Support for the Äspö project included predictive modeling of sorbing tracer transport in the TRUE-1 rock block, and analysis of two kilometer scale geochemical transport pathways for "Task 5".

This report provides a summary of work completed by Golder Associates during HY-11. Technical information about Golder Associates HY-11 support to JNC is provided in the appendices to this report as summarized in Table 1-1.

2. TASK 1: TRUE-BLOCK SCALE PROJECT

JNC participates as a full partner in the international Äspö TRUE-Block Scale experiment at the Äspö, Sweden Hard Rock Laboratory (HRL). The TRUE-Block Scale Site is illustrated in Figure 2-1. During H-12, Golder Associates supported JNC participation in the TRUE-Block Scale project through:

a) review of hydraulic tests, tracer tests, and structural data;

b) development of the site reference hydrostructural model;

c) implementation of the site reference discrete fracture network model using JNC/FracMan;

d) Flow and transport model calibration using FracMan/PAWorks with comparison to an extensive series of hydraulic tests designated Phase A and Phase B; and

e) "Blind" Prediction of sorbing tracer transport for the "Phase C" tracer experiments.

In addition, Golder participated in a series of TRUE Block Scale project meetings, and represented JNC in preparations for the project final report.

The discrete fracture network model developed by the JNC/Golder team is illustrated in Figures 2-2 and 2-3. This model combines deterministic discrete features, and background fracturing based on field measurements. Figures 2-4 and 2-5 illustrate the hydraulic behavior of the model, when compared to field measurements. Figures 2-6, 2-7, and 2-8 illustrate the calibration of the JNC/Golder PAWorks Channel Network (CN) model against in situ conservative tracer experiments at the 50 to 100 meter scale. These models all include special elements developed for JNC during HY-12 to model fracture intersection zone (FIZ) effects.

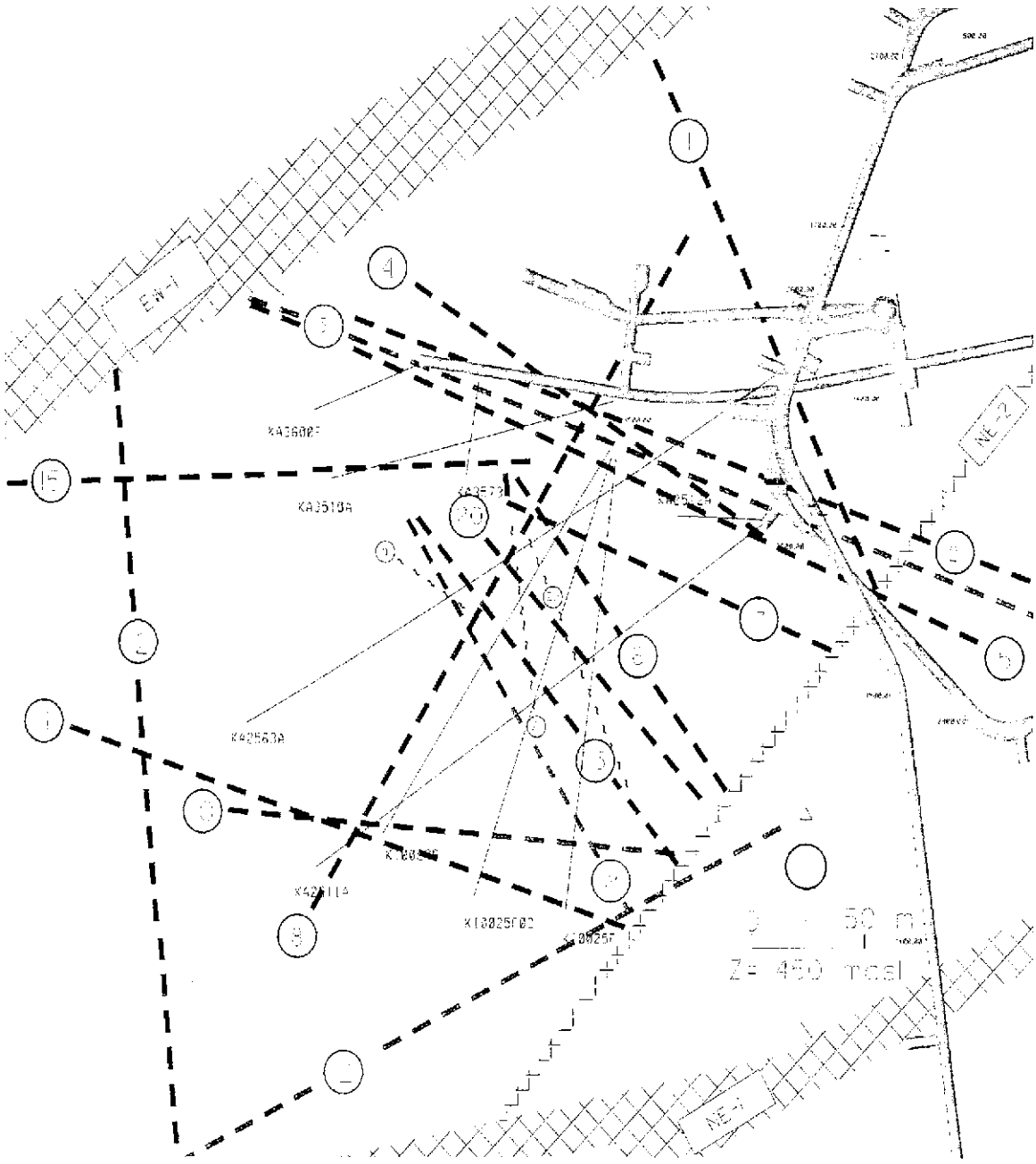

Figure 2-1: TRUE-Block Scale Experiment Site

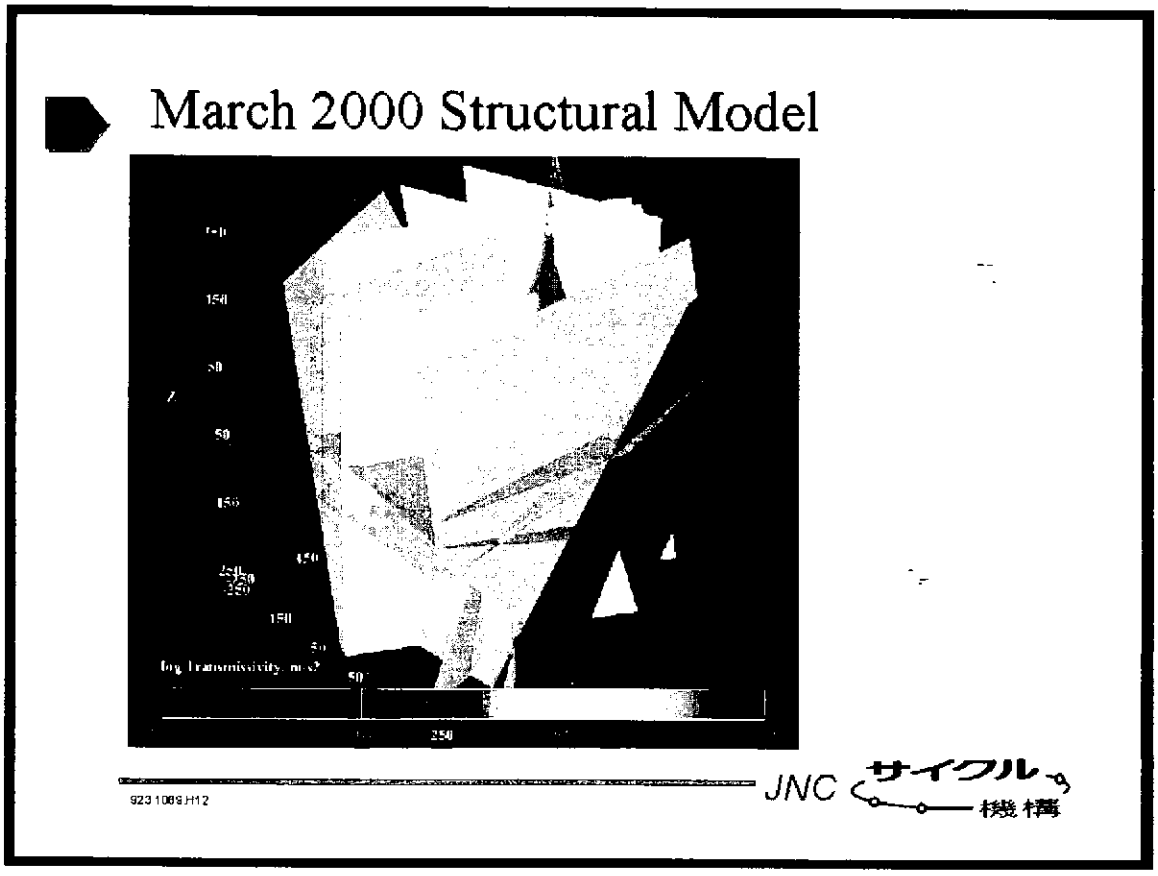

Figure 2-2: TRUE-Block Scale Deterministic Structures

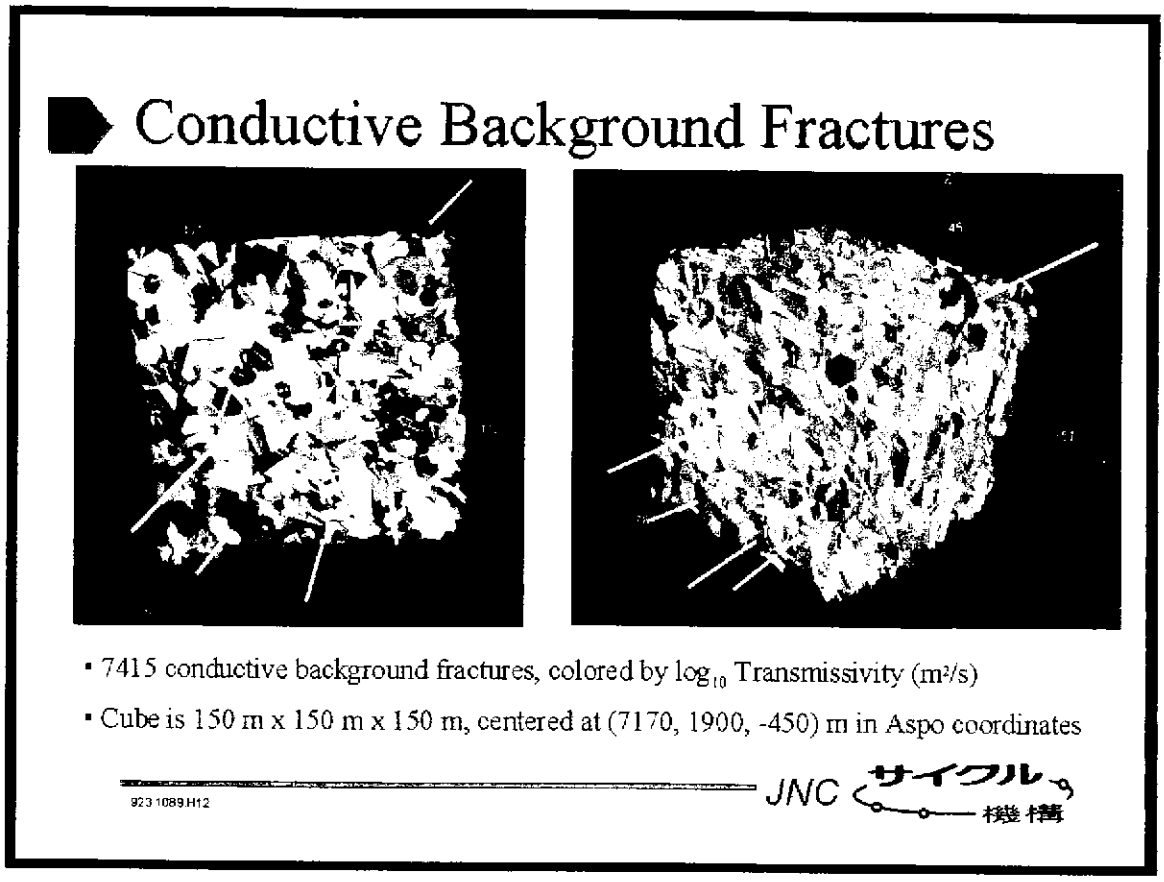

Figure 2-3: TRUE Block Scale Stochastic Discrete Feature Model

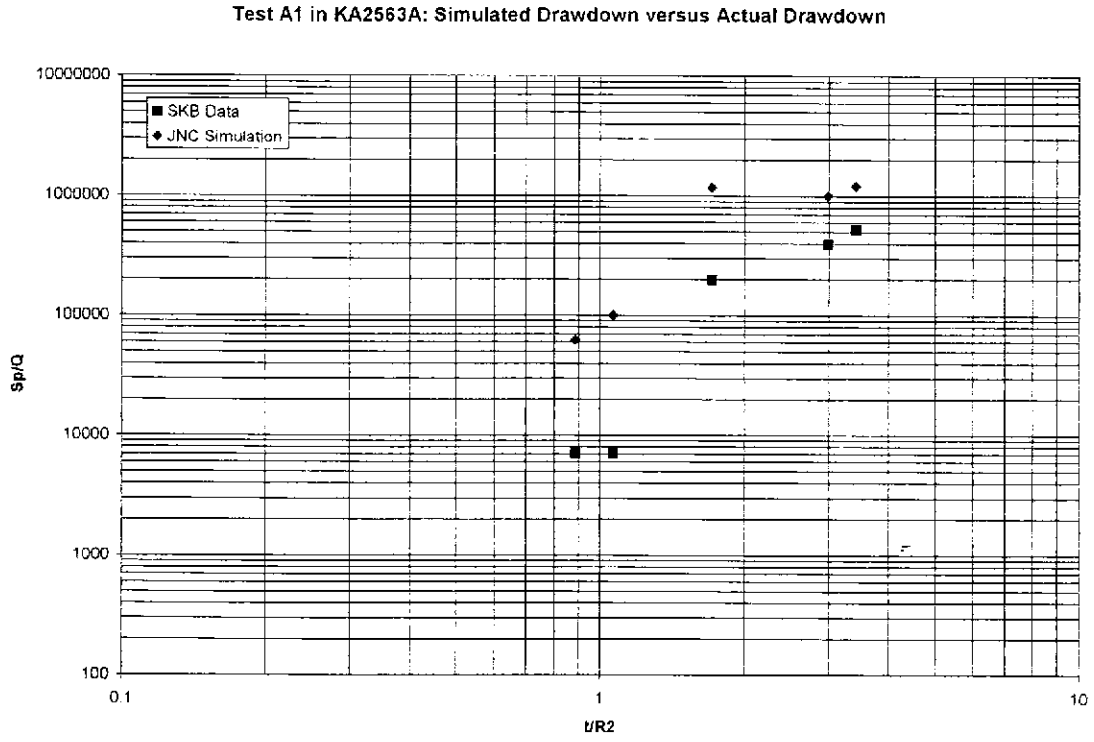

Figure 2-4: Hydraulic Model Calibration, Phase A-1 Distance Drawdown

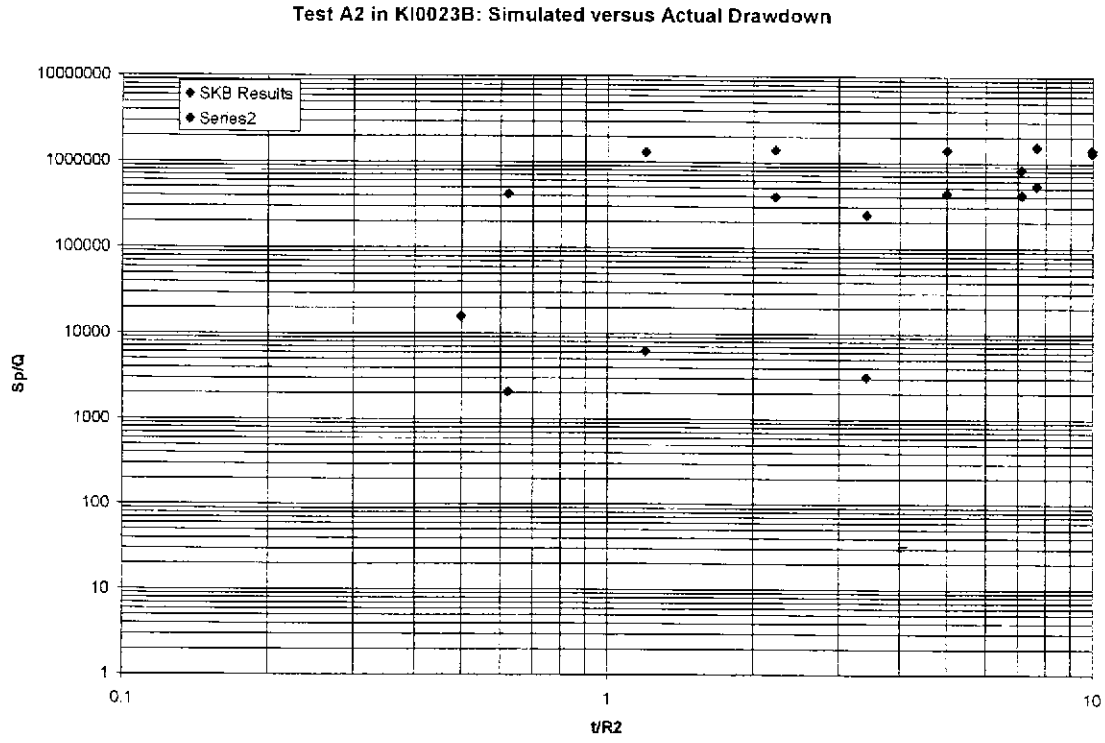

Figure 2-5: Hydraulic Model Calibration. Phase A-2 Distance Drawdown

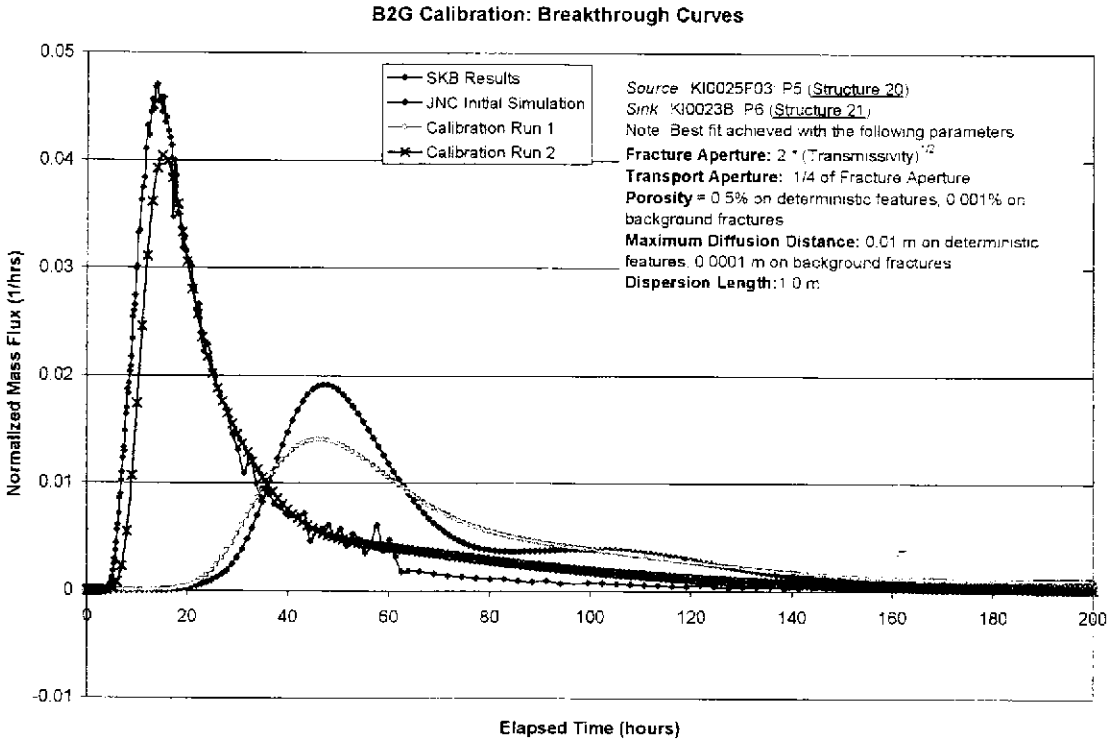

Figure 2-6: PAWorks Transport Model Calibration, Phase B Test 2G (Naphthionate)

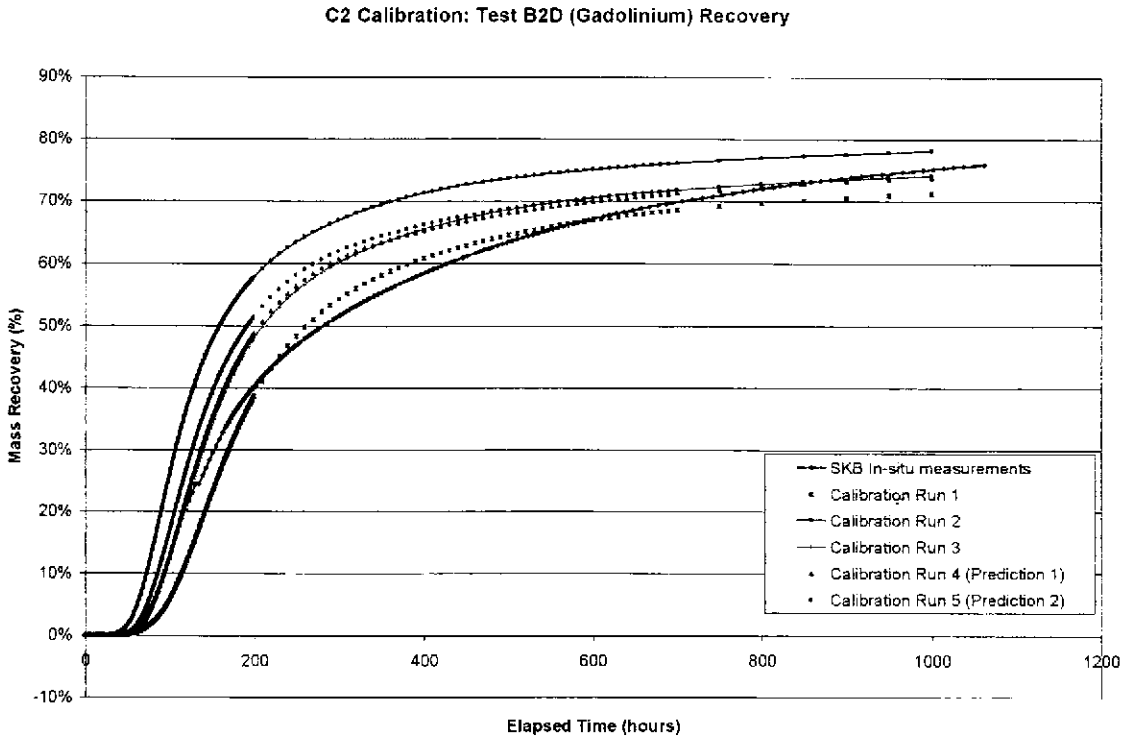

Figure 2-7: PAWorks Transport Model Calibration, Phase B Test 2D Recovery

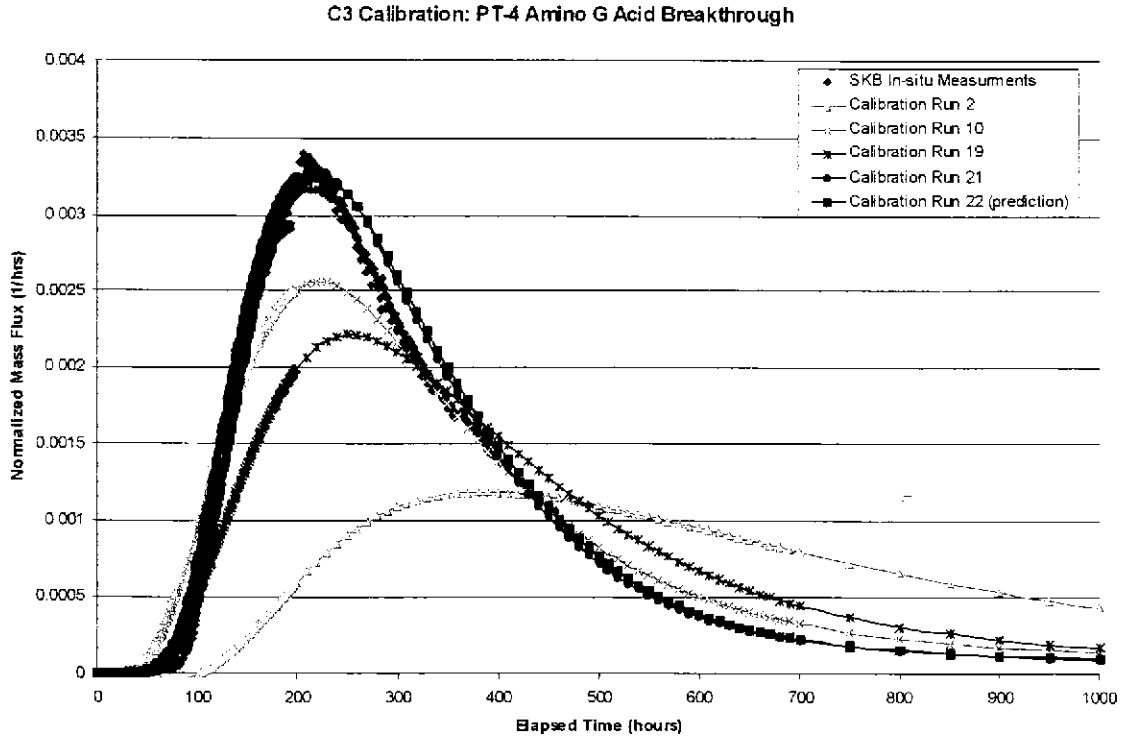

Figure 2-8: PAWorks Transport Model Calibration, PT-4 Amino G Breakthrough

3. TASK 2: ÄSPÖ TASK 5 INTEGRATED GEOCHEMICAL/ HYDROGEOLOGICAL ANALYSIS

The "Task 5" project is a 2 km scale simulation of flow and transport over a 7 year period at Äspö island, including the effects of variable density flow. "Task 5" includes development of a site scale geochemical model, and pathways analysis of geochemical end-members from initial spatial distributions and boundary conditions to breakthrough time histories in the Äspö tunnels. It also includes calibration and prediction of drawdowns and end-member breakthroughs in response to tunnel construction.

During H-12, Golder supported JNC through three subtasks:

- Task 2.1: BGS Geochemical End-member Analysis;
- Task 2.2: Golder/JNC Re-evaluation of End-member Spatial Conditions; and
- Task 2.3: Pathways Analysis and Reporting.

For each of these tasks, Golder worked directly with JNC Tono staff, coordinating with JNC Tokai staff. The final project report for "Task 5" produced during HY-12 incorporates comments of JNC reviews as well as two outside independent reviews carried out on behalf of the Äspö Task Force.

3.1 Task 2.1: BGS Geochemical End-Member Analysis

Geochemical end-member analysis was carried out by Mark Cave of the British Geological Survey (BGS) under subcontract to Golder. This model used a "chemometric" principal component analysis algorithm (Cave and Harmon 1997, Cave and Wragg 1997), which makes no initial assumptions about the nature of the end-members present, and which considered all the contributions to chemical variability in the groundwater.

The basic approach is illustrated in Figures 3-1 and 3-2. Here matrix A is the supplied groundwater data matrix and matrices B and C need to be found. The process for finding matrices B and C was carried in four-stages:

- PCA and eigenvalue analysis were initially used in a similar fashion to the M3 method.
- The varimax rotated loadings matrix from the PCA of matrix A, containing the initial groundwater compositions, were used to produce a first approximation of matrix B, which contains the mixing proportions.
- The "pseudoinverse" method for non-square matrices was then applied to matrices A and B, to produce a first approximation of matrix C, which contains chemical

components that contribute to the chemical variability in the groundwater, some of which should correspond approximately to end-members.

- Matrices B and C were refined iteratively using the 'pseudoinverse' method until both matrices contained estimates of mixing proportions and chemical component compositions that are consistent with the groundwater compositions in the original matrix A.

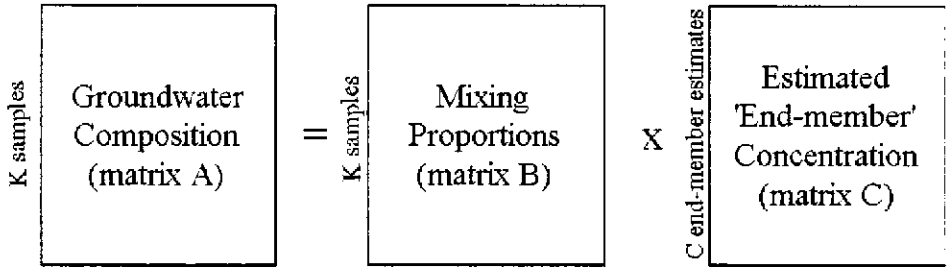

Figure 3-1: Relationships between matrices used in the revised modeling

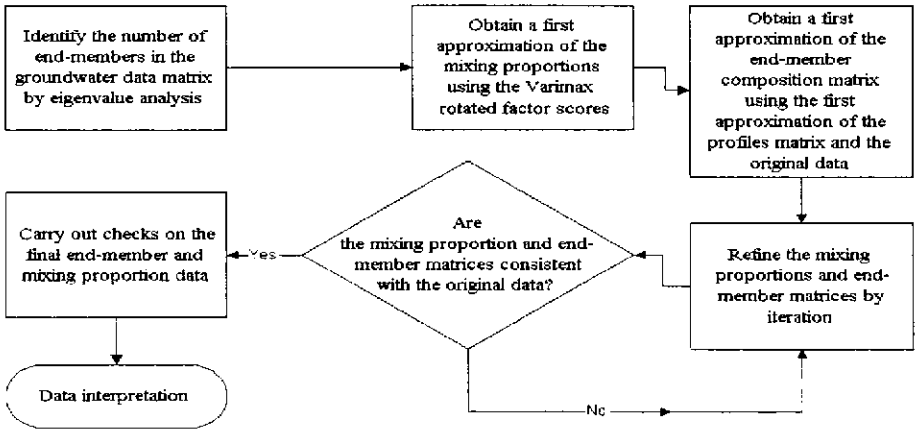

Figure 3-2: Summary of Principal Component Geochemical Analysis

It is important to note that the chemical components obtained from the new modeling are not principal components, but are derived from the principal components. Neither are the chemical components 'end-members' in the sense of the M3 end-members. However, it is expected that there should be some similarities between compositions of the new chemical components and the "M3 "components calculated by SKB.

To compare the results of the new modeling and the results of the M3 end-member modeling, the new mixing proportions were also expressed in terms of proportions of the original M3 end-members. This was done by a least squares approach, using the proportions of the new chemical components in each of the original M3 end-members and in each of the other waters as follows.

Figure 3-3 compares concentrations of a relatively reactive solute (Na) and a relatively unreactive solutes (Cl, $\delta^{18}O$ and δH) reconstructed from the statistically derived chemical components, and the actual concentrations. Similar plots were produced for all the constituents.

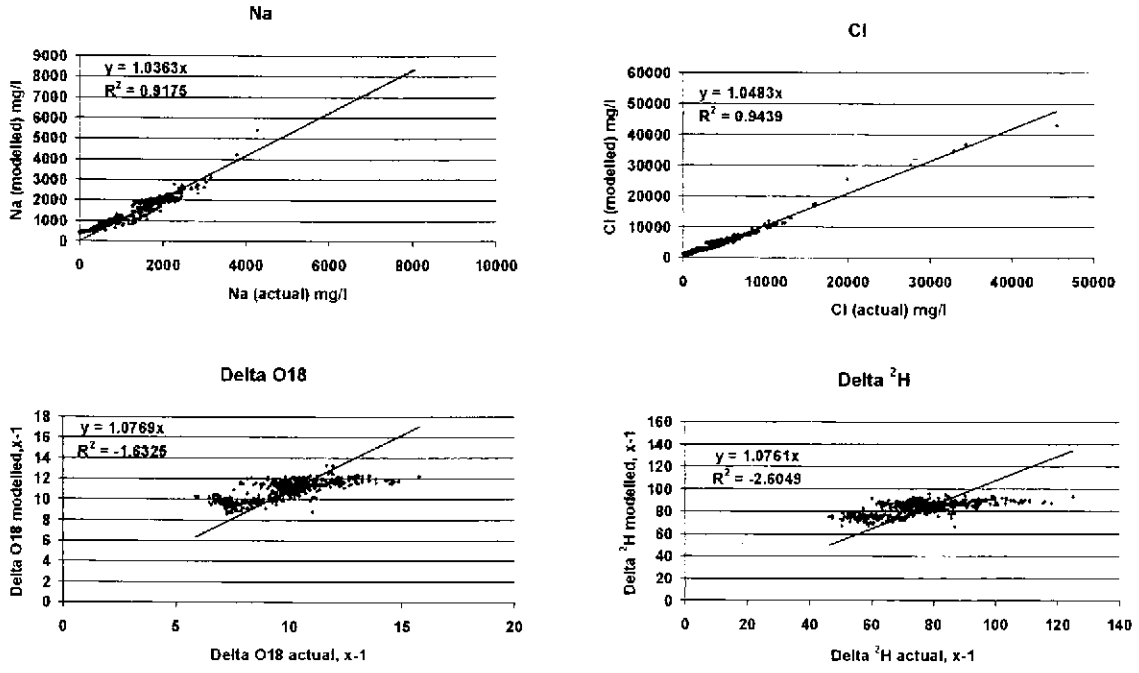

Figure 3-3: Performance of BGS Principal Component End-Member Analysis

Tables 3-1 and 3-2 illustrate the "M-3" geochemical and the PCA end-member analyses. The PCA end-member is objective, in that it does not bias toward "real" waters, but works directly from the available geochemical measurements. The PCA analysis has the advantage that it can be used to define end members with very little residual error.

	Na	K	Ca	Mg	HCO3	Cl	SO4	O18	D	Tr
Brine ref. w.	8500	45.5	19300	2.12	14.1	47200	906	-8.9	-44.9	4.2
Baltic Sea ref. w.	1960	95	93.7	234	90	3760	325	-5.9	-53.3	42
Glacial ref. w.	0.17	0.4	0.18	0.1	0.12	0.5	0.5	-21	-158	0
Meteoric ref. w.	0.4	0.29	0.24	0.1	12.2	0.23	1.4	-10.5	-80	100

Table 3-1: "M-3" Geochemical End members

Model 2 Component	Na	K	Ca	Mg	HCO3	Cl	SO4	O18	D	Tr
1	8508.6	5.1	17235.0	0.0	47.1	44001.5	800.3	-11.8	-75.7	14.6
2	2066.3	0.0	1379.1	169.1	225.4	6163.5	0.0	-8.8	-68.5	0.0
3	456.9	5.5	258.4	16.7	0.0	1207.9	79.8	-12.4	-94.2	0.0
4	0.0	1256.2	0.0	2020.1	505.6	0.0	0.0	0.0	0.0	492.0
5	0.0	0.0	0.0	0.0	22039.5	0.0	0.0	0.0	0.0	0.0
6	0.0	0.0	0.0	0.0	298.8	0.0	0.0	0.0	0.0	391.5
7	2021.3	17.8	205.4	8.0	0.0	3230.3	1284.4	-14.3	-107.9	0.0

Table 3-2: Principal Component Analysis Geochemical End Members

3.2 Task 2.2: Golder/JNC Re-evaluation of End-member Spatial Conditions

The approximation methods used to interpolate the spatial distribution of end-member initial conditions during H-11 were identified as a major source of uncertainty for the geochemical pathway predictions. Previous analysis used a form of kriging to distribute geochemical endmembers according to a spatial grid from the limited borehole sample locations. During HY-12, Golder carried out updated analyses to establish the initial spatial distribution of geochemical end-members. This analysis works from an assessment of the geochemistry on a fracture-zone by fracture-zone basis, and then extended the approximation to the rock mass assuming that the original chemistry in the background fractures is similar to the chemistry in adjacent major fracture zones.

The HY-12 geochemical initial condition interpolation algorithm is summarized as follows:

- Step 1: Project measured chemistry to adjacent major fracture zones.
- Step 2: Obtain location of particle using the PAWorks particle backtracking algorithm

- Step 3: If particle is not within a main fracture zone, project particle to the nearest zone
- Step 4: Interpolate chemistry from the chemistry on these fracture zones

For particles under Aspo Island, the interpolation was carried out using measured chemistry from under Aspo Island. For particles under the Baltic, the interpolation was carried out using measured chemistry from under the Baltic. This interpolation approach is limited by the number of available data points.

The resulting interpolation provided a significantly better match to values as observation points than the gridded approximation used during HY-11.

3.3 Task 2.3: Pathways Analysis and Reporting

During HY-12, Golder developed an improved pathways analysis algorithm for Task 5, based on the use of particle backtracking rather than graph theory pathways analysis. We used this approach to recalculate all of the Task 5 end-member transport pathways. The combination of improved end-members, improved initial conditions, and improved pathway analysis significantly reduced the error and uncertainty in the geochemical/hydrogeologic assessment when compared to that achieved during HY-11.

The particle back-tracking algorithm is summarized as follows: Particle back-tracking starts with a full series of transient "snapshots" of the head field within the 2 km scale model during the modeled period, for a total of 76 monthly time steps. Particle backtracking algorithm uses the "up-gradient" network from the sampling borehole interval to the outer boundaries of the model.

The particle backtracking pathways algorithm stochastically distributes particles at pipe intersections in proportion to the pipe flow rates to determine the spatial pattern of path. The number of particles taken by each pipe weights the relative importance of the pipe for the pathways from the geochemical initial conditions to the sink at the Äspö tunnel.

Advantage of this algorithm is that the upstream network finds all possible pipes. Therefore provided enough particles are used, results include all potential pathways, not just those identified as "most significant" by the pathway graphical search used in HY-11.

Example pathways produced by the particle backtracking pathway algorithm are shown in Figures 3-4 and 3-5. Figures 3-6 through 3-9 illustrate the improved matches obtained between measured and simulated end-member breakthroughs using the procedures developed during HY-12.

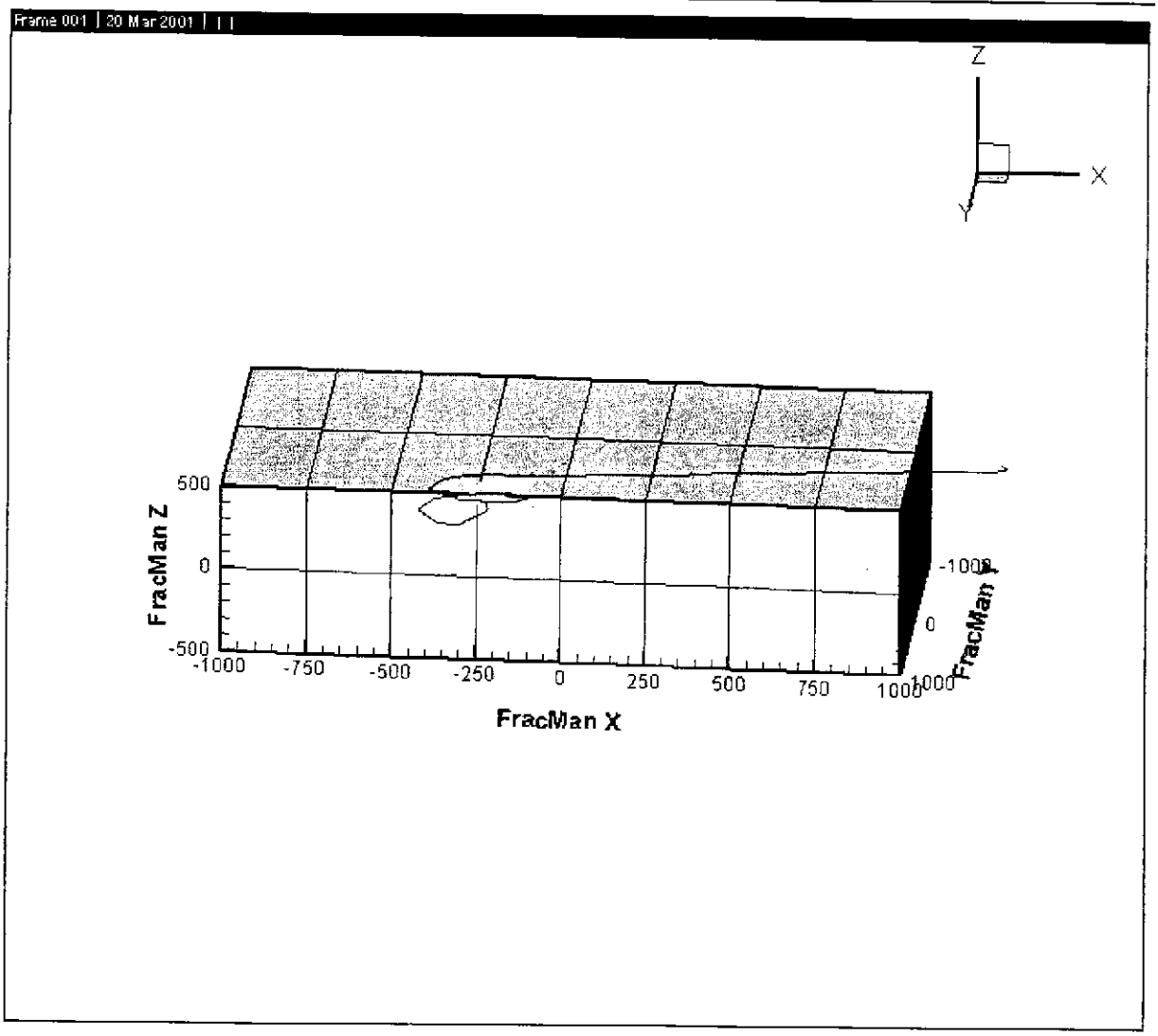

Figure 3-4 Pathways for SA2074A

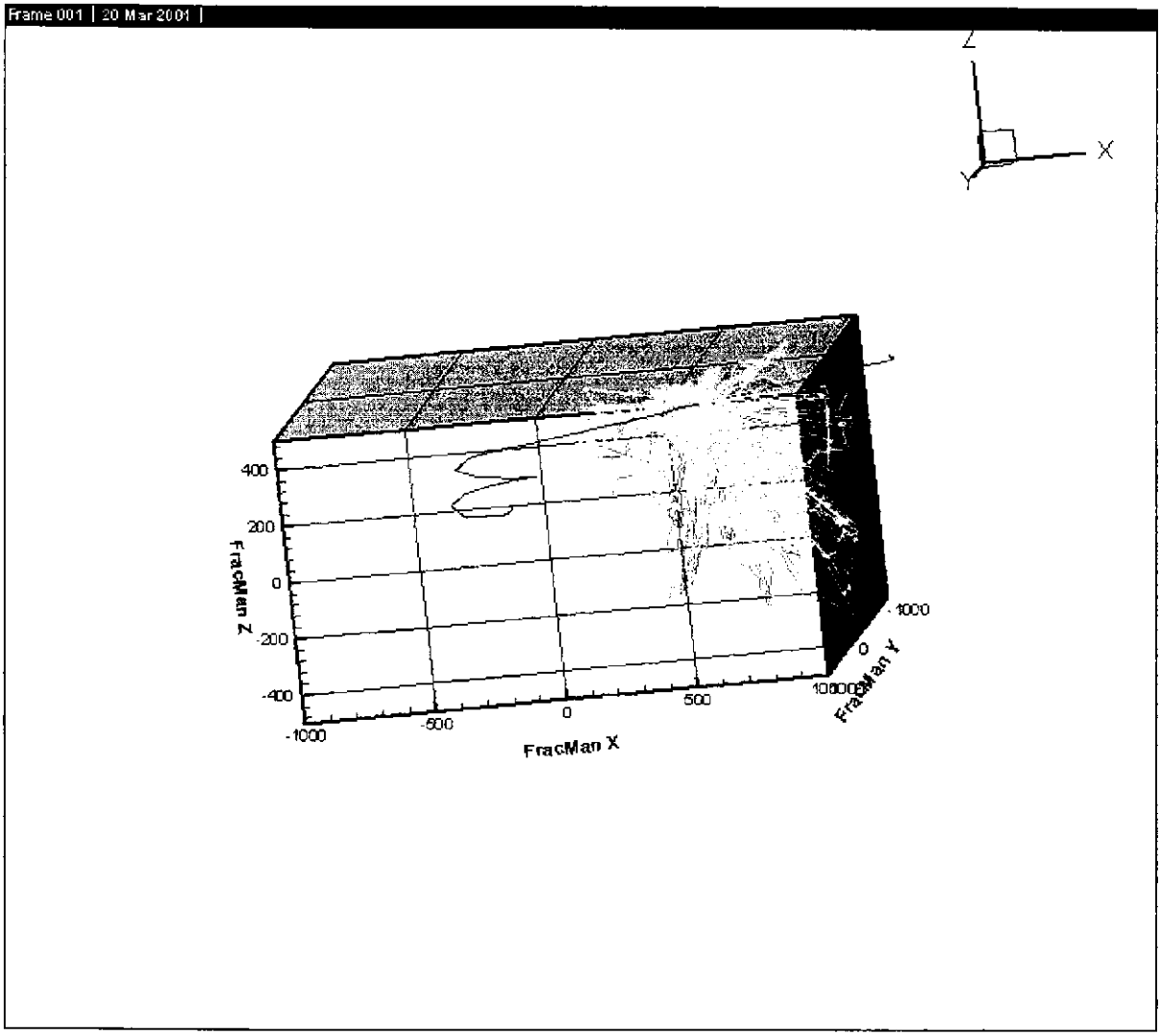

Figure 3-5: Pathways for SA0813B

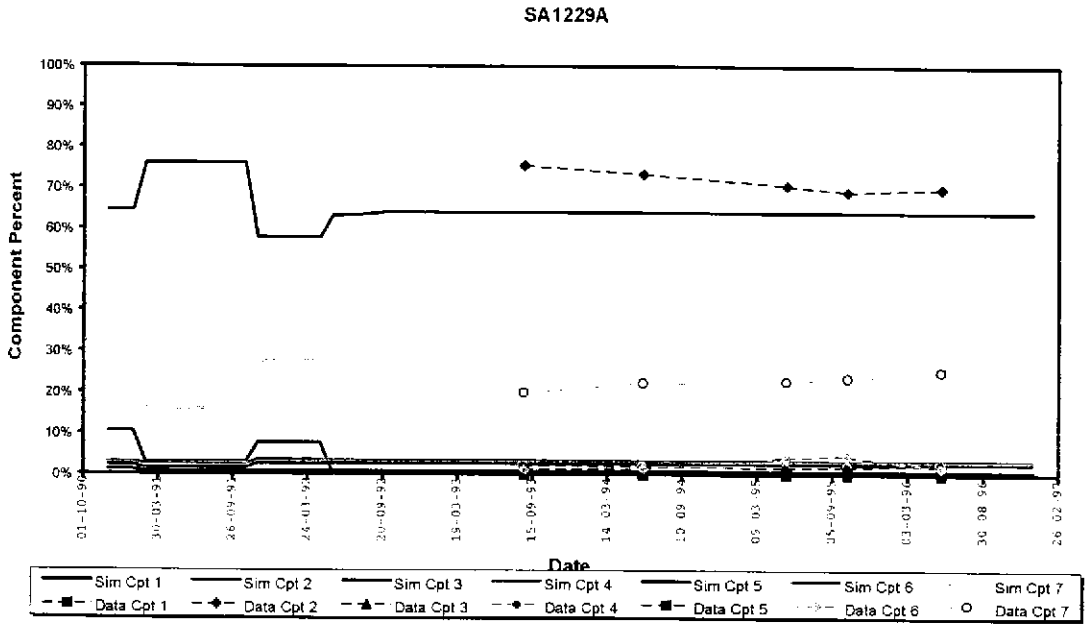

Figure 3-6: Component Percentages for SA-1229A

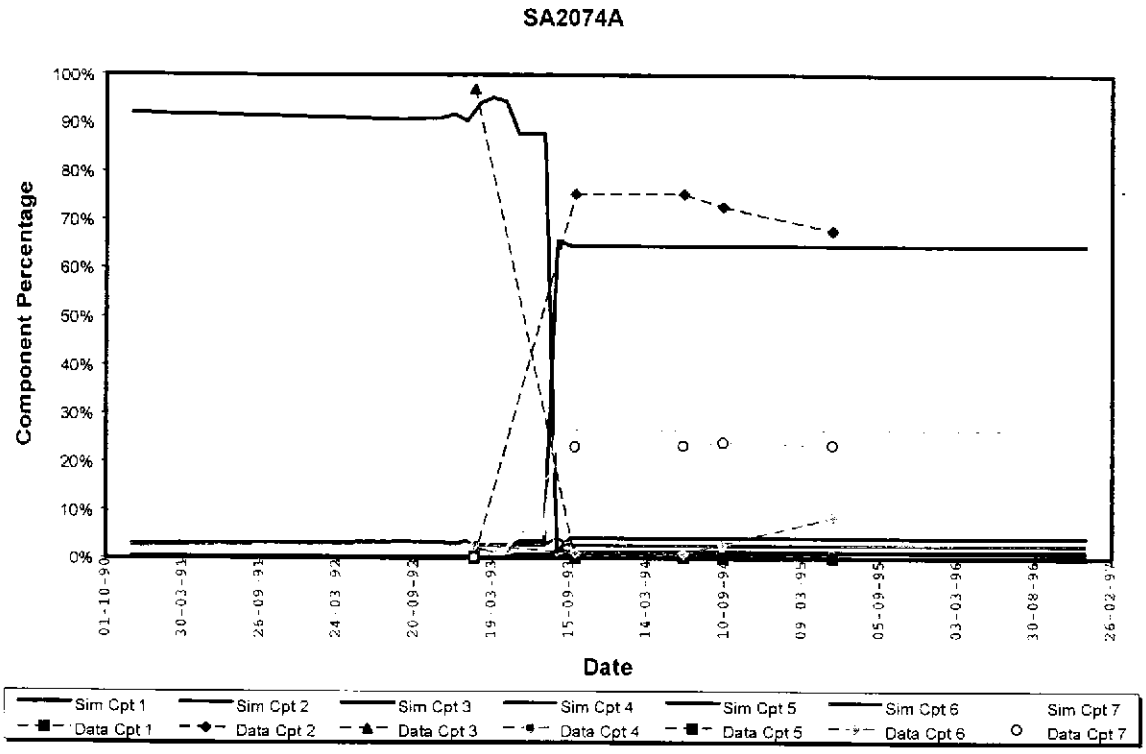

Figure 3-7: Component Percentages for SA 2074A

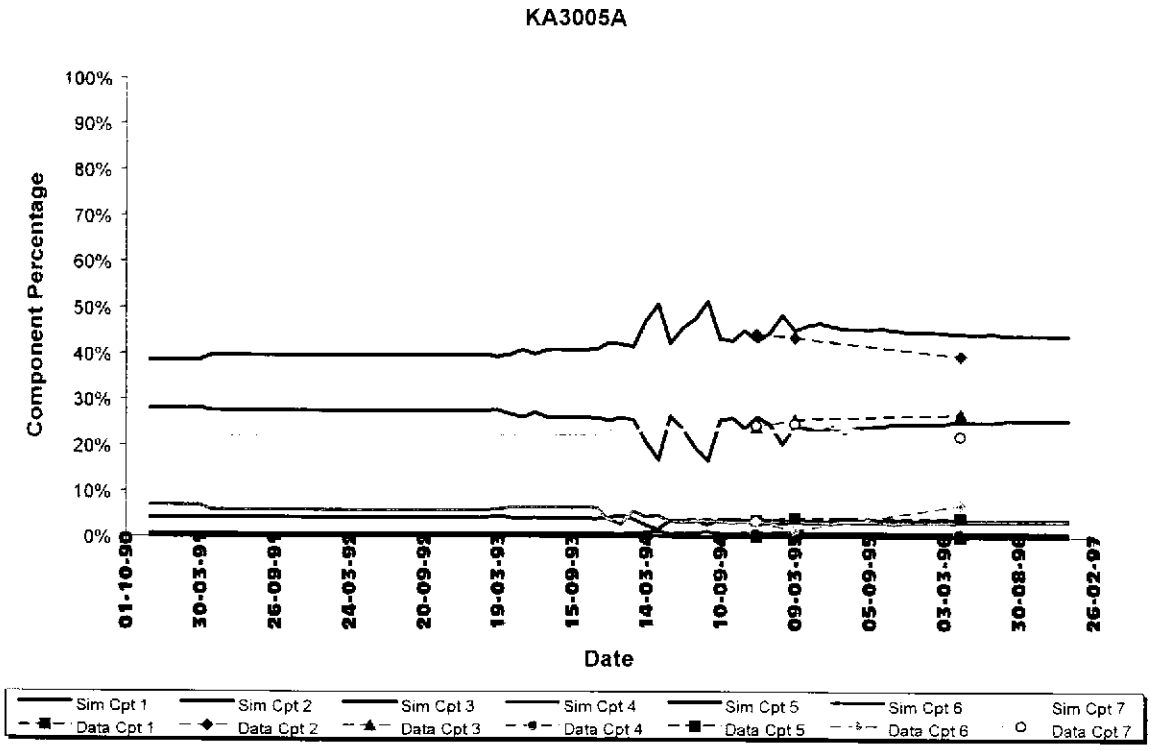

Figure 3-8: Component Percentages for KA-3005A

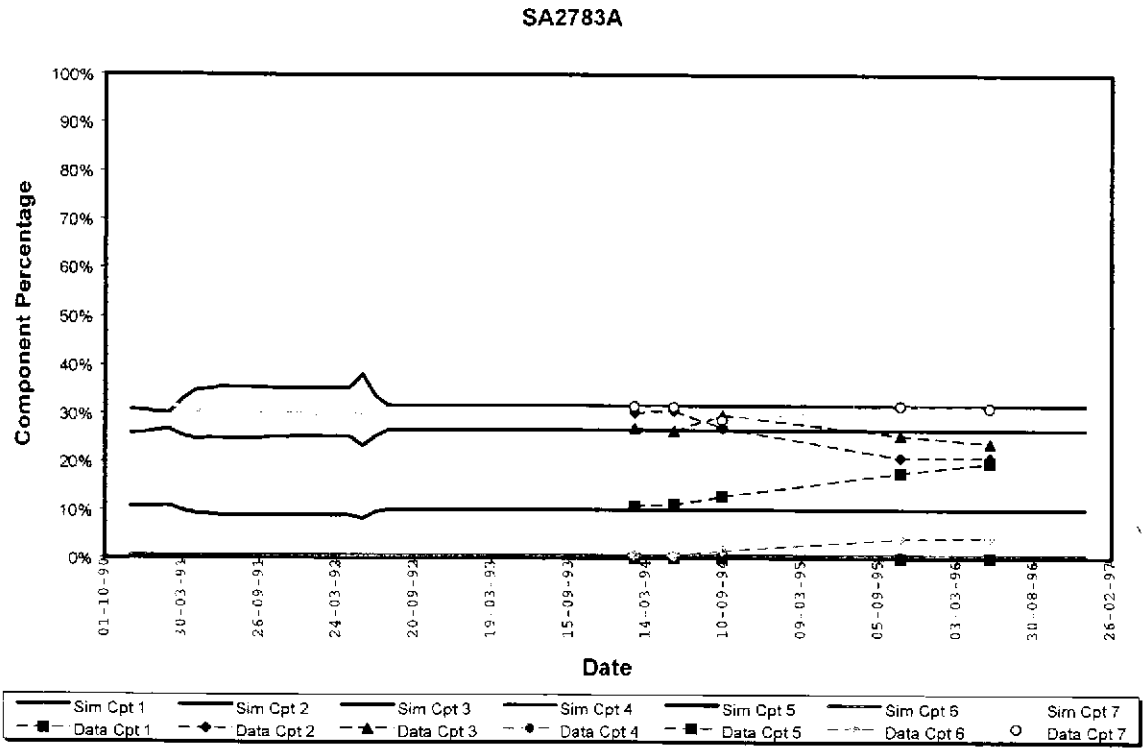

Figure 3-9: Component Percentages for SA-2783A

4. TASK 3.1: DISCRETE FEATURE ANALYSIS OF DATA FROM THE MIU SITE

During H-12, Golder assisted JNC in evaluating the spatial structure, orientation distribution, size, hydraulic, and transport properties of discrete features at the MIU site. Golder provided advice and assistance to JNC personnel for DFN modeling. Particular activities included:

- Advice for DFN analysis of fracture data;
- Advice for Fractal Analysis; and
- Review and Recommendations for DFN Flow and Transport Modeling at the Site Scale.

This main focus of HY-12 support for the MIU project was in preparation of a document providing recommendations for the proposed approach for the DFN modeling and groundwater simulation of the MIU project. Recommendations include a suggested methodology for constructing the discrete fracture network (DFN) model, and running the sensitivity analyses.

The review document highlighted the areas of the data analysis and model construction which have a strong effect on the modeling results, and to discuss, and make recommendations on, the approaches that may be used to achieve a useful model of the MIU site.

The following are addressed in the review document:

- Issues associated with the technical specification;
- Data analysis – methodology and associated problems;
- Size of DFN model and truncation;
- Structures in .SAB file;
- Boundary Conditions;
- LTG and "particle tracking";
- Calibration of model;
- Pathways analysis;
- Sensitivity analysis; and
- Choice of finite element.

5. CONCLUSIONS

During HY-12, Golder Associates' major accomplishments in support of JNC/Tono included the following:

- Refinement of the TRUE-Block Scale hydrostructural model, and implementation of that model as a discrete fracture network and channel network model;
- Calibration of the TRUE-Block Scale model against hydraulic interference and solute transort measurements;
- Prediction of "Phase A" conservative tracer and "Phase C" sorbing tracer transport experiments for the TRUE-Block Scale project;
- Support to DFN modeling for the MIU project; and
- Geochemical and hydrogeological analysis and simulation to quantify and reduce uncertainty in the site scale hydrogeochemical model of the Äspö island site for Task 5 of the Äspö Task Force on Modelling of Groundwater Flow and Transport of Solutes.

6. REFERENCES

Cave, M.R. and Wragg, J, 1997. Measurement of Trace Element Distributions in Soils and Sediments Using Sequential Leach Data and a Non-specific Extraction System With Chemometric Data Processing. *Analyst*, 122, 1211-1221.

Cave, M.R. and Harmon, K, 1997. Determination of Trace Metal Distributions in the Iron Oxide Phases of Red Bed Sandstones by Chemometric Analysis of Whole Rock and Selective Leachate Data. *Analyst*, 122, 501-502.

APPENDIX A

DISCRETE FRACTURE NETWORK AND CHANNEL NETWORK MODELING, TRUE BLOCK SCALE EXPERIMENT, ÄSPÖ, SWEDEN

ÄSPÖ HARD ROCK LABORATORY TECHNICAL NOTE

TN-02-XX

TRUE BLOCK SCALE PROJECT

CHANNEL NETWORK AND DISCRETE FRACTURE NETWORK ANALYSIS OF HYDRAULIC INTERFERENCE AND TRANSPORT EXPERIMENTS

W. Dershowitz[1], K. Klise[1], A. Fox[1]

S. Takeuchi[2], M. Uchida[2]

[1]Golder Associates, Seattle

[2]Japan Nuclear Cycle Development Institute (JNC), Tono and Tokai, Japan

February 2001

Keywords: Äspö, True Block Scale, FracMan, Tracer Transport, Fractured Rock Modeling

FORWARD

This report describes channel network and discrete fracture network analysis of hydraulic interference and tracer tests at the 100 meter scale in fractured granite, within the context of the Äspö TRUE Block Scale Project. This work was carried out by the JNC/Golder team, sponsored by the Japan Nuclear Cycle Development Institute (JNC), in Tono, Japan.

The modeling is based on a hydrostructural model developed from a combination of geological, geophysical, and hydrogeological data. This model was used to predict conservative tracer transport, and was then refined and re-calibrated for sorbing tracer transport.

ABSTRACT

This report describes channel network and discrete fracture network flow and transport modeling by the JNC/Golder team for the Äspö TRUE-Block Scale project Tracer Testing Stage (TTS). The fracture network design used for the model combines the deterministic features of the March 2000 revised structural model (Doe, 2000) and the stochastically-generated background fractures based on (Dershowitz, 2000).

The DFN/CN modeling described in this report was carried out to improve the understanding of flow and transport in fracture networks at the 50 to 200 meter scale. This was achieved by calibrating the models against hydraulic and conservative tracer experiments, and then using the resulting calibrated models to predict sorbing tracer transport. Particular emphasis was placed in these experiments on understanding of the differences between transport in single fractures and in fracture networks. These models include special elements developed to model fracture intersection zone (FIZ) effects.

This work was carried out in a series of model update, calibration, and prediction stages. Initial calibrations were purely hydrologic, and were used to produce predictions for conservative tracer transport. Later predictions focused on sorbing tracer transport using models calibrated to conservative tracer breakthrough. Parameters used to calibrate the model to the breakthrough and recovery of the in situ measurements include matrix porosity, diffusion distance, dispersion length, and transport aperture.

The sorbing tracer transport prediction of "Phase C" of the Tracer Test Stage program are compared to the in situ measurements. Of the14 tracers predicted, 10 tracers have recovery at the pumping location after the allotted time of the test. Several predictions result in good matches to the measured breakthrough. For the tracers which were poorly predicted, it was generally possible to improve the model by adjusting effective sorption parameters.

TABLE OF CONTENTS

LIST OF FIGURES

LIST OF TABLES

1. INTRODUCTION

This report describes the development and calibration of a discrete fracture network - channel network (DFN/CN) model for the TRUE-Block Scale site, and the use of this model for "blind" predictions of sorbing tracer breakthrough. The channel network (CN) model described in this report is based on the March 2000 Revised Äspö Structural Model (Doe, 2000) combined with stochastically-generated background fractures based on Dershowitz (2000).

The channel network was enhanced to include possible "Fracture Intersection Zone" (FIZ) channels at the intersection of conductive features where they could potentially influence solute recovery. These FIZ channels were assigned higher transmissivity and aperture. However, generic FIZ studies reported in Winberg et al.(2000) indicate that the primary effect of FIZ channels is in reducing mass recovery by providing pathways to alternative sinks within the rock mass.

The DFN/CN models were developed through three cycles of modeling: implementation, calibration, and prediction. Parameters used in previous model implementations were updated as the project hydrostructural model was updated. Phase C sorbing tracer predictions were made based on conservative tracer breakthrough measurements from Phase A and Phase B, together with earlier tracer tests. Sorption parameters were derived based on laboratory measurements (Winberg, 2000), together with calibrated values from the TRUE 1 single tracer experiments (Dershowitz et al., 2000).

2. DFN AND CN IMPLEMENTATION OF HYDROSTRUCTURAL MODEL

The hydrostructural model used to develop DFN/CN models is described in Winberg et al. (2001). Figure 2-1 and Figure 2-2 illustrate the TRUE-Block Scale hydrostructural model at the scale of the rock laboratory, and in the detailed region of the tracer tests. The model was synthesized on the basis of hydrological interpretations of pressure interference to drilling (
Figure 2-3), Posiva flow logs (
Figure 2-4), and hydraulic interference responses (Figure 2-5). The structural model also includes background fracturing based primarily on a combination of BIPS borehole imaging (Figure 2-6), geological insight, and Posiva flow logs.

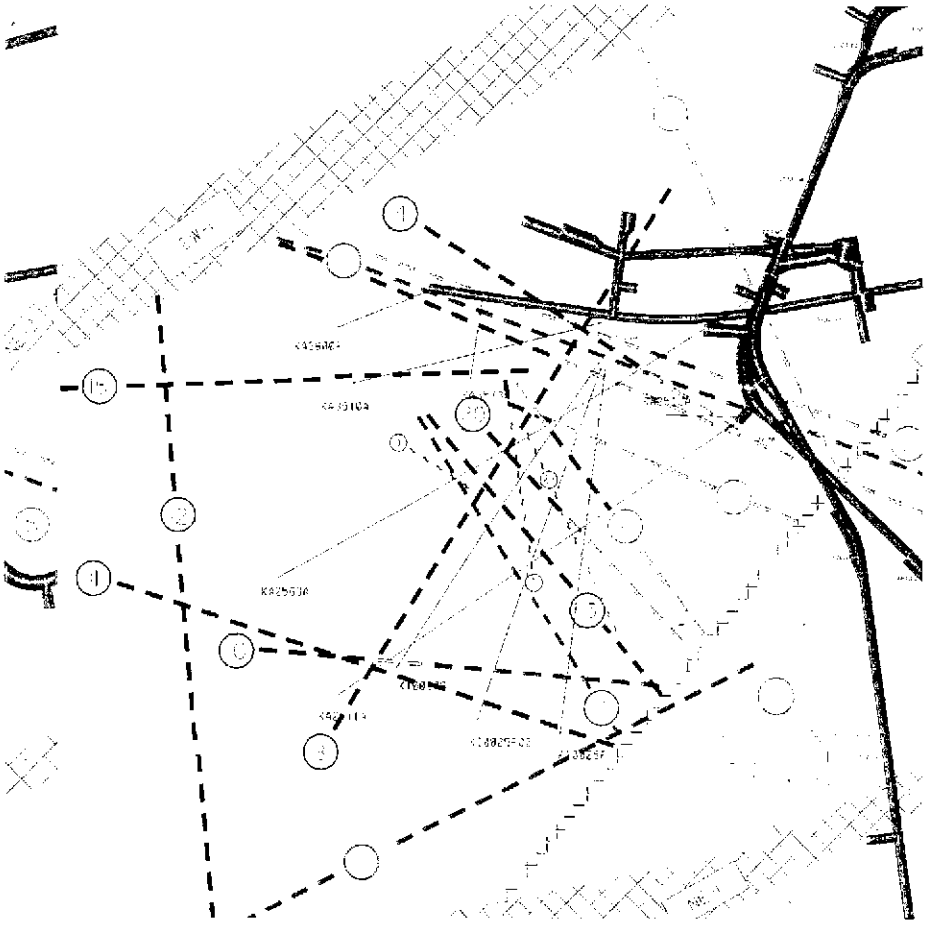

Figure 2-1 Äspö TRUE Block and Geologic Features

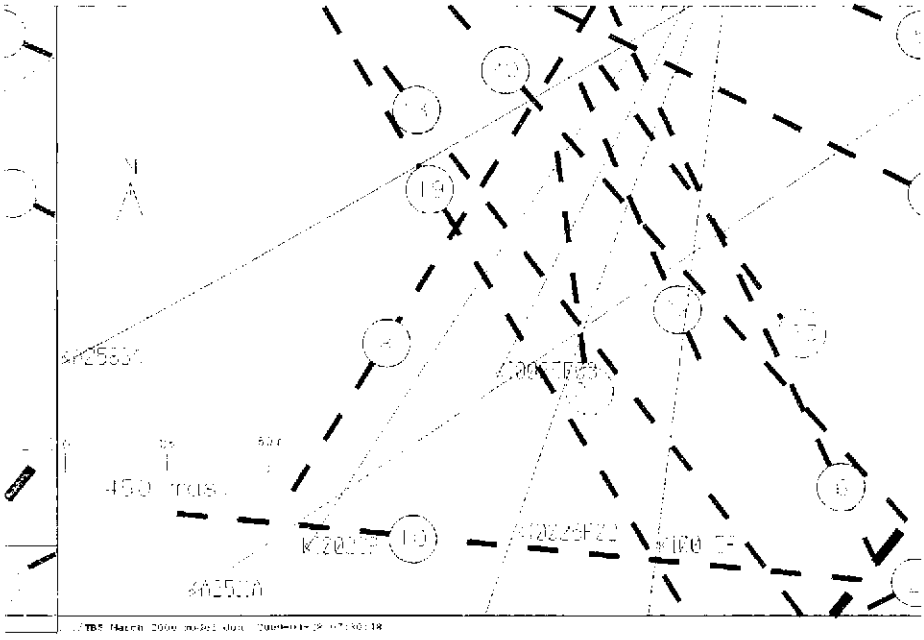

Figure 2-2 Geologic Model – Detail

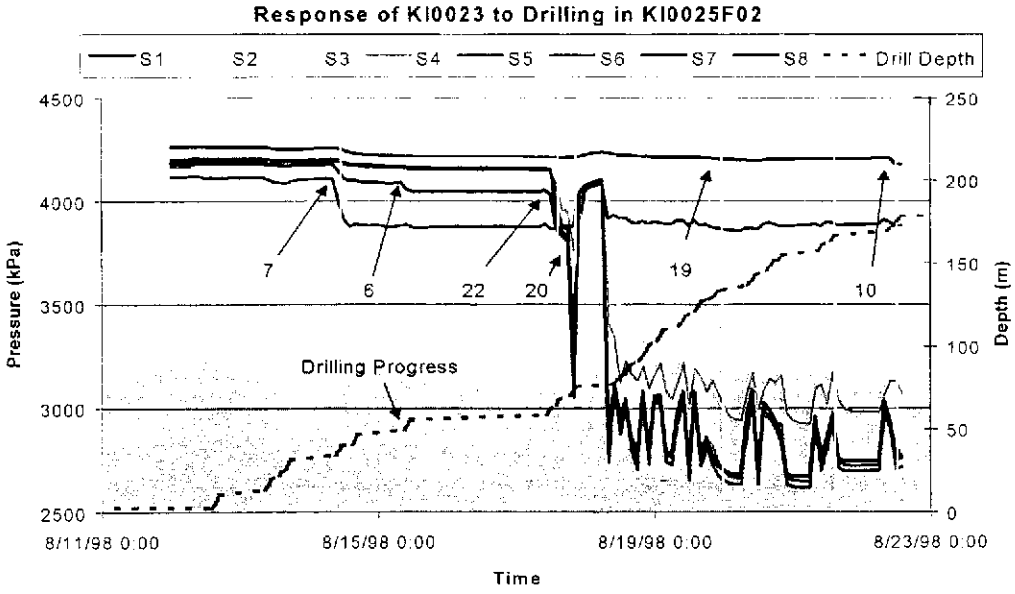

Figure 2-3 Drilling Response Data

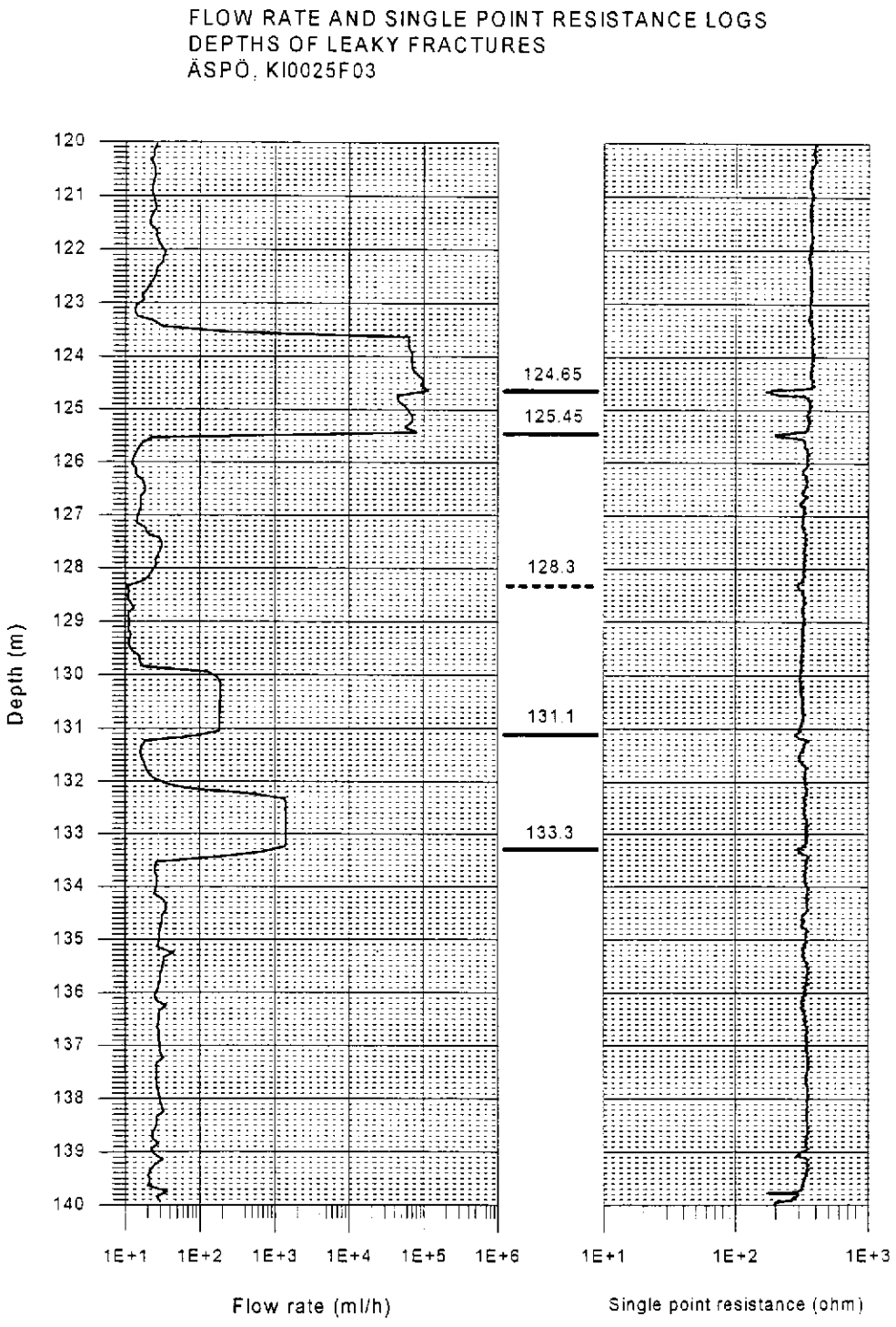

Figure 2-4 Posiva Flow Log Example

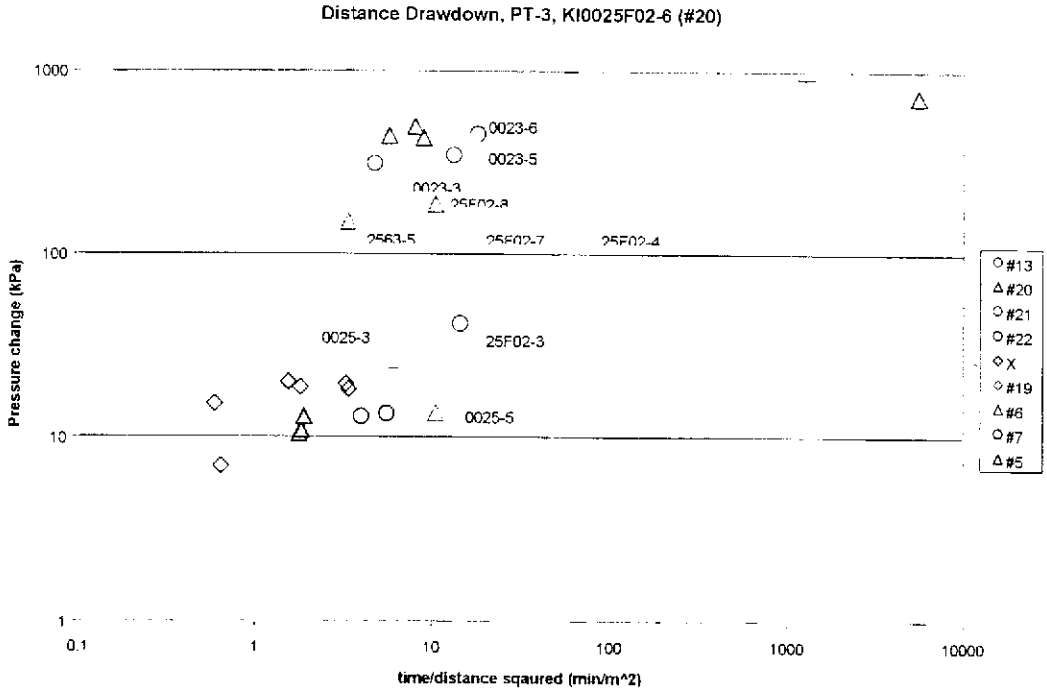

Figure 2-5 PT-3 Distance Drawdown (#20)

Figure 2-6 BIPS Features

The DFN/CN model incorporates the deterministic features contained in the March 2000 Revised Äspö Structural Model (Doe, 2000), and smaller, stochastically generated background fractures conditioned to borehole observations from the investigation in the tracer test stage (Dershowitz, 2000).

2.1 DETERMINISTIC FEATURES

Deterministic features were defined by directly implementing the March 2000 Revised Structural Model (Doe, 2000). The model is terminated along a 500m x 500m x 500m cube, centered at (1900, 7170, -450) in Äspö coordinates. Figure 2-7 shows a trace map view of this model at 450 meters below the surface. Figure 2-8 provides a three-dimensional visualization. Table 2-1 contains a summary of the features and their properties as incorporated into this model.

Table 2-1: Deterministic Features (after Doe, 2000)

Feature	strike	pole tr	dip
#6	327.50	237.50	88.6
#7	116.50	26.50	81.4
#13	322.80	232.80	66.4
#19	329.20	239.20	89.3
#20	318.50	228.50	84.93
#21	156.74	66.74	71.21
#22	154.64	64.64	69.02
#23	137.2	47.20	90
#24	130.24	40.24	81.62

Feature		Corners in Äspö Coordinates					
		1	2	3	4	5	6
#6	Easting	1784.327	1799.417	2118.921	2103.975		
	Northing	7420.639	7420.527	6919.361	6919.26		
	Elevation	-199.361	-700.79	-700.639	-199.507		
#7	Easting	1649.361	2150.793	2150.639	1649.45		
	Northing	7392.688	7143.232	7058.112	7307.397		
	Elevation	-199.361	-199.472	-700.639	-700.825		
#13	Easting	1842.699	2150.675	2150.66	1947.787	1649.385	1649.317
	Northing	7420.705	7014.25	6919.278	6919.305	7313.005	7420.613
	Elevation	-700.692	-700.551	-569.251	-199.295	-199.263	-347.88
#19	Easting	1730.108	1737.527	2036.671	2029.388		
	Northing	7420.649	7420.528	6919.351	6919.252		
	Elevation	-199.351	-700.793	-700.649	-199.502		
#20	Easting	1678.12	1737.532	2150.532	2150.665	2121.151	
	Northing	7420.609	7420.579	6953.287	6919.262	6919.338	
	Elevation	-199.481	-700.692	-700.674	-447.995	-199.461	
#21	Easting	1915.555	2130.957	1945.342	1729.951		
	Northing	7420.706	6919.275	6919.294	7420.487		
	Elevation	-199.294	-199.517	-700.706	-700.73		

Feature		Corners in Äspö Coordinates					
		1	2	3	4	5	6
#22	Easting	1936.065	2150.537	2150.52	1960.907	1723.467	
	Northing	7420.802	6968.196	6919.227	6919.378	7420.507	
	Elevation	-199.417	-199.457	-254.175	-700.782	-700.68	
#23	Easting	1720.653	1720.748	2150.533	2150.601		
	Northing	7420.575	7420.472	6956.347	6956.274		
	Elevation	-199.379	-700.765	-700.621	-199.533		
#24	Easting	1753.722	1649.372	1649.422	2150.684	2150.684	
	Northing	7420.443	7420.403	7411.863	6987.775	7084.454	
	Elevation	-199.168	-656.728	-700.739	-700.518	-199.444	

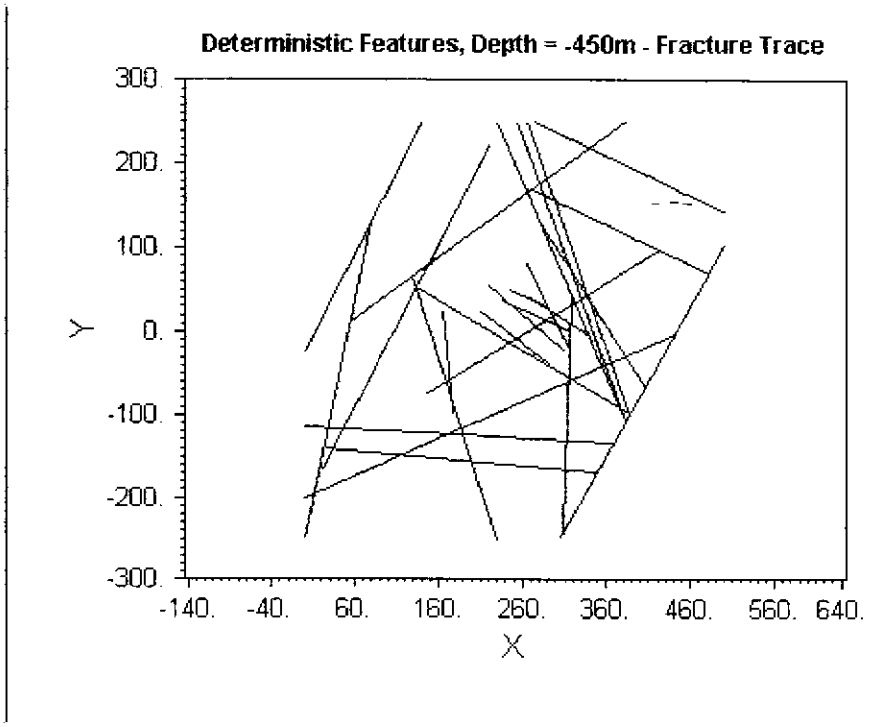

Figure 2-7: Trace Map of March 2000 Structural Model (Doe, 2000) Depth = 450m below surface

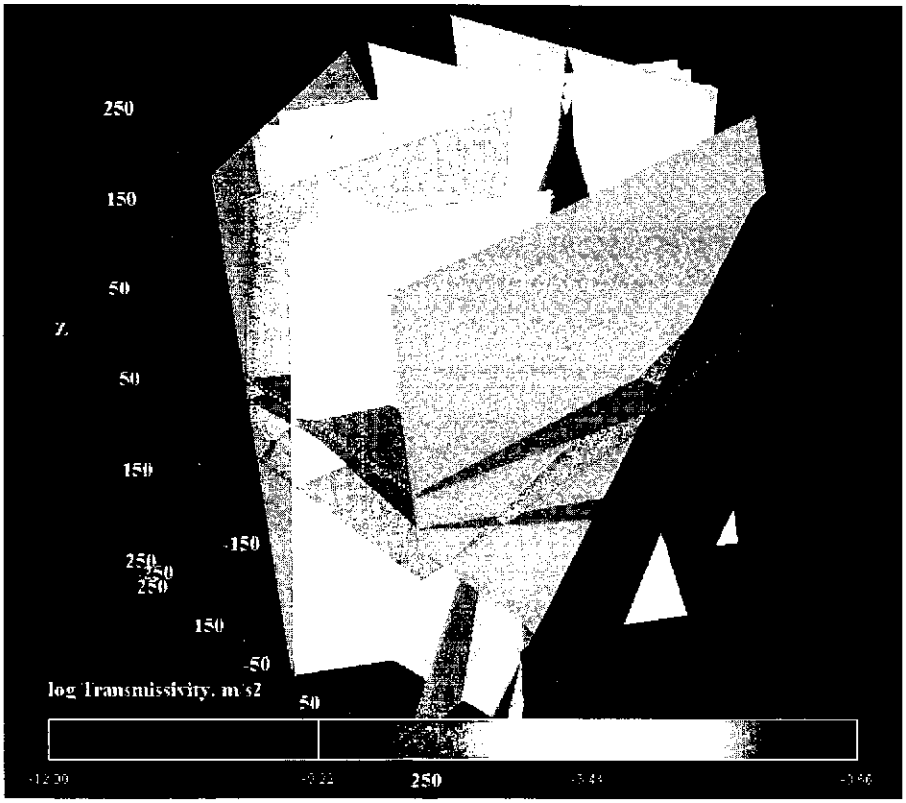

Figure 2-8: March 2000 Structural Model (Doe, 2000)

2.2 CONDITIONED STOCHASTIC BACKGROUND FRACTURES

In addition to the larger deterministic features of the March 2000 Revised Structural Model, the DFN/CN model contains stochastic background fractures conditioned to borehole data. These fractures are modeled on a smaller scale, and are present within a 150m x 150m x 150m cube inside the larger model. This cube is also centered at (1900, 7170, -450) in Äspö coordinates.

Borehole conditioning adjusts stochastically generated fractures based on global statistics (such as trace length, orientation, and transmissivity distributions) to match specific fracture observations in boreholes (Dershowitz et al, 1999). This allows for the development of models that precisely specify fracture geometry and properties where they are most important (i.e. at tracer injection holes, tunnel faces and observation wells).

The background fractures in this channel network model are derived from drill core logs, flow logging, and downhole camera logs (BIPS) from boreholes KA2511A, KA3510A, KA2563A, KI0025F, and KI0023B. In addition, preliminary POSIVA flow logs from KI0025F02 were incorporated into the model.

Table 2-2 presents a summary of properties for the stochastic background fractures, Figure 2-9 illustrates a realization of the stochastically generated fractures in the model.

Table 2-2 Stochastic Background Fracture DFN Properties (Dershowitz, 2000)

Parameter	Basis	Set #1	Set #2
Orientation Distribution	Two Fitted Sets to BIPS camera logs (NeurISIS)	Fisher Distribution Mean Pole (Trend, Plunge) = (211,0.6) Fisher Dispersion = 9.4	Fisher Distribution Mean Pole (Trend, Plunge) = (250,54) Fisher Dispersion = 3.8
Intensity P_{32}	Flowing Posiva Log Features 0.29 m^2/m^3 total	0.16 m^2/m^3 (55.2% of fractures)	0.13 (44.8% of fractures)
Transmissivity	Flowing Posiva Log Features, OxFilet Analysis of Packer Tests	Lognormal Distribution mean = -8.95 $\log_{10}$ m^2/s st.dev = 0.93 $\log_{10}$ m^2/s	Lognormal Distribution mean = -8.95 $\log_{10}$ m^2/s st.dev = 0.93 $\log_{10}$ m^2/s
Size Equivalent Radius	Hermanson et al. (1997)	Lognormal Distribution mean = 6 m st.dev. = 3 m.	Lognormal Distribution mean = 6 m st.dev. = 3 m.
Spatial Pattern	Distribution, Fractal and Geostatistical Analyses	Baecher Model in TTS Region Fractal ($D \approx 2.6$) for larger scale blocks.	Baecher Model in TTS Region Fractal ($D \approx 2.6$) for larger scale blocks.

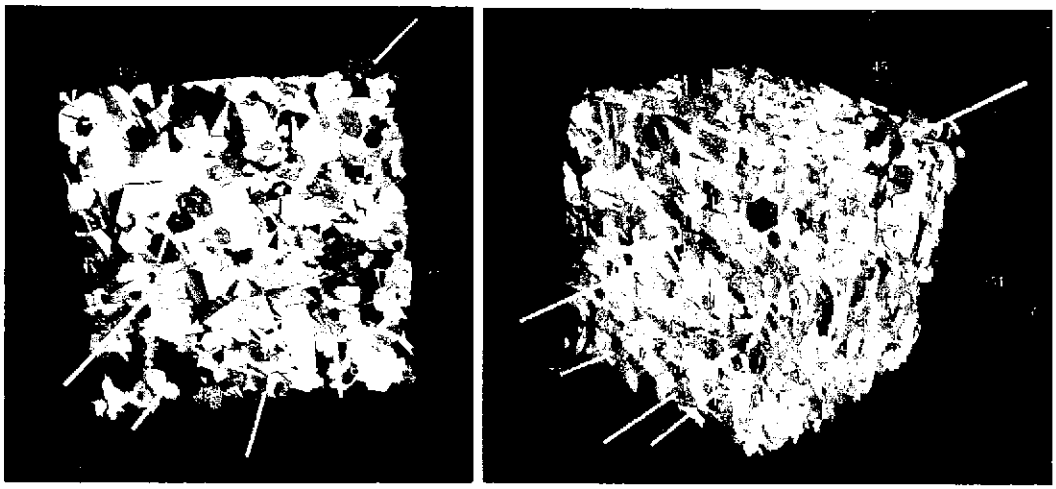

Figure 2-9 Conductive Background Fractures

7415 conductive background fractures, colored by log10 Transmissivity (m2/s). Cube is 150 m x 150 m x 150 m, centered at (7170, 1900, -450) m in Äspö coordinates.

2.3 CHANNEL NETWORK (CN) MODEL

2.3.1 Transforming of DFN Model to CN Model

Fracture networks represent a three-dimensional flow and transport regime made up of interconnected two-dimensional features (fractures). Channel networks are a method of reducing the complexity of flow and transport solutions within fracture systems to improve computational efficiency and the representation of channeling processes along fracture planes. They reduce flow and transport to a one-dimensional process along "stream tubes", which can significantly reduce processing time. A channel network model transforms a 3D discrete fracture network into a network of 1D pipes. Pipes are geometric connections between fracture traces formed by the intersection of two or more fractures (Dershowitz et al. 1998).

The pipes that make up the pathways within a channel network are, at the very basic level, derived from continuum streamlines defined by pressure contours. However, since both connectivity and flow in most fractured rocks are controlled by fractures, a smooth, continuous field of streamlines may not accurately define the flow field. A channel network takes these variations due to geometry into effect. Each fracture intersection is reduced from a line connecting two points to a single node. Channels, or "pipes", simply become lines connecting nodes. Pathways are composed of multiple pipes. Pipe properties, such as aperture, transmissivity, roughness and mineral infillings are either derived from the fractures themselves or are specified independently. Figure 2-10 illustrates the basic methodology behind the channel network approach.

A discrete fracture network (DFN) model is converted to channels through the use of the PAWorks software package (Dershowitz et. al., 1998). A 3-D network of fractures is first converted into a 1-D pipe network mesh. The finite-element code MAFIC (Miller et al, 1999) is then used to calculate

heads and fluxes at all nodes to produce a flow solution for the network. The PAWorks module analyzes transport pathways based on a search algorithm. Transport with PAWorks channel networks can be solved using the Laplace Transform Galerkin algorithm, which provides for advection-dispersion, sorption onto the fracture surface, diffusion into the rock matrix and stagnant (non-flowing) water adjacent to the flowing fracture, and for radionuclide decay.

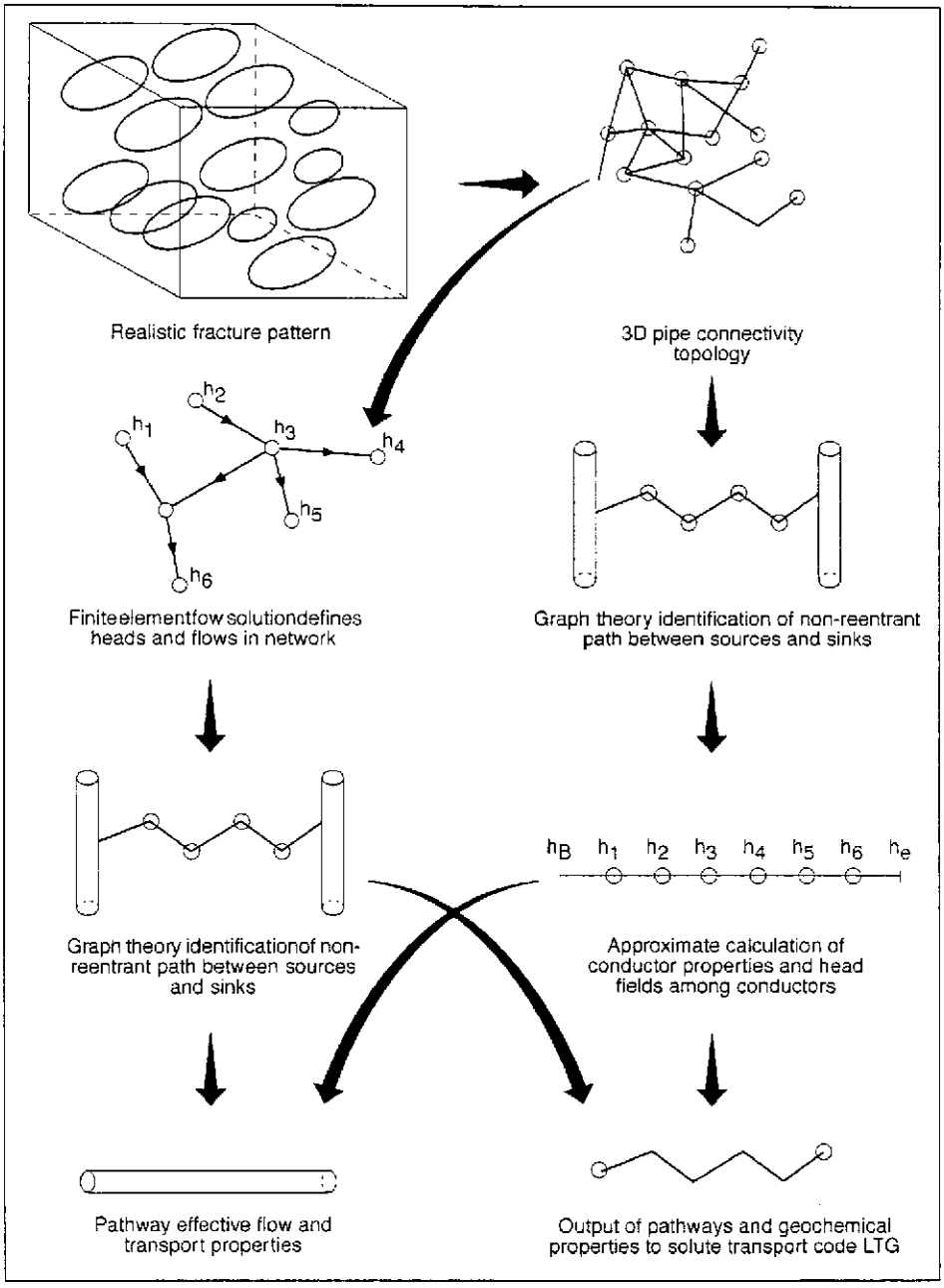

Figure 2-10: PAWorks Approach to channel network modeling

2.3.2 CN Model Implementation of the Äspö TRUE Block Scale DFN model

The DFN described earlier in this report forms the basis of this initial channel network model. The DFN contains 7632 fractures, 7602 of which

are conditioned stochastic background fractures that reside in a 150m x 150m x 150m cube within the larger 500m x 500m x 500m scale structural model.

Fractures contained within the DFN model are converted to pipes based on the following assumptions:

- Effective Pipe Generation:
  Pipes cannot overlap each other. Pipes cannot cross fracture traces on a given fracture surface. All traces on a fracture are connected, preventing isolated pipe clusters within a fracture. In addition, to prevent excessively long pathways, additional pipes are added so that the tortuous distance between two nodes does not exceed the effective pipe factor times the Cartesian distance.

  CN model effective pipe factor = 1.2

- Pipe "Aperture":
  Pipe aperture is derived from fracture transmissivity using a power-law relationship: Aperture = A*T B where A= 2, B=0.5, and T = Transmissivity

These parameters were derived from repeated experiments designed to simulate inflow into the TRUE boreholes.

- Pipe Width:
  The pipe flow width for a pathway is calculated based on the trace width of the fracture intersections forming the pipe. Pipe width is calculated from the tracelength (Dershowitz et al, 1998).

  The CN model pipe width used for these analyses was calculated from:

  $W_i' = W_{af} W_i / W_{area}$

  With the parameters:
  $X_{min} = 1$
  $X_{max} = 1$
  $W_{area} = 1$

  Where:
  $W_i = W_{area} * (X_{min} * L_{min} + X_{max} * L_{max})$
  W_{af} = width to area correction factor
  W_i' = pipe width corrected for W_{at}
  W_{area} = sum of $\{W_i L_i\} / A_f$
  W_i = width of pipe *i* calculated as above
  L_i = length of pipe *i*
  A_f = fracture area

  A value of W_{af} equal to 1.0 gives an equivalence of total pipe and fracture area.

  Figure 2-11 illustrates the parameters used in the calculation of pipe widths within the PAWorks code.

- Merge Distance:
  Any nodes that are closer together than the merge distance are merged together into one node.

  CN model merge distance = 0.0001 m

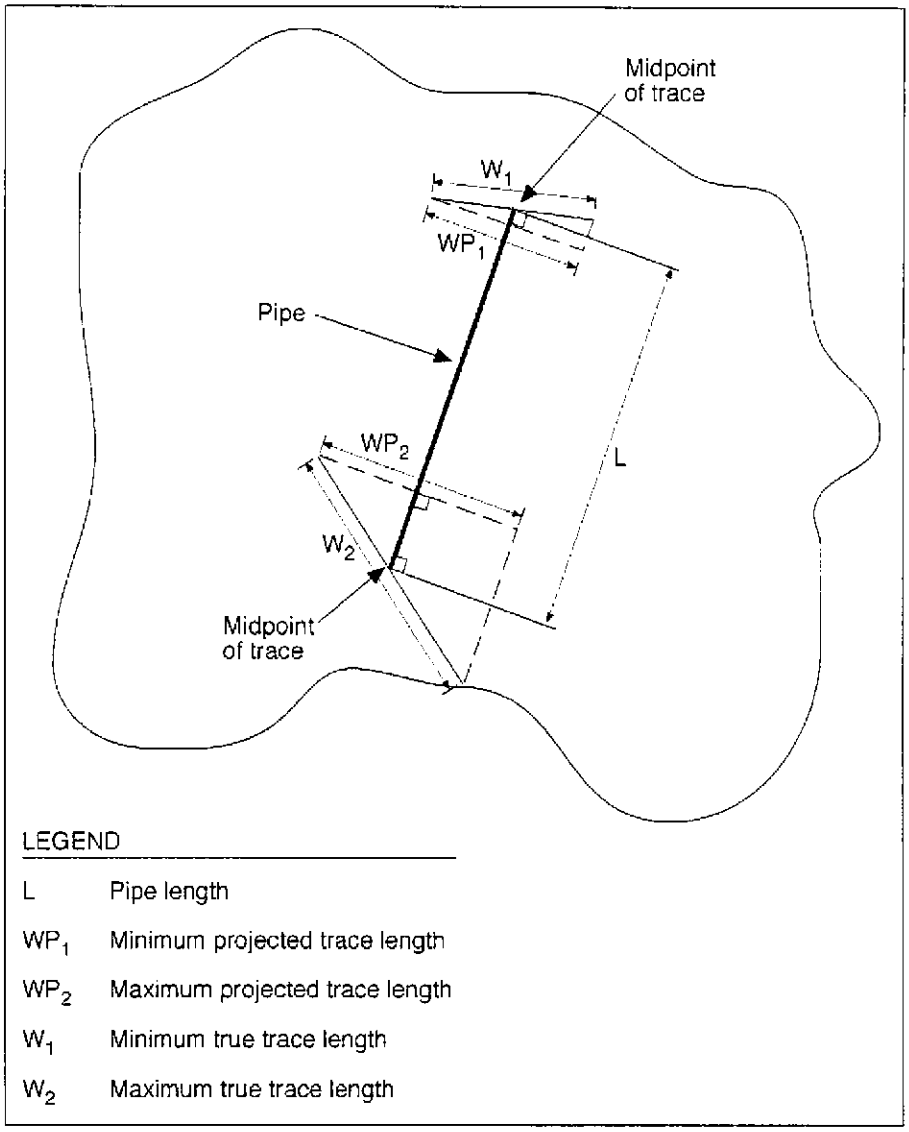

Figure 2-11 Parameters for Pipe Width Calculation

- Minimum Fracture Transmissivity:
  Any fracture with a transmissivity less than this value is eliminated from the CN model.

  CN model minimum transmissivity = 1.00×10^{-10} m^2/s

- External Model Boundaries:
  The external boundary of the preliminary CN model are the edges of the 500m x 500m x 500m cube of the March 2000 structural model. All external boundaries are modeled as constant head, and are set to the conditioned head field values presented by Holton (1999).

- Internal Boundaries:
  Two types of internal boundaries were used in the model: source zones and sink zones. Zones are described as the area between two packers (i.e. a "packer interval"). Sources and sinks were modeled as having a constant flux.

2.3.3 Fracture Intersection Zones (FIZ)

In a fracture network, the intersection between two features may be more damaged than the surrounding fracture area may behave as a distinct flow channel. Depending on the effects that fracturing has on existing fractures the fracture intersection zone (FIZ) can be developed as highly permeable flow channel or as flow barrier. The locations of the flow channels on any fracture surface are normally not known. In the case of significant structures whose locations are known, the location of the FIZ can be determined. This provides the opportunity to design hydraulic borehole tests in a way that the FIZ will be part of the flow channel network that is affected by the tests.

FIZ's are added to the CN model by adding pipes that connect the injection and withdrawal locations to the intersection of the deterministic features associated with the test. Figure 2-12 illustrates a generic pathway generated by the CN model and a pathway generated through the additional FIZ pipes.

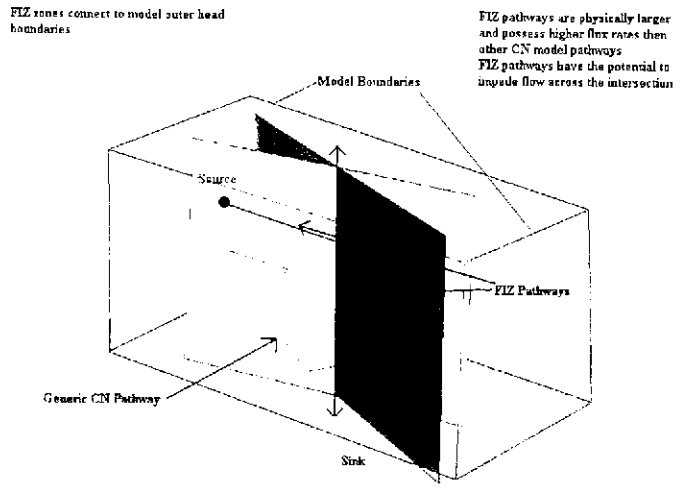

Figure 2-12 FIZ Conceptual Model

The intersection of the deterministic features is given properties associated with the fracture intersection zone (FIZ). FIZ regions have higher transmissivities and higher aperture than their associated features. Pipes along this intersection extend to features EW-1 and NE-2. A head gradient is established along the FIZ due to the natural gradient caused by the bounding features or by a head boundary explicitly placed at the FIZ end. Tracer tests crossing fracture intersection zones may experience mass loss due to enhanced retardation and/or diffusion, and by any head gradient along the FIZ.

To establish the connection between the FIZ and the boreholes, pipes are added to the channel network running from the FIZ to each borehole location on the two intersecting fractures. Each new node, where the added channel intersects the FIZ, is then connected. FIZs are terminated on the regional bounding features (NE-2, and EW-1) to improve the head solution within the TRUE block. Channels established within the intersection zone are added to the channel network prior to calculating the head field.

FIZ have the potential to present a larger surface area available for matrix diffusion and surface sorption (resulting in slower tracer recovery). Pipes within the FIZ were assigned a transmissivity of 1000 times greater than the higher transmissivity of the two intersecting features. Pipes that lie along fractures, connecting the boreholes to the FIZ, are given the same fracture properties as the fractures that they are associated with.

FIZ sections have fundamentally different hydraulic properties then the rest of the fracture network:

A) FIZ sections provide a high flux rate / large aperture "barrier", resulting in longer travel times

B) FIZ sections provide a large area for tracer dilution.

FIZ pipes were added to CN models to model the intersection of features 20 and 21 and the intersection of features 13 and 21. Figure 2-13 illustrates the location of the FIZ zone associated with each intersection. Figure 2-14 illustrates location of low heads in a Phase A tracer test.

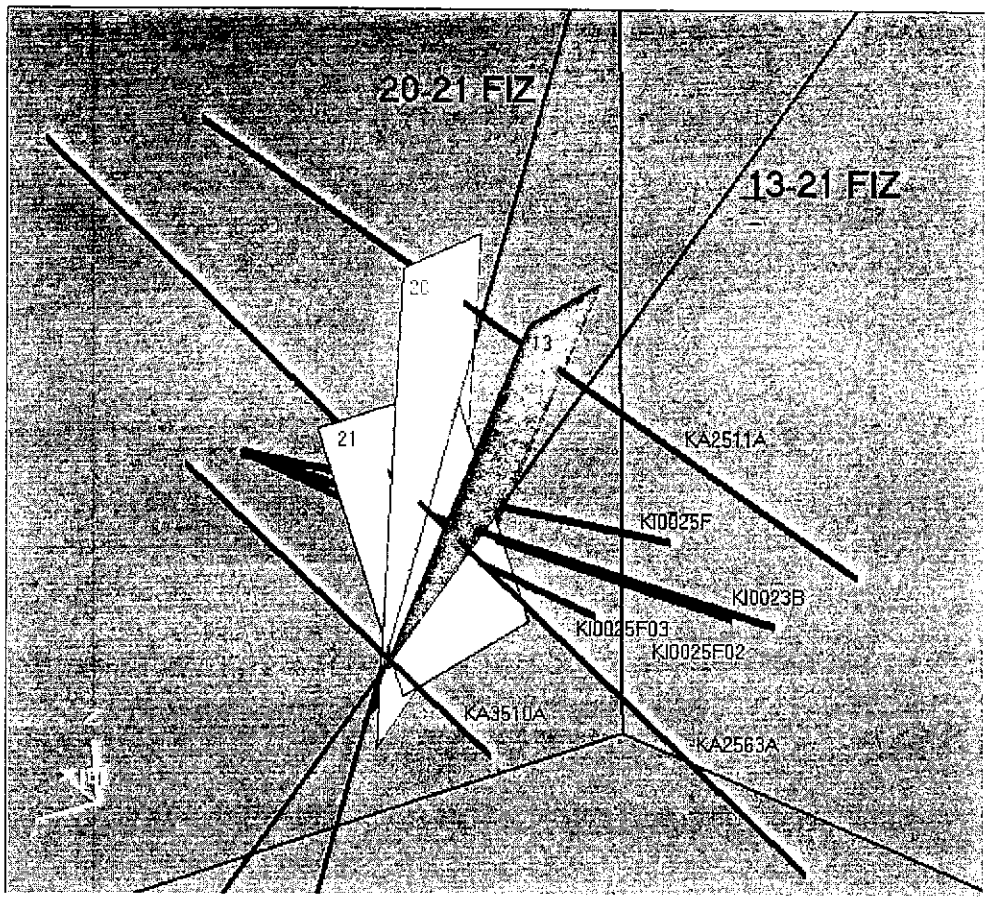

Figure 2-13 Location of #20/#21 FIZ and #13/#21 FIZ

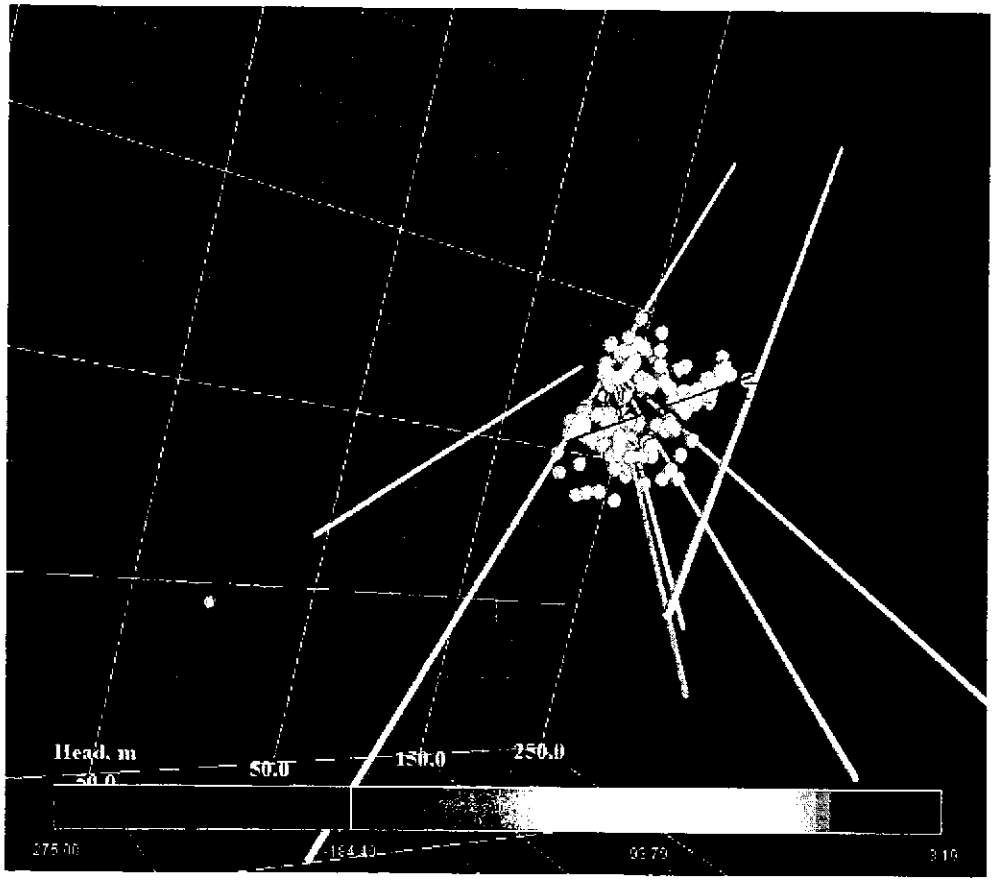

Figure 2-14 Location of low heads during a Phase A tracer test (including #20/#21 FIZ zone)

3. SIMULATIONS USING PRELIMINARY DFN MODEL

The simulations presented in this section show the progression of DFN model calibration. The preliminary DFN deterministic feature parameters are summarized in Table 3-1, while stochastically-generated background fracture properties are located in Table 2-2. The preliminary model deterministic features have a constant storativity of $1.00*10^{-6}$ and flow aperture equal to $2*\text{transmissivity}^{1/2}$ m^2/s. Two parameter calibrations are presented illustrating DFN model sensitivity: the effect that deterministic features have on distance drawdown, and the immobile zone influence on breakthrough times. Tracer test A4 was used in the following simulations. Test A4 parameters are listed in Table 3-2.

Table 3-1 Preliminary Deterministic Feature Parameters

Feature	Transmissivity (m^2/s)	Normal Vector			Area (m^2)
		x	y	z	
1	$1.00*10^{-6}$	-0.419	0.897	0.139	193.22
2	$1.00*10^{-6}$	0.95	-0.33	0.017	242.99
3	$1.00*10^{-6}$	-0.93	0.34	-0.151	247.42
4	$1.00*10^{-6}$	0.84	-0.53	-0.146	189.08
5	$1.00*10^{-6}$	-0.92	0.39	-0.008	248.74
6	$1.50*10^{-8}$	0.61	-0.80	0.047	5663.25
7	$1.70*10^{-6}$	0.93	-0.37	0.098	43539.19
8	$1.00*10^{-10}$	0.50	0.80	-0.352	222.4
9	$1.00*10^{-8}$	-0.84	0.54	-0.035	308.13
10	$5.30*10^{-8}$	0.95	-0.09	-0.311	13096.46
11	$1.00*10^{-6}$	-0.95	0.30	0.035	229.7
12	$1.00*10^{-10}$	-0.09	1.00	0	226.46
13	$5.00*10^{-8}$	0.63	-0.75	-0.213	9358.65
15	$2.00*10^{-11}$	-1.00	-0.04	0.035	203.12
16	$2.00*10^{-11}$	-0.02	0.31	-0.952	261.28
17	$2.00*10^{-11}$	0.08	0.04	-0.996	255.86
18	$1.00*10^{-6}$	-0.11	-0.25	-0.962	250.75
19	$1.70*10^{-6}$	0.53	-0.84	0.138	17958.34
20	$9.60*10^{-7}$	0.67	-0.74	-0.088	14966.42
21	$8.10*10^{-7}$	0.14	-0.98	-0.172	6663.6
22	$2.60*10^{-7}$	0.41	-0.89	-0.2	7289.85
Z	$5.00*10^{-6}$	-0.87	-0.44	0.225	243.55
EW-1	$1.20*10^{-5}$	-0.86	-0.48	-0.199	255.91
EW-3	$1.70*10^{-5}$	-0.96	-0.20	-0.191	221.5
NE-1	$2.20*10^{-4}$	0.85	0.44	-0.301	227.04
NE-2	$1.20*10^{-7}$	-0.57	-0.79	-0.225	242.73
NNW-7	$7.50*10^{-6}$	0.42	-0.90	-0.087	199.74

Table 3-2 Tracer Test A4 Parameters

Tracer	Source	Feature
Uranine	KI0023F03: P5 (66.5 - 74 m)	20
Amino G Acid	KI0023F03: P6 (59.5 - 65.5 m)	22
RhodamineWT(2)	KI0023F03: P7 (55 - 58.5 m)	?

Sink Location	KI0023B:P6 (70.4 - 71.4 m)	Feature 20
Pumping Rate	2.30 l/min	
Pumping Duration	17370 minutes (~ 12 days)	

3.1 DISTANCE DRAWDOWN SIMULATIONS

Comparisons between the distance drawdown results measured in the field, and as computed in the preliminary CN model, were used to calibrate the properties of the major features in the DFN model. The external boundaries of the modeled region were the edges of the 500m x 500m x 500m cube. All external boundaries were modeled using a constant head boundary condition, and were set to the conditioned head field values presented by Holton (1999). Connectivity between the deterministic features and the outer boundary establish the steady state head field across the CN model. The finite-element code MAFIC was used to compute a flow solution for each test. The pre-test heads across the $500m^3$ block are displayed in Figure 3-1, while Figure 3-2 displays a contour map of pre-test heads at the models center, looking towards the Äspö HRL tunnel. Figure 3-3 and Figure 3-4 display post-test heads across the TRUE Block Scale region. The pumping location for test A4 is KI0023B. Figure 3-5 contains in situ and predicted distance drawdown data.

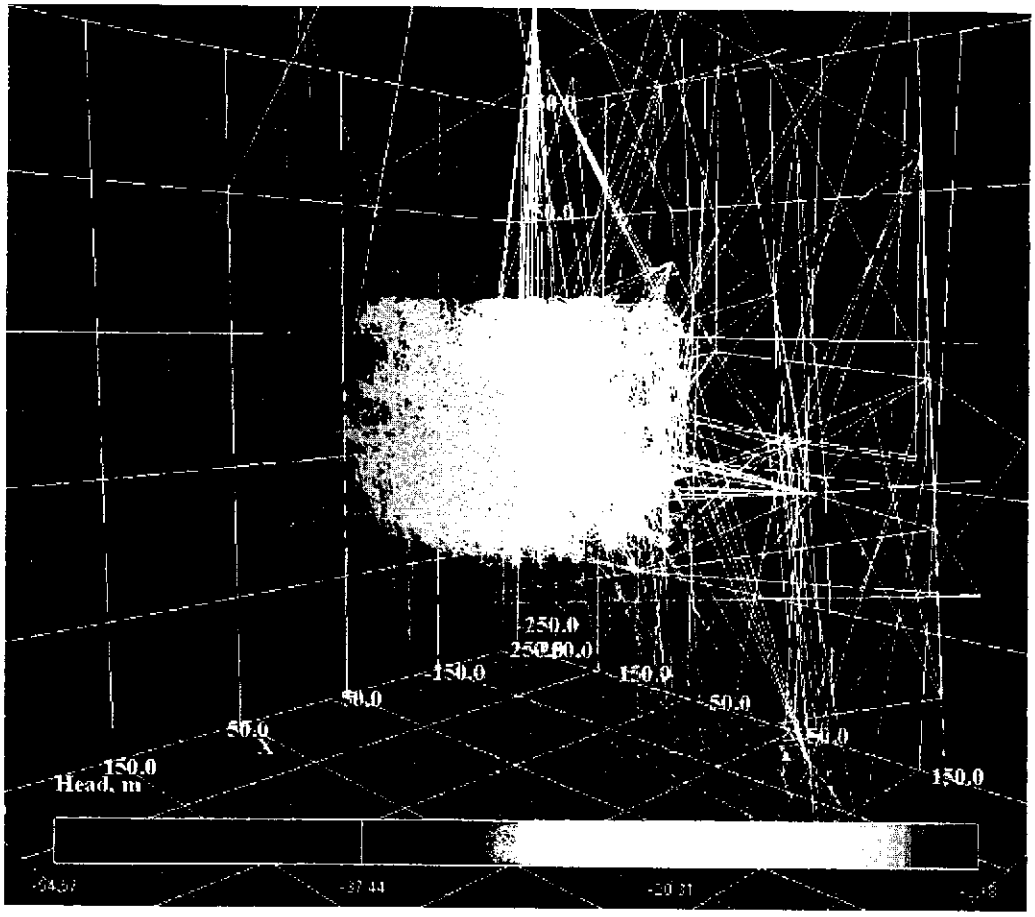

Figure 3-1 TTS Test A-4: Pre-test heads

CN Model Mesh, with pipes colored by head (m)

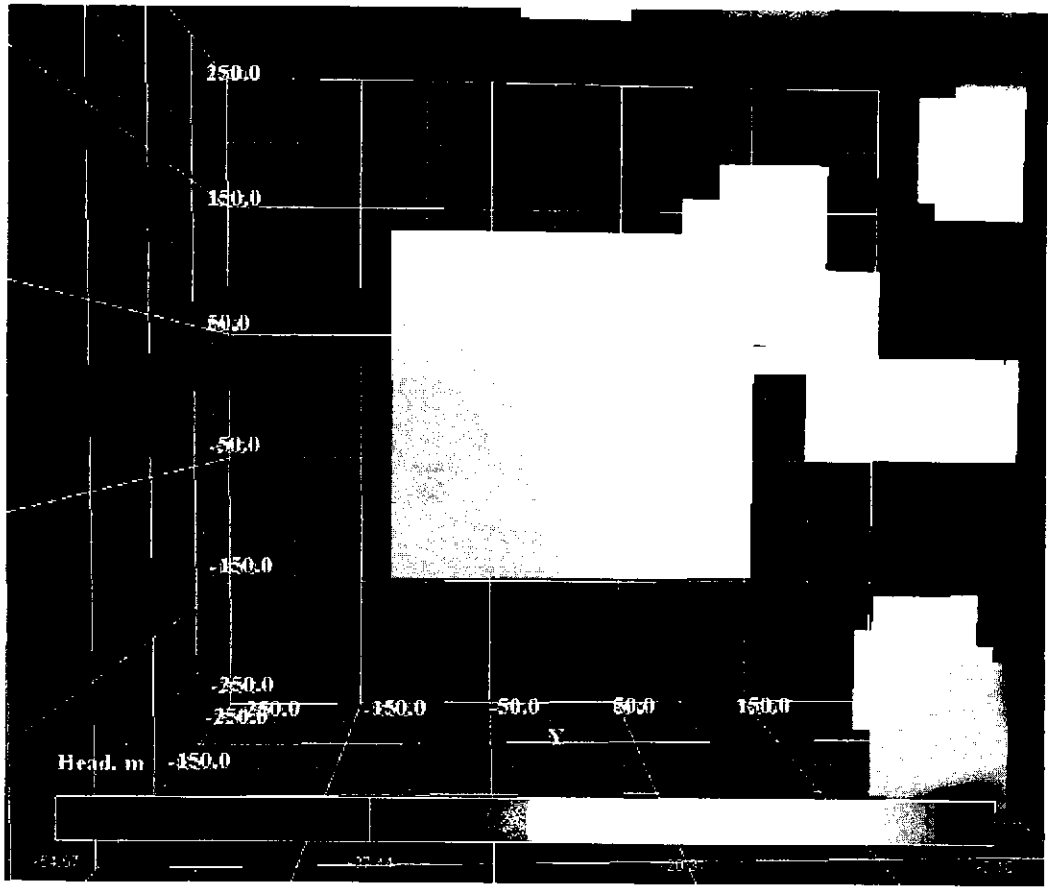

Figure 3-2 TTS A-4: Pre-test Head Contour Map.

View is looking towards Äspö HRL tunnel. Trace map is centered at approximately model center (7170m, 1900m, -450m), Grid colored by head (m)

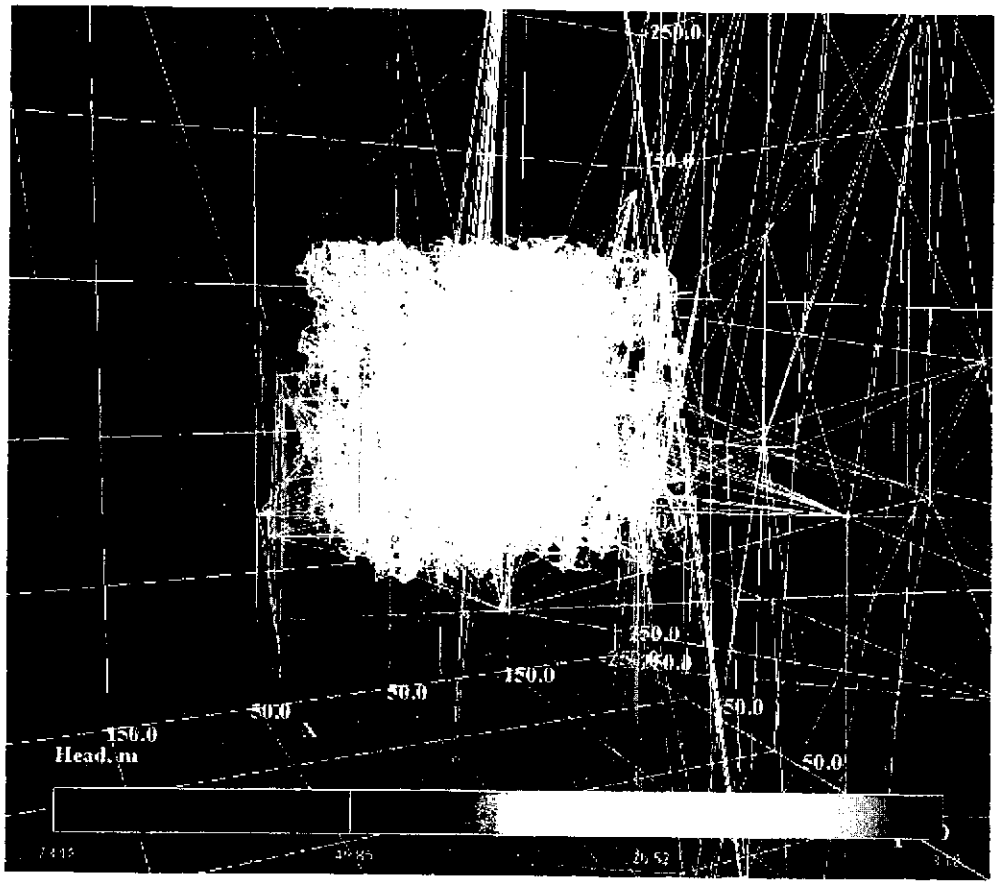

Figure 3-3 TTS A-4: Post-test Heads [CN Model Mesh, with pipes colored by head (m)

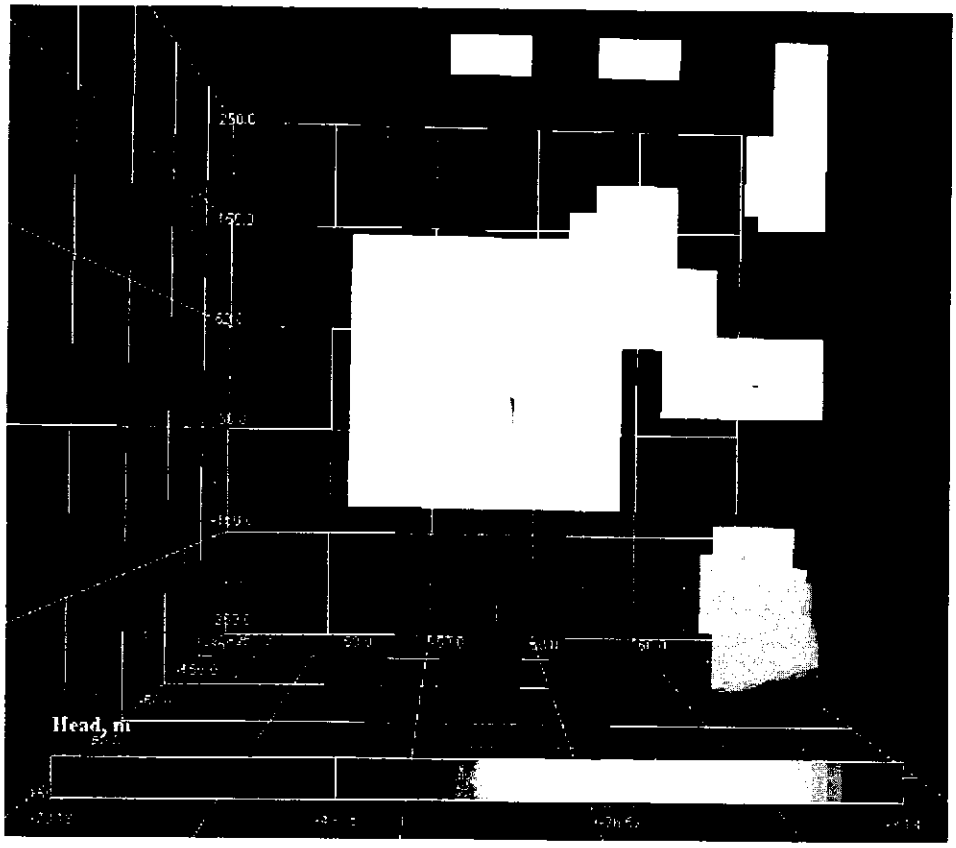

Figure 3-4 TTS A-4: Post-test Head Contour Map. View is looking towards Äspö HRL tunnel. Trace map is centered at approximately model center (7170m, 1900m, -450m). Grid colored by head (m)

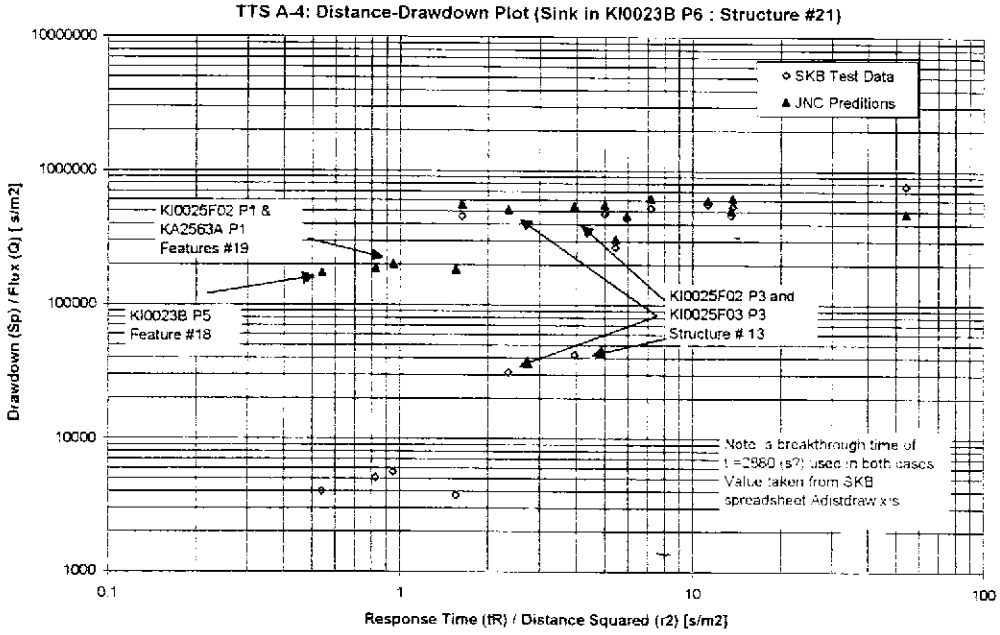

Figure 3-5 Test A-4: Distance - Drawdown

3.2 TRACER TEST SIMULATIONS

The tracer tests were modeled using the Laplace Transform Galerkin transport code, LTG (Dershowitz et al, 1998). LTG is a finite element code that incorporates advection, dispersion, surface sorption, and diffusion into multiple immobile zones.

Three calibrations to the tracer Test A-4 (from the KI00F03 borehole section) were carried out; breakthrough and recovery data was compared to the in situ measurements. Figure 3-6 through Figure 3-10 show the breakthrough and recovery for tracers Uranine, Rhodamine WT, and Amino G Acid. These initial simulations had the following parameters: aperture = 2*transmnissivity$^{1/2}$, dispersion length = 1.5 m. The initial calibration, "Initial Prediction", had no immobile zones. Simulations B and C show the effect of adding immobile zones to the model. Simulation B has a matrix porosity of 2% and maximum diffusion distance of 0.1 m, simulation C has matrix porosity and diffusion distance of 2% and 1 m respectively. The figures show that the increasing the diffusion distance greatly enhances the initial breakthrough time match of the simulated data to the measured breakthrough of Uranine and Amino G Acid. The addition of immobile zones in Simulations B and C also decreases the recovery of the tracer during the test.

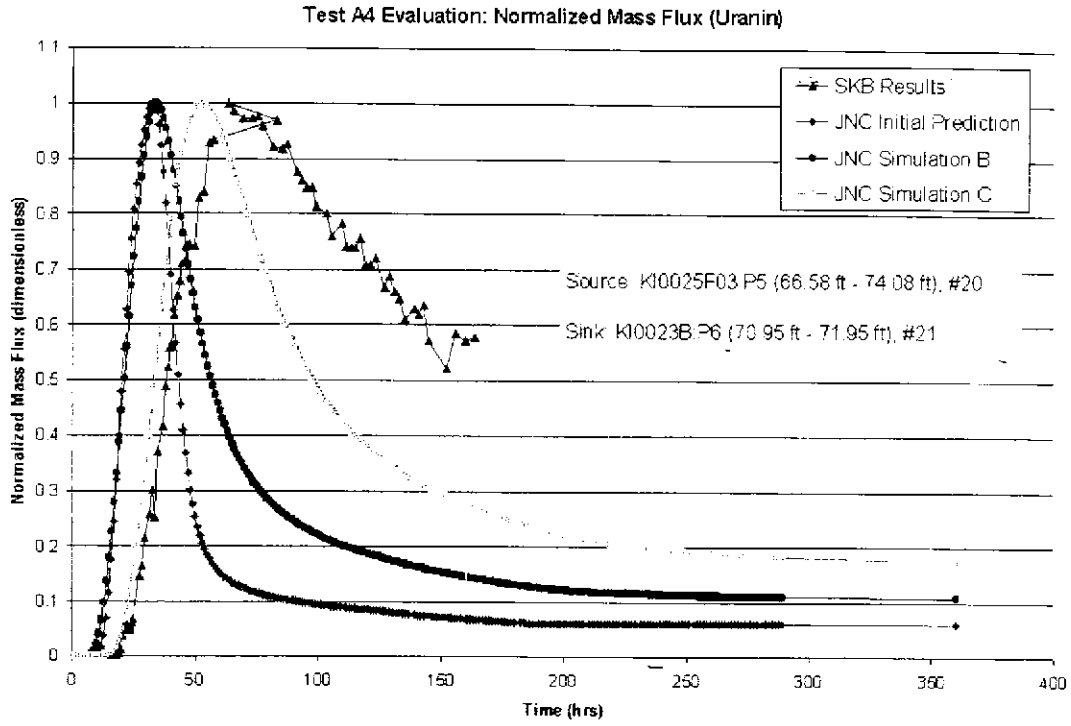

Figure 3-6 TTS A-4: Uranine Breakthrough

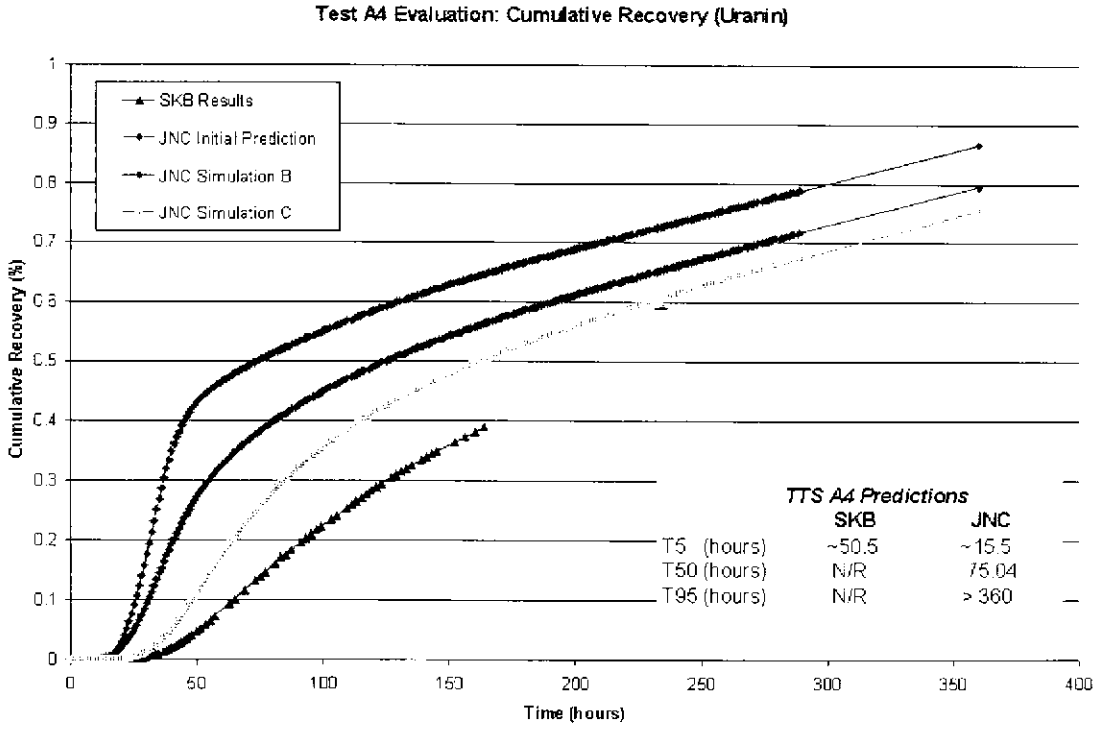

Figure 3-7 TTS A-4: Uranine Recovery

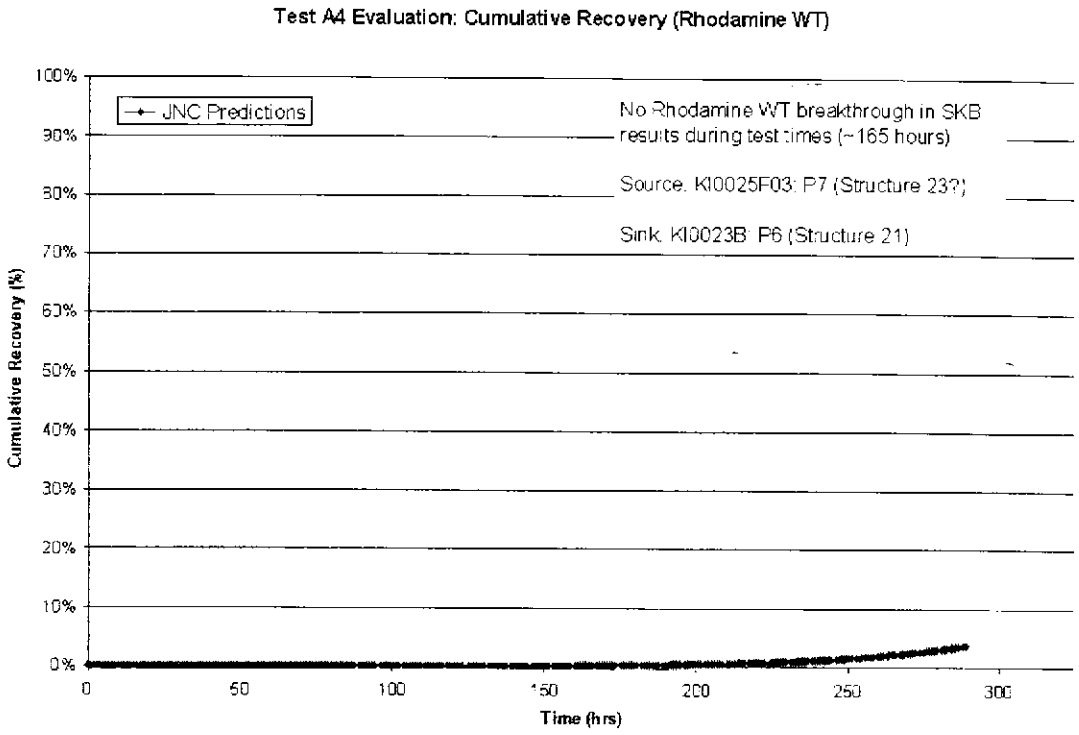

Figure 3-8 TTS A-4: Rhodamine WT

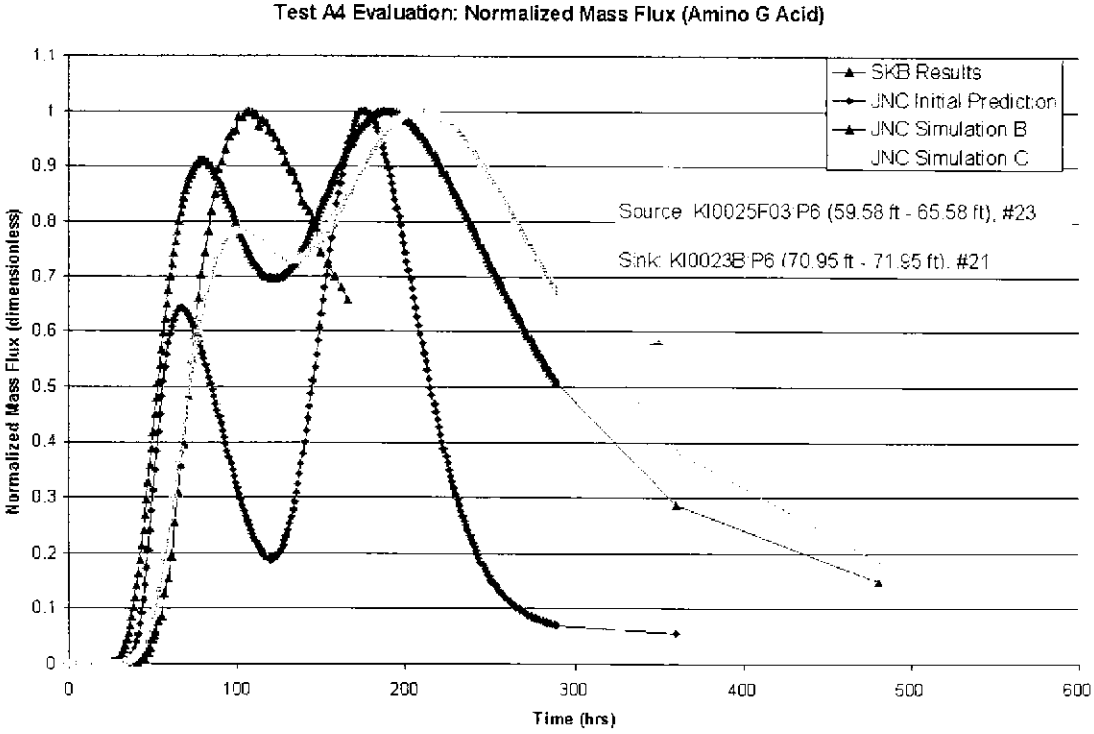

Figure 3-9 TTS A-4: Amino G Acid Breakthrough

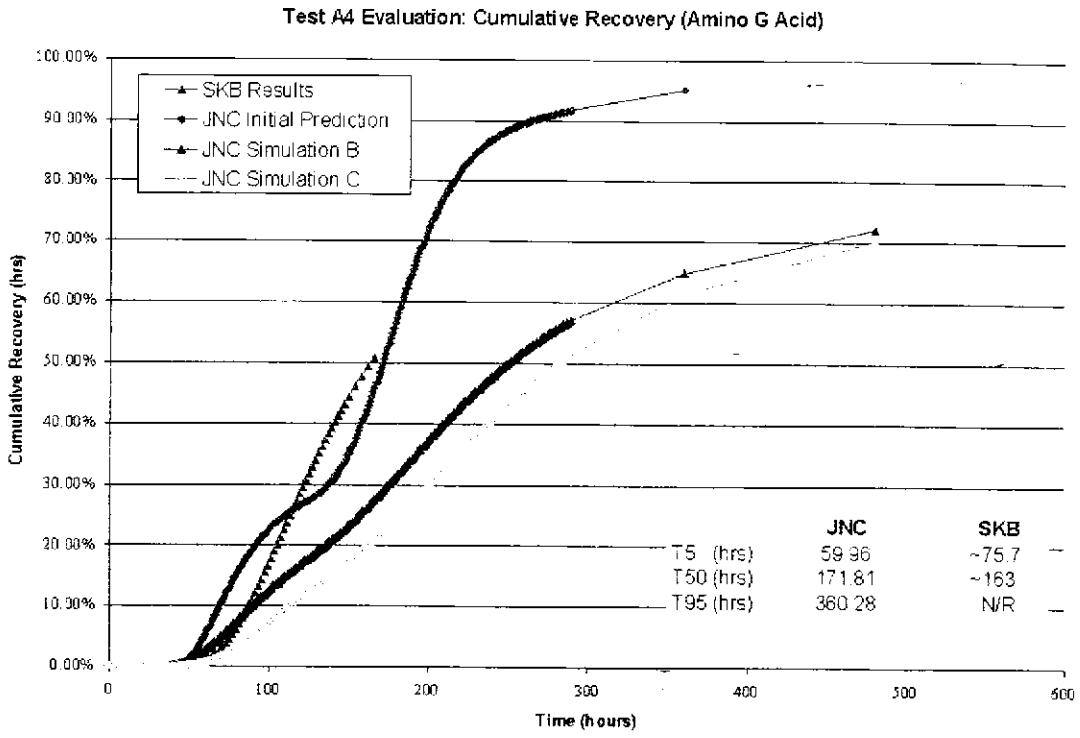

Figure 3-10 TTS A-4: Amino G Acid Recovery

3.3 POTENTIAL MODEL CORRECTIONS

Comparison between the SKB in situ distance drawdown data and distance drawdowns established from test A4 in the preliminary CN model shows good late time matches. Early time drawdowns, associated with features13, 18, and 19 result in greater variance between the in situ and simulated data. Simulated drawdowns appear to be an order of magnitude higher than those observed on site. Improving the distance drawdown matches would include changing the connectivity of feature 13 and modifying the transmissivities of features 18 and 19.

Test A-4 was used to illustrate the effects that the immobile zone has on the recovery and breakthrough of the tracers. Of the three tracers injected in test A-4, Uranine showed improvements in $T_5/T_{50}/T_{95}$ matches when immobile zones were added to each fracture. In situ Rhodamine recovery was below background levels; Simulated Rhodamine recovery is below 5% both with and without immobile zones. The modeled Amino G Acid recovery was slowed by the presence of immobile zones; the slower recovery improves the match to the measured breakthrough time.

4. HYDRAULIC INTERFERENCE SIMULATIONS

This section of the report describes the CN hydraulic interference simulations using the March 2000 Structural Model (Doe, 2000). These simulations also included stochastically generated background fractures, conditioned to borehole observations from the investigation in the tracer test stage (Dershowitz, 2000). Table 4-1 summarizes the deterministic feature parameters that went into the CN model. This model is considered the base case structural model. All hydraulic interference tests use tracer test A1 for simulations. Table 4-2 contains tracer test A1 parameters.

Table 4-1 Deterministic Feature Parameters of the March 2000 Structural Model (Doe, 2000)

Feature	Transmissivity (m^2/s)	Normal Vector			Area (m^2)
		X	Y	Z	
1	$1.00*10^{-6}$	-0.419	0.897	0.139	193.22
2	$1.00*10^{-6}$	0.95	-0.33	0.017	242.99
3	$1.00*10^{-6}$	-0.93	0.34	-0.151	247.42
4	$1.00*10^{-6}$	0.84	-0.53	-0.146	189.08
5	$1.00*10^{-6}$	-0.92	0.39	-0.008	248.74
6	$1.00*10^{-7}$	-0.537	0.843	0.025	5944.3
7	$1.80*10^{-5}$	-0.885	0.44	-0.15	12746
8	$1.00*10^{-10}$	0.50	0.80	-0.352	222.4
9	$1.00*10^{-6}$	-1	0	0	0.79
10	$5.30*10^{-8}$	0.95	-0.09	-0.311	13096.46
11	$1.00*10^{-6}$	-0.95	0.30	0.035	229.7
12	$1.00*10^{-10}$	-0.09	1.00	0	226.46
13	$1.70*10^{-7}$	-0.554	0.73	0.4	15517.3
14	$1.00*10^{-12}$	-1	0	0	0.03
15	$2.00*10^{-11}$	-1.00	-0.04	0.035	203.12
16	$1.00*10^{-8}$	-0.02	0.31	-0.952	261.28
17	$2.00*10^{-11}$	0.08	0.04	-0.996	255.86
18	$1.00*10^{-11}$	-0.11	-0.25	-0.962	250.75
19	$1.80*10^{-7}$	-0.513	0.859	0.013	26583.7
20	$9.60*10^{-7}$	-0.66	0.746	0.088	18938.3
21	$8.10*10^{-7}$	-0.374	0.87	-0.322	8009.34
22	$3.70*10^{-7}$	-0.4	0.844	-0.358	4648.02
23	$6.79*10^{-9}$	-0.679	0.734	0	1203.66
24	$2.98*10^{-8}$	-0.755	0.639	-0.146	1172.34
Z	$5.00*10^{-6}$	-0.87	-0.44	0.225	243.55
EW-1	$1.20*10^{-5}$	-0.86	-0.48	-0.199	255.91
EW-3	$1.70*10^{-5}$	-0.96	-0.20	-0.191	221.5
NE-1	$2.20*10^{-4}$	0.85	0.44	-0.301	227.04
NE-2	$1.20*10^{-7}$	-0.57	-0.79	-0.225	242.73
NNW-7	$7.50*10^{-6}$	0.42	-0.90	-0.087	199.74

Table 4-2 Tracer Test A1 Parameters

Tracer	Source	Feature
Sink Location	KI0025F03: P5 (66.5 - 74 m)	20
Pumping Rate	2.05 l/min for the first 305 minutes of the test, 2.70 l/min for the remaining 3675 minutes.	
Pumping Duration	3980 minutes (~ 3 days)	

4.1 SIMULATIONS WITH BASE STRUCTURAL MODEL

A distance drawdown plot was created to compare the in situ and simulated drawdown at specified features with the base structural model. Test A1 compared drawdowns at features 6, 13, 19, 20, 21, and 22 to the in situ measurements. The greatest amount of variance between measured and simulated drawdown occurs on feature 19. Figure 4-1 shows the distance drawdown plot for test A1.

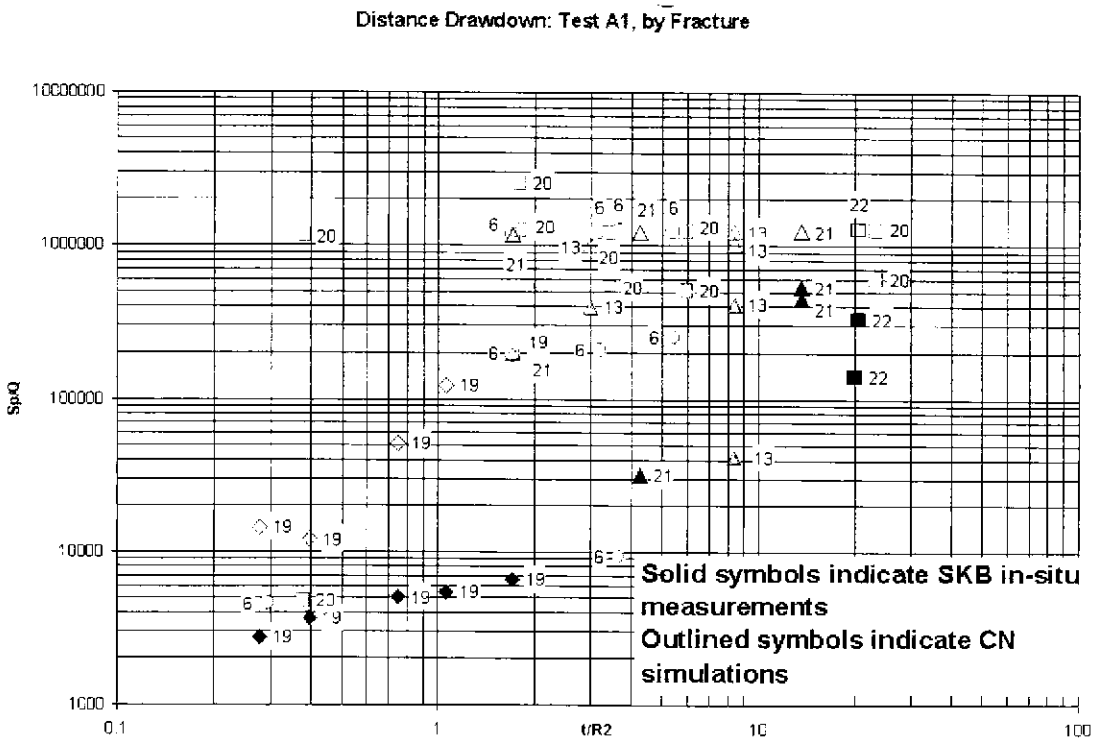

Figure 4-1 Distance - Drawdown Comparison for the March 2000 Structural Model (Doe, 2000)

4.2 ADJUSTMENTS TO TRANSMISSIVITY

To improve the distance drawdown match, simulations were carried out with different transmissivity values given to deterministic features. Transmissivity was decreased on the sub-horizontal deterministic features. Decreasing the transmissivity of the sub-horizontal features results in less hydraulic connectivity between the vertical features. The transmissivity of features 16, 17, and 18 was decreased by 3 orders of magnitude. Feature 16 transmissivity

decreased from $1.00*10^{-8}$ m^2/s to $1.00*10^{-11}$ m^2/s. Features 17 and 18 transmissivity decreased from $1.00*10^{-11}$ m^2/s to $1.00*10^{-14}$ m^2/s. Figure 4-2 illustrates the distance drawdown plot with the modified transmissivities. In general, the distance drawdown matches did not improve due to modifying the transmissivities of the subhorizontal features.

Simulated drawdowns were best calibrated the to in situ measurements by modifying the transmissivity of features 5 and 16. Feature 5 transmissivity was increased from $1.00*10^{-6}$ m^2/s to $1.00*10^{-5}$ m^2/s and feature 16 transmissivity reduced from $1.00*10^{-8}$ m^2/s to $1.00*10^{-11}$ m^2/s. Figure 4-3 illustrates the distance drawdown matches with the transmissivities of features 5 and 16 modified. This change resulted in better drawdown matches to features 6, 13, 20, 21, and 22. These changes in transmissivity had little effect on feature 19.

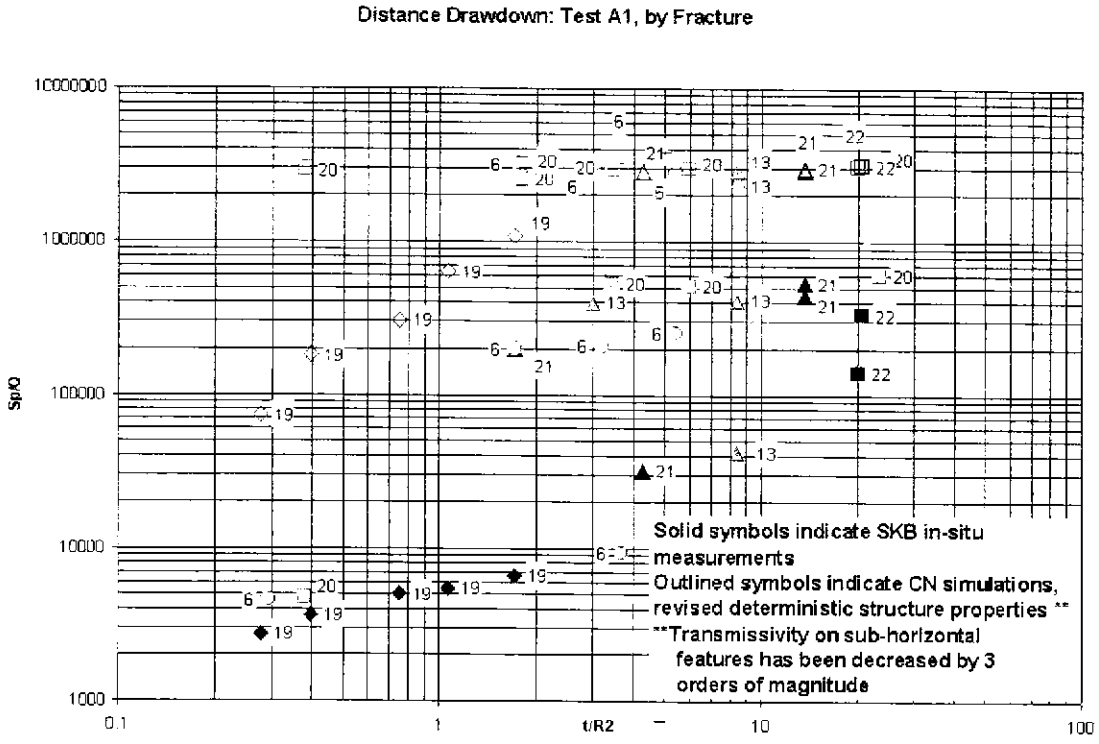

Figure 4-2 Distance Drawdown, Modified features 16, 17, and 18

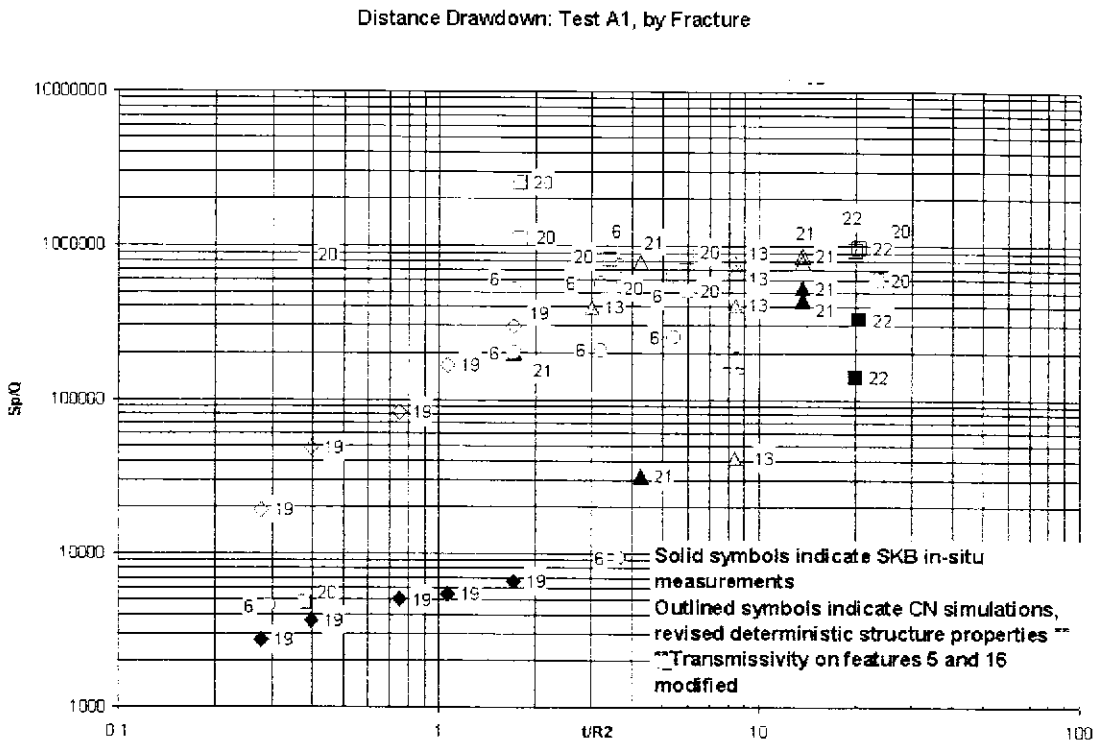

Figure 4-3 Distance Drawdown, Modified feature 5 and 16

4.3 ADJUSTMENTS TO CONNECTIVITY

The March 2000 Structural Model (Doe, 2000) was modified by increasing the connectivity of the network. To improve the simulated drawdown of feature 19, the overall size of the feature was expanded to increase the connectivity of the feature. Feature 19 was extended to connect to features EW-1 and NE-2. The size of feature 6 was also increased to improve the distance drawdown comparisons between simulated and measured values. Feature 6 was extended to connect with feature 5. Increasing the connectivity of features 6 and 19 increased the simulated drawdown matches of all features.

4.4 SIMULATIONS WITH THE REVISED STRUCTURAL MODEL

Modifications in the revised structural model include adjustments to the model connectivity and transmissivity. Table 4-3 summarizes the changes in the March 2000 Structural Model. Numbers in bold indicate changes from the Preliminary DFN model described in Section 2. Figure 4-4 contains the distance drawdown plot with the revised structural model.

Table 4-3 Deterministic Feature Parameters of the Revised March 2000 Structural Model (Doe, 2000), bold value indicate modified parameters

Feature	Transmissivity (m^2/s)	Normal Vector			Area (m^2)
		x	y	z	
1	$1.00*10^{-6}$	-0.419	0.897	0.139	193.22
2	$1.00*10^{-6}$	0.95	-0.33	0.017	242.99
3	$1.00*10^{-6}$	-0.93	0.34	-0.151	247.42
4	$1.00*10^{-6}$	0.84	-0.53	-0.146	189.08
5	**$1.00*10^{-5}$**	-0.92	0.39	-0.008	248.74
6	$1.00*10^{-7}$	-0.537	0.843	0.025	**6698.04**
7	$1.80*10^{-5}$	-0.885	0.44	-0.15	12746
8	$1.00*10^{-10}$	0.50	0.80	-0.352	222.4
9	$1.00*10^{-6}$	-1	0	0	0.79
10	$5.30*10^{-8}$	0.95	-0.09	-0.311	13096.46
11	$1.00*10^{-6}$	-0.95	0.30	0.035	229.7
12	$1.00*10^{-10}$	-0.09	1.00	0	226.46
13	$1.70*10^{-7}$	-0.554	0.73	0.4	15517.3
14	$1.00*10^{-12}$	-1	0	0	0.03
15	$2.00*10^{-11}$	-1.00	-0.04	0.035	203.12
16	**$1.00*10^{-11}$**	-0.02	0.31	-0.952	261.28
17	$2.00*10^{-11}$	0.08	0.04	-0.996	255.86
18	$1.00*10^{-11}$	-0.11	-0.25	-0.962	250.75
19	$1.80*10^{-7}$	-0.513	0.859	0.013	**46344.9**
20	$9.60*10^{-7}$	-0.66	0.746	0.088	18938.3
21	$8.10*10^{-7}$	-0.374	0.87	-0.322	8009.34
22	$3.70*10^{-7}$	-0.4	0.844	-0.358	4648.02
23	$6.79*10^{-9}$	-0.679	0.734	0	1203.66
24	$2.98*10^{-8}$	-0.755	0.639	-0.146	1172.34
Z	$5.00*10^{-6}$	-0.87	-0.44	0.225	243.55
EW-1	$1.20*10^{-5}$	-0.86	-0.48	-0.199	255.91
EW-3	$1.70*10^{-5}$	-0.96	-0.20	-0.191	221.5
NE-1	$2.20*10^{-4}$	0.85	0.44	-0.301	227.04
NE-2	$1.20*10^{-7}$	-0.57	-0.79	-0.225	242.73
NNW-7	$7.50*10^{-6}$	0.42	-0.90	-0.087	199.74

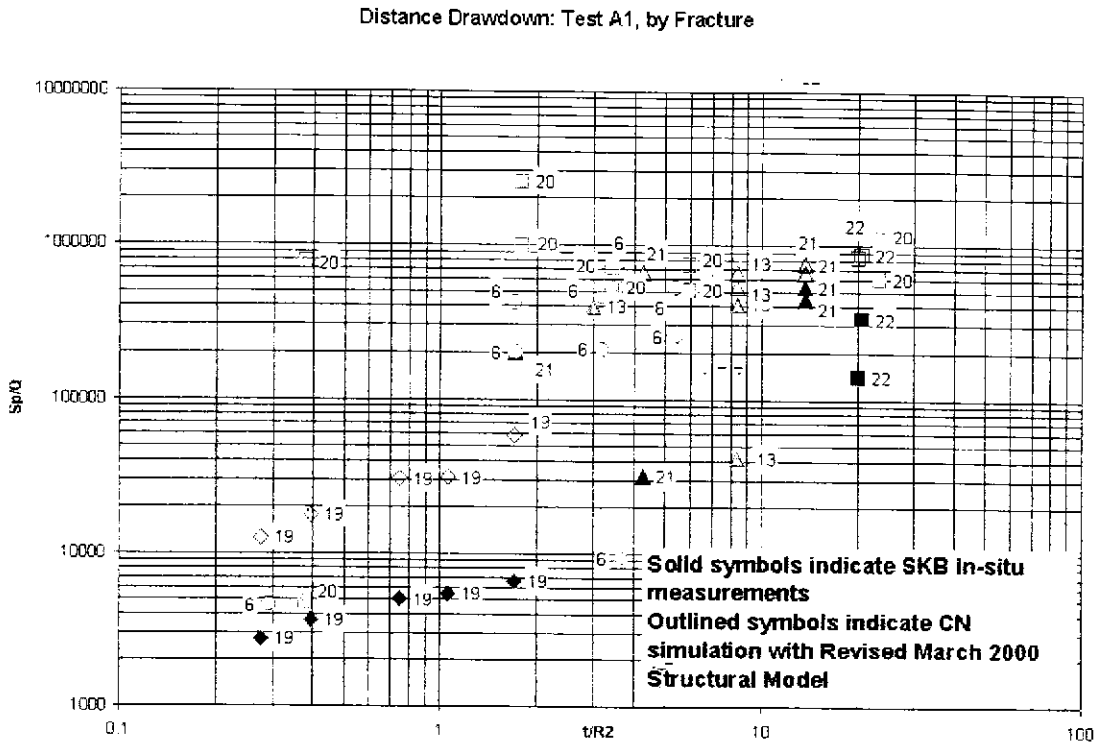

Figure 4-4 Distance Drawdown Comparison for the Revised March 2000 Structural Model

5. FRACTURE INTERSECTION ZONE STUDIES

FIZs provide a high flux rate / large aperture "barrier", resulting in longer travel times and a larger area for tracer dilution. The magnitude of the FIZ effect on the tracer test largely depends on the transmissivity and aperture of the FIZ. Simulated tracer tests were run with and without FIZ pipes added to the CN model to establish the relationship between FIZ properties and the surrounding structures. TTS A4 and A5 were used to model the effects of the FIZ.

FIZ pipes were added to existing CN models by hand, and were connected directly to source and sink locations. FIZ pipes were extended to the external boundary and are therefore effected by the constant head field at the outer boundary established by Holton (1999). Multiple simulations using FIZ transmissivities greater than the host fracture transmissivity were compared with the measured recovery of each tracer. Figure 5-1 illustrates a generic pathway generated by the CN model and a pathway generated through the additional FIZ pipes.

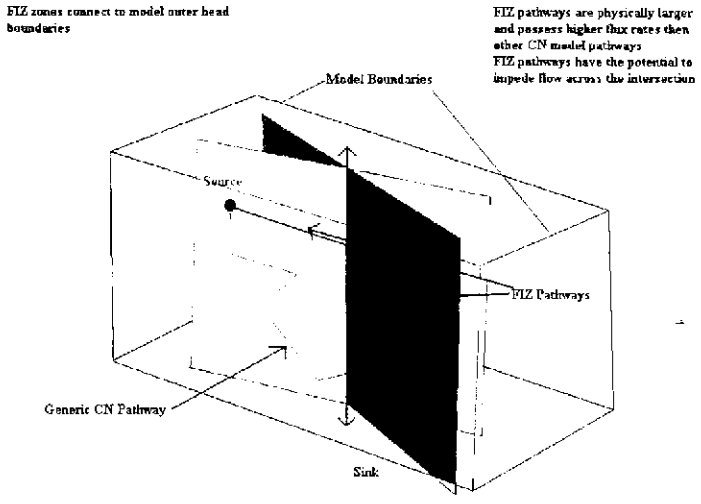

Figure 5-1 FIZ Conceptual Model

5.1 FIZ SIMULATIONS

Tracer tests A-4 and A-5 were chosen to study the effects of FIZ because of their recovery response and travel path. Both tests had tracers that returned less than 100% tracer at the recovery location and both tracer tests cross deterministic feature intersections on their travel path from source to sink. Test A-4 crosses the 20/21 FIZ and has a measured recovery of 40%. Test A-5, from a source location of KI0025F02: P3 crosses FIZ 20/21 and has no

recovery measured above background levels. Tracer injected from KA2563A: S4 and KI0025F02: P5 in test A-5 travel on feature 20 from source to sink and have much higher recoveries of 66% and 132% respectively. Other tracer tests associated with test A-5 do not cross the 20/21 FIZ.

5.1.1 TTS A-4: FIZ Simulation Parameters

Tracer test A-4 injects three conservative tracers, Uranine, RhodamineWT, and Amino G Acid, from KI00F03. The source and sink locations as well as assocated features and pumping rate for tracer test A4 are listed in Table 5-1. The source and sink locations are associated with features 20 and 21 respectively. The A-4 tracer test simulations were run varying transmissivity and aperture to find the best fit to the in situ data. Table 5-2 displays the FIZ parameters used in the FIZ simulations for test A-4.

Table 5-1 Tracer Test A4 Parameters

Tracer	Source	Feature
Uranine	KI0023F03: P5 (66.5 - 74 m)	20
Amino G Acid	KI0023F03: P6 (59.5 - 65.5 m)	22
RhodamineWT(2)	KI0023F03: P7 (55 - 58.5 m)	?

Sink Location	KI0023B:P6 (70.4 - 71.4 m)	Feature 20
Pumping Rate	2.30 l/min	
Pumping Duration	17370 minutes (~ 12 days)	

The initial JNC prediction was run with the following parameters: dispersion length of 0.5 m, deterministic/background fracture aperture equals 2*Transmissivity$^{1/2}$, and no FIZ effects. FIZ pipes were added to the CN model to improve the calibration. Early time measured recovery was improved with greater FIZ transmisssivity. Realization 4, with a transmissivity of 2.0×10^{-5} m^2/s, results in the best fit for early time recovery. The aperture of the FIZ in this realization is 6.196×10^{-3} m, equivalent to a relationship for aperture of 1.4*Transmissivity$^{1/2}$. Figure 5-2 and Figure 5-3 display the FIZ geometry used in test A4. Figure 5-2 shows pipes that connect boreholes to the 20/21 FIZ on structure 20 and Figure 5-3 shows pipes that connect boreholes the 20/21 and 13/21 FIZ on structure 21. Figure 5-4 illustrates the effect of the FIZ on the breakthrough and recovery of Uranine in test A-4.

Table 5-2 FIZ Simulation Parameters

Realization	Transmissivity of 20/21 FIZ (m^2/s)	Aperture of FIZ (m)
Realization 1	9.6×10^{-6} (10x greater than fracture 20)	6.196×10^{-3}
Realization 2	9.6×10^{-5} (100x greater than fracture 20)	6.19×10^{-3}
Realization 3	3.0×10^{-5}	6.19×10^{-3}
Realization 4	2.0×10^{-5}	6.196×10^{-3}

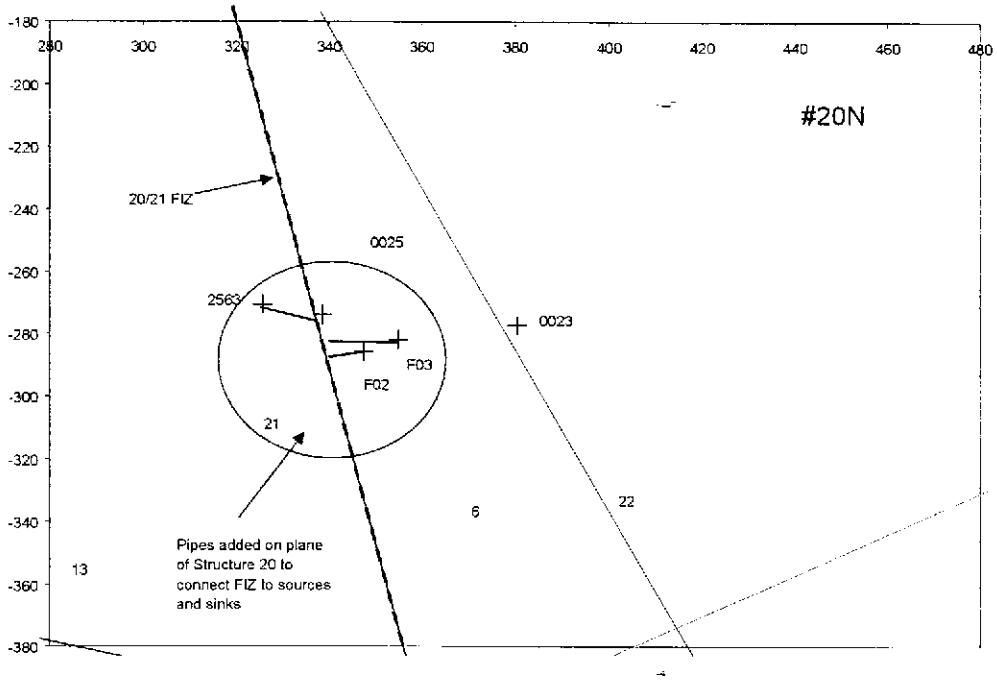

Figure 5-2 FIZ Pipes in plane of Feature 20

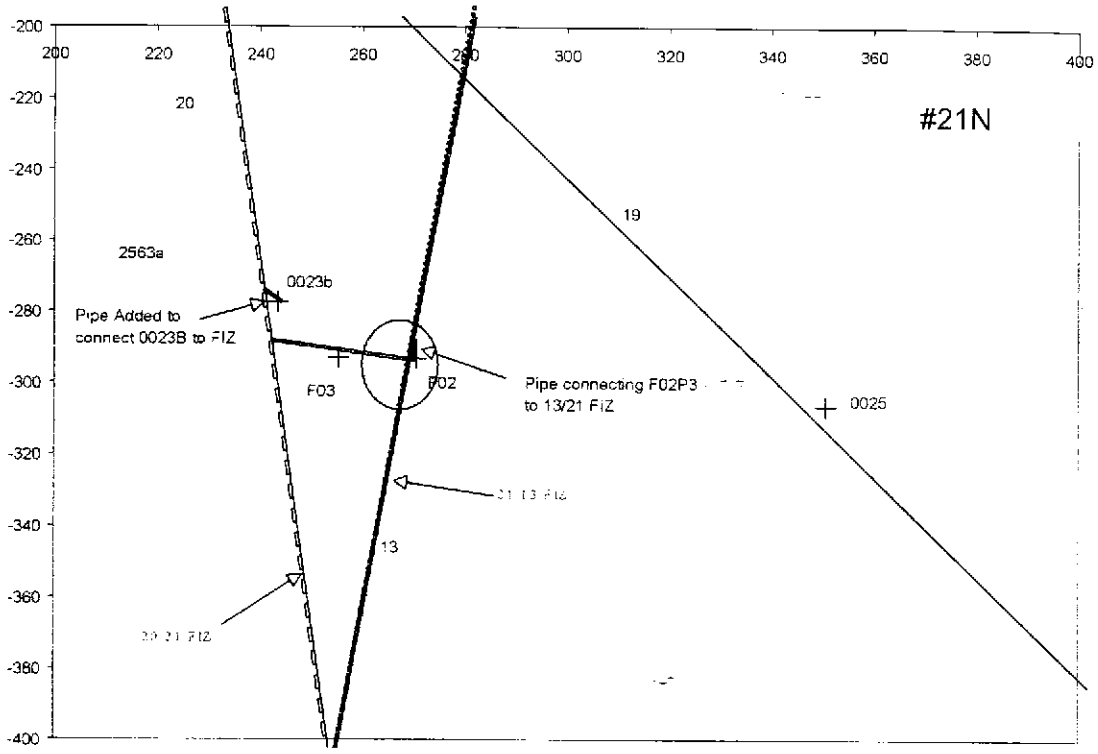

Figure 5-3 FIZ pipes in plane of Feature 21

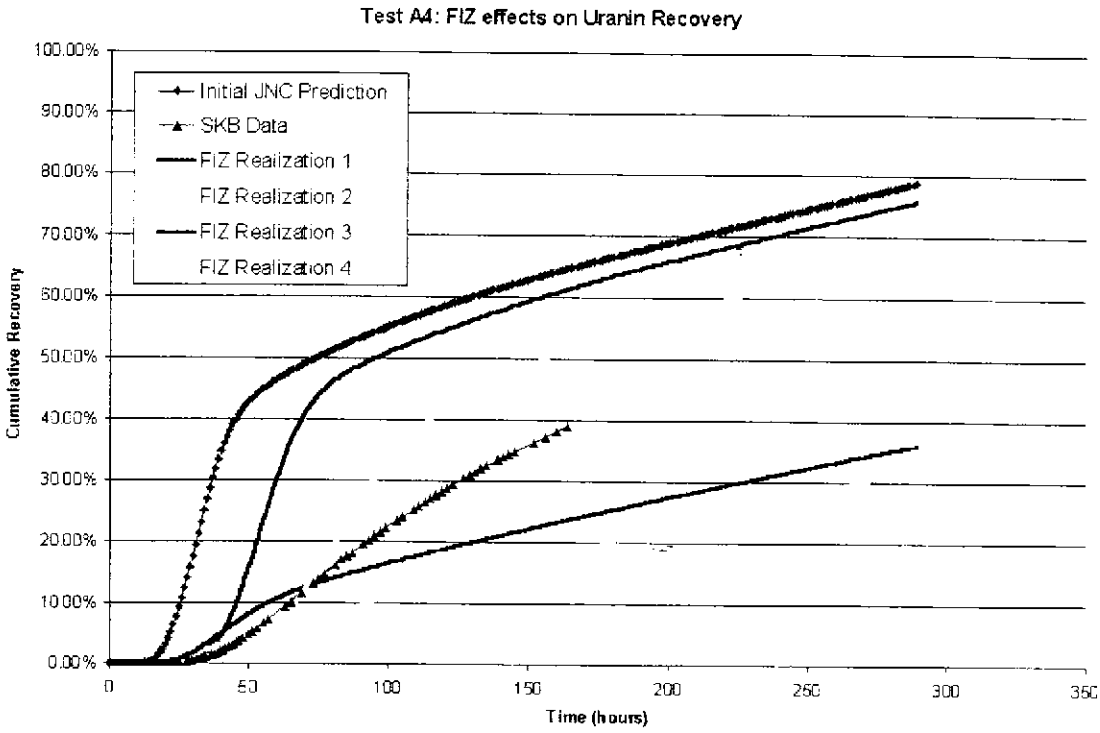

Figure 5-4 A4:Uranin Recovery with FIZ

5.1.2 TTS A-5: FIZ Simulation Parameters

Tracer test TTS A-5 injects five conservative tracers: RhodamineWT(1), Uranine, Napthionate, RhodamineWT(2), and Amino G Acid. The source and sink locations for each tracer are noted in Table 5-3. Figure 5-5 and Figure 5-6 display the post-test heads across the tested region.

Table 5-3 Tracer Test A5 Parameters

Tracer	Source	Feature
Rhodamine WT(1)	KA2563A: S4 (187.0 - 190.0 m)	20
Uranine	KI0025F02: P3 (94.4 - 99.25 m)	13, 21
Napthionate	KI0025F02: P5 (73.3 - 77.25 m)	20
RhodamineWT(2)	KI0025F02: P6 (64.0 - 72.3 m)	22
Amino G Acid	KI0025F03: P6 (59.5 - 65.5 m)	22
Sink Location	KI0025F03: P5 (66.5 - 74.5 m)	Feature 20
Pumping Rate	2.60 l/min	
Pumping Duration	54380 minutes (~ 38 days)	

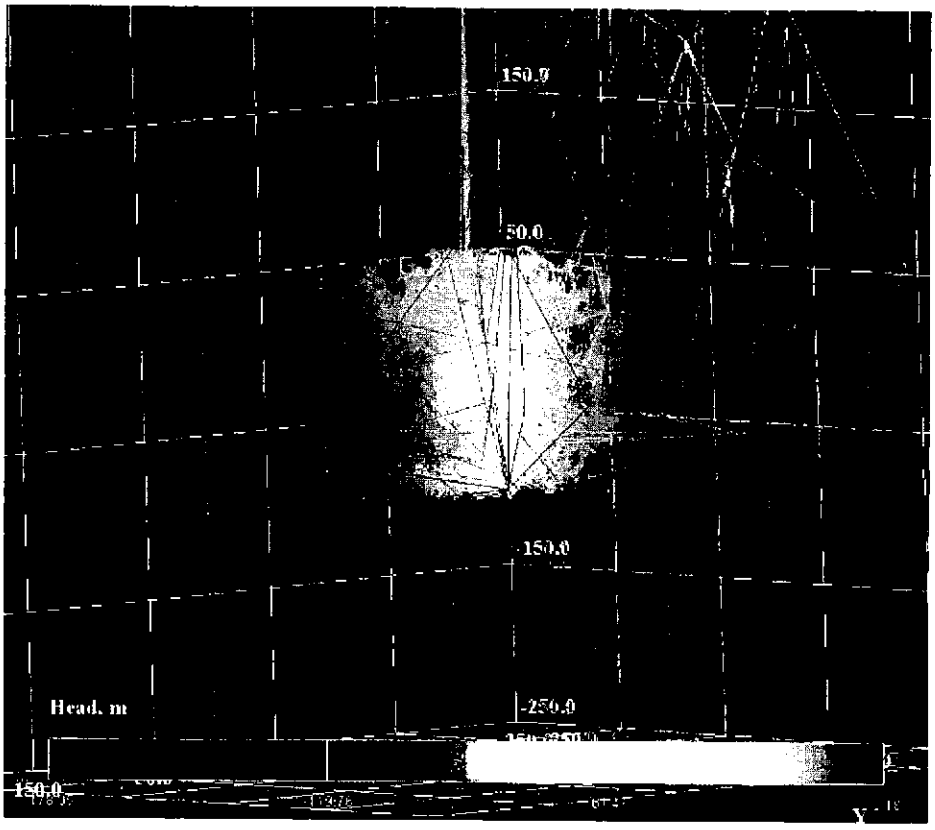

Figure 5-5 TTS A-5: Post-test Heads, CN Model Mesh, with pipes colored by head (m)

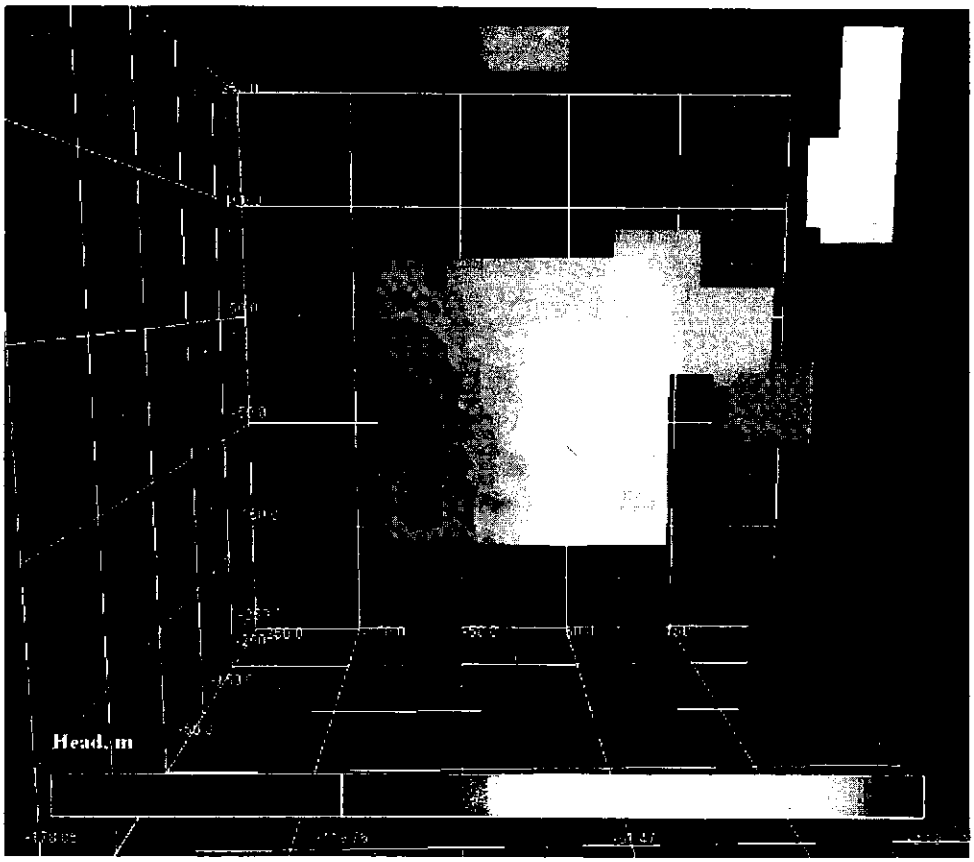

Figure 5-6 TTS A-5: Post-test Head Map View is looking towards Äspö HRL tunnel. Trace map is centered at approximately model center (7170m, 1900m, -450m) Grid colored by head (m)

Initial JNC recovery predictions were compared to recovery of tracers after adding FIZ pipes. The results are shown in Figure 5-7 through Figure 5-15.

The transmissivity of the 20/21 FIZ and the 13/21 FIZ were 9.6 x 10^{-6} m^2/s and 8.1 x 10^{-6} m^2/s respectively (10 times the transmissivity of the hosting fractures). The dispersion length was set to 1.5 m and the aperture of the FIZ followed the relationship 2*transmissivity$^{1/2}$. SKB observed no recovery of Uranine during the test duration (639 hours); the addition of the 13/21 FIZ with the previously noted parameters reduced the recovery of Uranine from 95% to 0%. RhodamineWT(1) recovery declined form 97% to 60%, Napthionate recovery declined from 99% to 74%, RhodamineWT(2) declined from 96% to 45%, and Amino G Acid recovery decreased from 97% to 47%. See Table 5-4 for a comparison of simulated recovery to measured recovery.

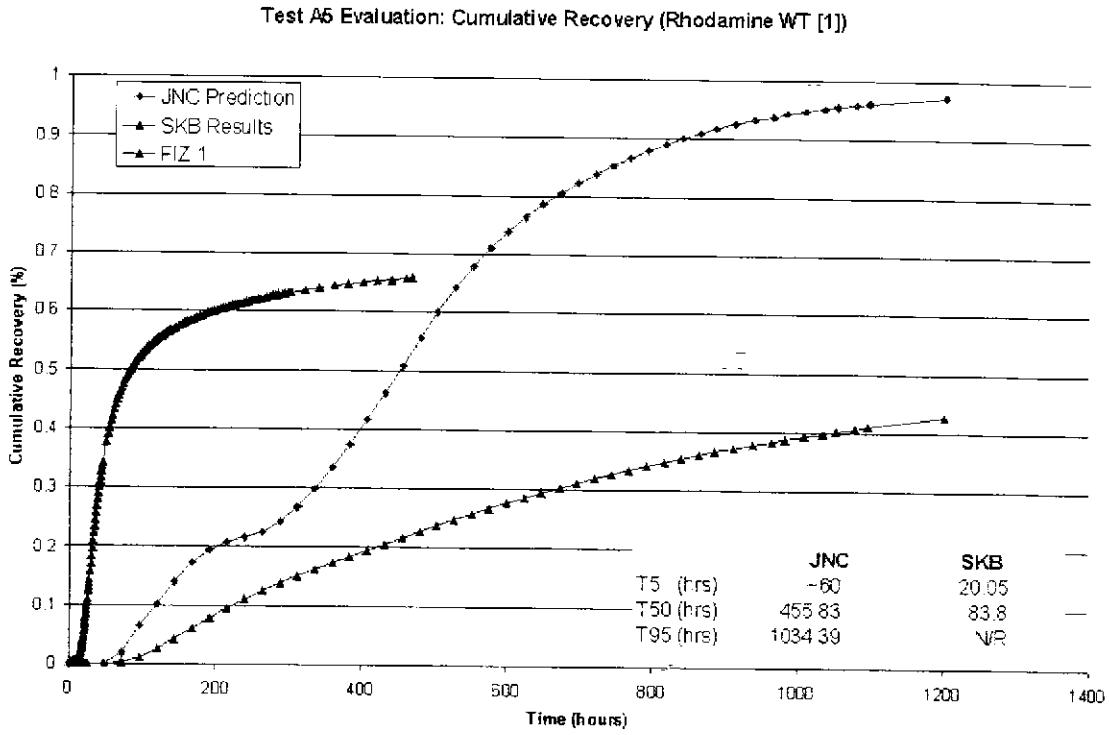

Figure 5-7 A5: Rhodamine Recovery with FIZ

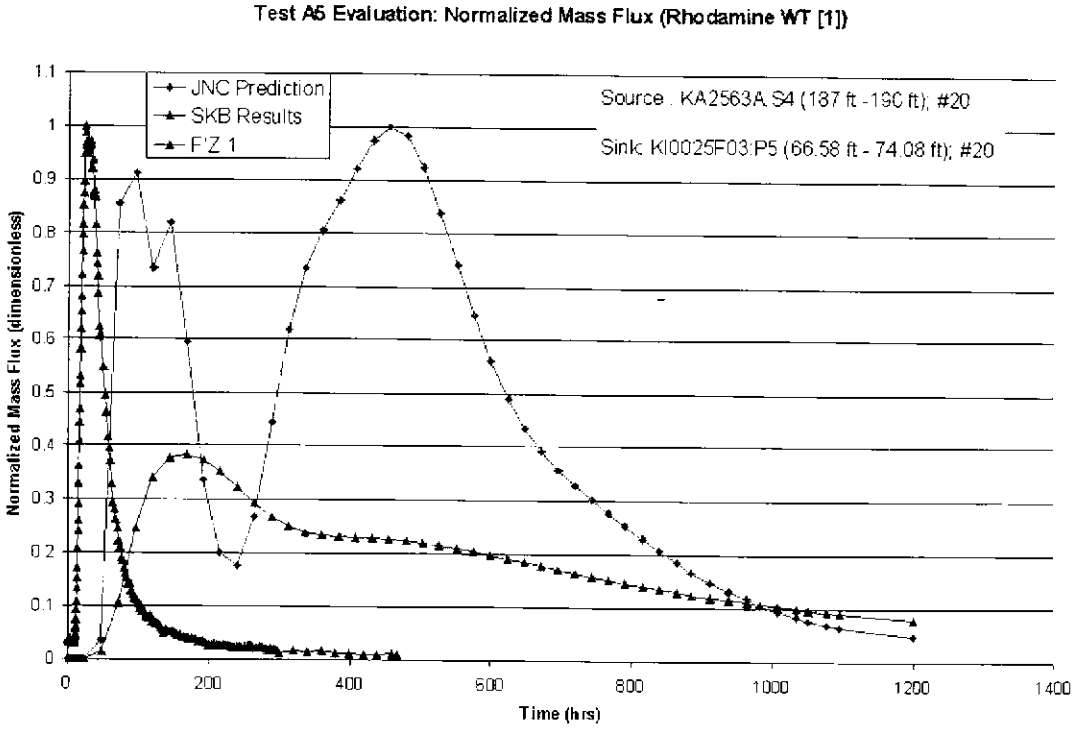

Figure 5-8: Rhodamine WT(1) Breakthrough with FIZ

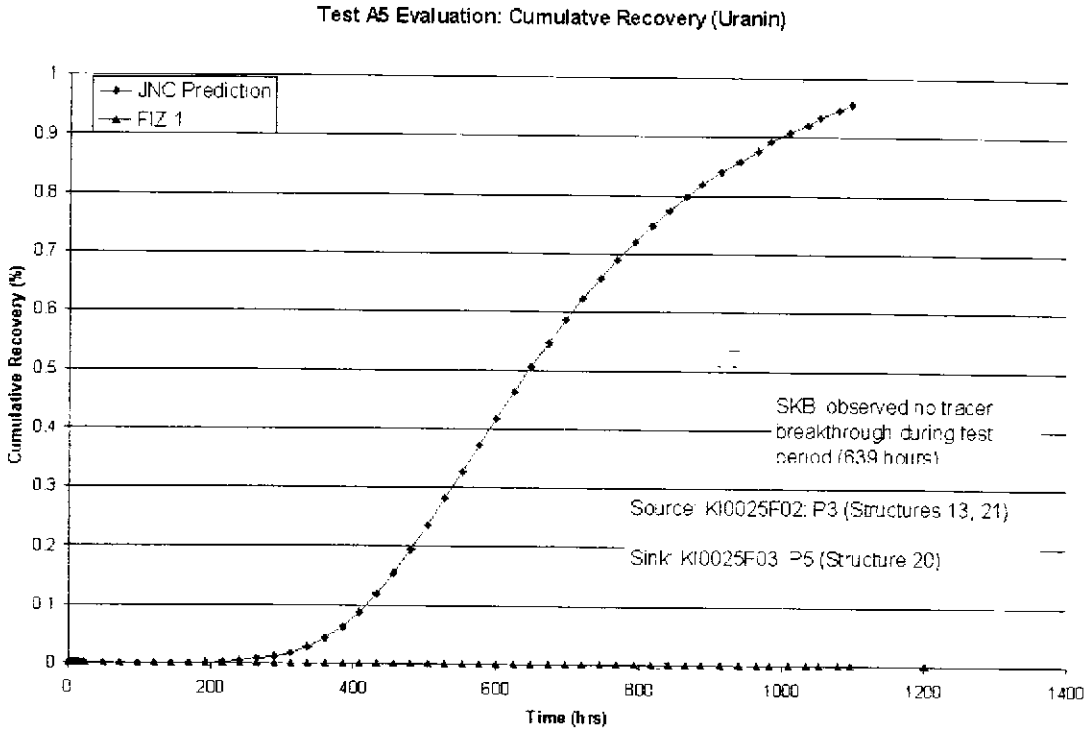

Figure 5-9 A5: Uranine Recovery with FIZ

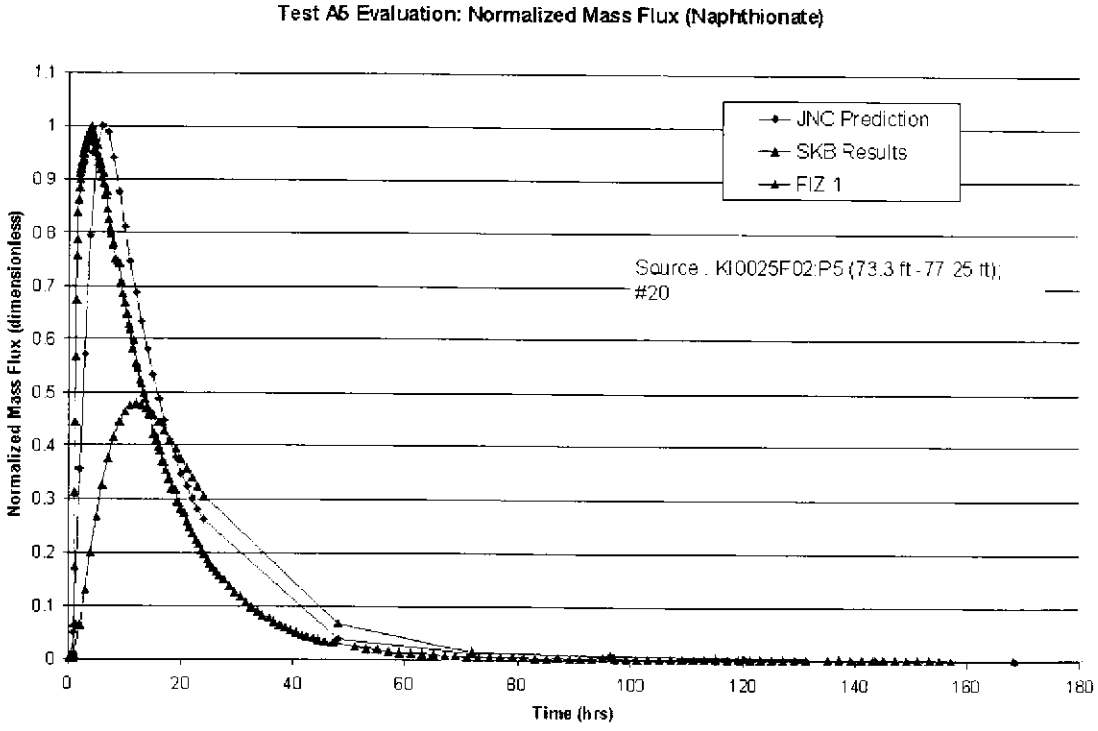

Figure 5-10 TTS A-5: Napthionate Breakthrough

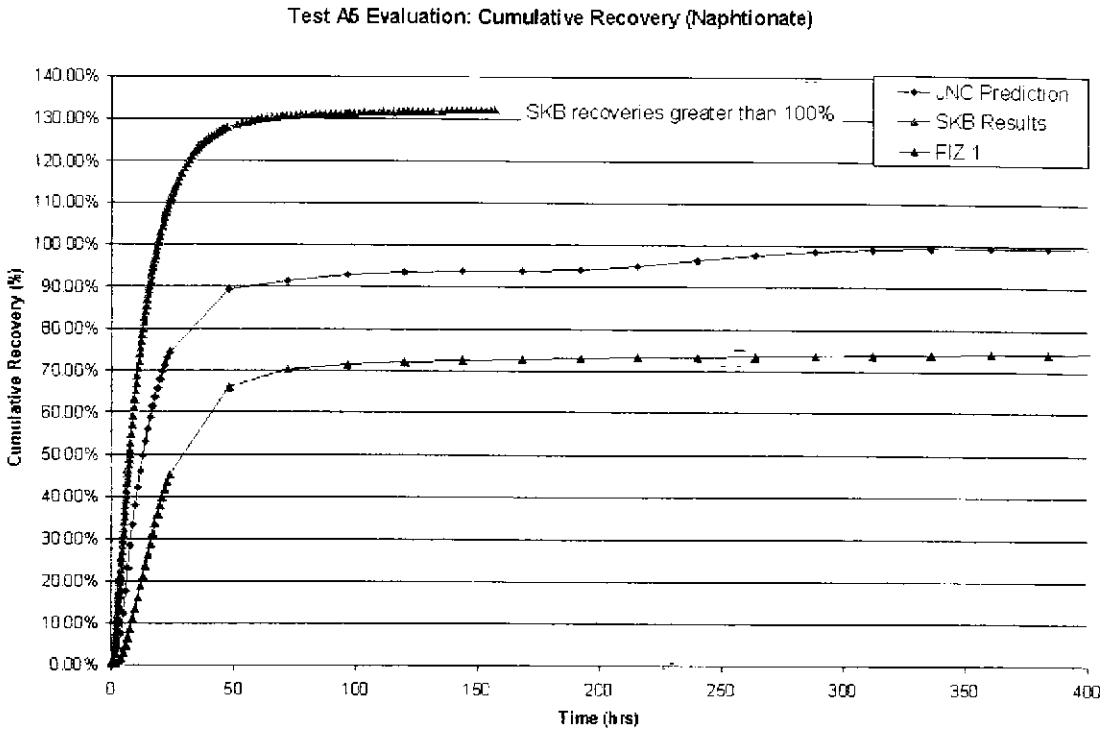

Figure 5-11 TTS A-5: Napthionate Recovery

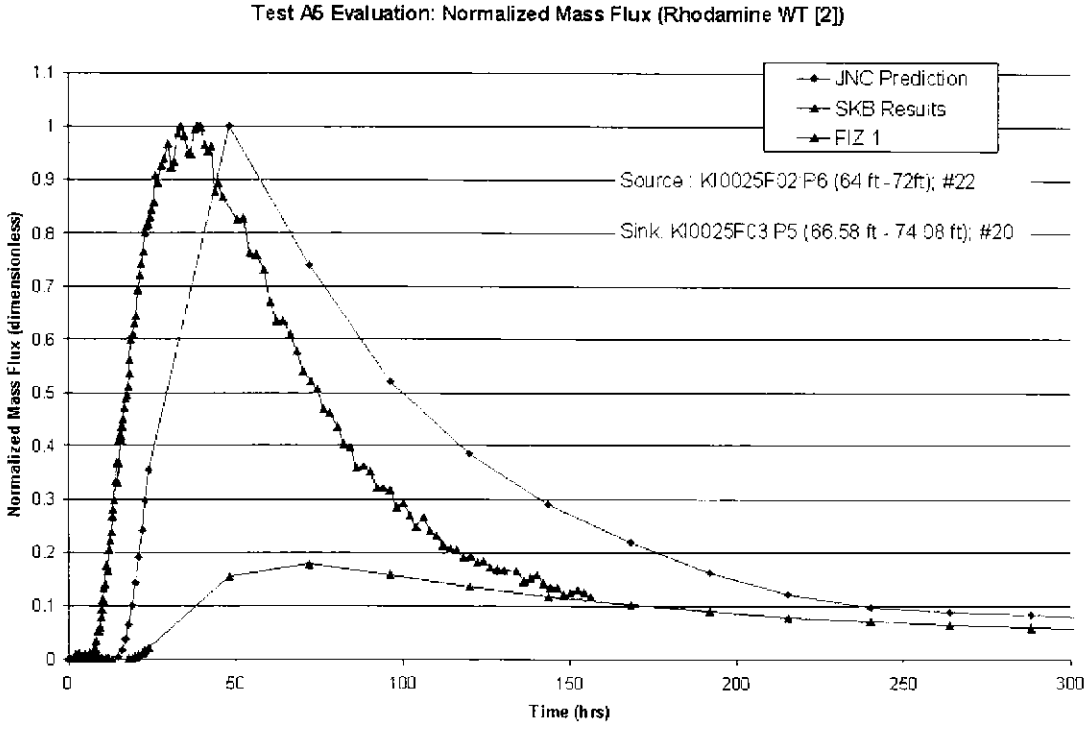

Figure 5-12 TTS A-5: Rhodamine WT(2) Breakthrough

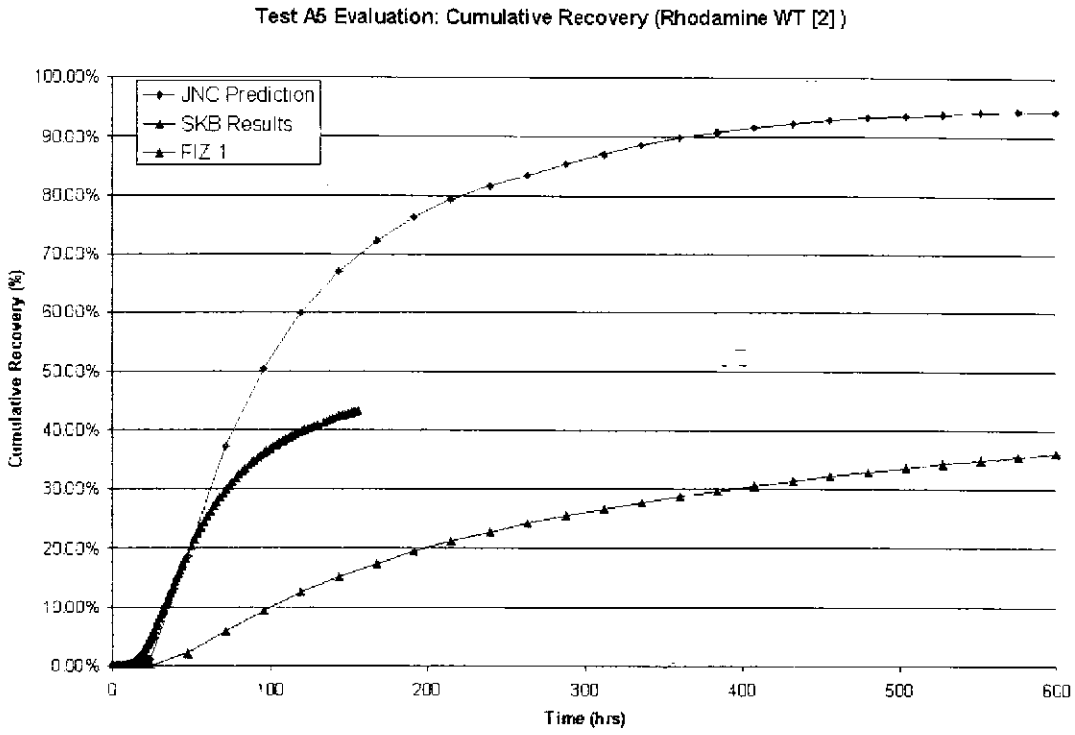

Figure 5-13 TTS A-5: Rhodamine WT(2) Recovery

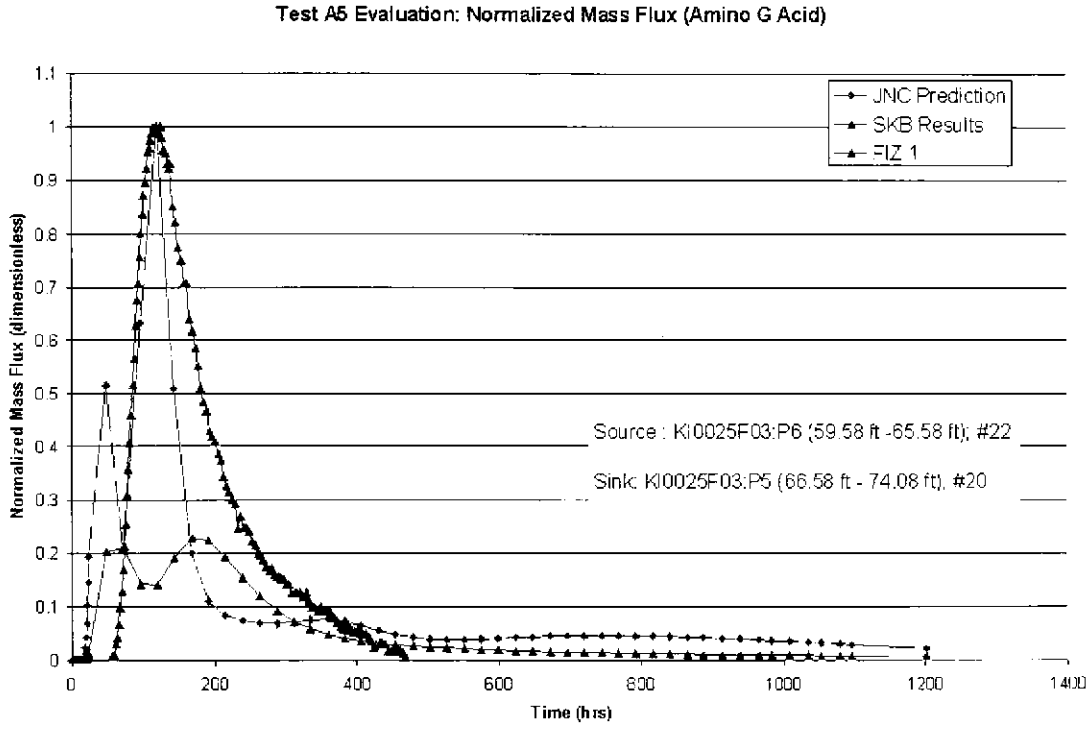

Figure 5-14 TTS A-5: Amino G Acid Breakthrough

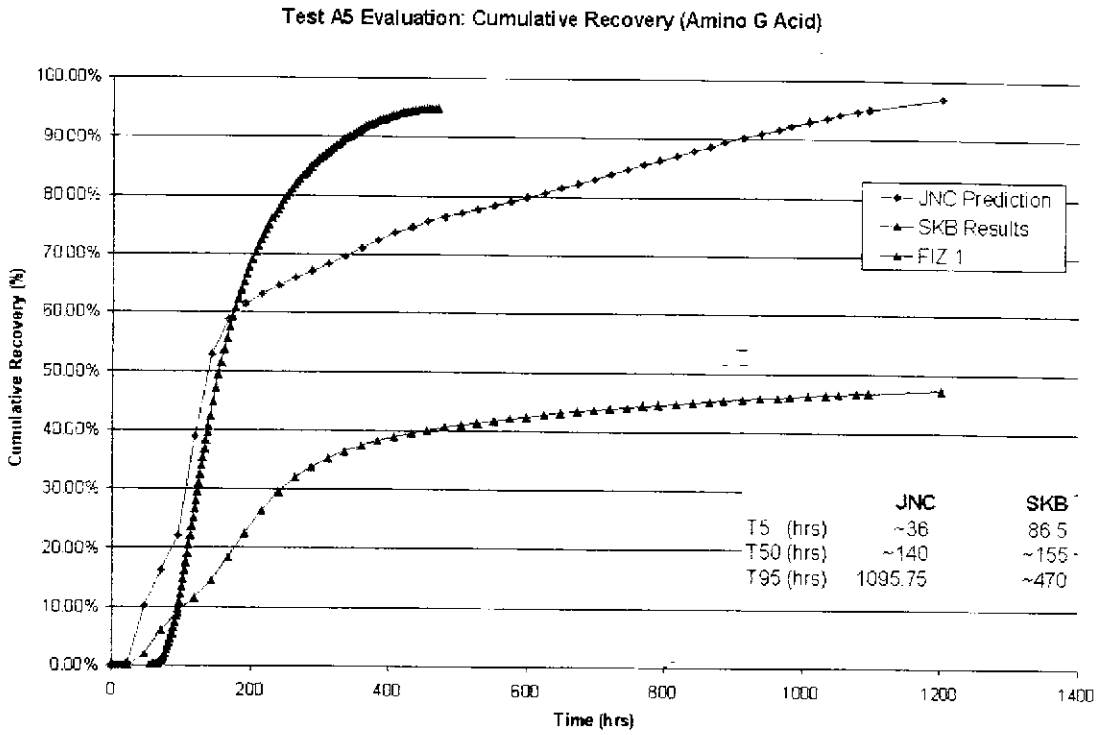

Figure 5-15 TTS A-5: Amino G Acid Recovery

Table 5-4 % Recovery, Measured versus Simulated

Tracer	Measured Recovery	Estimated Ultimate Recovery	Baseline Simulated Recovery	Simulated Recovery with FIZ 1
Rhodamine WT(1)	66%	70%	97%	43%
Uranine	0%	0%	95%	0%
Napthionate	132%	132%	100%	76%
RhodamineWT(2)	43%	55%	96%	45%
Amino G Acid	95%	97%	97%	47%

6. TRANSPORT SIMULATIONS

Based on the previously calibrated Phase A and Phase B tracer tests, CN transport simulations were undertaken for the Phase C testing. Conservative tracers were injected in three locations for the Phase C tests. Each of these tests terminated at the same location, with approximately the same pumping rate. The CN model used to model the tracer tests was based on the March 2000 Revised Äspö Structural Model (Doe, 2000), combined with stochastically-generated background fractures based on Dershowitz (2000). Test C-1 is calibrated to Phase B Test 2g, Test C-2 is calibrated to Phase B Test 2d, and Test C-3 is calibrated to Pre-Test Stage Test #4 results.

The source location has an injection rate derived from in situ recovery data.

For each test, the injection rate is estimated by multiplying the in situ concentration by an estimated injection rate until the cumulative mass injection falls within the margin of error established by the in situ injected mass. Injection rates were found for all tracers that fell within the margin or error. Table 6-1 displays the source and sink locations for each test, the deterministic feature associated with the packed off section of the source and sink, and injection and pumping rates.

Table 6-1 Phase C Test Locations

Test	Injection Location and Associated Feature	Injection Rate	Recovery Location and Associated Feature	Recovery Rate
C1	KI0025F03:P5 Feature 20, 21	7.50×10^{-7} m^3/s (0.0450 l/min)	KI0023B:P6 Feature 21	3.43×10^{-5} m^3/s (2.05 l/min)
C2	KI0025F03:P7 Feature 20	$.67 \times 10^{-7}$ m^3/s (1.02 l/min)	KI0023B:P6 Feature 21	$.43 \times 10^{-5}$ m^3/s (2.05 l/min)
C3	KI0025F02:P3 Feature 13	4.00×10^{-8} m^3/s (0.00240 l/min)	KI0023B:P6 Feature 21	3.33×10^{-5} m^3/s (2.00 l/min)

After converting the fracture model into a channel network and adding FIZ pipes at the intersection of the relevant deterministic features, the finite-element code MAFIC was used to produce an initial flow solution and associated head field.

6.1 TRANSPORT PROPERTIES

In developing the CN model used for transport simulation, the following base transport properties were used:

1. Transport Width = Flow Width
2. Fracture Aperture = 2 *Transmissivity$^{1/2}$, unless otherwise noted
3. Dispersion Length = 0.25 - 2.0 m
4. Free water diffusion (D_w) of Helium = 0.078864 m^2/yr (based on particle size)
5. Transport properties of metal complexes assumed to be the same as fluorescent dyes (Andersson,2000)
6. Matrix porosity of ranges from the bulk measured matrix porosity to values several percentage points higher than the bulk value, and represents damage zones along large-scale features
7. Background fractures have very low porosities

Simulations were calibrated to the measured breakthrough and recovery data of the provided conservative tracers. Phase C conservative tracers are assigned a diffusivity of $1.00*10^{-9}$ m^2/yr, a decay rate of $9.39*10^{-15}$ per year, matrix partition coefficient (Kd) of 0.0 m^3/kg, and a surface sorption of 0.0 m, with the exception of Helium which has a diffusivity of $2.50*10^{-9}$ m^2/yr. Calibrated parameters were then used to predict the recovery and breakthrough curves of sorbing tracers.

Figure 6-1 displays the TRUE Block Scale CN model with pipes colored by log transmissivity values. Figure 6-2 displays the CN model with pipes colored according to head.

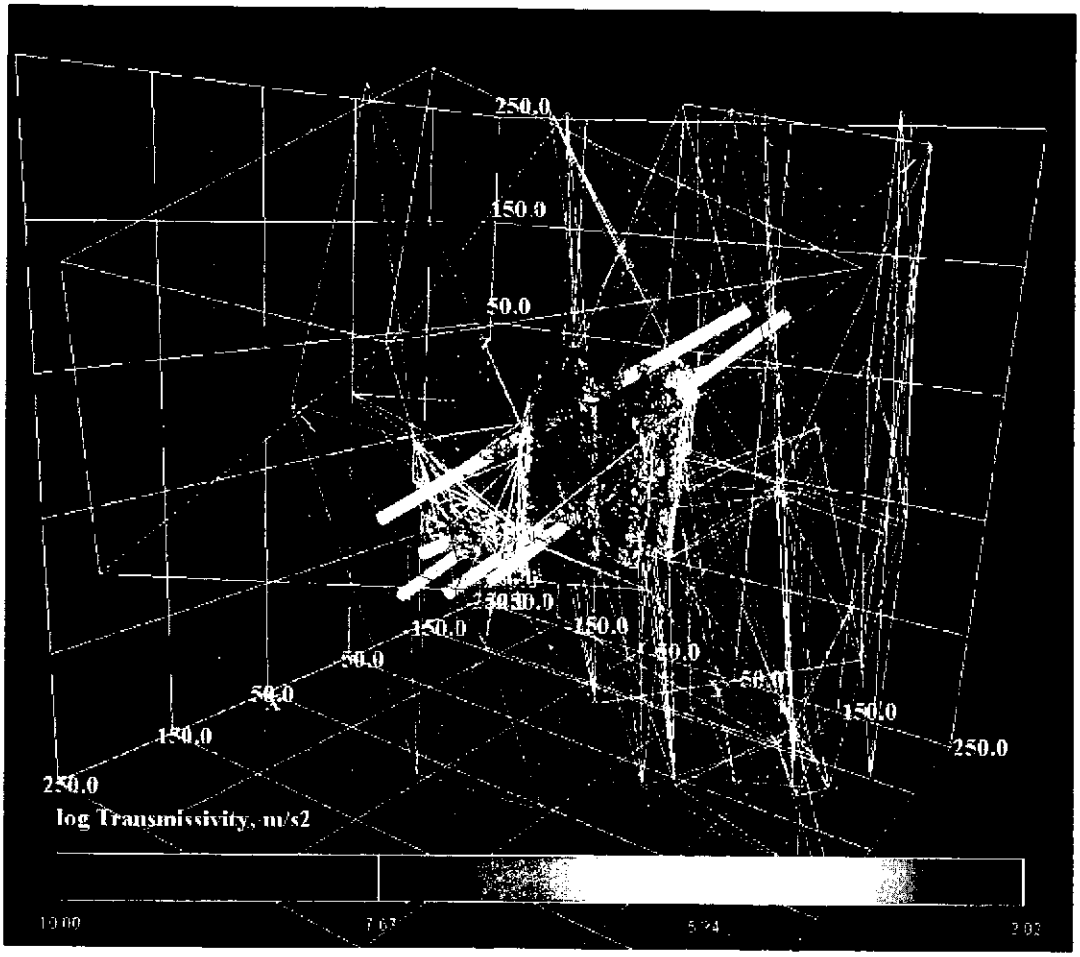

Figure 6-1 TRUE Block Scale CN model.

Note: Boreholes are not to scale. Pipes are colored by log10 of Transmissivity.

Figure 6-2 TRUE Block CN Model. Figure illustrates post-test heads from calibration runs (B2D) for Test C2 prediction.

Note: boreholes are not to scale.

6.2 CONSERVATIVE TRACER TESTS

Each test was calibrated to in situ measurements of conservative tracers. Calibration simulations were set up to model existing tracer tests (Phase A, Phase B). Simulations were calibrated by modifying diffusion distance, matrix porosity, dispersion length, and transport aperture. Transport aperture is reported as a percentage of the flow aperture, where flow aperture equals $2*\text{Transmissivity}^{1/2}$ in the fractures and $0.2*\text{Transmissivity}^{1/2}$ in the FIZ region. The matrix porosity used in these simulations is higher than the mass matrix porosity of the rock. The higher porosity values used are assumed to be aby the with damaged, or gauged, zone on either side of the fracture. The diffusion distance is the maximum distance solute can be transported into the rock or non-flowing pore space. Dispersion length refers to the longitudinal dispersion length and is used in transport calculations. Each test underwent a second set of calibrations using the diffusion distance and matrix porosity from TRUE 1 Task4F. The diffusion distance of 0.01 m and matrix porosity of 3% calibrated from TRUE 1 Task 4F were held constant while dispersion length and aperture were modified to find the best fit to the in situ measurements.

Calibrations were fitted to the in situ breakthrough curves and recovery curves. The calibrated model that best fits the measured breakthrough and recovery data for each test is described below.

6.2.1 Test C1 Calibration

The conservative tracers used to calibrate test C-1 were Napthionate and Helium-3. The two tracers were injected into borehole KI0025F03 section P5 and were recovered at borehole KI0023B section P6. The tracers differed by their diffusivity value: Napthionate has a diffusivity value of 0.0315576 m/yr, while the diffusivity of Helium-3 equals 0.078894 m/yr. Test C-1 traveled entirely on Feature 21. The in situ conservative tracer recovery and breakthrough measurements were best matched by Simulation Run #2. The matrix porosity in Run #2 differs between the background fractures and the deterministic features, equaling 0.001% and 0.5% respectively. The diffusion distance is set to 0.1 mm for the background fractures and 1 cm for the deterministic features. The flow aperture is 25% of the flow aperture and the dispersion length is 1 m.

Figure 6-3 through Figure 6-6 show breakthrough and recovery comparisons between measured and simulated data. Table 6-2 displays the input parameters for the calibration runs displayed in the breakthrough and recovery figures.

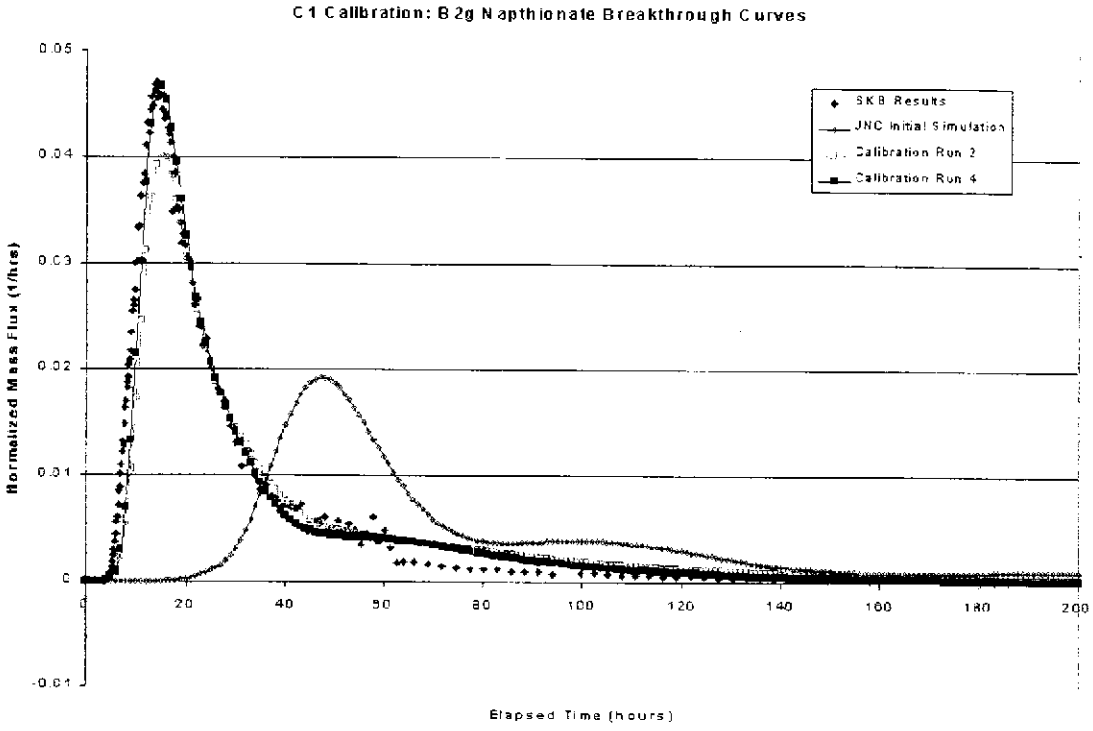

Figure 6-3 B2G: Napthionate Breakthrough

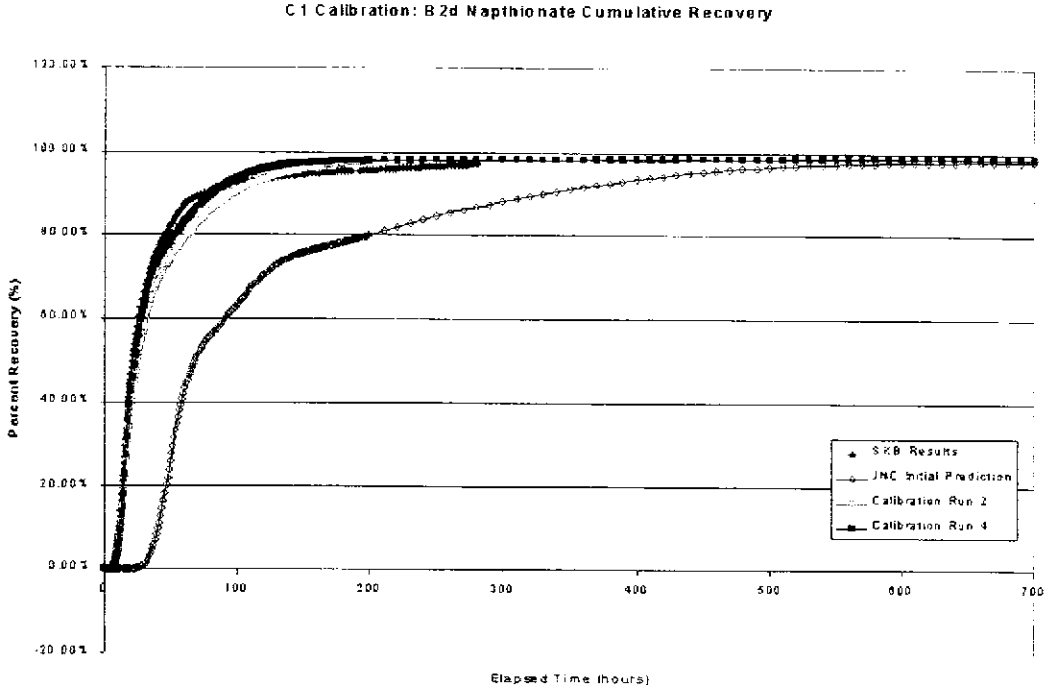

Figure 6-4 B2G: Napthionate Recovery

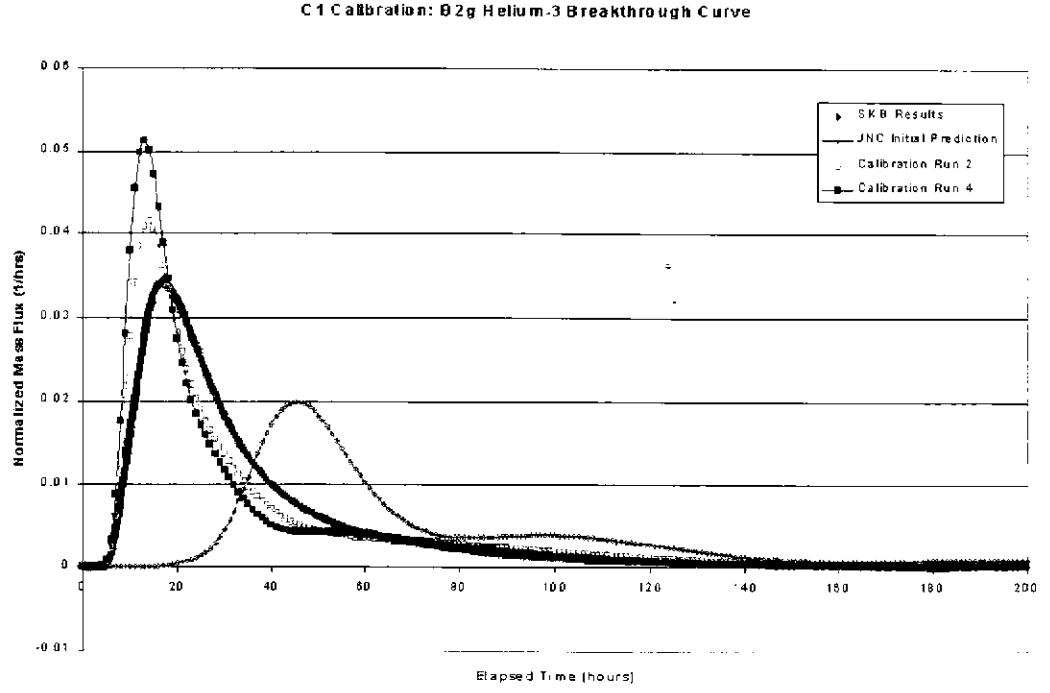

Figure 6-5 B2G: Helium-3 Breakthrough

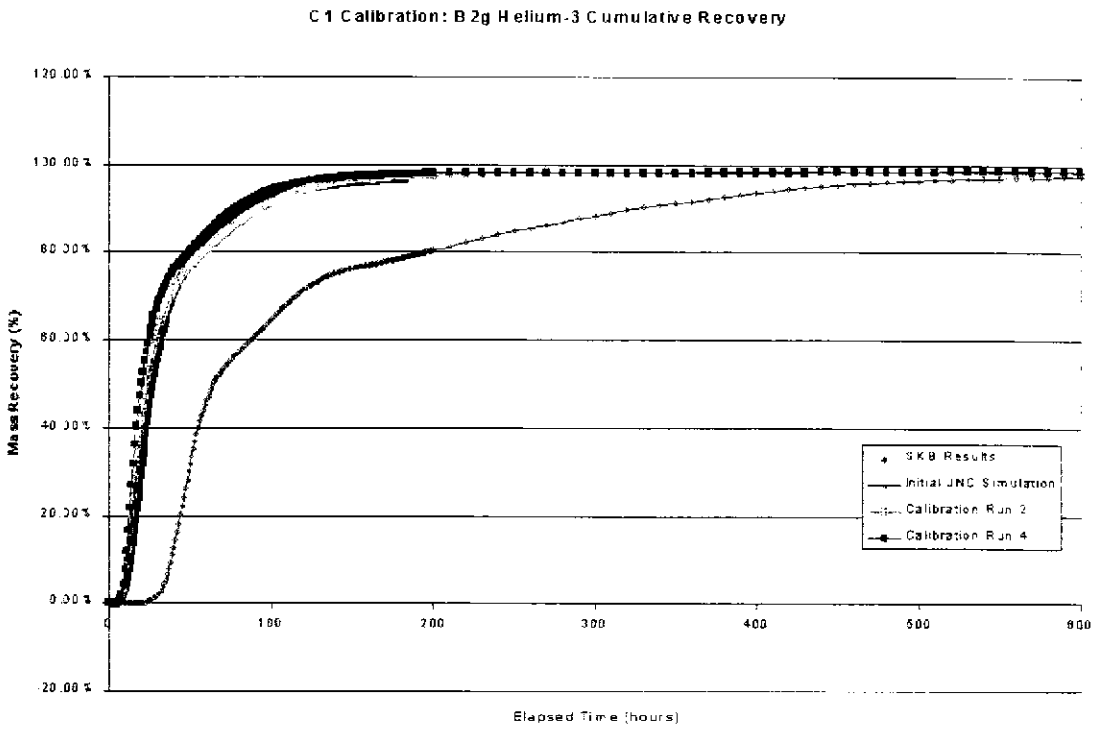

Figure 6-6 B2G: Helium-3 Recovery

Table 6-2 Test C-1 Calibration Parameters

Calibration Run	% Porosity	Diffusion Distance (m)	Dispersion Length (m)	Transport Aperture (m)
2	0.001% on background fractures, 0.5% on deterministic fractures	0.0001 on background fractures, 0.01 on deterministic fractures	1	0.25*flow aperture
4	0.5% on background fractures, 0.001% on deterministic fractures	0.01 on background fractures, 0.0001 on deterministic fractures	1	0.25*flow aperture

The results of the Test C-1 calibration show the difficulty in matching both of the conservative tracers to the in situ measurements. The conservative tracers differ in diffusivity values, Helium has a diffusivity of $2.50*10^{-9}$ m^2/yr while Napthionate has a diffusivity og $1.00*10^{-9}$ m^2/yr. The Helium tracer is highly sensitive to changes in matrix porosity and maximum diffusion distance. The relationship between flow aperture and transmissivity, $0.25*Transmissivity^{1/2}$, was found to produce better fits to the measured data. Napthionate matches both the breakthrough and recovery curves with a high accuracy. The low diffusion distances and matrix porosity on both deterministic features and background fractures suggest that little tracer is moving into the immobile zone. The diffusion length of 1 m is approximately 6% of the total flow path along deterministic features from source to sink. A transport aperture equal to 25% of the flow aperture was calibrated by fitting the early time first recovery of the tracer at approximately 10 hours.

6.2.2 Test C2 Calibration

The conservative tracer used to calibrate test C-2 is Gadolinium. The tracer was injected into borehole KI0025F03 section P7 and was recovered at borehole KI0023B section P6. Test C-2 traveled from feature 20 to feature 21. In situ conservative tracer recovery and breakthrough data was best matched by Simulation Run #17g. The model had a matrix porosity of 0.5% for the background fractures and 0.001% for the deterministic features. The diffusion distance was 3mm on the background fractures and 0.01mm on the deterministic features. Transport aperture was set to 13.5% of the flow aperture and the diffusion length was 0.25m. Figure 6-7 and Figure 6-8 contains the calibrated simulations from test C-2. Figure 6-9 illustrates channel pathways from the source to the sink locations. Table 6-3 displays the input parameters for the calibration runs displayed in the breakthrough and recovery figures.

Test C-2 experiences a 15% mass loss during the duration of the test. The simulated model for Test C-2 allows for mass loss due to the 20/21 FIZ. In this simulation, the FIZ is responsible for diverting mass away from the pumping location, thus decreasing the total amount of tracer that is recovered at the sink location.

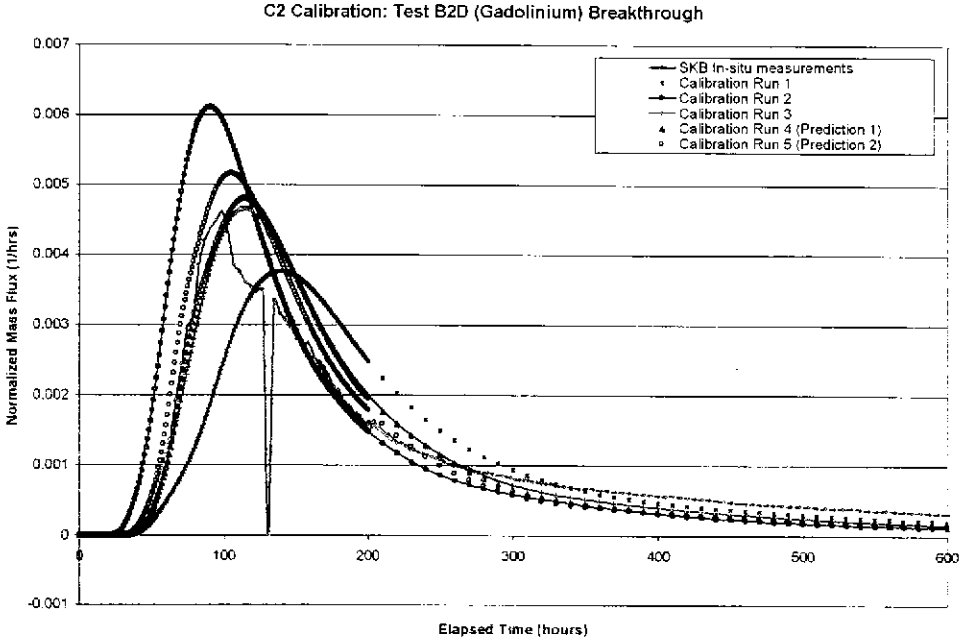

Figure 6-7 B2D: Gadolinium Breakthrough

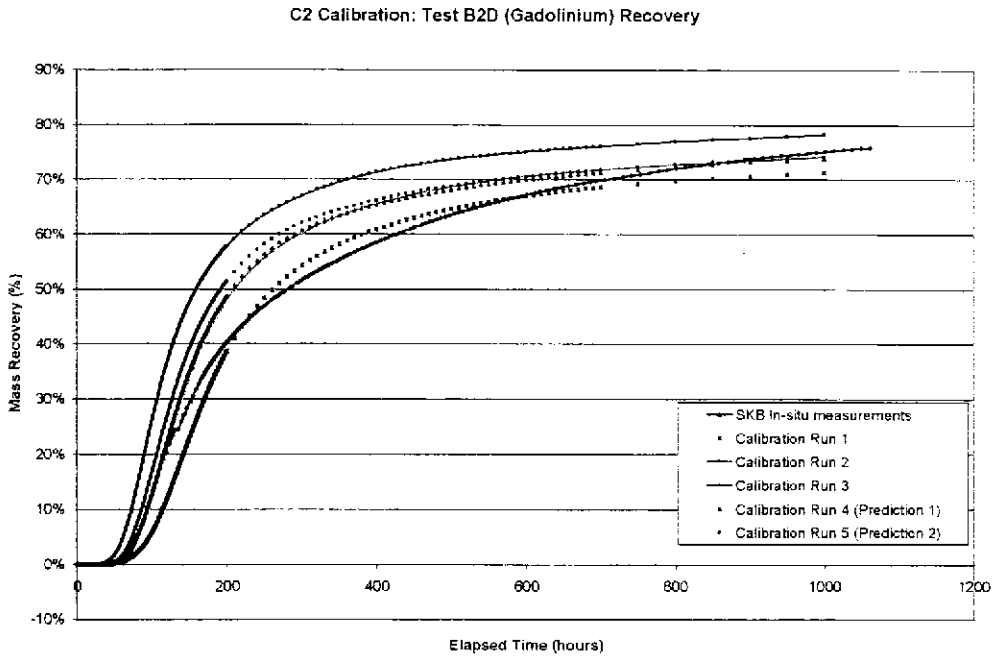

Figure 6-8 B2D: Gadolinium Recovery

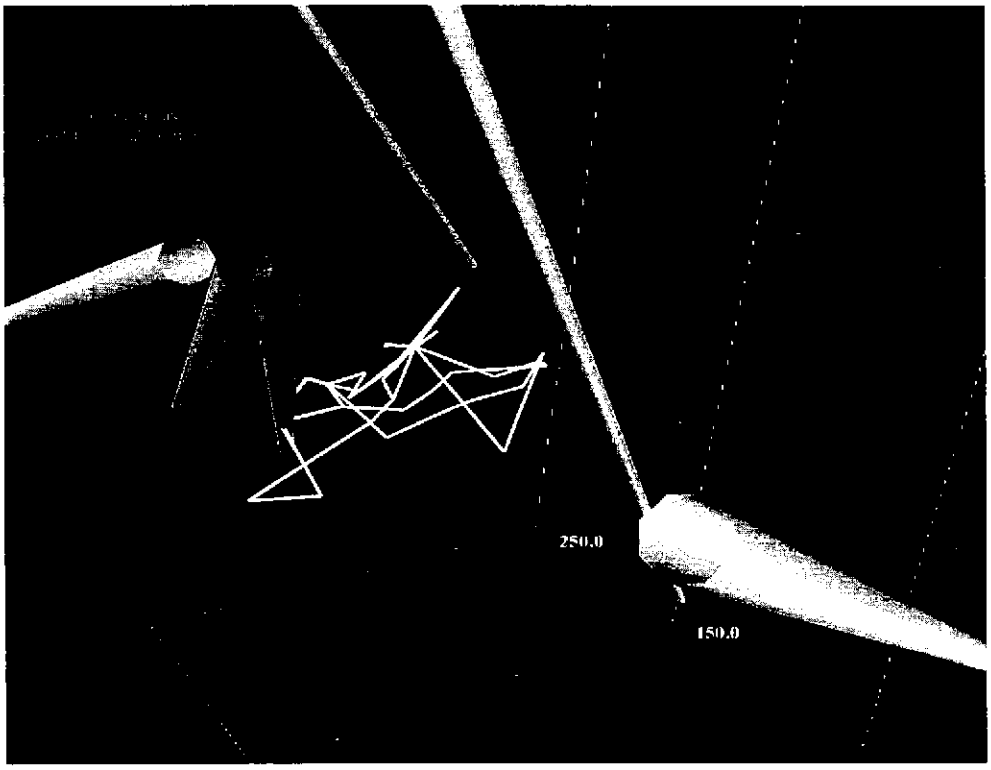

Figure 6-9 C2 Calibration: B2D transport pathways, consists of 4 sample pathways of varying path lengths

Table 6-3 Test C-2 Calibration Parameters

Calibration Run	Porosity	Diffusion Distance (m)	Dispersion Length (m)	Transport Aperture
1	1%	0.005	0.5	0.2*flow aperture
2	1%	0.001	0.25	0.1*flow aperture
3	1%	0.001	0.75	0.15*flow aperture
4	0.50%	0.003 on background fractures, 0.00001 on deterministic fractures	0.25	0.15*flow aperture
5	0.5% on background fractures, 0.001% on deterministic fractures	0.003 on background fractures, 0.00001 on deterministic fractures	0.25	0.135*flow aperture

The results of the Test C-2 calibration show difficulty in matching the peak mass flux. Early and late recovery times are good, but the mid-time results were difficult to match using realistic parameters. The low diffusion distances and matrix porosity on both deterministic features and background fractures suggest that little tracer was moving into the immobile zone. The small dispersion length, approximately 2% of the travel distance along deterministic features, length attests to the steep recovery curve. The transport aperture of 13.5% of the flow aperture was obtained by fitting the early time recovery of the tracer at approximately 50 hours.

6.2.3 Test C3 Calibration

The conservative tracer used to calibrate test C-3 is Amino G Acid. The tracer is injected into borehole KI0025F02 section P3 and is recovered at borehole KI0023B section P6. Test C-3 travels from feature 13 to feature 21. The in situ conservative tracer recovery and breakthrough data was best matched for Run #22. This model had a matrix porosity of 1%, a diffusion distance of 1mm, the transport aperture was 30% of the flow aperture, and the diffusion length was 2m. Figure 6-16 and Figure 6-17 show the comparison of measured and simulated tracer breakthrough and recovery respectively. Table 6-4 displays the calibration parameters of simulations displayed in the following figures.

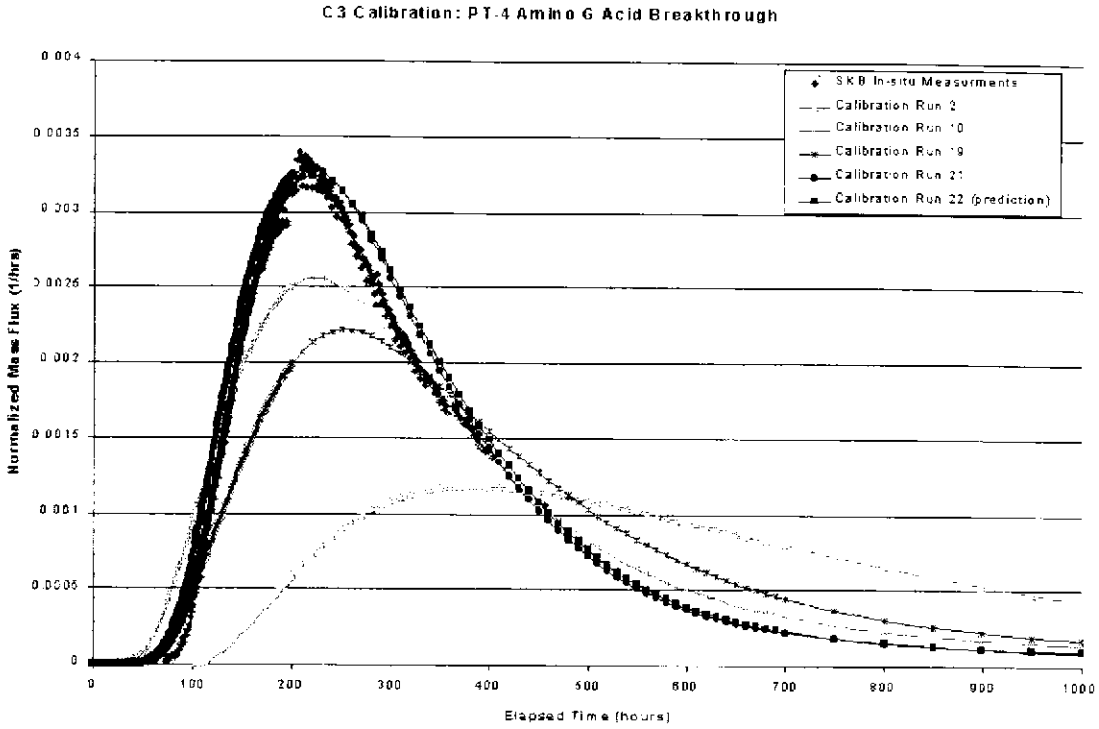

Figure 6-10 PT4: Amino G Acid Breakthrough

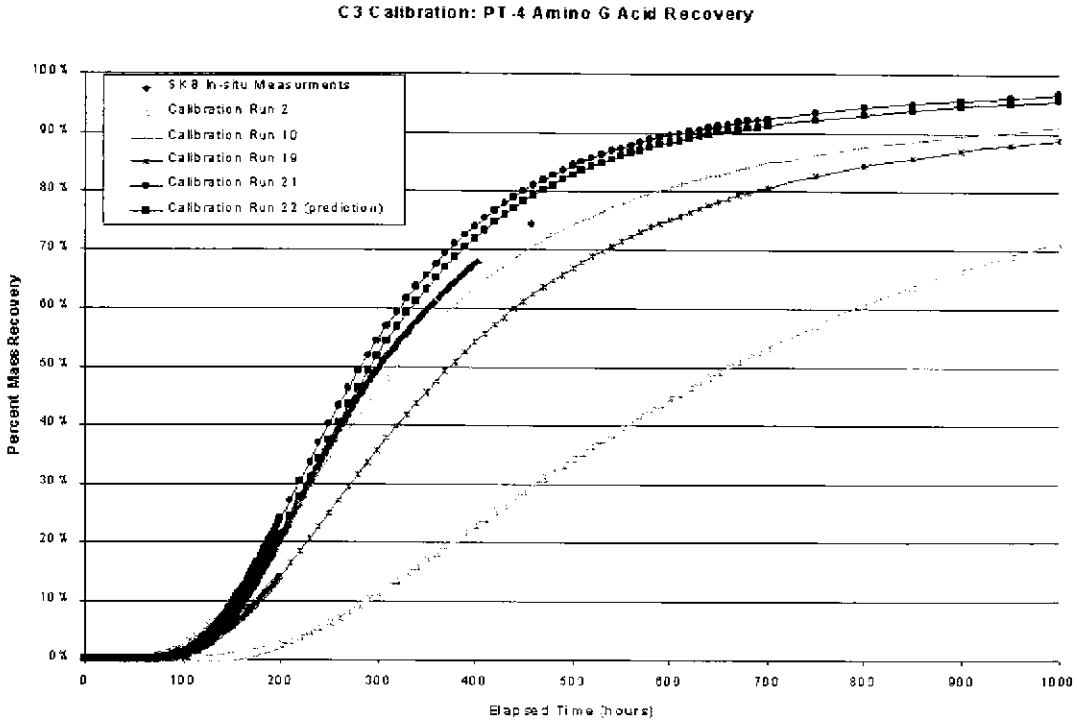

Figure 6-11 PT4: Amino G Acid Recovery

Table 6-4 Test C-3 Calibration Parameters

Calibration Run	Porosity (%)	Diffusion Distance (m)	Dispersion Length (m)	Transport Aperture (m)
2	1%	0.01	10	flow aperture
10	1%	0.01	5	0.22*flow aperture
19	1%	0.01	5	0.3*flow aperture
21	1%	0.0001	2.5	0.3*flow aperture
22	1%	0.001	2	0.3*flow aperture

The Test C-3 calibration resulted in a late time recovery result higher than that of the measured recovery. Mass flux matches after the peak breakthrough were improved by decreasing the dispersion length. Early time mass flux matches were improved with decreased diffusion into the matrix. The matrix porosity of 1% and diffusion distance of 1 mm attests to little surface sorption. The dispersion length of 2 m is approximately 6% of the travel path along the deterministic features from source to sink.

6.2.4 Calibrations with TRUE 1 Parameters

All Phase C tracer tests were calibrated a second time using the diffusion distance and matrix porosity from the TRUE 1 Task 4F calibrations. Modifying only the dispersion length and the aperture, the best calibrated simulation using the TRUE 1 parameters was compared to the calibration results from TRUE BS and to the in situ measurements. Simulations using the TRUE 1 Task 4F diffusion distance of 1 cm and the matrix porosity of 3% were not able to achieve the high recoveries and high mass flux peak seen in the Phase C tests with realistic dispersion length and aperture parameters. The results of these calibrations can be seen in Figure 6-12 through Figure 6-17. The best fit calibration from TRUE BS is displayed along with the best fit calibration run using the diffusion distance and porosity parameters from TRUE 1 Task 4F. Figure 6-17 PT4: Amino G Acid Recovery – TRUE 1 Task 4F Calibration.

Table 6-5 displays the input parameters for the best match calibration using the TRUE 1 Task 4F parameters.

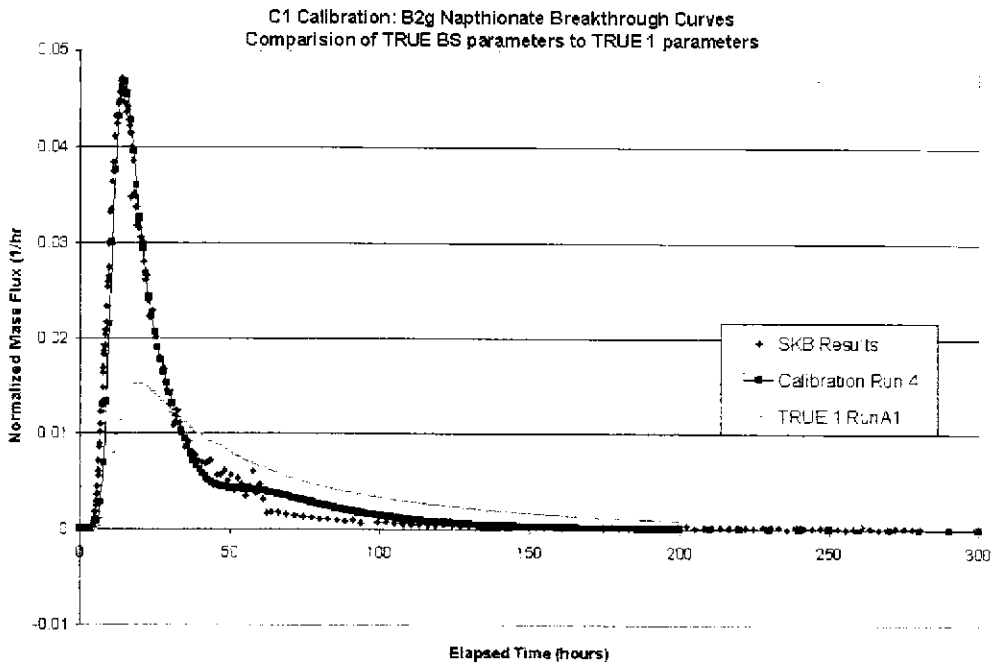

Figure 6-12 B2G: Napthionate Breakthrough - TRUE 1 Task 4F Calibration

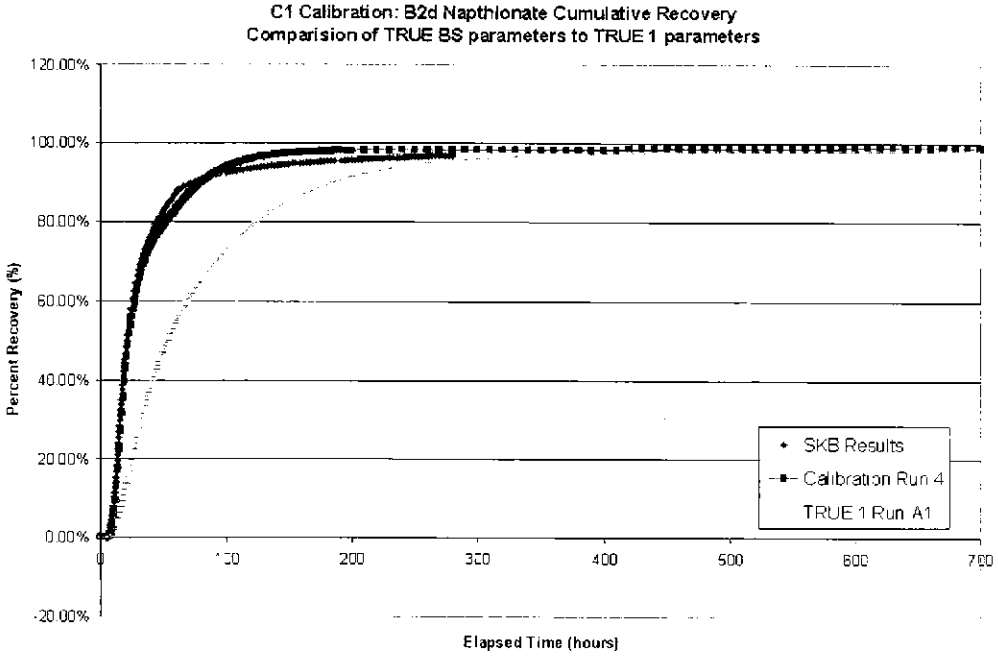

Figure 6-13 B2G: Napthionate Recovery - TRUE 1 Task 4F Calibration

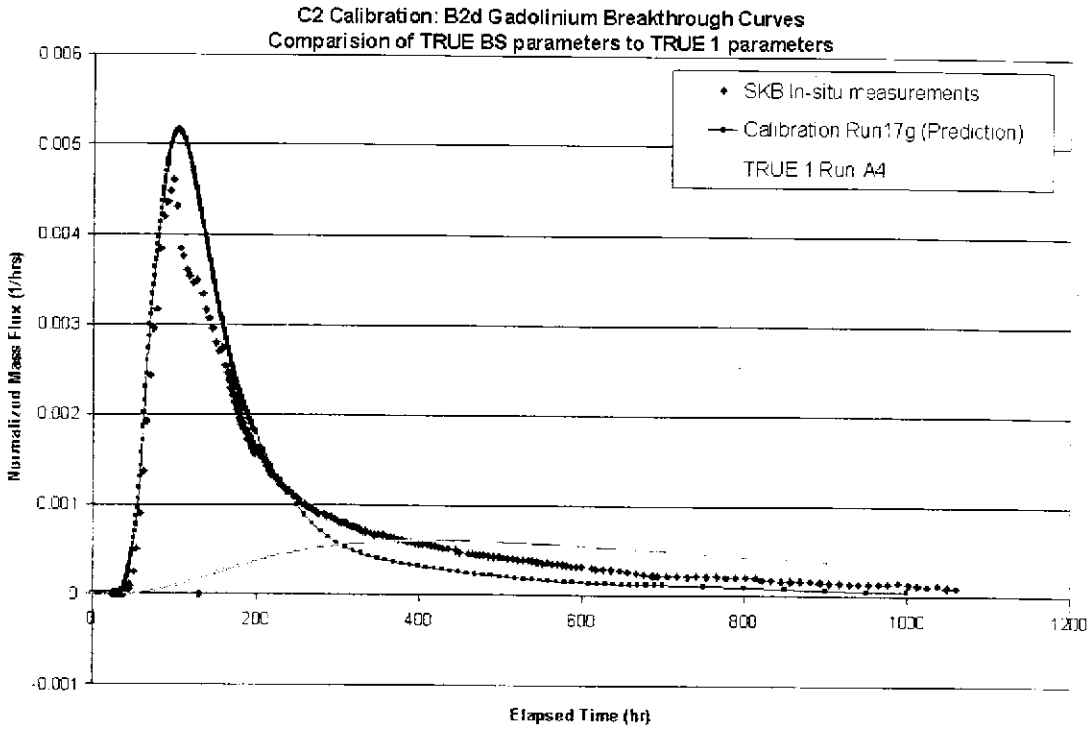

Figure 6-14 B2D: Gadolinium Breakthrough - TRUE 1 Task 4F Calibration

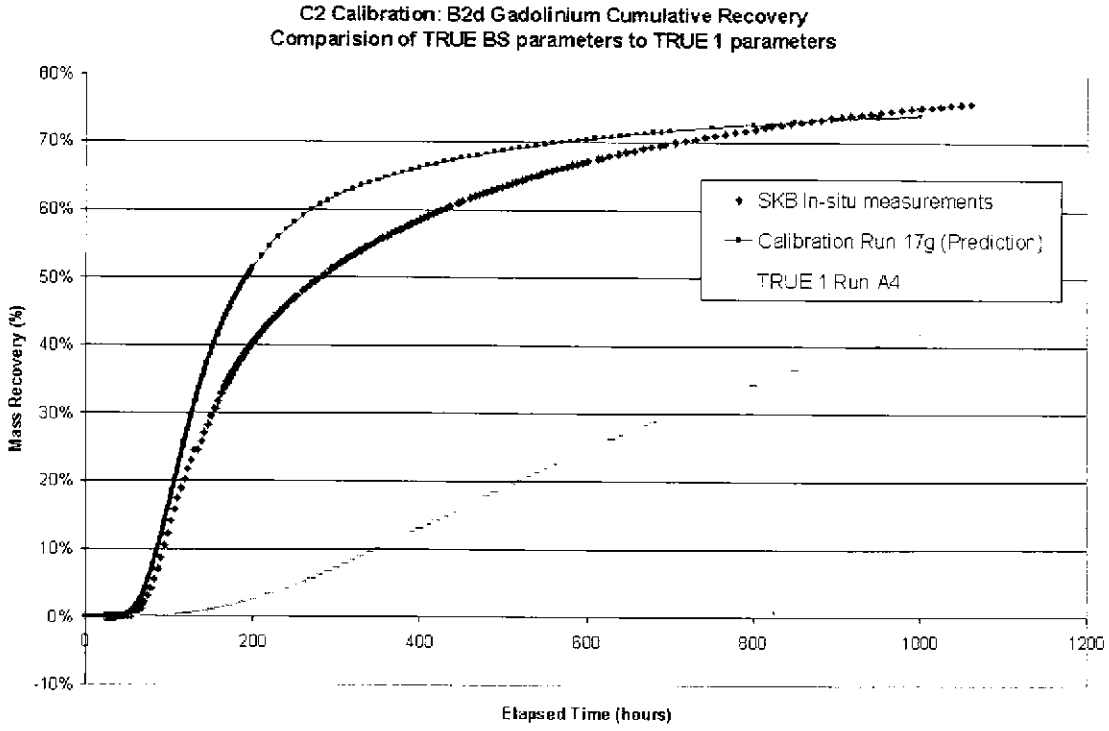

Figure 6-15 B2D: Gadolinium Recovery - TRUE 1 Task 4F Calibration

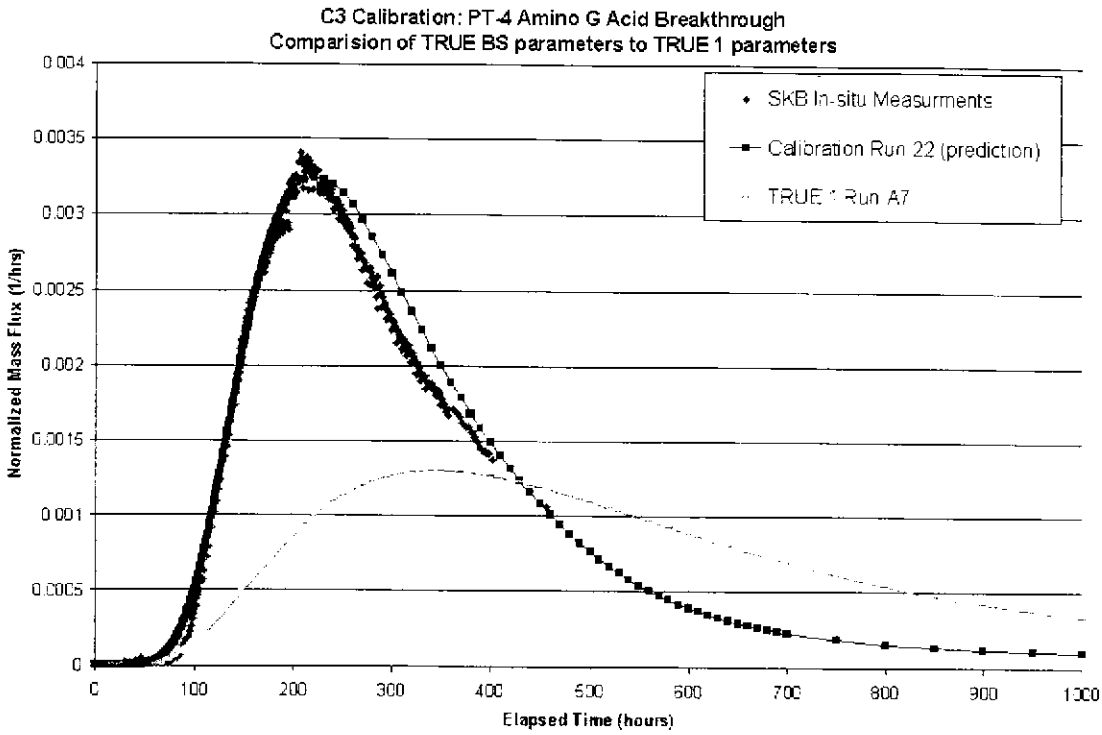

Figure 6-16 PT4: Amino G Acid Breakthrough - TRUE 1 Task 4F Calibration

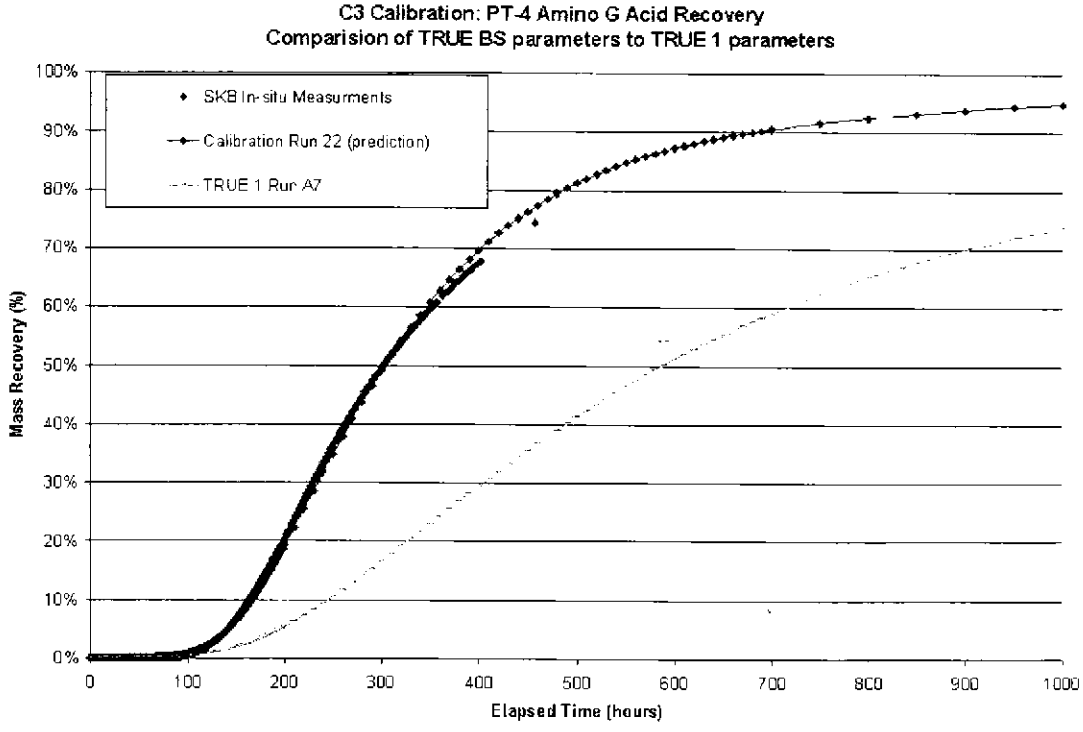

Figure 6-17 PT4: Amino G Acid Recovery - TRUE 1 Task 4F Calibration

Table 6-5 TRUE 1 Task 4F Calibration Parameters. Values highlighted in red are fixed parameters for the TRUE 1 Task 4F calibration

Test	Calibration Run	Matrix Porosity	Diffusion Distance (m)	Transport Aperture (m)	Diffusion Length (m)
C1	Calibration Run #4	0.001% Deterministic, 0.5% Background	0.0001 Deterministic, 0.01 Background	0.25*Transport Aperture	1
	TRUE 1 Task 4F	3%	0.01	0.3*Transport Aperture	2.5
C2	Calibration Run #17g	0.001% Deterministic, 0.5% Background	0.00001 Deterministic, 0.003 Background	0.135*Transport Aperture	0.25
	TRUE 1 Task 4F	3%	0.01	0.025*Transport Aperture	10
C3	Calibration Run #22	1%	0.001	0.3.*Transport Aperture	2
	TRUE 1 Task 4F	3%	0.01	0.37*Transport Aperture	10

6.2.5 Multiple Background Fracture Realizations

Multiple realizations of the stochastically generated background fractures were preformed to compare the effects of different background fracture sets on the transport of tracers. 90% to 100% of the injected mass travels through pipes associated with background fractures over the duration of the test. The effects of various background fractures realizations on the best fit calibrated simulation can be seen in Figures 6-18 through Figure 6-20

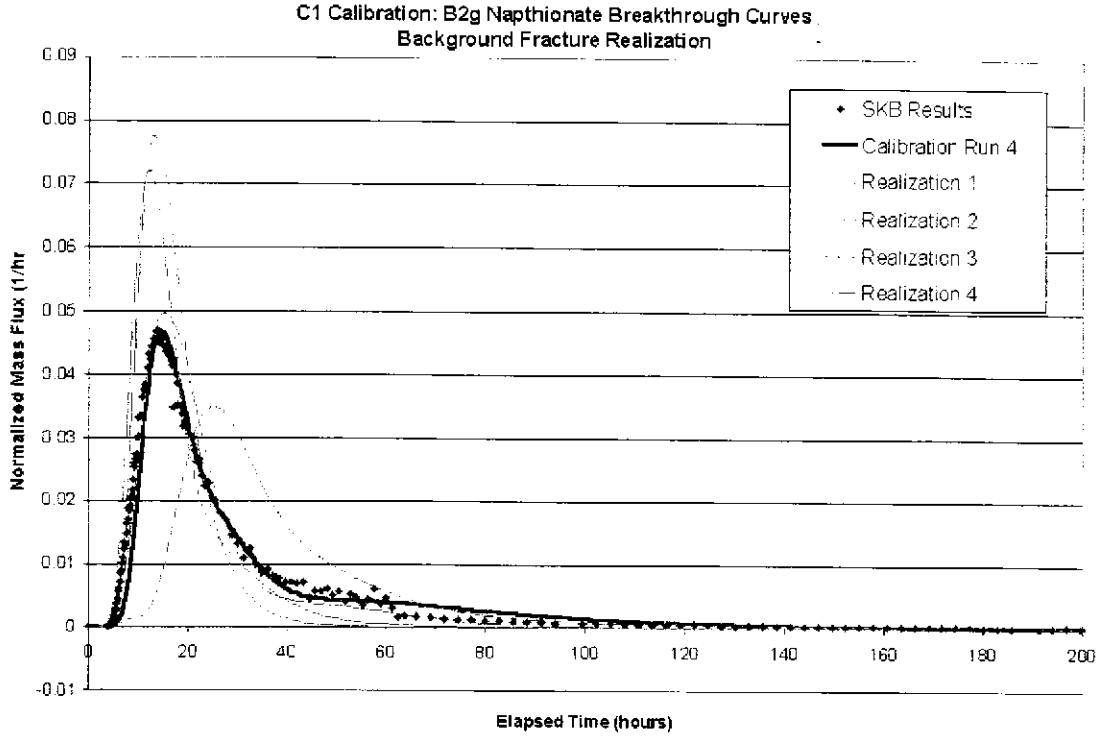

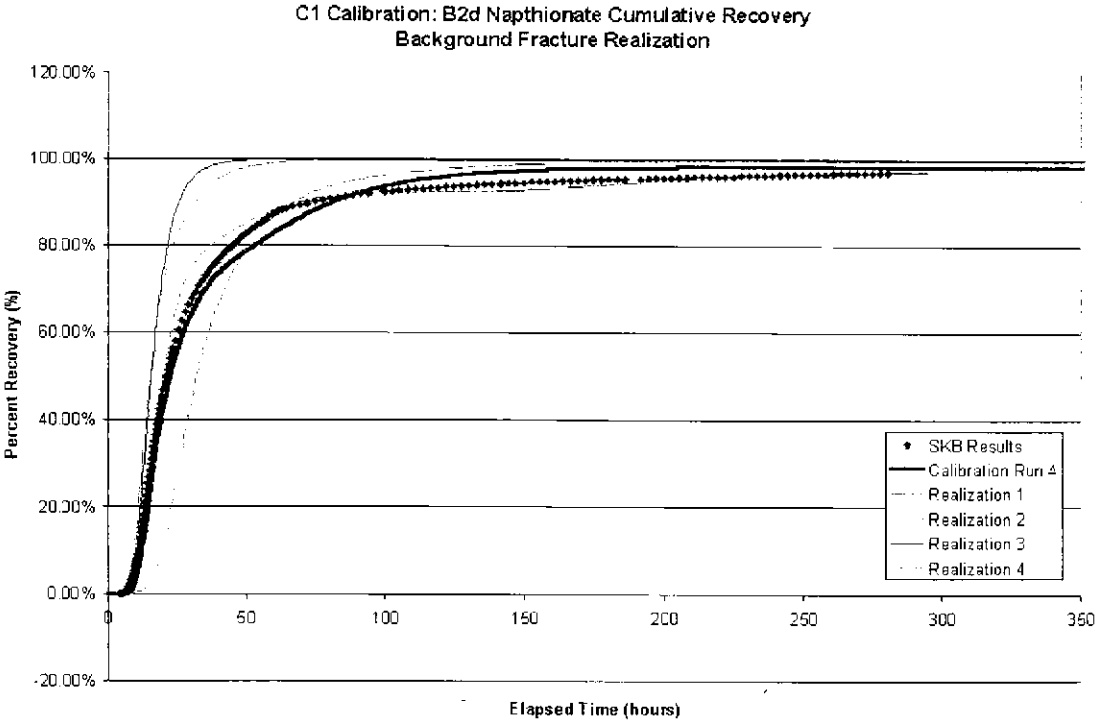

Figure 6-18 Multiple Realization Comparison of Test C-1

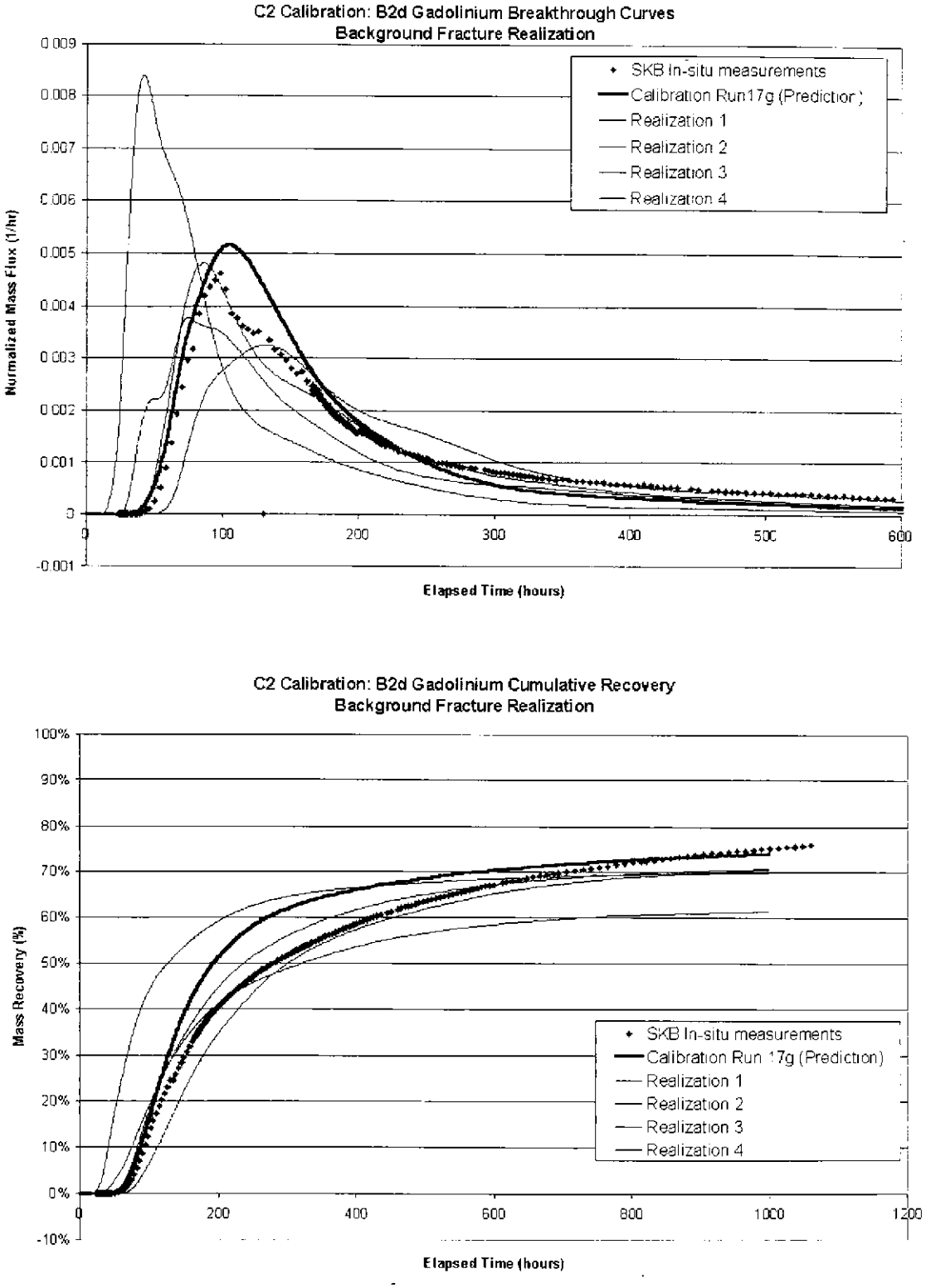

Figure 6-19 Multiple Realization Comparison of Test C-2

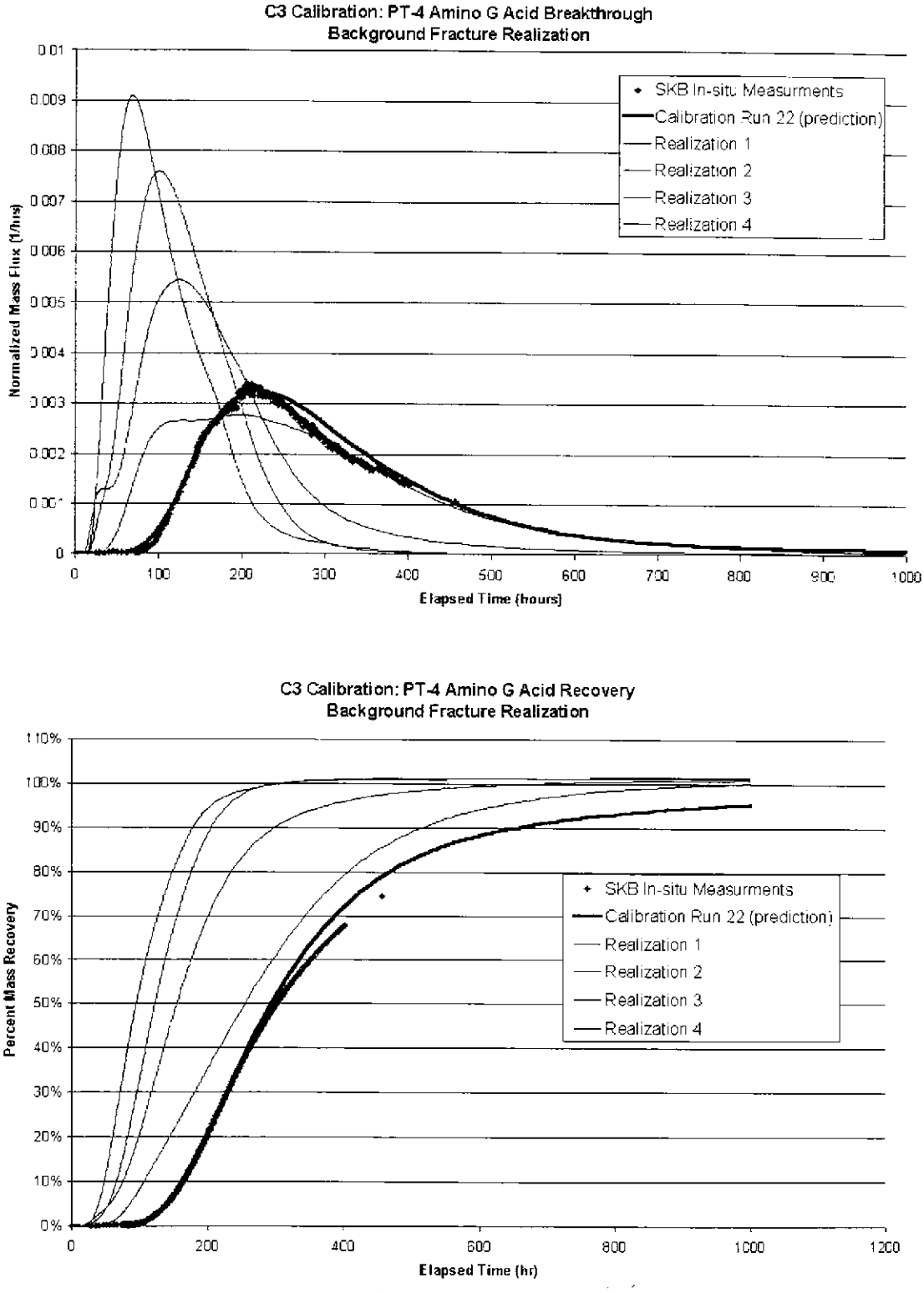

Figure 6-20 Multiple Realization Comparison of Test C-3

6.3 SORBING TRACER TESTS

Calibrated models of the Phase C conservative tracers were used to predict the transport of sorbing tracers. Six sorbing tracers were injected at the source location of test C-1: Br-82, Na-24, K-42, Ca-47, Rb-86, and Cs-134. Four sorbing tracers were injected at the source location of test C-2: Re-186,

Ca-47, Ba-131, and Ca-137. Sorbing tracers HTO, Na-22, Sr-85, Rb-83, and Ba-133 were injected into the source location of test C-3. Prediction injected activities were derived from integration to match the SKB activity. The injection flux rate was calculated by re-integrating injection mass so that the activity of the injected tracers matches that of the activity reported by SKB. The flow rate was calibrated to HTO. Injection profiles for the sorbing tracer are located in Figure 6-21 through Figure 6-23. Table 6-6 through Table 6-8 contains SKB injected activities and the injected activity used in the sorbing tracer simulations.

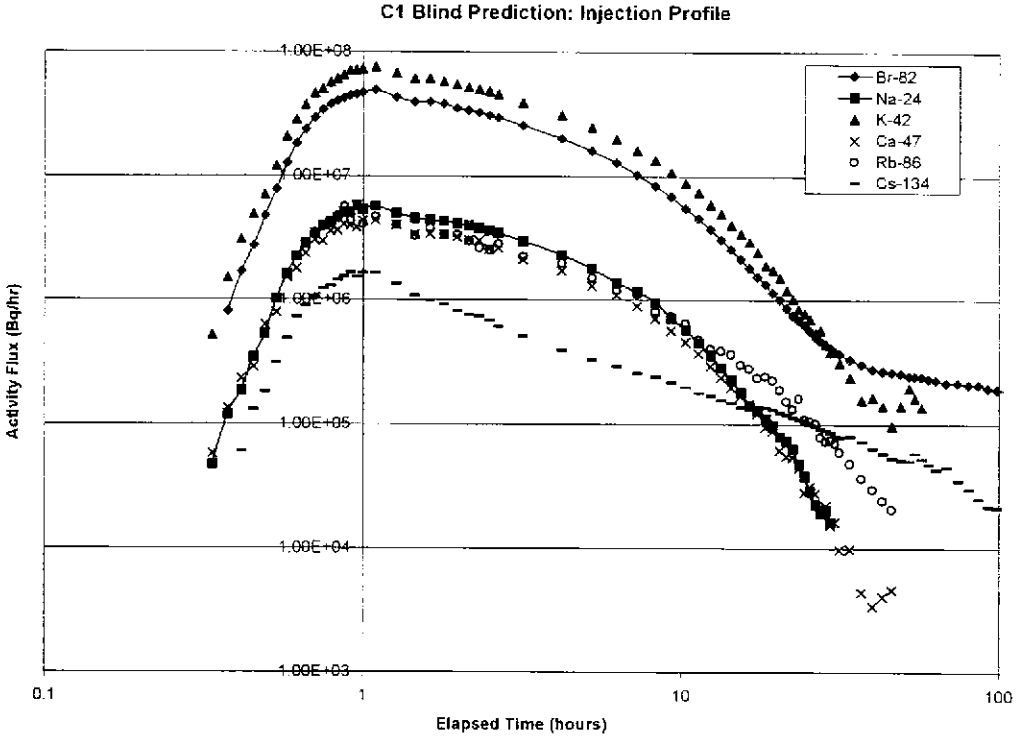

Figure 6-21 C-1 Injection Profile

Table 6-6 C-1 Injection Activity

Tracer	SKB Injection Activity (Bq)	Simulation Injected Activity (Bq)
Br-82	1.38E+08	2.5129E+08
Na-24	1.56E+07	2.5523E+07
K-42	2.29E+08	3.6097E+08
Ca-47	1.07E+07	1.9730E+07
Rb-86	1.33E+07	2.3783E+07
Cs-134	7.79E+06	1.4418E+07

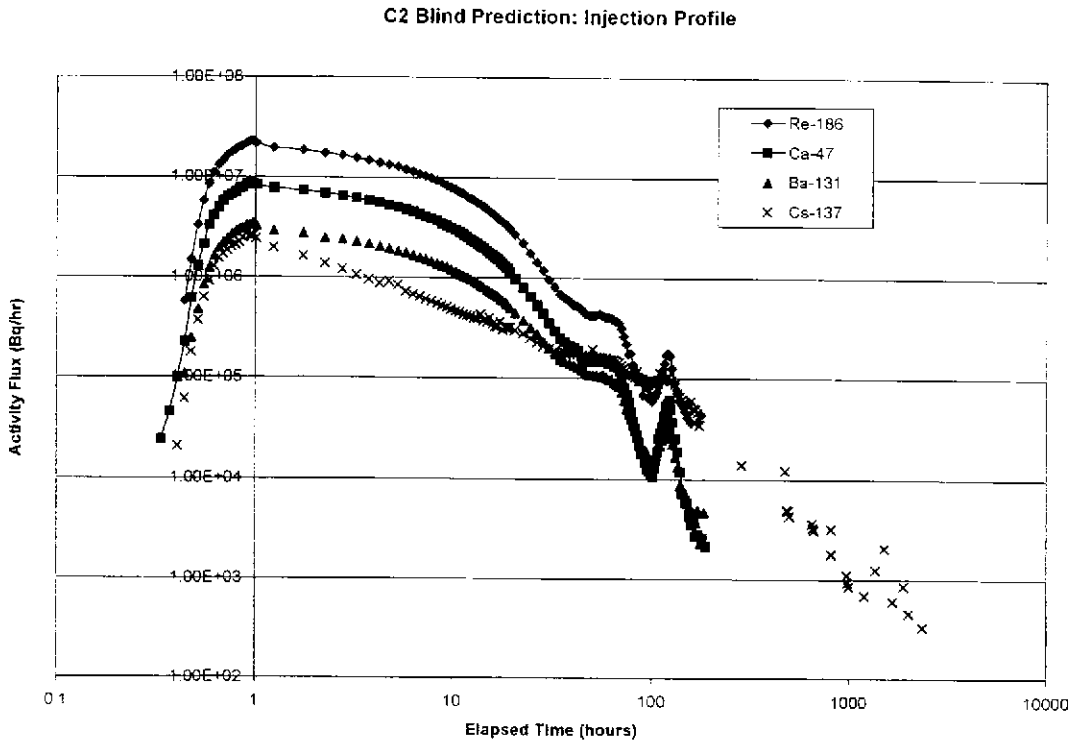

Figure 6-22 C-2 Injection Profile

Table 6-7 C-2 Injection Activity

Tracer	SKB Injection Activity (Bq)	Simulation Injected Activity (Bq)
Re-186	1.71E+08	*2.29E+08*
Ca-47	5.64E+07	*8.69E+07*
Ba-131	2.57E+07	*3.69E+07*
Cs-137	2.35E+07	*4.07E+07*

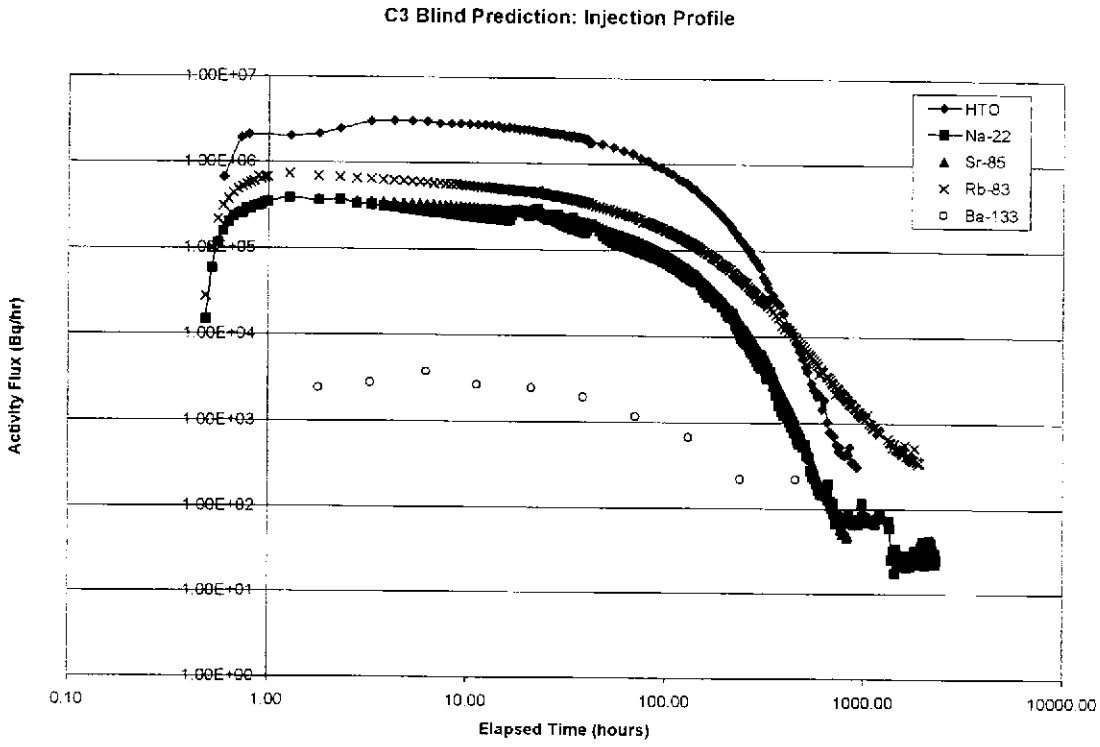

Figure 6-23 C-3 Injection Profile

Table 6-8 C-3 Injection Activity

Tracer	SKB Injection Activity (Bq)	Simulation Injected Activity (Bq)
HTO	2.4394E+08	2.5235E+08
Na-22	2.1606E+07	2.2610E+07
Sr-85	2.2105E+07	2.6398E+07
Rb-83	4.5895E+07	5.4249E+07
Ba-133	5.5446E+05	3.4989E+05

6.3.1 Phase C Blind Predictions

Flow aperture, diffusion distance, dispersion length, and matrix porosity resulting from the calibration of conservative tracers to in situ conservative measurements were used to predict the response of sorbing tracers to the Phase C tests. All prediction simulations were run without decay. Table 6-9 contains the sorbing parameters from TRUE 1 Task 4F. Figure 6-24 through Figure 6-29 contain the blind predictions.

Table 6-9: Blind Prediction Sorbing Parameters, Kd and Ka values from TRUE 1 Task 4F

Tracer	Kd (m^3/kg)	Surface Sorption Ka (m)	Free Water Diffusivity (m^2/yr)
Ba-131	$1.25*10^{-05}$	$6.08*10^{-04}$	0.026193
Ba-133	$1.25*10^{-05}$	$6.08*10^{-04}$	0.0262
Br-82	0	0	0.06564
Ca-47	$6.25*10^{-07}$	$3.04*10^{-05}$	0.024994
Cs-134	$8.30*10^{-05}$	$4.03*10^{-03}$	0.064882
Cs-137	$1.67*10^{-04}$	$8.12*10^{-03}$	0.064882
HTO	0	0	0.0757
K-42	$2.00*10^{-04}$	$9.72*10^{-03}$	0.063115
Na-22	$2.70*10^{-07}$	$1.31*10^{-05}$	0.0420
Na-24	$2.70*10^{-07}$	$1.31*10^{-05}$	0.041972
Rb-83	$2.08*10^{-05}$	$1.01*10^{-03}$	0.0641
Rb-86	$2.08*10^{-05}$	$1.01*10^{-03}$	0.064062
Re-186	0	0	0.0316
Sr-85	$1.04*10^{-06}$	$5.05*10^{-05}$	0.0249

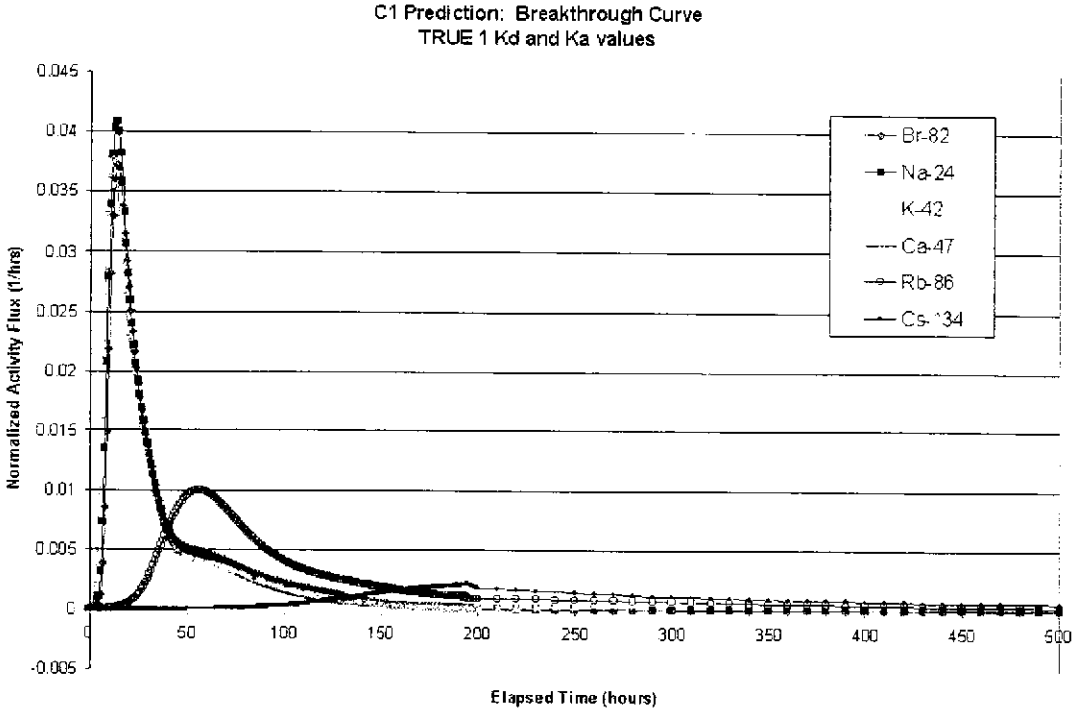

Figure 6-24 C-1 Blind Prediction Breakthrough

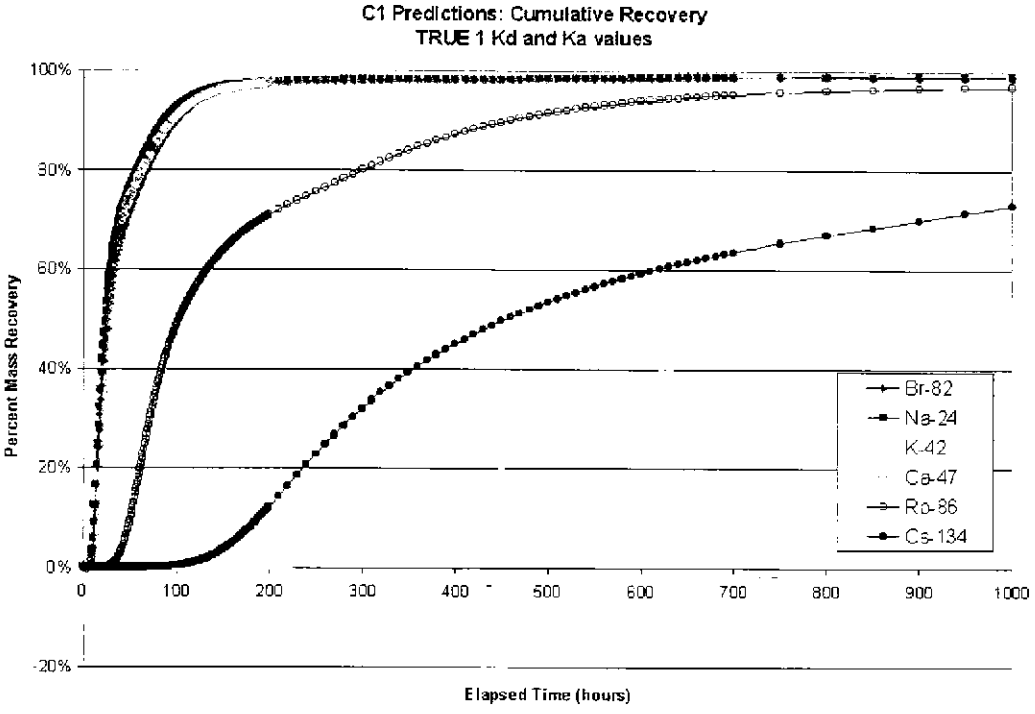

Figure 6-25 C-1 Blind Prediction Recovery

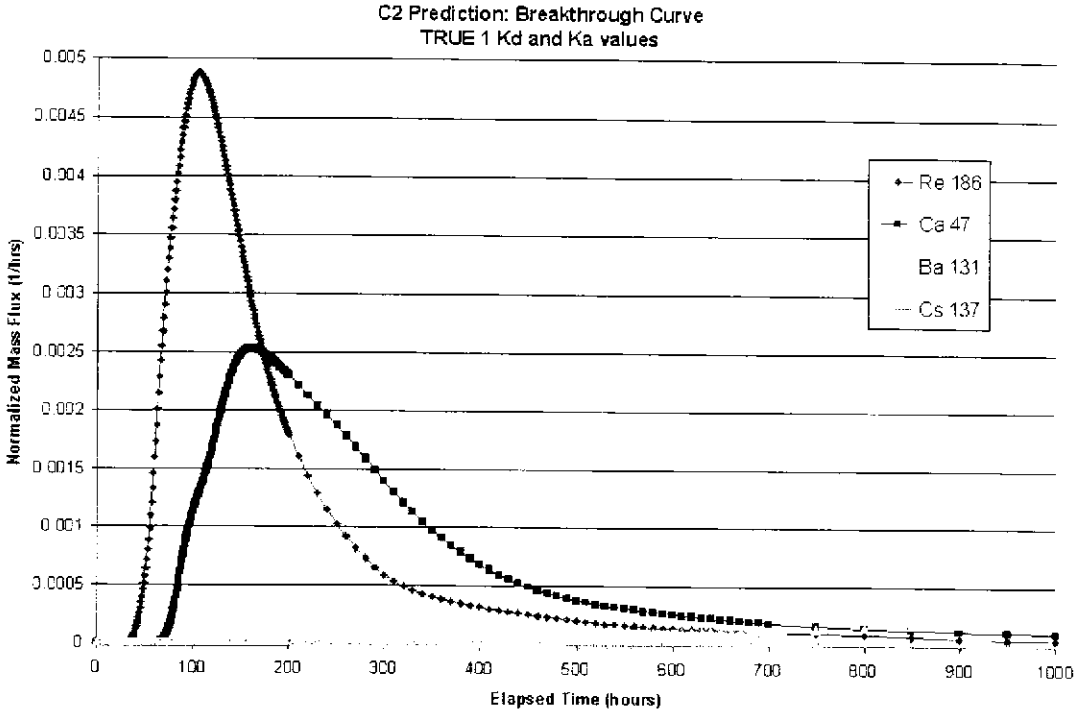

Figure 6-26 C-2 Blind Prediction Breakthrough

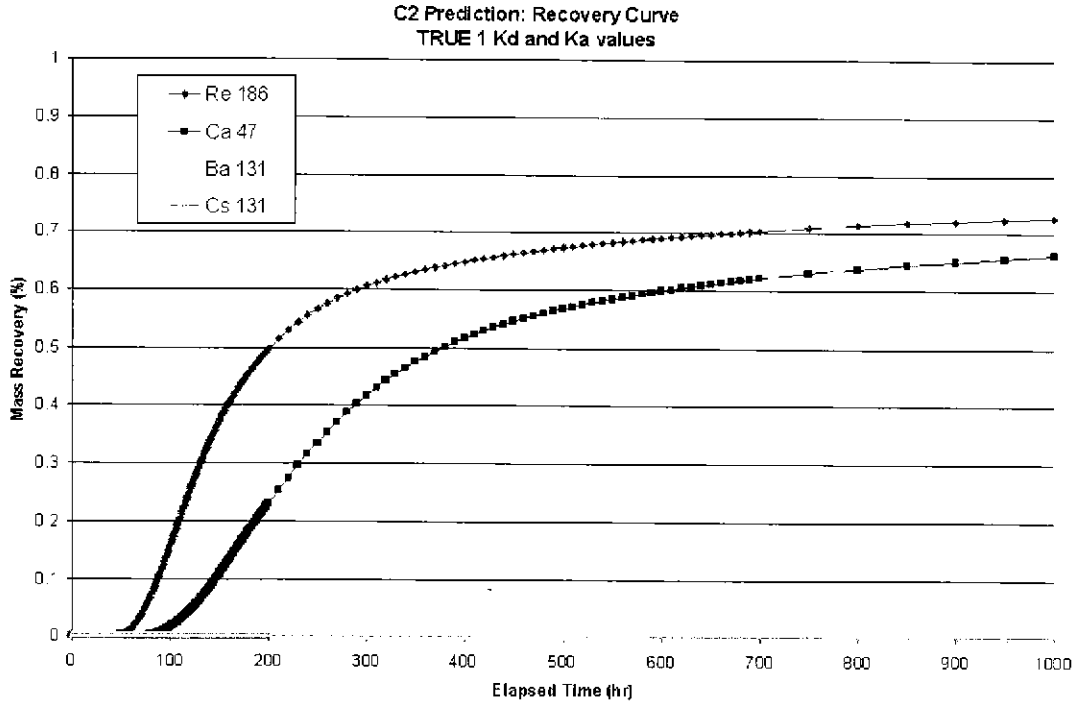

Figure 6-27 C-2 Blind Prediction Recovery

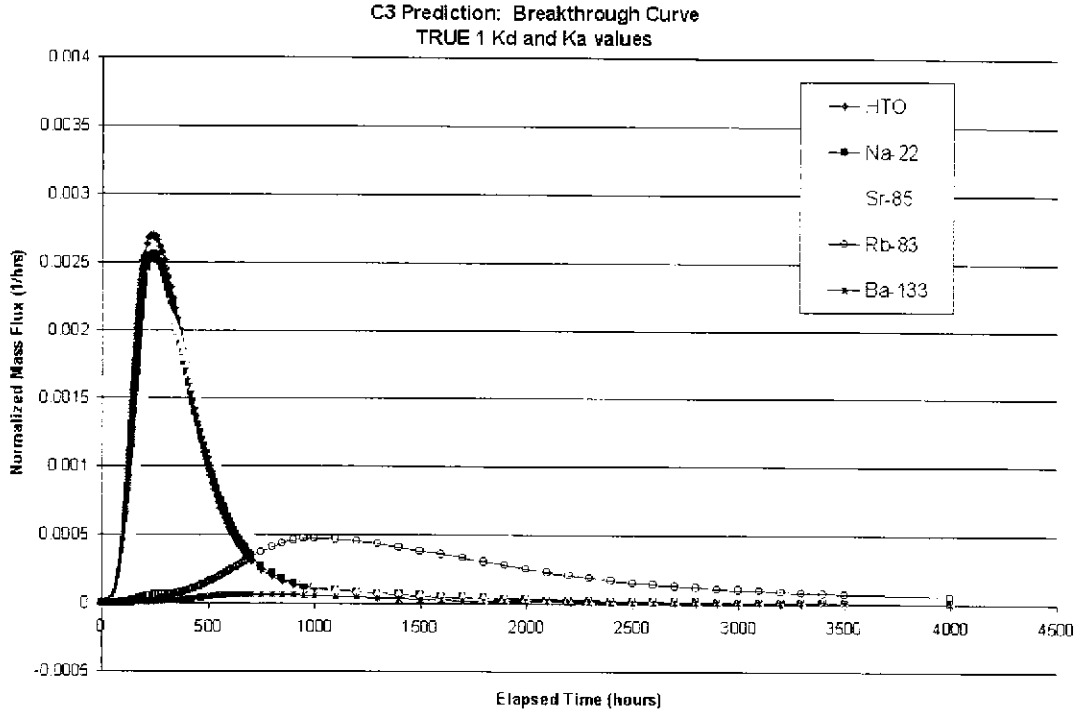

Figure 6-28 C-3 Blind Prediction Breakthrough

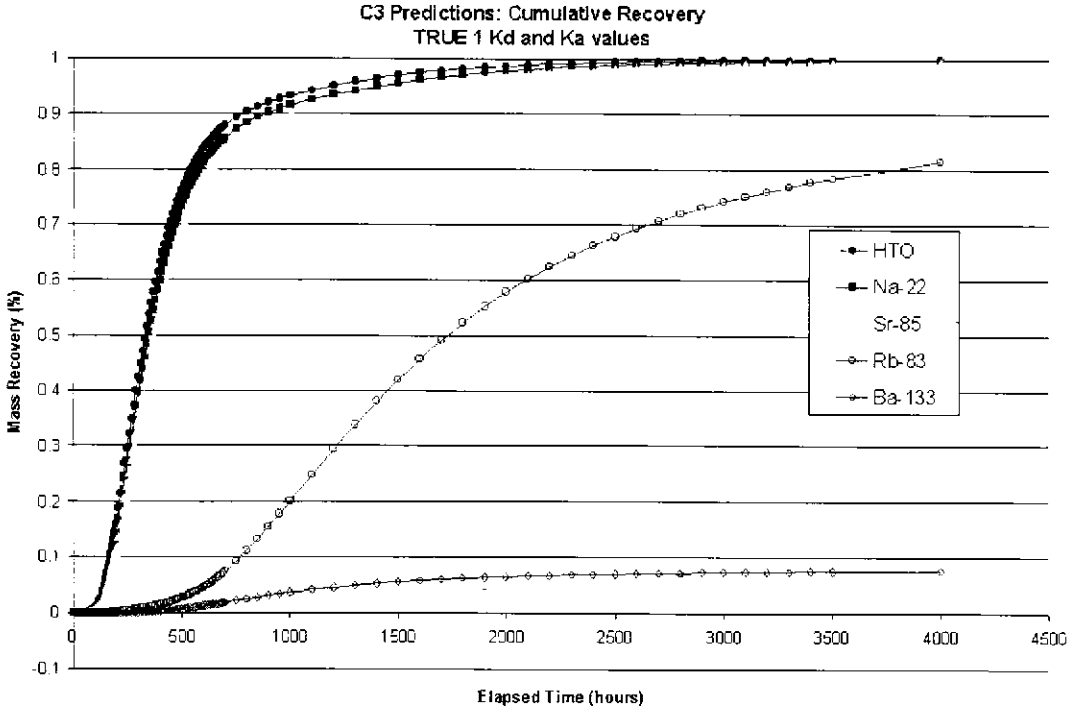

Figure 6-29 C-3 Blind Prediction Recovery

After the predictions were made, SKB in situ data for sorbing tracers was released. The T_5, T_{50}, T_{95} values from the measured data was compared to the blind prediction T_5, T_{50}, T_{95} values. Table 6-10 displays the results of the comparison of blind predictions to in situ measurements. Of the 15 tracers ran through the prediction simulations only 11 are compared to in situ data. The remaining 4 tracer recoveries were below background levels.

Table 6-10 Comparison of T5, T50, and T95 Values of Blind Predictions and In situ Measurements

TRACER		T5	T50	T95	% Recovery
Br-82	In situ	9.01	21.01	49.02	111%
	Blind Prediction	11	26	131	100%
Na-24	In situ	11.01	27.01	104.68	96%
	Blind Prediction	11	24	121	100%
K-42	In situ	21.01	104.68	Na	52%
	Blind Prediction	320	750	Na	92%
Ca-47	In situ	15.01	46.02	262.71	98%
	Blind Prediction	11	26	131	100%
Rb-86	In situ	67.54	403.42	Na	67%
	Blind Prediction	45	104	660	99%
Cs-134	In situ	526.42	Na	Na	39%
	Blind Prediction	160	450	2600	97%
Re-186	In situ	92.88	255.18	Na	80%
	Blind Prediction	74	200	Na	73%
Ca-47	In situ	377.013	721.32	Na	68%
	Blind Prediction	123	370	Na	66%
HTO	In situ	227.33	822.33	Na	73%
	Blind Prediction	148	330	1200	100%
Na-22	In situ	336.33	1481.33	Na	70%
	Blind Prediction	152	350	1400	100%
Sr-85	In situ	640.08	2967	Na	52%
	Blind Prediction	173	400	1900	99%

6.3.2 Sorbing Tracer Calibration

Sorbing tracer calibration consisted of modifying the sorbing tracer parameters to calibrate the predicted recovery and to the in situ data. To ensure that the conservative tracer calibrated model was not altered during sorbing tracer calibration, only tracer specific parameters were altered. Blind predictions, run with TRUE 1 Task 4F sorption parameters (as

shown in Table 6-9), were then rerun with the sorbing parameters of TRUE BS. TRUE BS sorption parameters are presented in Table 6-11.

Where neither the TRUE 1 nor the TRUE BS sorption parameters established a good fit to the in situ measured data, a Kd value was calibrated to the tracer directly. Table 6-12 details the change in Kd values where calibration was necessary to provide a good fit. No calibration was done on tracers Br-82 or Na-24, both predicted with Test C1, due to the good fit with the TRUE 1 sorbing parameters. All other simulated tracer breakthrough and recovery data improved, as compared with in situ data, with the modified Kd and Ka values. Generally, early recovery times are better fits than later recovery times. The percent change in Kd value is based of the TRUE 1 Task 4F Kd value. T5, T50, and T95 for all sorbing tracer simulations, predicted and calibrated, are compared to the in situ measurements in Table 6-13.

Table 6-11: Sorption Parameters from TRUE BS

Tracer	Kd (m^3/kg)	Surface Sorption Ka (m)	Free Water Diffusivity (m^2/yr)
Ba-131	$2.00*10^{-04}$	0	0.026193
Ba-133	$2.00*10^{-04}$	0	0.0262
Br-82	0	0	0.06564
Ca-47	$5.20*10^{-06}$	0	0.024994
Cs-134	$8.00*10^{-04}$	0	0.064882
Cs-137	$8.00*10^{-04}$	0	0.064882
HTO	0	0	0.0757
K-42	$2.00*10^{-04}$	0	0.063115
Na-22	$2.80*10^{-05}$	0	0.0420
Na-24	$2.80*10^{-05}$	0	0.041972
Rb-83	$1.40*10^{-03}$	0	0.0641
Rb-86	$1.40*10^{-03}$	0	0.064062
Re-186	0	0	0.0316
Sr-85	$4.70*10^{-06}$	0	0.0249

Table 6-12: Sorbing Tracer Calibration Parameters

Tracer	Kd (m^3/kg)	Surface Sorption Ka (m)	% Change from Blind Prediction Sorbing Parameters
Ba-131	No in situ data given		
Ba-133	No in situ data given		
Br-82	0	0	0%
Ca-47	$6.25*10^{-06}$	$1.13*10^{-07}$	+1000%
Cs-134	$4.57*10^{-04}$	$8.23*10^{-06}$	+550%
Cs-137	No in situ data given		
HTO	$5.00*10^{-06}$	$9.00*10^{-08}$	Na (prediction Kd = 0)
K-42	$1.00*10^{-05}$	$1.80*10^{-07}$	+5%
Na-22	$8.75*10^{-06}$	$1.58*10^{-07}$	+3241%
Na-24	$2.70*10^{-07}$	$1.31*10^{-05}$	0%
Rb-83	No in situ data given		
Rb-86	$1.03*10^{-04}$	$1.85*10^{-06}$	+495%
Re-186	$3.00*10^{-07}$	$5.40*10^{-09}$	Na (prediction Kd = 0)
Sr-85	$3.34*10^{-04}$	$6.01*10^{-06}$	+32115%

Table 6-13: Comparison of Predictions and Sorbing Tracer Calibrations (STC) with In situ Data

Test	Tracer		T5	T50	T95	% Recovery
C1	Br-82	In situ	9.01	21.01	49.02	111%
		Prediction TRUE 1	11	26	131	100%
		Prediction TRUE BS	10	26	131	100%
		SCT	no calibration			
	Na-24	In situ	11.01	27.01	104.68	96%
		Prediction TRUE 1	11	24	121	100%
		Prediction TRUE BS	10	25	200	100%
		SCT	no calibration			
	K-42	In situ	21.01	104.68	Na	53%
		Prediction TRUE 1	320	750	Na	92%
		Prediction TRUE BS	12	32	850	99%
		SCT	27	61	380	99%
	Ca-47	In situ	15.01	46.02	262.71	98%
		Prediction TRUE 1	11	26	131	100%
		Prediction TRUE BS	10	24	130	100%
		SCT	13	46	280	99%

Test	Tracer		T5	T50	T95	% Recovery
	Rb-86	In situ	67.54	403.42	Na	67%
		Prediction TRUE 1	45	104	660	99%
		Prediction TRUE BS	15	74	Na	94%
		SCT	171	410	2800	97%
	Cs-134	In situ	526.42	Na	Na	39%
		Prediction TRUE 1	160	450	2600	97%
		Prediction TRUE BS	18	123	3400	96%
		SCT	1300	3300	Na	57%
C2	Re-186	In situ	92.88	255.18	Na	80%
		Prediction TRUE 1	74	200	Na	73%
		Prediction TRUE BS	74	200	Na	73%
		SCT	100	280	Na	69%
	Ca-47	In situ	377.01	721.32	Na	68%
		Prediction TRUE 1	123	370	Na	66%
		Prediction TRUE BS	102	400	Na	67%
		SCT	310	Na	Na	44%
C3	HTO	In situ	227.33	822.33	Na	73%
		Prediction TRUE 1	148	330	1200	100%
		Prediction TRUE BS	148	330	1200	100%
		SCT	260	660	Na	94%
	Na-22	In situ	336.33	1481.3	Na	70%
		Prediction TRUE 1	152	350	1400	100%
		Prediction TRUE BS	183	430	2200	99%
		SCT	340	900	Na	91%
	Sr-85	In situ	640.08	2967	Na	52%
		Prediction TRUE 1	173	400	1900	99%
		Prediction TRUE BS	153	350	1400	100%
		SCT	850	2500	Na	71%

7. CONCLUSIONS

The JNC/Golder team successfully implemented a discrete fracture network/channel network model for the Revised March 2000 (Doe, 2000) structural model for the TRUE-Block Scale rock volume. The model has been calibrated against hydraulic interference, and against conservative tracer transport, and then used for prediction of sorbing tracer transport. Although the selected effective sorption parameters did not always produce good predictions, the model was able to match the general pattern of tracer retention. Mass loss from the experimental volume is modeled through the use of fracture intersection zone (FIZ) features.

8. REFERENCES

Andersson, P. Personal communication, 2000.

Dershowitz, W. Conductive background fractures in the area investigated in the Tracer Test Stage (TTS). Äspö Hard Rock Laboratory, International Technical Document ITD-00-03., January 2000.

Dershowitz, W., T. Foxford, E. Sudicky, D.A. Shuttle, and Th. Eiben. PAWorks: Pathways analysis for discrete fracture networks with LTG solute transport. User Documentation, Version 1.5. Golder Associates, 1998.

Dershowitz, W., G. Lee, J. Geier, T. Foxford, and Eric Ahlstrom. FracMan Interactive Discrete Feature Data Analysis, Geometric Modeling, and Exploration Simulation. User Documentation, Version 2.6. Golder Associates Inc., 1999.

Doe, T. (2000). Updated March 1999 Hydrostructural Model. TRUE Block Scale Project Correspondence. SKB, Stockholm.

Hermanson, J; Follin, S.; and Wei, L., 1997. Structural analysis of fracture traces in boreholes KA2563A and KA3510 and in the TBM tunnel. Swedish Nuclear Fuel and Waste Management Company, Aspo Hard Rock Laboratory, Technical Note TN-97-31b. SKB, Stockholm.

Holton, D. Boundary conditions for sub-models at the Äspö TRUE Block site. Äspö Hard Rock Laboratory International Technical Document ITD-99-XX. March 1999

Miller, I., G. Lee, and W. Dershowitz. MAFIC: Matrix/Fracture Interaction Code with heat and solute transport. User Documentation Version 1.6, Golder Associates Inc. 1999.

Winberg, A., ed (2000). TRUE Block Scale Project, Final Report of the Detailed Characterization Stage. SKB International Cooperation Reporet ICR-00-02. SKB, Stockholm

Winberg, A., Andersson, P., Hermanson, J., Byegård, J., Cvetkovic, V. and L. Birgersson. 2000. "Final report of the first stage of the tracer retention understanding experiments. "Swedish Nuclear Fuel and Waste Management Company (SKB), Technical Report TR-00-07. ISSN 1404-0344.

Winberg, A., (ed), 2001. "Final Report, TRUE Block Scale Project, Hydrostructual Model Development", Appendix B (in preparation).

APPENDIX B

ÄSPÖ TRUE BLOCK SCALE PROJECT, MARCH ´00 STRUCTURAL AND HYDRAULIC MODEL BASED ON BOREHOLE DATA FROM KI0025F03

TRUE BLOCK SCALE PROJECT

March ´00 Structural and Hydraulic Model Based on Borehole Data from KI0025F03

DRAFT

Jan Hermanson

Thomas Doe

Golder Associates Inc

March 2000

Keywords:

Table of contents

List of Figures

List of Tables

1 Introduction

This report presents an update of the structural model of the TRUE Block Scale experimental volume based on the drillings of borehole KI0025F03 through the centre of the block.

The iterative process of updating the structural geological model of the block is an ongoing process, which has previously been presented in three technical notes. The first model was based on the drillings of KA2563A and KA3510A and was reported by Hermanson and Follin (1997). Subsequent updates have been presented in the October 1997 model by Hermanson (1997) and in the September 1998 model by Hermanson (1998). The last structural model update was presented in Hermanson (2000) with a hydraulic reconciliation of the conductive structures by Doe (2000).

This report concentrates on borehole KI0025F03 and will only refer to investigations done previously in the block. All defined deterministic structures in the model are presented in this report for completeness and easy accessibility although only a few have changed and two additional structures has been added. The methodology for updating the structural model is presented in **Figure 1-1**.

The following data have been utilised for the KI0025F03 structural model update;

- BIPS/Boremap data of KI0025F03 (CD-ROM 981009)
- POSIVA flowlog of boreholes KI0025F03 delivered through GEOSIGMA (990215)

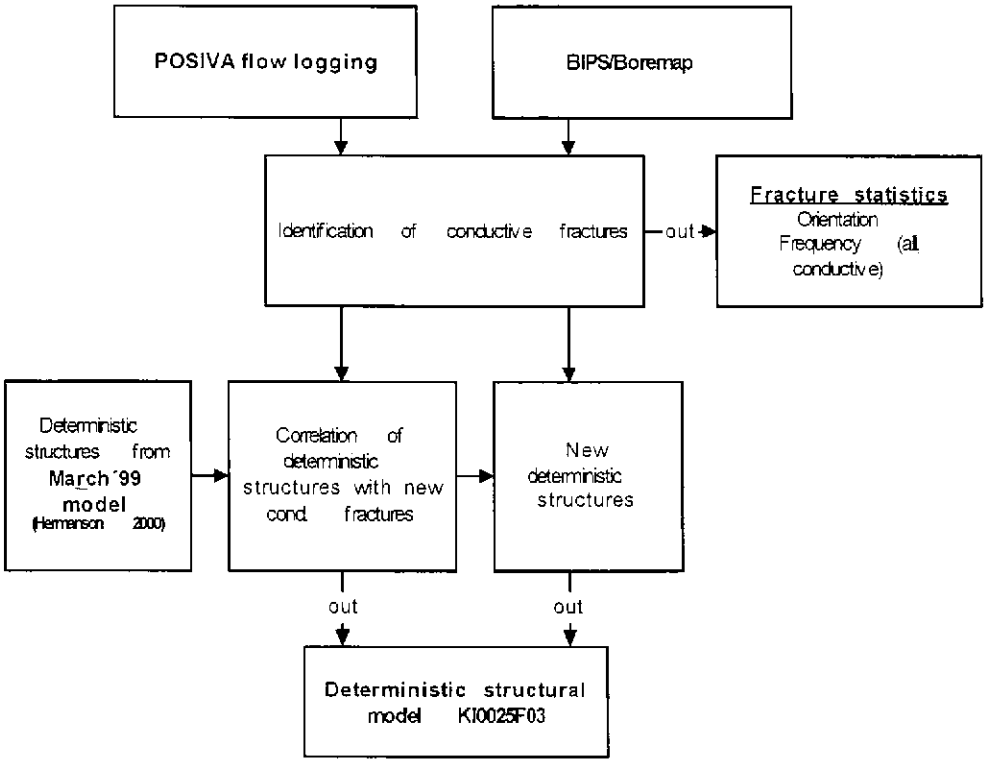

Figure 1-1. *Methodology for updating the structural model*

2 Data sources

2.1 BIPS/Boremap data in KI0025F02

The characterisation of KI0025F02 has been performed using the Boremap system which includes data for rocktypes and discontinuities. The location, orientation and length of the borehole is given in Table 2-1. The borehole is more or less parallel and drilled in-between boreholes KI0025F and KI0023B. The maximum distances between these two boreholes varies between less than 2 m at the collar to 47 m (KI0025F) and 96 m (KI0023B) at the end of the borehole.

Table 2-1. Borehole data for KI0025F02

KI0025F02	
Collar coordinates	
Easting (m)	1952.753
Northing (m)	7238.494
Elevation (m)	-448.534
Direction	
Bearing (deg)	199.9692
Inclination (deg)	-25.4835
Drilling	
Start date/time	980810 09:14
Stop date/time	980825 10:20

The lithology of the rock block is given in **Figure 2-1** and is dominated by diorite intermingled by small sections of fine-grained granite. Greenstone exists in minor fragments in the diorite. The rock types in the investigated boreholes do not differ from what is generally observed in the other boreholes.

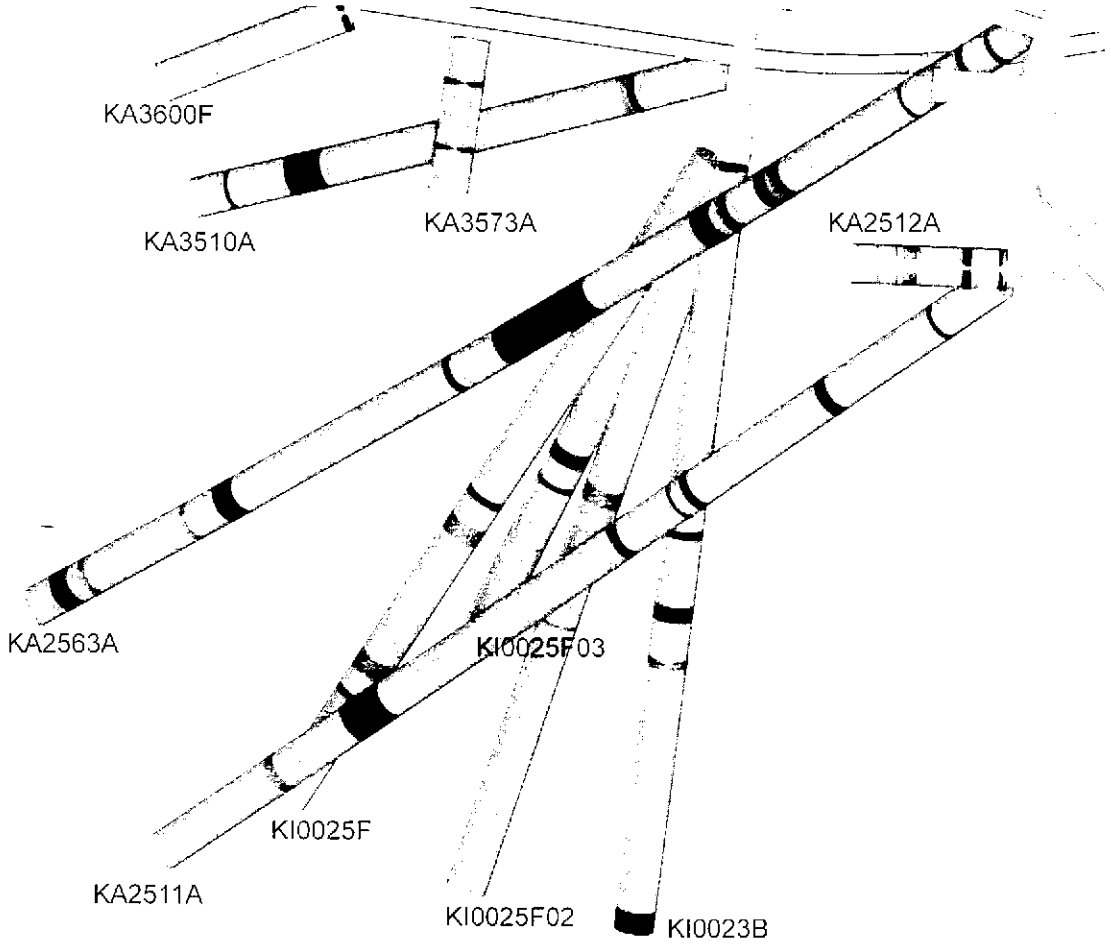

Figure 2-1. *Lithology of the TRUE block scale boreholes.*

KI0025F03 exhibits complex fracturing in the sections between 50 to 60 m and 84 to 100 m. These sections do not necessarily correspond to high inflow as will be discussed below. The fracturing in KI0025F03 is very similar to that observed in KI0025F02. However, it deviates from what is found in KI0025F, just to the east of KI0025F02 which has large sections with lower fracture frequencies. As the distance between the two boreholes KI0025F03 and KI0025F is maximum 51 m the difference in brittle behaviour implies that there exist something that divides the fracturing into different domains, one which is more fractured than the other. This difference must lie east of KI0025F02 as fracturing is similar in KI0025F02 and F03. The maximum distance to KI0025F02 is approximately23 m. The average fracture frequency is around 2 fractures per meter which is equivalent with KI0025F02.

Fracture orientations along KI0025F03 reveal two dominant fracture sets, steep northwesterly trending fractures and subhorizontal fractures. There exists a weak northeasterly fracture set which is equivalent with the fracturing in KI0025F, KI0025F02 and KI0023B. This pattern is common throughout the HRL (Munier 1997, Hermansson 1998, Rhén et al (1997). Fractures mapped as open consists of approximately 40% of the total amount and show a pattern which is similar to **Figure 2-2** but more pronounced in the northwesterly direction..

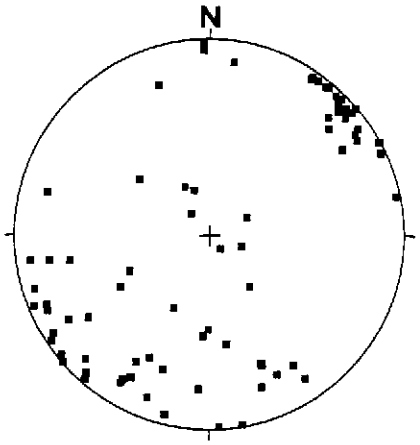

Figure 2-2. *Fracture orientations of all fractures in KI0025F03 plotted as poles to fracture planes on a lower hemisphere equal area projection.*

2.2 The POSIVA flow log and its correlation to conductive fractures in KI0025F03.

POSIVA flow logging has previously been performed in boreholes KI0025F02, KA2563A, KA3510A and KA2511A. Borehole KI0025F03 has also been completely covered by this logging method. The complete logs of all boreholes are published by Rouhianen et al. (1999) and will not be presented here. However, parts of the flow log of KI0025F03 is recreated in **Figure 2-3** to illustrate how highly conductive fractures have been recorded.

A certain amount of water seeps through as the packers are moved along the borehole and results in a background flow noise in the log. Only peaks do correspond to discrete inflow points. To extract the conductive fracture frequency along the borehole inflow points with a sufficiently large inflow was coupled to fractures along the borehole. Conductive fractures were identified in sections with substantial inflow above the background noise. Eighty-three inflow points were coupled to fractures by correlating the bore-map database of natural fractures with the significant inflow points. The threshold value for identifying conductive fractures varies in inflow between 100 to 650000 ml/hr depending on how well a single inflow point stands out from the background noise . If a lower threshold value for inflow was to be chosen, more inflow points and consequently more conductive fractures would be identified. Whatever threshold value to use must be argued for when designing a particular numerical model. From a structural-hydraulic conceptual model point of view it is considered well enough to locate the largest conductive structures of the block.

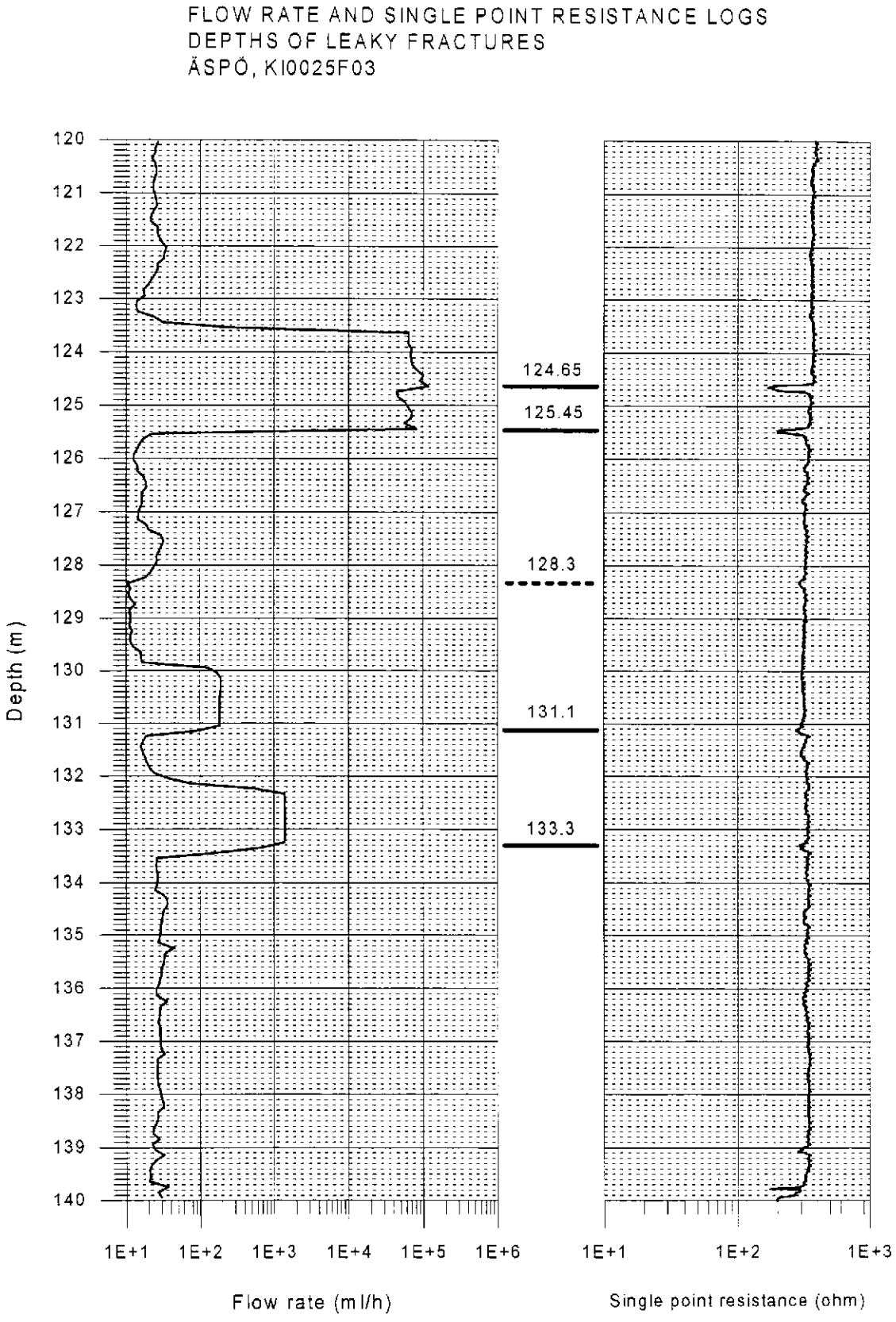

Figure 2-3 *Example of the POSIVA flow log of KI0025F03, section 120 to 140 m from Rouhianen et al. (1999).*

Figure 2-4 shows the conductive fracture frequency of borehole KI0025F03 based on the BIPS/POSIVA flow log correlation. The average frequency of conductive fractures is similar between the boreholes KA2563A, KA2511A, KI0025F and KA3510A and suggests that the major flow paths in the network occur in a distinct proportion of the fractures with little variations throughout the block. The identified conductive fractures based on the POSIVA flow log is given in Appendix B. The average conductive fracture frequency is 0.62 fractures per meter.

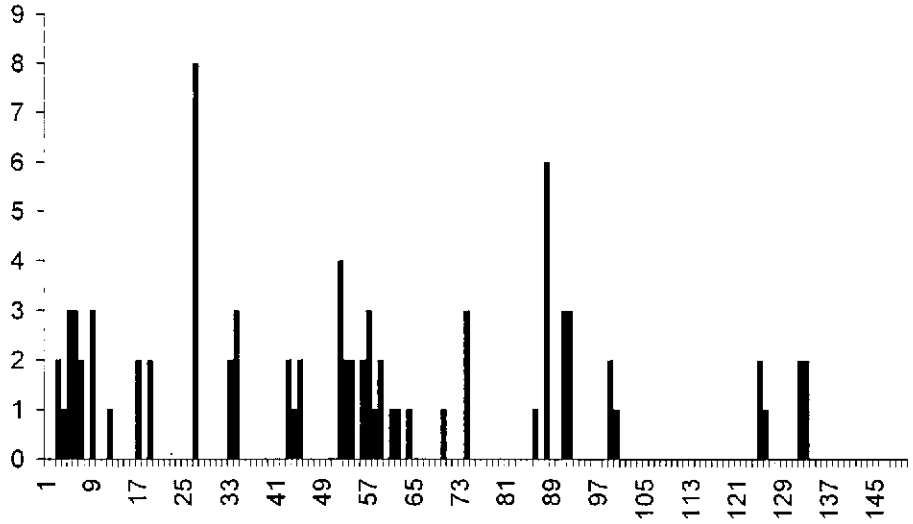

Figure 2-4 *Conductive fracture frequency of borehole KI0025F03 based on the inflow points from the POSIVA flow log and corresponding fractures in these sections.*

The simplified fracture classification presented by Hermansson (1998) has not been extensively performed when doing the identification of possible conductive fractures. The classification had its origin at the time when only 5 m packer tests existed in the boreholes, forcing the geologist to make a qualified guess which fracture within one 5 m section that was conductive. The classification has now become somewhat obsolete with the extensive usage of the POSIVA flow log equipment. It is now in most cases possible to identify exactly the fracture or the fractures that conducts water within a 10 cm section. Hermansson (2000) showed that less than 40% of all the inflow points > 1000 ml/hr could be explained by the geologically most probable conductors. The initial interpretation is that this is not a successful system for finding conductive fractures. However, it is recognised that fractures that are conductive may be connected to a geological structure of significance, not necessarily being the major structure. This interpretation assumes that the geological structures work as the major conductors even if the actual conductive fractures may be splays or other fractures related to the geological structures, c.f. **Figure 2-5**. It also requires that the geological structures have been reactivated and show brittle behaviour in or around the core of the structure. However, mapping only the conductive fracture geometry will not reveal the system of conductors that governs transport over larger distances. Hermansson and Tullborg (in prep) use the geology in the True Block Scale volume to explain the larger pattern that governs flow in this part of the laboratory.

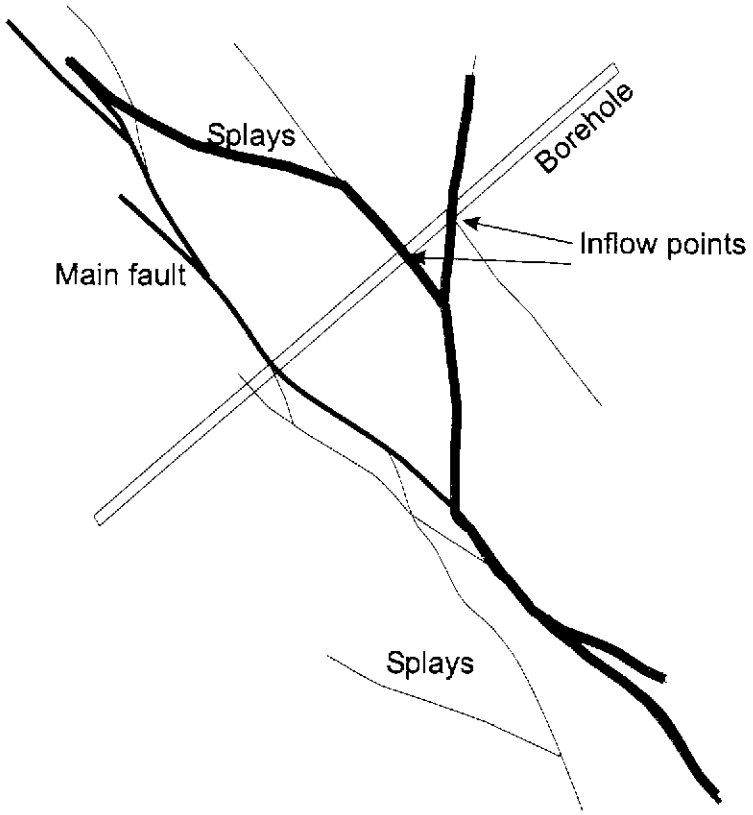

Figure 2-5 *Illustration of geological structures such as faults (thick black line) and splay fractures (thin black lines) and how the water (blue line) follows the main structure but not necessarily along the main fault plane. This effect implies that single inflow points along a borehole may give a skewed picture of what structure governs flow in the volume.*

3 March 1999 Structural model

The conceptualisation of the structural model is constrained by what is considered to be flowing or conductive structures. There are a wide choice of possible geological features in each borehole that has to be delimited by either detailed hydraulic logs coupled to fractures or by geological indications if no other information is available. The tracer tests in TRUE Block Scale are to be performed in conductive pathways which may or may not follow the major geological features in the model. The structural model aims at reflecting the conductive pathways, although this may complicate the impression of the different geology along the pathway. However, the hypothesis illustrated in **Figure 2-5** emphasises the fact that water flows through portions of large faults but also along splay fractures connected to other splays or faults. The structural model focus on interpreting the locations of the major inflow points as well as making an attempt to couple the larger geological features to this system.

The structural model presents a selection of possible conductive features intersecting the studied rock volume outside of larger zones. Even though the POSIVA flow log has an incredible solution it still measures inflow at discrete points in the rockmass. A structural model attempts to connect these points of hydraulic inflow to features extending between boreholes. The aid for doing this extension is

- orientation of single intersections
- radar or seismic reflectors
- geological signature

With the knowledge that by geophysics and geology alone we can determine no more than 2/5 of the most conductive structures we need to make use of focussed hydraulic tests to study the connectivity of the block. An hydraulic approach will be presented under chapter 4.

This chapter describes the structural geological character of each structure and presents this in a conceptual model of the largest conductors in the block.

Figure 3-1 shows all fractures mapped as open based on the BIPS and core analysis made in the Boremap system before drilling borehole KI0025F03. This figure can serve as an good example of illustrating the potential complexity of the fracture network that could be involved in flow and transport.

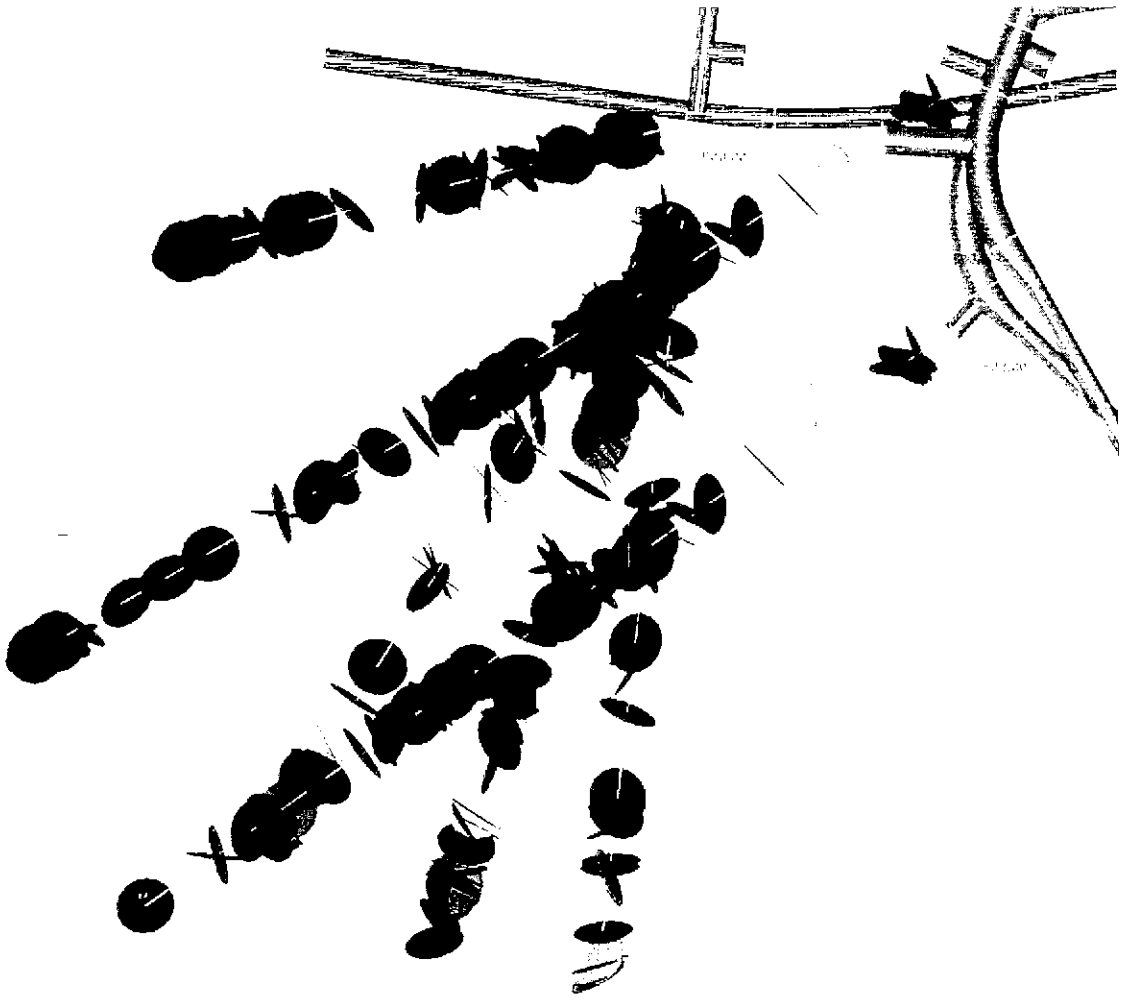

Figure 3-1. *All fractures mapped as open (from BIPS) in all TRUE Block Scale boreholes except KI0025F03.*

3.1 Differences from the March ´99 structural model

Based on the previously presented background data from the POSIVA flow log and the BIPS system, correlation of this material is done with information in the March ´99 structural model. New information has had the following impact of the previous model;

- the new borehole KI0025F03 has invoked detailed information primarily in the centre of the block.
- the POSIVA flow log has with its detailed resolution slightly changed the exact location of features #6, #7, #13, #19 and #20, #21, #22 and added another structure called #23.

The following features are not updated from the March ´99 structural model but details are again given here for completeness;**Feature number, Type** according to Hermansson (1998).

1. Fracture
This structure appears as an open fracture at L=12.5 m in KA2563A. A magnitude 1U radar reflector is interpreted to intersect KA2563A at L=11.9 m. Large steep water-bearing fractures in the TBM tunnel sections around 2600 m, and in the F-tunnel coincide with a planar interpolation of this feature trending 335/82. The average width is estimated to 1 cm on the single intercept in KA2563A.

2. Fracture-Zone
A fairly steep structure (109/89) associated with fractured and oxidised core at L=11.1 m, and at L=12.3 m in KA3510A (large open fracture with cavities). Similar geology is found also in KA2563A at L=68.5 m. A water-bearing fault at tunnel section L=2511 m is sub-parallel to this structure. The fracturing in the core section of Ka2563A is characterised by a network of fractures with cavities and epidotized fillings. The average width of the structure is estimated to 82 cm.

3. Zone
A steep sub-parallel structure to no. 2 (110/81) intersecting KA3510A at L=37.5 m and KA2563A at L= 68.5 m. Both intercepts are characterised by severe fracturing and faulting, brecciation and core crush (zone). There are radar indications in both cores. The width varies between 220 - 40 cm in KA2563A and KA3510A, respectively.

4. Fracture-Fault
This feature, trending 302/82, intersects KA2563A at L= ca 94 m and is associated with an inflow of around 40 l/min. A possible intercept of this structure is located at L=12.9 m in KA3510A. The intercept in KA2563A is characterised by oxidised and altered host rock with calcite filled fractures with cavities. A planar interpolation of structure 4 to KA2511A returns an intercept at L= ca 23 m where the rock show similar geological characteristics as in KA2563A. The section 23.08-26.6 has a recorded inflow of 30 l/min. If structure 4 is extended to intersect KA2511A, it is interpreted to intersect Structure 5 somewhere between KA2563A and KA2511A. Hydraulic responses from both drilling records and from the recently performed interference tests support that structures 4 and 5 are hydraulically coupled. The structure seem to be fairly consistent in width in all intercepts and has an average width of ca 10 cm.

5. Fracture-Fault
A structure associated with large inflows in both KA3510A, KA2563A, KI0025F and KI0023B. Interpreted to intersect at L=47.7 m in KA3510A, at L=102-103 m in KA2563A, at L = 4.9 m in KI0025F and at L=7.2 m in KI0023B. The extreme inflow in KA2563A at L = 103 m (700 l/min) occur through a fault with 0.5-1 cm calcite and possible lithified gouge filling which is partly eroded. The fault has no clearly visible ductile precursor and occurs in diorite with no signs (such as decrease in grain size or chemical dissolution of minerals) of previous tectonic events. The feature consists of a smaller fracture ending at an almost orthogonal angle to the fault and could be interpreted as a splay fracture. A fair bit of displacement has occurred along the fault plane as opposite sides match badly.

This structure seem to consist of one or a few major inter-linked fracture planes with rather thick (mm to cm) calcite filling, at times with idiomorphic crystals giving the structure a high porosity. The planar extent (113/90) is striking as the structure is

identified over a distance of at least 50 m and show more or less the same orientation. The connection to KA2511A is interpreted to occur through structure 4. Hydraulic responses is observed in the innermost section of KA2512A. Geologically this section contains subparallel fracturing to both structures 5 and 4.

8. Fault-Zone
This steeply dipping structure is interpreted to intersect the TBM tunnel, the F-tunnel, KA3510A and KA2563A. However, its angle in relation to KA2563A makes it difficult to determine the exact intersection point. Steep faults in the F- tunnel and in the TBM tunnel are well traced to KA3510A from 15.5 m up to 17.4 m in highly foliated, oxidised and altered diorite. The structure is interpreted to intersect KA2563A at around L=220-250 m. The specific intercept seems to be distributed over a larger distance consisting of foliated and altered diorite with a group of faults filled with epidote and calcite. Radar reflectors are interpreted in both KA3510A and KA2563A. As the intercept is more intense in KA3510A, the structure is either diverting into several smaller fault structures or diminishing beyond KA2563A. The average width is 50 cm although its total width in KA2563A may be in the order of several metres if it diverts into smaller branches.

10. Fracture-Fault-Zone
Both radar and seismics in boreholes KA2563A, KA2511A and in KI0023B support the current interpretation of structure 10. This is a variable structure appearing as a zone in one intercept in KI0023B, single faults and fractures in KA2563A and KA2511A, respectively. The orientation of the radar reflector in KA2511A (111/85) is consistent in orientation with the crosshole seismic reflector in KA2563A (115/79). Fractured fine-grained granite dominate in KA2511A whereas greenstone is also present in the other intercepts. Fracturing is more intense in the contact between the fine-grained granite and the greenstone. The intercept in KI0023B exhibits a zone-like characteristic and dominates the width of the structure which varies between less than a cm in KA2511A to 30 cm in KI0023B.

11. Fault
This structure is indicated by crosshole seismic and radar in KA2511A at L=259 m. Indications in KA2563A consist of a steep and a sub-horizontal open fault in diorite. Current interpretation of orientation is 288/88. The width is approximately 15 cm, but may vary as it is picked up by crosshole seismics. It has not been tested in any hydraulic test program and little is known of its connectivity.

12. Unknown type
A seismic reflector beyond the limit of all boreholes is interpreted as being a possible boundary zone as proposed by the previous block scale siting investigation. Orientation is 355/90.

15. Fault
A radar reflector and a number of faults in KA3510A describe this structure. At 117.90-120.89 m, 15 faults intersect KA3510A in fine-grained granite. There is a cm wide sub-parallel calcite filled fracture in the middle of this group, although it is sealed in the drill core, it may well be conductive in more porous sections outside the borehole. It seem possible that these fractures take part in the measured slow increase in inflow as registered during drilling of this borehole. Structure 15 is indicated by hydraulic

responses in the innermost sections of KA3573A and is also supported by radar reflectors in the same section. Preliminary results from interference tests indicate that structure 15 may be in contact with several other structures, in particular structure 7 and possibly also structure 6. Orientation is interpreted to 268/88.

16. Zone

Evidence for a gently dipping fine-grained granite body intersecting KA2563A at L= ca 56 m and associated with a greenstone and massive faulting and core crush in KA2511A at L = 104-105 m. This structure is also supported by a seismic crosshole reflector and the orientation of the sub-horizontal rock contacts in both KA2563A and in KA2511A. The structure can be described as a fractured lithological body with variable thickness, extent and degree of fracturing rather than a traditional zone. However Structure 16 may be an important hydraulic connector between steep NW trending zones. The orientation is estimated to 177/18 and the average width to 110 cm.

17. Fracture

This structure is also most probably a gently dipping fine-grained granite associated with greenstone in KA2563A at L=109 m, and with an intensely deformed fine-grained granite in KA2511A at L= 133 m. However its structural impact occur as a fracture in the contact or in the fine-grained granite. The lithological body is interpreted to follow a gently dipping cross-hole seismic reflector intersecting KA2563A at L=110.5 m and KA2511A at L=125 m. Previous seismic investigations in KA2511A also show a gently dipping reflector at this depth. There are also several sub-horizontal faults in KA2511A, in section L = 130 - 132 m, associated with altered diorite and fine-grained granite, calcite and epidote fillings. This structure is geologically more prominent than zone 16, but is not necessarily a conductive structure as the deformation (in KA2511A) is ductile and not brittle. Sub-horizontal structures are interpreted to act as hydraulic connectors, but seem to show a very heterogeneous conductive character. The orientation is estimated to 245/05 and the average width to 190 cm.

18. Fracture-Swarm-Fault

The last identified gently dipping fine-grained granite structure is supported by both radar and seismic in KA2563A and KA2511A. It is currently interpreted to be a dry intercept even if there exist a 20 l/min inflow in KA2511A which is measured in the interval up to L=242 m. However, as this structure intersects at L=242.5 m the inflow is not interpreted to be associated with this structure but rather to a steep structure at L=240.5 m (Structure 10). Inspection of the core shows a fault crush with a parallel epidotized fault in KA2511A. The main fault has chlorite and some calcite fillings and occurs in fine-grained granite (close to the contact with the diorite). The host rock in this core section (25 cm) is influenced by hydro-thermal activities In KA2563A it occurs at L= 109 m with a similar geological signature. This structure is also strengthened by a radar reflector in KA2563A at L=191 m and a seismic reflector in KA2511A at L=240 m. The width is estimated to 20 cm and the orientation is 024/16. Further, it is also identified as a fracture swarm in KI0023B at L=75.5 m, supported by radar and seismic evidence. However, the performed interference test program by Andersson et al (1998) show, in a test in KA2563A that there exist no connectivity in structure 18.

Z. Zone
The Z structure is a large zone, unlike all other structures found in the drilled boreholes in the TRUE Block Scale experiment as regards to its geological characteristics. This structure is identified by a large section of core crush from L = 188 m to the end of the borehole which is also confirmed by the BIPS image. During the drilling it was featured by successively increased inflow and mobilisation of unconsolidated material. A mineralogical analysis performed by Tullborg (1998) show that the characteristics of this zone is similar to the characteristics of Zone NE-1, with brecciated, crushed and faulted rock with large portions of altered host rock, (diorite and fine grained granite). The contents of fault gouge in the analysed sample was low, possibly due to that gouge may have been flushed out during drilling and uptake of the core. Geometrically, this zone is sub-parallel to NE-2, EW-3 and NE-1. However, based on the conceptual model of the site scale zones (Rhén, 1997), zone NE-1 is located over 80 m south of the Z structure, and EW-3 is approximately 30 m south of the Z structure. However, zones NE-2, EW-3 and NE-1 are not well identified in this particular part of the HRL. Splay structures and minor branches to these major zones may therefore exist. It is interpreted that the Z structure is such a branch of either EW-3 or NE-1. The characteristics of zone NE-2 is completely different, dominated by mylonites, and a few conductive faults.

NE-2 This zone is NE-2 and data for this zone can be obtained from Rhén et al (1997). No intercepts in this zone have been identified in the TRUE Block Scale set of boreholes.

EW-1 This zone is EW-1 and data for this zone can be obtained Rhén et al (1997).

EW-3 occur as a zone deviating westwards from NE-1. Data for this zone can be obtained from Rhén et al (1997).

3.2 New and updated interpretations

The fractures that could be correlated to the POSIVA flow log in borehole KI0025F03 are illustrated in **Figure 3-2**. A systematic control of interpreted intercepts in the March'99 structural model showed that with the POSIVA flow log it was possible to identify the specific conductive fracture among many possible fractures in a borehole section. Table 3-1 shows data for old and new intercepts interpreted to be part of identified conductive structures. The new information do in most cases induce minute changes of the orientation of the structures. However, one new conductor, #23, have been identified.

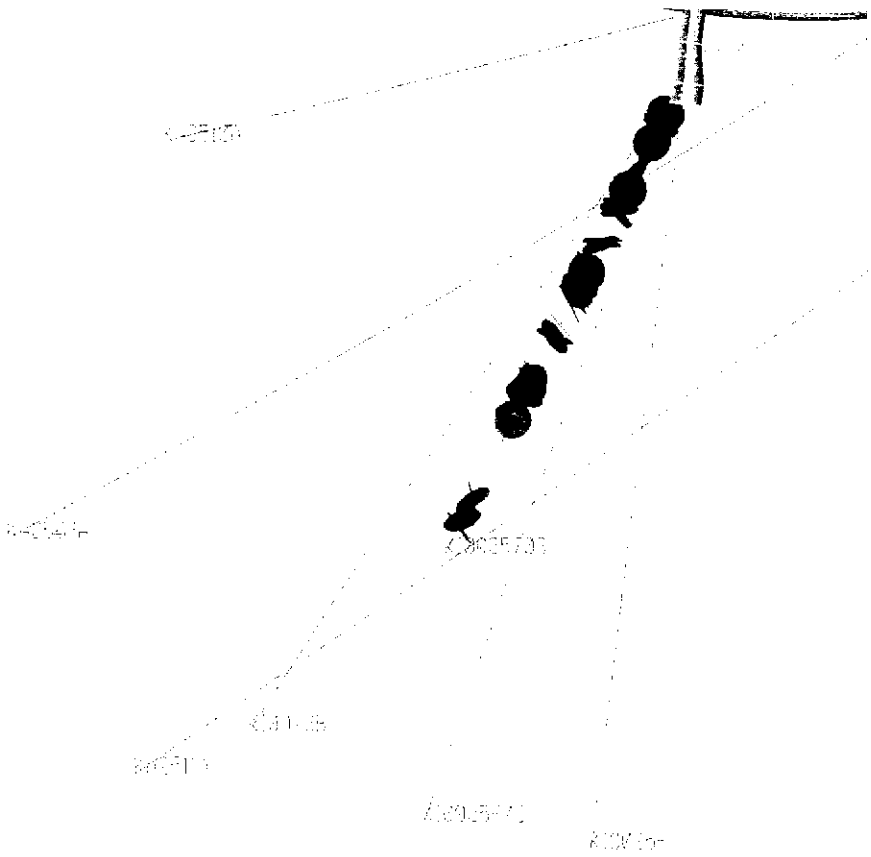

Figure 3-2. *Illustration of the fractures that can be correlated to sections of high inflow in borehole KI0025F03.*

The geological signature of identified intercepts of structures #6, #7, #13, #19, #20, #21, #22 and #23 are shown in Appendix B.

Structure #6 is observed in boreholes KI0025F03, Ki0025F02, KI0025F, KA2511A, KA2563A and KI0023B. These intercept points correlate well with observed inflow points in these boreholes. However, the geological signature is not simple throughout all intercepts which either suggests a variable geology along its structure or, more likely that flow goes through more than one fracture. The geology is similar in KI0025F02, F03 and in KI0023B with a main fault infilled partly with calcite. The complete ductile structure has a width which varies between 5 to 10 cm although only one edge of is reactivated and show

Table 3-1. Intercepts of identified structures. Red text shows new intercepts and black text shows the SeMarch'00 structural model data.

	KA2563A			KA2511A			KA3510A			KI0025F			KI0023B			KI0025F02			KI0025F03		
#	Depth	Strike	Dip	Depth	Strike	Dip	Depth	Strike	Dip	Depth	Strike	Dip	Depth	Strike	Dip	Depth	Strike	Dip	Depth	Strike	Dip
1	12.5	335	82																		
2	68.5	135	87				11.1	309	75												
3	68.5	135	87				37.5	106	81												
4	94.4	296	74	23.1	300	80	12.9	115	89												
5	103.0	114	89				47.7	138	75	4.9	307	57	7.2	112	87						
6	157.2	309	89	100.1	340	71				(61.8)	342	86	44.2	88	83	52.3	317	89	51.9	136	81
7	153.4	111	73	38	143	87				43.5	253	84	42.2	103	87	39.9	126	70	43.0	88	84
8	242.4	26	84				16.1	232	89												
9	230.0	123	88																		
10	351.3	124	80	240.5	127	85							170.7	298	83						
11				258.2	288	88															
12																					
13	207.0	321	86										85.6	318	89	93.9	140	83	87.9	338	87
15							118.0	269	88												
16	56.3	11	40	104.7	233	18															
17	108.9	222	34	132.4	270	16															
18	194.3	12	18	242.5	155	9							75.5	348	41						
19	237.9	343	76	198.2	324	87				166.4	336	84	111.6	342	87	133.0	334	87	124.7	339	86
20	188.7	316	82	122	321	73				87.7	336	77	69.8	157	82	74.7	134	89	73.2	326	64
21										(166.4)	338	74	71.1	123	86	97.9	354	77	91.9	296	59
22										88.8	340	81				66.8	337	88	63.2	154	87
23																59.2	125	80	56.8	301	77
24										37.1	301	82	31.8	308	76	33.9	307	72	33.8	135	75
Z										192.1	243	77									

Figure 3-3 illustrates the complete updated March 1999 structural model. Table 3-1 shows a summary of all interpreted intercepts of the March 1999 structural model.

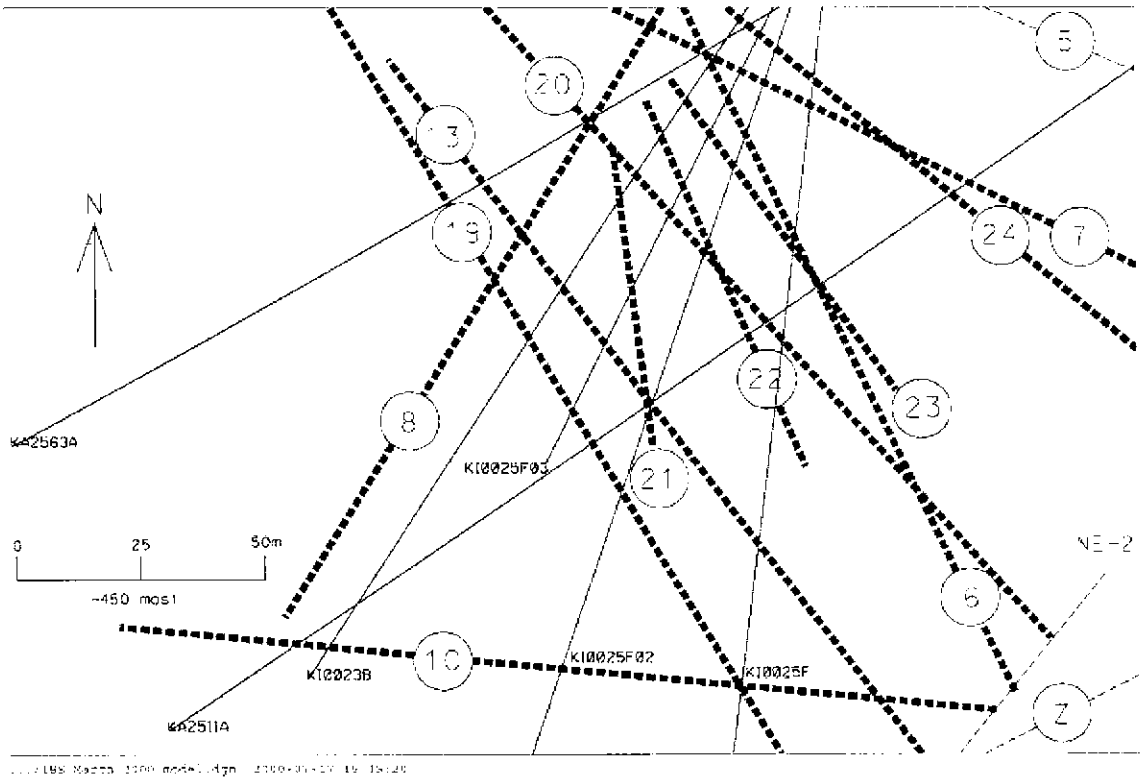

Figure 3-3. Structural model March 2000 with the proposed subordinate structures #23 and #24.

4 Hydraulic Reconciliation

Not all geologic structures are hydraulically significant. This chapter discusses how the significant structures can be identified, and it provides data on the location and extent of these structures. This report is an update of Doe (1999) to include data from KI0025F03, which was drilling in August 1999.

Doe (1999) presented a reconciliation of the hydraulic and structural geologic information on the TRUE Block Scale volume. The study pointed out that a subset of the September 1998 geologic structures, #6, #7, #10, #13, #19, #20, were hydraulically significant in the central part of the block. The study also described the hydraulic evidence for structures #21 and #22 that Hermanson had defined in the March 1999 model as part of a search for conducting features that could connect the sub-parallel structures #13 and #20. The reconciliation report also proposed an additional structure, #23, that lay between Structures #22 and #6.

4.1 Pressure Responses to Drilling

The main sources of hydraulic data are the Posiva flow logs (Rouhaininen and Heikkinen, 1999), hydraulic tests (Gentzschein and Ludwigson, 2000), and pressure response to drilling, which are presented in this report. The main criteria for identifying a hydraulically significant structure are the following:

- Indications of outflow during drilling or during flow logging
- Pressure responses in other boreholes when the structure is penetrated by drilling
- Pressure responses across multiple boreholes during hydraulic tests

Pressure measurements during drilling provide a very effective tool for identifying hydraulic connections. Such data were important for preparing earlier versions of the hydro-structural model. When a drill from an underground-collared hole penetrates a conducting feature it creates a sink that reduces the pressure in that conductor and other connected conducting features. If the conductor is reasonably transmissive, this pressure response can propagate rapidly through the conducting network.

Within the TRUE Block Scale volume, these pressure responses appear as nearly immediate, sharp pressure reductions. Figure 4-1 shows KI0025F02's pressure responses as a function of time for the drilling of KI0025F03. The figure includes the drilling progress versus time, and light grey vertical lines show the times where the structural model would predict the intersection of major structures.

The pressure-time plot for KI0025F03 intersects every major hydraulic structure in the TRUE Block Scale volume except for Structure #10. One would expect that this structure would have been intersected had KI0025F03 been drilled as deeply as KI0025F02.

Table 4-1 presents the pressure responses to drilling for each structure intersected and each monitoring interval. These pressure responses form a matrix that shows the connectivity of the structures. The responses suggest that some degree of connection exists between all the structures, but there is particularly good connection among Structures #6, #23, #22, #20, #21, and #13. We will refer to this as the Structure #20 network, as Structure #20 is the dominant and most extensive feature in the group. Although each of these structures produces distinct pressure responses, each intersection causes some response throughout the Structure #20 network.

Based on the response matrix of Table 4-1, we can conclude that the drilling of KI0025F03 confirms the basic hydraulic-structural model of the 1999 reconciliation report, and it provides some further information on two issues identified in Doe (1999), specifically, the continuity of Structure #13 and the existence of an additional structure between #6 and #22. In addition, the analyses of drilling responses to KI0025F03 suggest an additional structure, which we refer to as Structure #24, which may lie shallow of Structure #6 and #7 but deeper than Structure #5. These clarifications are described below.

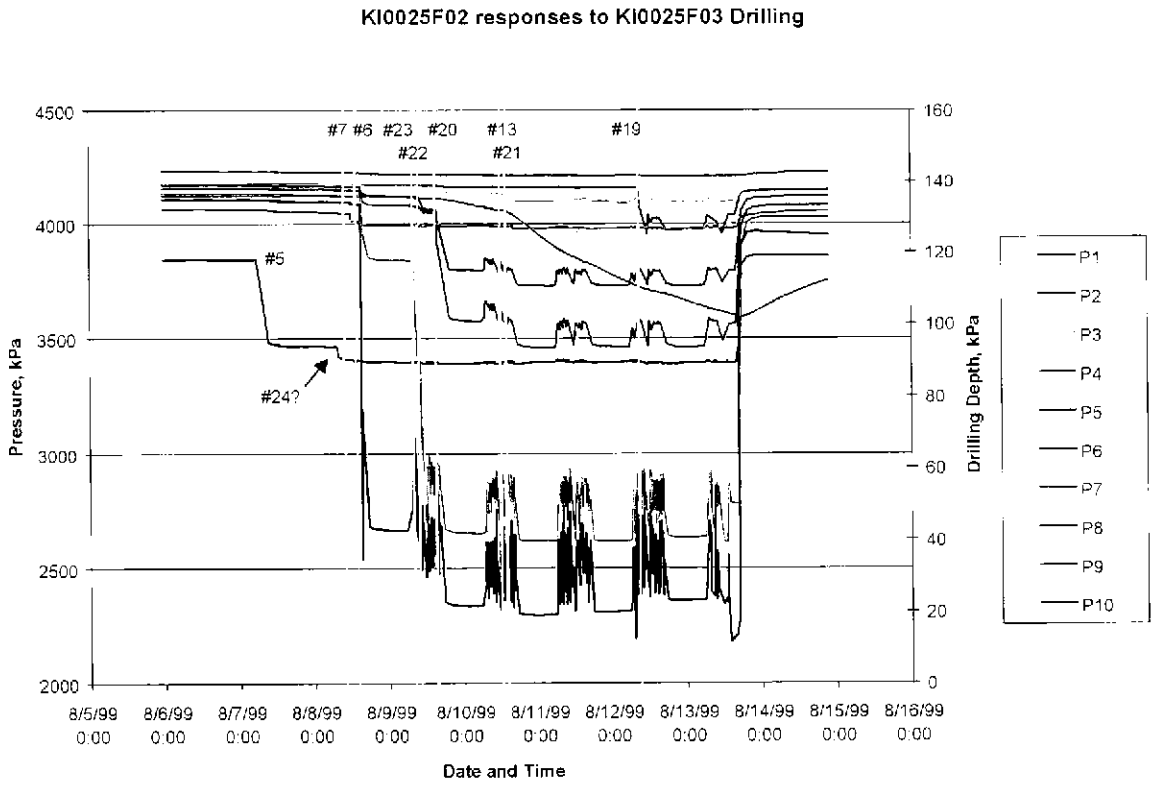

Figure 4-1. Pressure responses of KI0025F02 to drilling in KI0025F03.

Table 4-1. Pressure responses to Drilling KI0025F03

Monitoring Intervals	Expected Structure	Pressure Responses (kPa) by Structure in KI0025F03									
		#5	#24?	#7	#6	#23	#22	#20	#13	#21	#19
KA2563:S1	#19	-	-	-	-	-	-	12	-	-	140
KA2563:S2	#19	-	-	-	-	-	-	12	-	-	143
KA2563:S3	#13	-	-	-	54	3	19	305	118	122	-
KA2563:S4	#20	-	-	-	69	5	23	416	116		-
KA2563:S5	#6,7,21	5	-	7	58	9	15	60	6	46	-
KI0023B:P1	#10	-	-	-	-	-	-	-	-	-	4
KI0023B:P2	#19	-	-	-	-	-	-	-	-	-	182
KI0023B:P3	-	-	-	-	33	-	23	226	57	130	-
KI0023B:P4	#13	-	-	-	58	6	15	320	144	145	-
KI0023B:P5	-	-	-	-	68	4	21	413	137		-
KI0023B:P6	#21	-	-	-	65	4	21	424	123		-
KI0023B:P7	#6,20	-	-	-	102	8	24	398	112		-
KI0023B:P8	#7	14	-	15	10	-	-	-	-	-	-
KI0023B:P9	#5	261	37	-	-	-	-	-	-	-	-
KI0025F02:P1	#10	-	-	-	-	-	-	-	-	-	-
KI0025F02:P2	#19	-	-	-	-	-	-	-	-	-	180
KI0025F02:P3	#13, 21	-	-	-	-	-	-	24	36		-
KI0025F02:P4	-	-	-	-	-	-	-	-	-	-	-
KI0025F02:P5	#20	-	-	-	69	4	27	470	85		-
KI0025F02:P6	#22	-	-	-	42	7	53	263	66		-
KI0025F02:P7	#23	-	-	12	280	1125	-	61	33		-
KI0025F02:P8	#6	-	-	12	1411	-	-	327	38		-
KI0025F02:P9	#7	-	-	50	-	-	-	-	-	-	-
KI0025F02:P10	#5	377	70	-	-	-	-	-	-	-	-
KI0025F:S1	Z	-	-	-	-	-	-	-	-	-	13
KI0025F:S2	#19	-	-	-	-	-	-	-	-	-	23
KI0025F:S3	-	-	-	-	-	-	-	-	-	-	23
KI0025F:S4	#20,22	-	-	-	53	3	13	396	124		-
KI0025F:S5	#6	14	7	34	10	-	-	6	10		-
KI0025F:S6	#5	186	263	-	-	-	-	-	-	-	-

There are several points worth noting in Table 4-1. The most important is the ambiguity in distinguishing Structures #21 from #13. One goal of KI0025F03 was to get a better definition of these two structures in a hole where they were clearly separated from other structures and from one another. Unfortunately, the pressure data are very noisy in the time period when these structures are intersected. This noise seems to occur mainly during periods of drilling, hence, when drilling ceases one can see clearly the pressure drops across the monitoring array that are associated with Structures #13 and #21. In most holes Table 4-1 shows the total pressure changes across both structures. With some imagination one might see a separation of the two pressure responses, and these cases are noted by giving separate pressure responses for Structures #13 and #21.

Based on the pressure responses and on the locations of conductors in the boreholes, Table 4-2 provides a matrix of which features appear in which boreholes. There is some ambiguity in this matrix for structures that are part of the Structure #20 network. Because Structure #20 intersects all boreholes except for KA2511A, every borehole has some pressure response to every structure that is part of the Structure #20 network.

This ambiguity applies to the interpretation of Structure #6 in KI0025F. There is no significant transmissivity in KI0025F in the area where Structure #6 should intersect. However, there are good pressure responses to #6 in KI0025F:S4 (which is the Structure #20 intercept), and KI0025F:P5 (which contains Structure #7 and the location where #6 should be). The possibility that the lack of a flowing point for Structure #6 is further made ambiguous by the possibility that the structure is present but does not flow locally due to channelling. Because KI0025:P5 has a Structure #6 response, and little or no Structure #20 response, the matrix of borehole intersections includes KI0025F and Structure 6 as a match but with a question mark. Other intersections that similarly ambiguous are noted with question marks.

The matrix of Structures and boreholes is very important for determining features truncations and corner locations as discussed in the following section. Using this information we have prepared a structure map at Elevation = -477 in Figure 4-2. This map terminates Structures according to which boreholes they intersect or do not intersection.

Table 4-2 Summary of structure intersections with boreholes

Structure	KI0025F	KI0025F03	KI0025F02	KI0023B	KA2563A
#5	x	x	x	x	x
#24	x	x	x	x	
#7	x	x	x	x	
#6	?	x	x	x	x
#23		x	x		
#22	x	x	x		
#20	x	x	x	x	x
#13		x	x	x	x
#21		x	x	x	x
#19	x	x	x	x	x
#10			x	x	

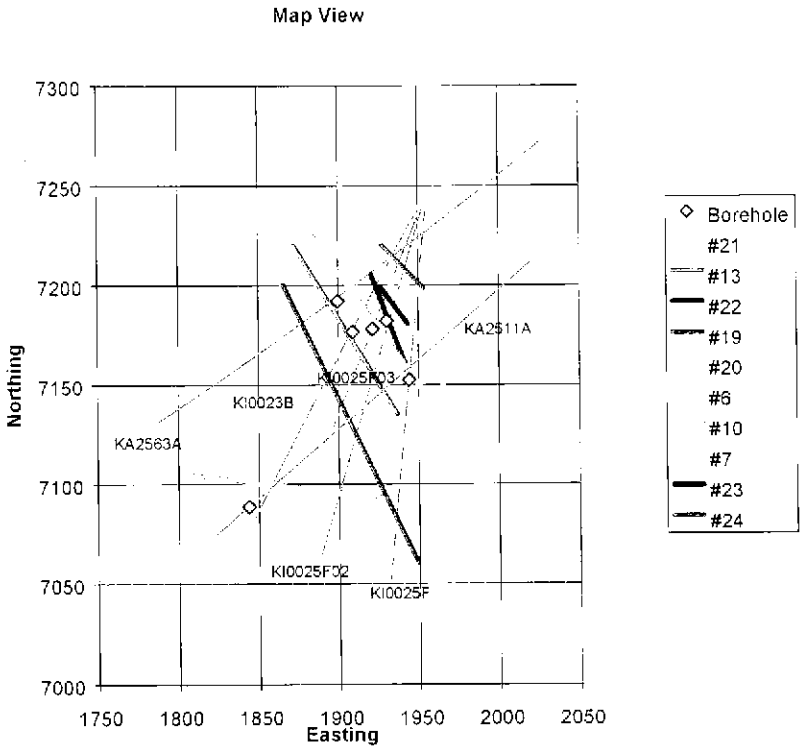

Figure 4-2. Map of Hydraulically Significant Structures are Elevation =-477

4.2 Further Definition of Structure #13

The continuity of Structure #13 has been a source of some ambiguity since the drilling of KI0025F02 and KI0025F03. The ambiguity first arose in with respect to pressure responses of KI0025F03:P3, which should contain Structure #13, to sinks in other parts of the structure. The reconciliation report (Doe, 1999) noted that monitoring interval KI0025F02:P3 had markedly lower drawdown responses of KI0025F02:P3 to pumping in both Structure #20 and Structure #13. This attenuated pressure response of the zones that should contain Structure #13 was shared by both KI0025F02:P3 and KI0025F03:P3 as shown by the Phase Q interference tests (Andersson, and others, 2000).

An inspection of KI0025F02:P3's response to drilling of KI0025F03 appears in Figure 4-1. This pressure record is unusual for Structure #13 in having little pressure response to any other hits than the intersection with the conductor that is in the Structure #13 position.

There are at least two possible explanations for the low responsiveness of the apparent Structure #13 intercepts in KI0025F02 and F03. The low responsiveness may suggest that Structure #13 is discontinuous or that the KI0025F02 and F03 intercepts represent a

different structure. The possibility of non-connectivity is at odds with observations of tracer dilution responses in these intervals to pumping in other parts of the #20-#13 network.

A second explanation involves some other water source that acts as a reservoir. Such as a reservoir of water near these two intercepts can act as a constant-pressure boundary that reduces the pressure response to pumping of more distant sources. The burden for testing this hypothesis lies in identifying such a reservoir.

The possible candidate for reservoir that can act as a constant-pressure boundary is the intersection of Structures #13 and #21. Appendix C contains in-plane maps of each structure. The #13-#21 intersection can be seen in Figures C-9 and C-10. This intersection passes very close to these intersections, which is not surprising given the small separation of these structures in KI0025F02 and KI0025F03.

4.3 Structure #23

The reconciliation report (Doe, 1999) suggested the existence of a structure between Structure #6 and Structure #22 in KI0025F02.Monitoring interval KI0025F02:P7 isolates the proposed location of this structure. At the appropriate depth, the drilling of KI0023F03 produced a strong pressure response in this monitoring interval (Figure 4-1, Table 4-1). This response confirms the existence of this structure and its continuity in KI0025F03.

This additional hydraulic structure appears in KI0025F03 as well. Based on TV and core logs, this feature is now identified as Structure #23. The structure appears definitively in only KI0025F02 and KI0025F03. It is not defined in either KI0025F or KA2563A. Its existence in KI0023B is uncertain, but could be confirmed through Posiva flow logging if the hole is opened in the future. The character of Structure #23 is different KI0025F03 than in KI0025F02, in that the former hole has three or four possible flowing features on the Posiva log, while in KI0025F02 it appears as a clear single flowing features.

4.4 Structure 24

An inspection of the drilling responses to KI0025F03 suggested the existence of an additional structure lying somewhat shallower than Structures #6 and #7. The main evidence is is pressure response to drilling at a depth between 33.8 and 36.8 meters in KI9925F03. This responses appears in all holes except for KA2563A. It appears in KI0025F02 (Figure 4-1), and it is particularly strong in KI0025F (Appendix Figure C-4). A review of drilling response records from previous boreholes reveals a consistent response to this structure. Other evidence comes from the flow logs and the borehole television data.

This structure is indicated by inflow points in boreholes KI0025F02 and KI0025F03 as shown in the POSIVA flow logs by Ruuhianen and Heikkinen (1998 and 1999). The intersection points in KI0023B, KI0025F, F02 and F03 fall nearly into a single plane (+/- 10 cm) with an orientation of 130/82. The structure consists of an open calcite

infilled fracture with limited impact of the surrounding host rock. However, the intercept in KI0025F03, c.f. Appendix B, shows signs of alteration and plastic deformation around the structure. There exists an alternative structure in KI0025F02 at 34.9 m, although this deviates from the generally planar fit shown by the other intercepts.

In the corner model with terminations, Structure #24 is given a relatively small size. The reason for this assignment is avoidance of structures #6 and #7. Structure #6 in particular is connected to the Structure #20-#13 network, and were Structure #24 part of this system it should have created some pressure response in that network (Table 4-1), which it does not. Structure #24 shares monitoring intervals with Structure #5 in most boreholes. It may be part of a common network with Structure #5, however this may be difficult to test given the connections between these structures through the boreholes.

4.5 Summary of Hydro-Structural Model

As mentioned above, the drilling and testing data from KI0025F03 largely confirm the previous hydro-structural model presented in Doe, 1999. The major features of the model are the following:

- Structure #20 is the major central structure; it is the core of a network that includes #6, #23, #22, #13, and #21.
- Structure #19 intersects all holes except KA2511A. It has possible connections to the Structure #20 network either through Structure #13 or through background fractures.
- Structure #13 has unusual pressure responses in KI0025F02 and F03 that may indicate either a discontinuity in the structure or a constant-pressure boundary formed by its intersection with Structure #21. Structure #13 does not appear in KI0025F.
- Structure #21 is part of the Structure #21 network with intersections in KI0025F02, KI0025F03, KI0023B, and possibly KA2563A. There are still some ambiguities regarding Structure #21 as it mostly appears close to other structures in boreholes.
- Structures #22 and #23 are confirmed by the KI0025F03 data.
- KI0025F03 strongly suggests an additional structure, #24 shallow to Structures #6 and #7. This features does not make connections with #6 and #7. It is steeply dipping and likely has little effect on the behaviour of the hydraulics in the core area of the TRUE Block Scale volume.

Figure 4-3 shows a revised schematic of the connections of the structures along with transmissivity data.

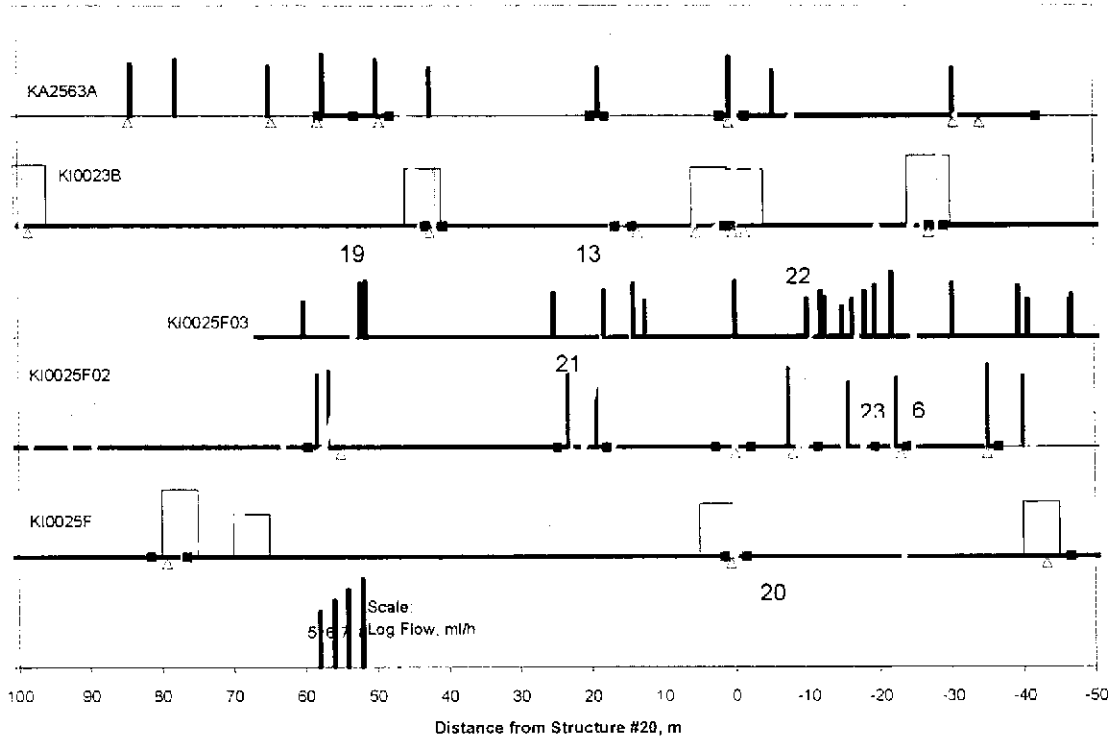

Figure 4-3. Schematic representation of boreholes and structures with transmissivity data.

4.6 Structure Locations

4.6.1 Locations and Feature Equations

Table 4-4 provides the equations for the planes that best fit the intersections with each borehole. These equations use all holes including KI0025F03. The planes are close to those described in Doe (1999). The largest differences occur for Structures #21 and #22 which had relatively few points for the previous determinations.

Each equation describes a plane having an equation of the form $ax + by + cz + d = 0$. Some structures, particularly #6 appear to have some non-planarity that accounts for discrepancies of up to a few meters in the locations on some boreholes. Adjustments for packer locations to account for planar assumptions are discussed in Section 4.5.3.

4.6.2 Corners

The corners for the features are calculated in two ways: (1) corners of structures that are extended to the edge of the 500-m TRUE block, and (2) corners using terminations of structures based on holes not intersected by the structure.

Table 4-4 gives the corner locations assuming the structures extend to the limits of the 500-m TRUE block. This approach ignores evidence that the features have limited extent.

The second method of calculating the corners (Table 4-5) uses the exclusion information from the boreholes. This method starts by taking the trace of the structure at elevation –477, which is about the center of the main borehole array. Each trace is truncated to avoid intersections with boreholes where the structure does not appear. This truncation includes KA2511A, which limits the extent of the otherwise unbounded Structures #7, #6, #19, and #20.

A three-dimensional calculation of the fracture extends this trace in the dip direction of the structure by an amount equal to the trace length. This produces a square structure centered on elevation = -477.

We then prepared a visualisation of the model to inspect intersections. The following adjustments were made to provide expected connections in the network:

- Upward extension of #13 to intersection #19 and provide connections for #19 into the other structures;
- Upward and downward extension of Structure #22 to connect over its full width with Structures #20 and #6;
- Upward extension of #23 to provide connections with #22.

4.6.3Virtual Packer Locations

The structural model represents features as planes. While this is a close approximation, it is not perfect, and there can be differences of up to a few meters between the model's location of a structure in any given borehole and its actual location. Due to these differences, the structural model may place structures at the same depths as actual packer locations. We have prepared a chart of virtual packer locations that adjusts the packer locations to be consistent with the depths in the models to avoid this cover-up problem. Few packers required adjusting, and those that were adjusted were moved by minor distances. Table 4-6 gives the virtual packer locations.

Table 4-3. Structure Plane Equations

Feature Plane Equations, March '00 Model						
Structure	a	b	c	d	Strike	Dip
#6	-0.8429	-0.5374	-0.0253	-5487.00	327.5	88.6
#7	0.4404	0.8851	-0.1504	7299.84	116.5	81.4
#13	-0.7303	-0.5535	-0.4003	-5172.72	322.8	66.4
#19	-0.8586	-0.5125	-0.0126	-5285.73	329.2	89.3
#20	-0.7464	-0.6596	-0.0884	-6129.78	318.5	84.93
#21	0.8698	0.3739	-0.3221	4504.55	156.74	71.21
#22	0.8437	0.3999	-0.3580	4672.57	154.64	69.02
#23	0.7337	0.6794	0.0000	6304.34	137.2	90.0
#24	0.6391	0.7552	-0.1457	6753.70	130.24	81.62
#10	-0.0916	-0.9458	-0.3117	-6736.05	275.53	71.84

Table 4-4. Corners for Structure planes extended to the TRUE block boundary.

Structure		Corners					
		1	2	3	4	5	6
#6	Easting	1784.327	1799.417	2118.921	2103.975		
	Northing	7420.639	7420.527	6919.361	6919.26		
	Elevation	-199.361	-700.79	-700.639	-199.507		
#7	Easting	1649.361	2150.793	2150.639	1649.45		
	Northing	7392.688	7143.232	7058.112	7307.397		
	Elevation	-199.361	-199.472	-700.639	-700.825		
#13	Easting	1842.699	2150.675	2150.66	1947.787	1649.385	1649.317
	Northing	7420.705	7014.25	6919.278	6919.305	7313.005	7420.613
	Elevation	-700.692	-700.551	-569.251	-199.295	-199.263	-347.88
#19	Easting	1730.108	1737.527	2036.671	2029.388		
	Northing	7420.649	7420.528	6919.351	6919.252		
	Elevation	-199.351	-700.793	-700.649	-199.502		
#20	Easting	1678.12	1737.532	2150.532	2150.665	2121.151	
	Northing	7420.609	7420.579	6953.287	6919.262	6919.338	
	Elevation	-199.481	-700.692	-700.674	-447.995	-199.461	
#21	Easting	1915.555	2130.957	1945.342	1729.951		
	Northing	7420.706	6919.275	6919.294	7420.487		
	Elevation	-199.294	-199.517	-700.706	-700.73		
#22	Easting	1936.065	2150.537	2150.52	1960.907	1723.467	
	Northing	7420.802	6968.196	6919.227	6919.378	7420.507	
	Elevation	-199.417	-199.457	-254.175	-700.782	-700.68	
#23	Easting	1720.653	1720.748	2150.533	2150.601		
	Northing	7420.575	7420.472	6956.347	6956.274		
	Elevation	-199.379	-700.765	-700.621	-199.533		
#24	Easting	1753.722	1649.372	1649.422	2150.684	2150.684	
	Northing	7420.443	7420.403	7411.863	6987.775	7084.454	
	Elevation	-199.168	-656.728	-700.739	-700.518	-199.444	

Table 4-5. Corners of Structures based on terminations for non-intersections of boreholes. Local coordinates are referenced to the center of Structure #20.

Structure		Corners				Centers		DFN Input Data	
		1	2	3	4	Global	Local	Width	Length
#6	Easting	1900.12	1963.88	1902.69	1966.45	1933.28	14.07	118.60	118.63
	Northing	7249.22	7149.22	7250.78	7150.78	7200.00	-15.01		
	Elevation	-417.70	-417.70	-536.30	-536.30	-477.00	0.00		
#7	Easting	1885.40	1985.90	1877.60	1978.10	1931.75	12.53	112.25	113.55
	Northing	7237.62	7187.62	7222.43	7172.43	7205.03	-20.04		
	Elevation	-420.87	-420.87	-533.13	-533.13	-477.00	0.00		
#23	Easting	1926.76	1943.43	1926.76	1943.43	1935.09	15.88	24.53	49.06
	Northing	7198.00	7180.00	7198.00	7180.00	7189.00	-4.01		
	Elevation	-452.47	-452.47	-501.53	-501.53	-477.00	0.00		
#22	Easting	1933.48	1954.81	1903.29	1924.62	1929.05	9.83	49.80	93.34
	Northing	7211.16	7166.16	7196.85	7151.85	7181.51	3.48		
	Elevation	-439.65	-439.65	-526.80	-526.80	-483.22	-6.22		
#20	Easting	1875.46	1955.00	1883.44	1962.98	1919.22	0.00	120.11	120.58
	Northing	7226.46	7136.46	7233.52	7143.52	7184.99	0.00		
	Elevation	-416.94	-416.94	-537.06	-537.06	-477.00	0.00		
#13	Easting	1844.39	1908.82	1890.79	1955.21	1899.80	-19.41	106.66	145.49
	Northing	7198.82	7113.82	7234.04	7149.04	7173.93	11.06		
	Elevation	-397.01	-397.01	-530.33	-530.33	-463.67	13.33		
#21	Easting	1908.28	1942.67	1881.06	1915.45	1911.87	-7.35	87.08	91.98
	Northing	7235.87	7155.87	7224.18	7144.18	7190.03	-5.04		
	Elevation	-433.46	-433.46	-520.54	-520.54	-477.00	0.00		
#19	Easting	1864.97	1948.53	1866.75	1950.31	1907.64	-11.58	163.04	163.05
	Northing	7199.49	7059.49	7200.51	7060.51	7130.00	54.99		
	Elevation	-395.48	-395.48	-558.52	-558.52	-477.00	0.00		
#10	Easting	1799.34	1923.24	1807.46	1931.36	1865.35	-53.87	124.48	131.07
	Northing	7084.83	7072.83	7125.05	7113.05	7098.94	86.05		
	Elevation	-414.76	-414.76	-539.24	-539.24	-477.00	0.00		
#24	Easting	1931.11	1957.10	1923.34	1949.34	1940.22	21.00	34.06	34.93
	Northing	7220.00	7198.00	7220.00	7198.00	7209.00	-24.01		
	Elevation	-459.97	-459.97	-494.03	-494.03	-477.00	0.00		

Table 4-6. Virtual packer locations for March '00 Structural Model; blue indicates location changes from actual.

Virtual Packer Locations and Interval Segments													
KI0025F03		*KI0025F02*		*KI0023B*		*KA2563A*		*KI0025F*		*KA2511A*	
P-setting		P-setting		P-setting		S-setting		S-setting		T-setting	
Pkr10	**2.6**	Pkr10	2.4	Pkr9	3.6	Pkr8	145	Pkr6	4	Pkr8	5
	3.58		3.4		4.6		146		5		6
Pkr9	**47.00**	Pkr9	37.5	Pkr8	40.45	Pkr7	186	Pkr5	41.5	Pkr7	64
	48.00		38.5		41.45		187		42.5		65
Pkr8	54.08	Pkr8	50.7	Pkr7	42.45	Pkr6	190	**Pkr4**	**85.5**	Pkr6	95
	55.08		51.7		43.45		191		**86.5**		96
Pkr7	58.58	Pkr7	55.1	Pkr6	69.95	Not monitored		Pkr3	89.5	Pkr5	102
	59.58		56.1		70.85	Pkr5	205		90.5		103
Pkr6	65.58	Pkr6	63	Pkr5	71.95		206	**Pkr2**	**160**	Pkr4	110
	66.58		64		72.95	Pkr4	208		**161**		111
Pkr5	74.08	Pkr5	72.3	Pkr4	83.75		209	Pkr1	169.5	Pkr3	138
	75.08		73.3		84.75	Not monitored			170.5		139
Not monitored		Pkr4	77.25	Pkr3	86.2	**Pkr3**	**233.00**	End	193.66	Pkr2	170
Pkr4	84.00		78.25		87.2		**234**				171
	85.00	Pkr3	92.35	Pkr2	110.25	Pkr2	241			Pkr1	238
Pkr3	88.08		93.35		111.25		242				239
	89.08	Pkr2	99.25	Pkr1	112.8	Pkr1	246			END	293
Pkr2	92.58		100.25		113.7		247				
	93.58	**Pkr1**	**138**	END	200.71	Not monitored					
Pkr1	100.08		**139**			END	362				
	101.08	END	204.18								
END	141.7										

4.6.4 Transmissivity Data for Structures

Table 4-7 updates the transmissivity data for the Structures reported in Doe, 1999. The data for KI0025F03 are taken directly from Gentzschein and Ludvigson, 2000. The only modifications summing the results of separate tests that span a single structure. Gentzschein and Ludvigson's tests 3 and 4 span Structure 23, which has mulitple conductive segments. Similar summations were made for tests 5 and 6 (Structure #22) and tests 8 and 9 (Structure #13).

Table 4-7. Transmissivity data for March '00 Structural Model

Structure	KI0025F			KA2563A	KI0023B		KI0025F02		
	Buildup (Safir)	Buildup (Jacobs)	Pump Test	Pump Test	Buildup	Pump Test	Buildup	Flowdim	Pump Test
7	9.0E-07	1.3E-05	3.7E-05	2.1E-05	1.8E-05	4.0E-05	1.7E-06	1.8E-05	x
6	x	x	x	x	4.0E-07	x	1.5E-08	1.0E-07	x
23	x	x	x	x	x	x	5.3E-09	6.7E-09	x
22	1.8E-07	5.1E-07	8.5E-07	x	x	x	2.6E-07	3.7E-07	x
20				8.7E-07	9.6E-07	9.6E-07	6.5E-07	5.9E-07	6.90E-07
21	x	x	x	x	8.1E-07		9.6E-09	2.8E-09	x
13	x	x	x	4.5E-08	5.8E-08	3.20E-07	1.5E-09	1.7E-07	x
19	1.1E-05	2.9E-05	x	x	3.9E-06	x	1.7E-06	1.8E-07	x
10	x	x	x	x	4.5E-06	x	5.3E-08	1.2E-07	x

Structure	KI00125F		KA2563A	KI0023B		KI0025F02	
	Packer Log	Flow Test	Posiva Log	Packer Log	Flow Test	Posiva Log	Flow Test
7	6.2E-08	4.10E-07	-	-	1.6E-05	>1.6E-07	1.8E-06
6	x	x	2.2E-08	1.7E-06	3.3E-08	1.1E-08	1.5E-08
24	x	x	x	x	x	x	x
23	x	x	x	x	x	5.4E-09	1.1E-08
22	4.4E-08	1.60E-08	x	x	x	>1.0E-07	3.3E-07
20			>1.9E-07	8.9E-08	1.4E-07	>1.2E-07	1.1E-06
21	x	x	6.8E-09	1.5E-07	6.9E-07	2.8E-08	5.0E-08
13	x	x	2.7E-08	3.3E-08	9.8E-08	3.9E-09	4.6E-09
19	8.9E-07	1.40E-06	9.4E-08	1.2E-07	1.2E-06	>1.1E-7	1.1E-07
10	x	x	x	2.2E-07	2.7E-06	3.3E-08	5.3E-08

Table 4-7 Continued, Transmissivity data for March '00 Structural Model

KI0025F03		
Posiva Log	Flow Test	Buildup
6.30E-08	x	x
2.10E-07	1.10E-07	6.80E-08
2.98E-08	x	x
2.00E-08	1.30E-08	1.50E-08
3.50E-08	x	8.30E-09
7.50E-08	6.10E-07	6.10E-07
2.10E-08	9.60E-09	3.90E-09
6.70E-08	4.40E-08	3.80E-08
1.20E-07	x	1.30E-06
x	x	x

5 REFERENCES

Andersson, P, Ludvigsson, J-E, Wass, E., (1998). True Block Scale Project, preliminary characterization stage. Combined interference tests and tracer tests. Performance and preliminary evaluation. Äspö Hard Rock Laboratory, Technical Note TN-98-XX. Swedish Nuclear Fuel and Waste Management Company.

Adams, J., 1998. Preliminary results of selective pressure build up tests in borehole KI0023B. Technical Note TN 98-27b. Äspö Hard Rock Laboratory. Swedish Nuclear Fuel and Waste Management Company, Stockholm

Carlsten, S., 1998. Prototype repository project. Borehole radar measurements in KA3573A, KA3600F and G-boreholes. Äpö Hard Rock Laboratory progress report HRL-98-16. Swedish Nuclear Fuel and Waste Management Company, Stockholm.

Carlsten, S., 1999. True block scale project. Results from borehole radar measurements in KI0025F02. International technical document ITD-99-02. Swedish Nuclear Fuel and Waste Management Company, Stockholm.

Dahlström, L.O., 1998. Test Plan for the Prototype repository. Äspö Hard Rock Laboratory Progress Report HRL-98-24. Swedish Nuclear Fuel and Waste Management Company, Stockholm.

Gentzshein, B. and J.-E. Ludwigson, 2000, Single-hole hydraulic tests and short-term interference tests in KI0025F03, SKB Äspölaboratoriet International Technical Document ITD-00-05. Swedish Nuclear Fuel and Waste Management, Stockholm.

Hermanson, J., Follin, S., 1997, TRUE Block Scale Project. Update of the structural model using characterisation data from KA2563A, KA3510A and KA2511A. Scoping stage. SKB Äspölaboratoriet Technical Note TN-97-19b. Swedish Nuclear Fuel and Waste Management, Stockholm.

Hermanson, J. 1997, TRUE Block Scale Project. Update of the structural model using characterisation data from KA2511A and KI0025F. SKB Äspölaboratoriet Technical Note TN-97-35b. Swedish Nuclear Fuel and Waste Management, Stockholm

Hermanson, J., 1998. TRUE Block Scale Project, preliminary characterisation stage. September 1998 structural model; Update using characterisation data from KI0023B. SKB Äspölaboratoriet Technical Note TN-98-18b. Swedish Nuclear Fuel and Waste Management, Stockholm.

Patel, S., Dahlström, L.O., Stenberg, L., 1997. Characterisation of the rock mass in the Prototype repository at Äspö HRL. Stage 1. Äspö Hard Rock Laboratory Progress Report HRL-97-24. Swedish Nuclear Fuel and Waste Management Company, Stockholm.

Rhén,I, Gustafson, G., Stanfors, R., Wikberg, P. Geoscientific evaluation 1997/5 (in press). Models based on site characterisation 1986-1995 1997. SKB Technical Report, TR 97-06. Swedish Nuclear Fuel and Waste Management Company.

Rouhiainen, P., P. Heikkinen, 1999. Difference flow measurement in borehole ki0025f03 at the Äspö HRL. International Technical Document, ITD 99-26. Swedish Nuclear Fuel and Waste Management Co.

Appendix A Fractures in inflow sections in KI0025F03

djup [m]	flöde [ml/h]	strykning [°]	stupning [°]	egna kommentarer	kärnkarterarens kommentarer
0					Äspödiorit, grå medelkornig ögonförande svagt förskiffrad, α=50 °
2.4	400	298	29	tydlig	
2.4		296	34	ej synlig	
3.6	650,000	350	62	tydlig	3.50: α=50 °, calcit, Q=5,74
4.7	2,000	311	87	tydlig	4.50: α=55 °, calcit, klorit
4.7		328	84	ej synlig	
4.7		123	86	ej synlig	
5.7	35,000	299	72	5.6 bred och tydlig	
5.7		312	84	knappt synlig	
5.7		139	86	knappt synlig	
6.3	200	244	68	tydlig, matt	
6.3		329	73	omvänd sinus, ej synlig	
8.2	100	134	84	ytterkant med nedanstående	
8.2		134	84	ytterkant med ovanstående	
8.2		129	87	ej synlig	
11.6	70	071	20	synlig	10-11: 10 cm pegmatit
16.8	60	015	75	parallell med nedanstående, synlig	
16.8		015	75	parallell med ovanstående, synlig	
18.3	40	236	77	ej öppna, endast färgskiftning	
18.3		236	77	ej öppna, endast färgskiftning	
26.4	6,500	123	85	26,3 synlig spricka under	
26.4		128	86	26,3 synlig spricka under	
26.7	1,500	321	87	synlig spricka i 26,6, i övrigt flera ej synliga, se nedan	
26.7		315	79		
26.7		050	12		
26.7		050	12		
26.7		260	88		
26.7		198	14		
32.4	3,000	274 x 2	68 x 2	"dubbelspricka" synlig	32-33: röd finkornig granit
32.4		071	70		34-35: röd finkornig granit
33.8	35,000	135	75	klar öppning, ytterligare 6 sprickor under (osynliga)	36-37: röd finkornig granit
33.8		145	80	eventuellt även denna och nedanstående	
33.8		134	87		
43.0	80,000	088	84	bred spricka	
43.0		267	88	knappt synlig	
43.4	20,000	098	78	varierad sprickbredd, tydligare nedanför utan sinus, ?	
44.1	800	088	88	fem sinus, två synliga band, ?	46-47: röd finkornig granit
44.1		251	71		47-48: röd finkornig granit
51.4	250,000	147	79	osynlig	48-50: röd finkornig granit
51.4		145	80	osynlig	51-53: omvandlad diorit, mylonit ?, Qtot=11,4
51.4		132	86	osynlig	
52.0	300,000	136	81	bred	
52.9	4,000	154	17	knappt synlig, denna eller nedanstående, ?	
52.9		232	27	ej synlig	
53.8	35,000	352	82		
53.8		337	80		

55.2	10,500	147	70	klar öppning	
55.5	10,500	138	71	bredast av ytterligare tre sprickor	
56.9	2.000	300	64	lika bred som nedanstående	
56.9		301	77		
56.9		063	23	delvis bred	
57.2	200	343	83		
58.3	500	336	37	bredare än nedanstående	
58.3		330	44		
60.7	45,000	125	86	60,6 knappt synlig	
61.3	45,000	138	83	61,2 knappt synlig	
63.2	3.000	154	87	bred	63: röd finkornig granit
69.6	60	319	89	knappt synlig	
73.2	120,000	326	64	73,1 tiotal sprickor	73: Qtot=16 l/min
73.2		151	89		
73.2		291	78		
85.8	2.000	326	87		86,5-90: röd finkornig granit
87.4	75,000	137	85		
87.5	50.000	338	87	bred	
87.5		139	81	måttlig	
87.8	30.000	351	72	bred	
87.8		335	81		
87.8		039	38		
90.6	6.000	261	47	endast färgskiftning	
90.6		274	43	eventuellt även denna och nedanstående	
90.6		271	40		
91.4	20.000	301	75		
91.9	10,500	296	59		92: röd finkornig granit, Qtot=20,4 l/min
91.9		289	62		
98.5	8,000	284	84	?	96,5-98: röd finkornig granit
98.9	8,000	296	59		
99.6	90	231	7		102-103: grönsten
124.7	100,000	237	68	bred	110: Q2-slim 25 grader, 20 mm
124.7		168	87	eventuellt även denna	117-118: röd finkornig granit, Qtot=19,2 l/min
125.5	70,000	139	89	tydlig	120: grå finkornig granit
131.1	200	248	60	rött område, denna och närmaste nedan bredast	2 parallella kloritsprickor vittrade, kalcit vittrad
131.1		248	61		127,5-128,5: grönsten, Qtot=24,0
131.1		248	61		131: grönsten
133.3	1.500	144	83		132: grönsten
141.3				slut	142: Qtot=24,4, BH slut 141,72 m, Qtot=25 l/min (öppet borrhål)

Appendix B Geological signature (BIPS) of intercepts on key structures

Structure #6

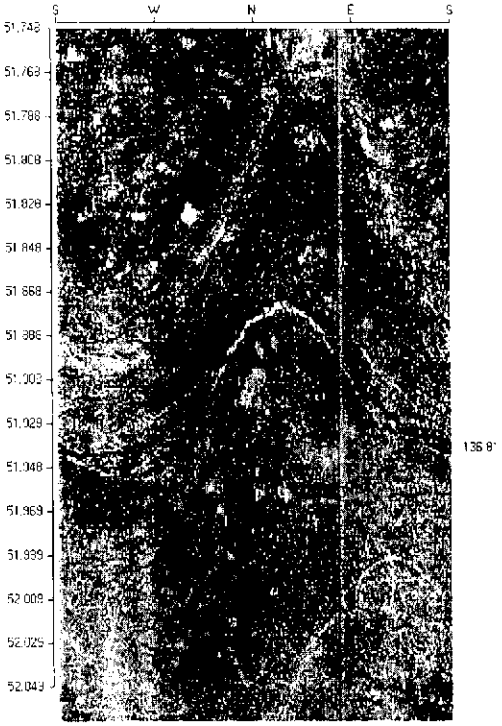

KI0025F03
L=51.9 m (136/81)

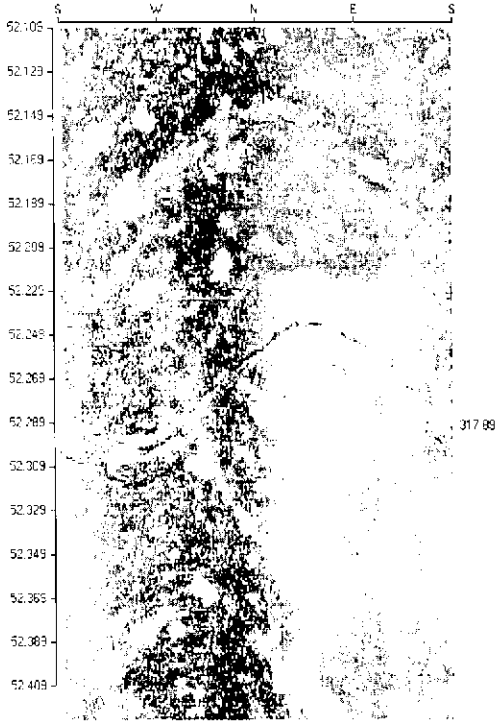

KI0025F02
L = 52.3 m (317/89)

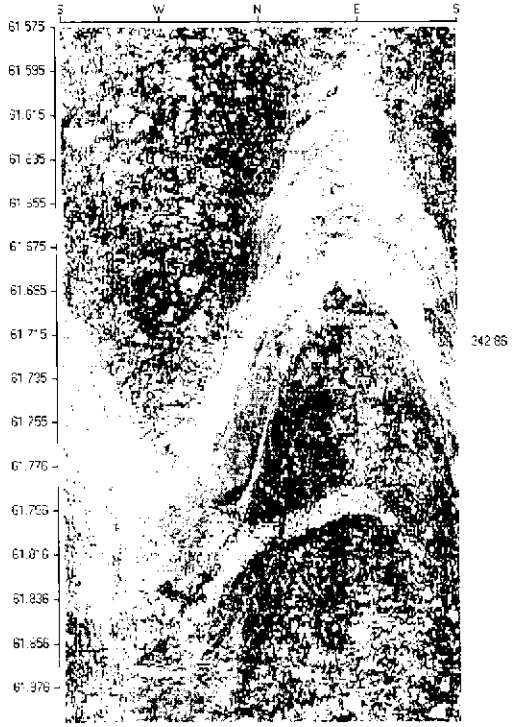

KI0025F
L = 61.8 m (342/86)

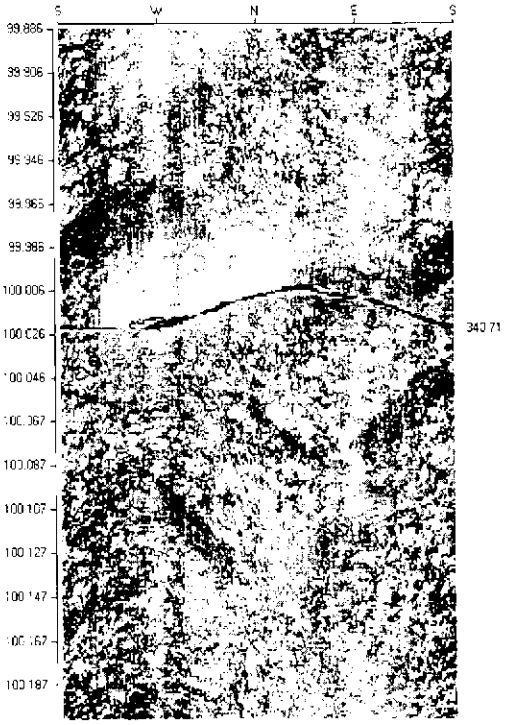

KA2511A
L = 100.1 m (340/71)

Structure #6

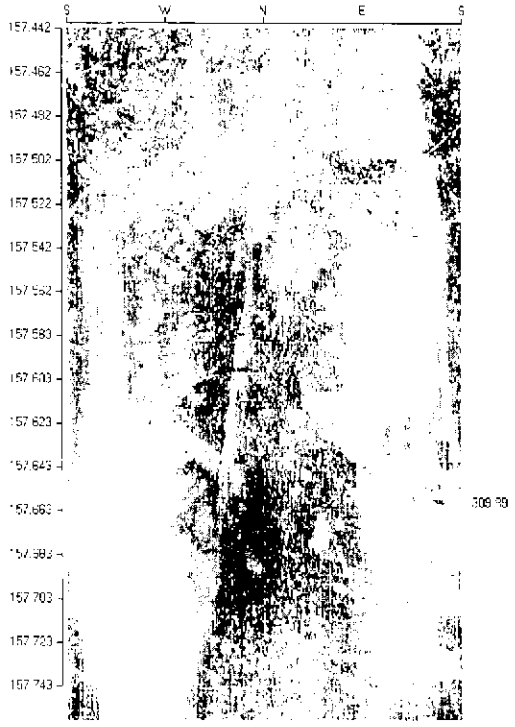

KA2563A
L = 157.2 m (309/89)

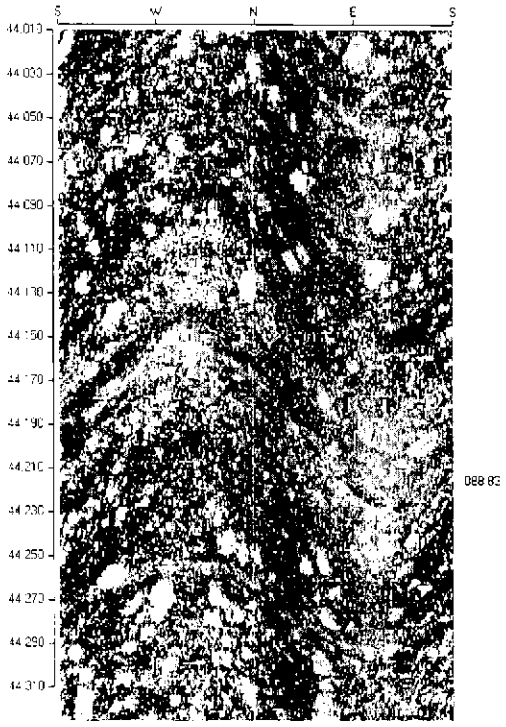

KI0023B
L = 44.2 m (88/83)

Structure #7

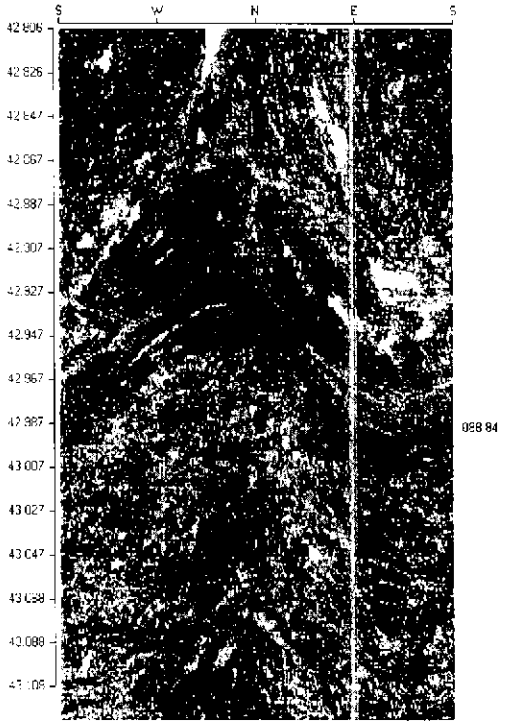

KI0025F03
L = 43.0 m (88/84)

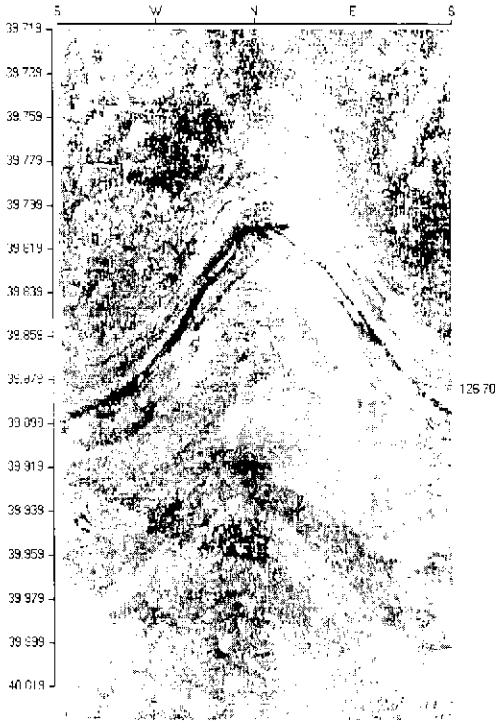

KI0025F02
L = 39.9 m (126/70)

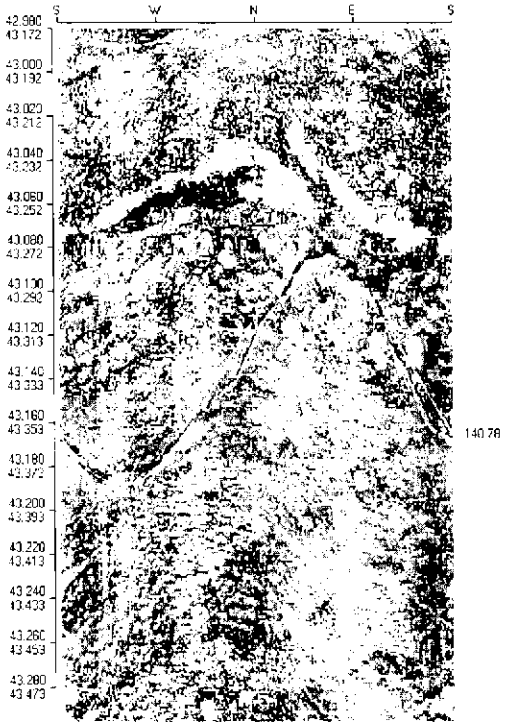

KI0025F
L = 43.2 m (140/78)

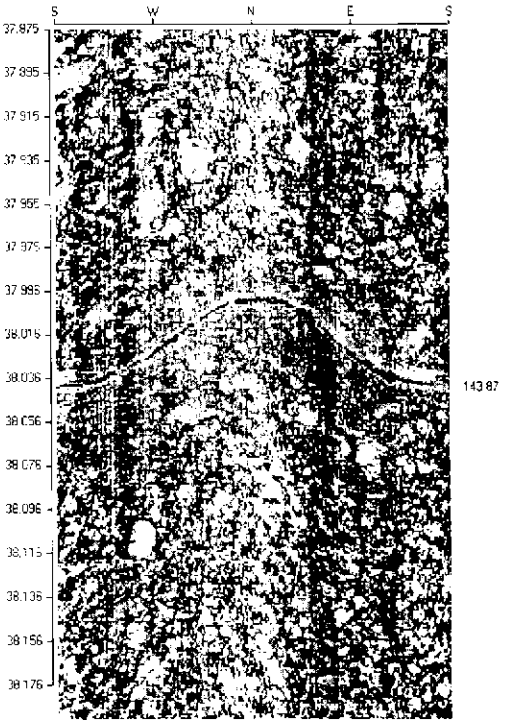

KA2511A
L = 38 m (143/87)

Structure #7

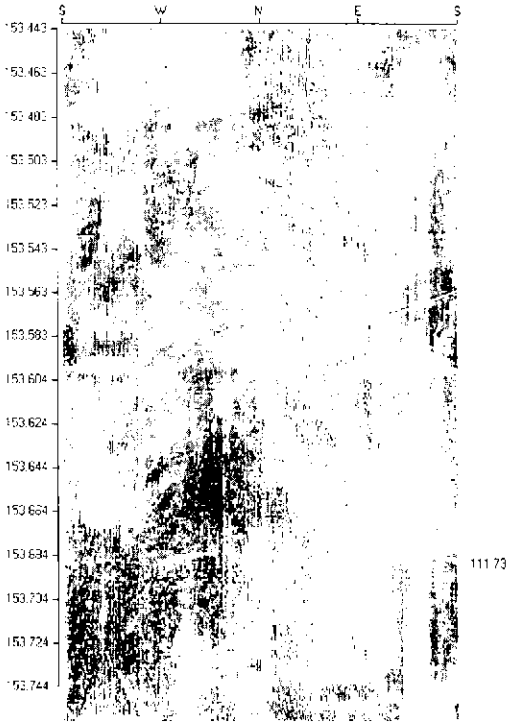

KA2563A
L = 153.4 m (111/73)

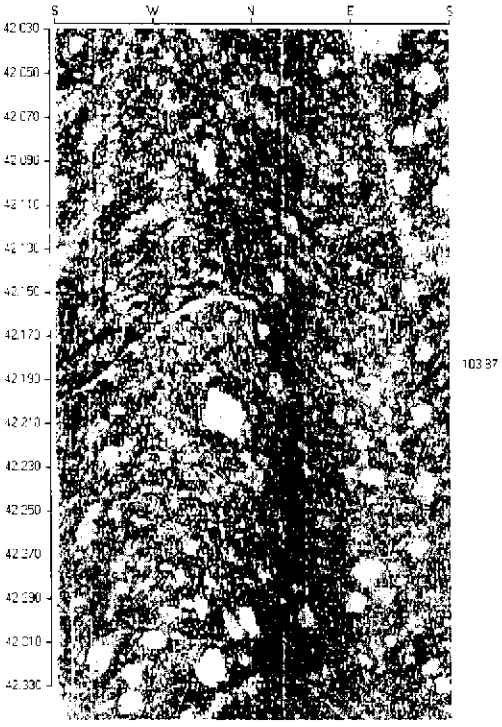

KI0023B
L = 42.2 m (103/87)

Structure #13

KI0025F03
L = 87.5 m (338/87)

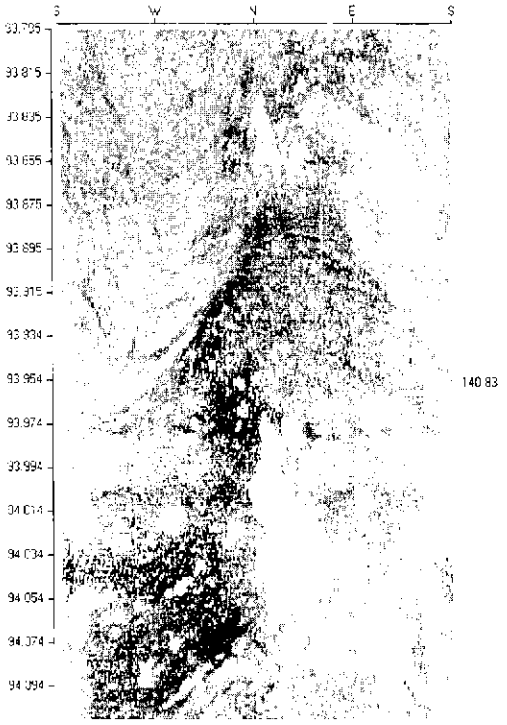

KI0025F02
L = 93.0 m (140/83)

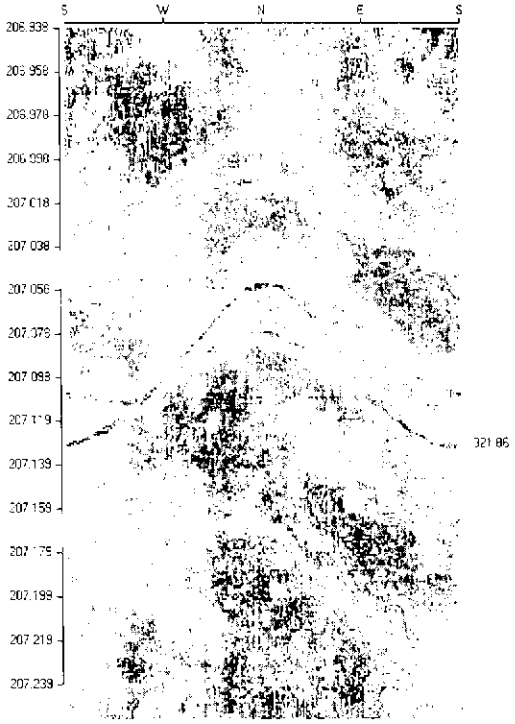

KA2563A
L = 207.0 m (321/86)

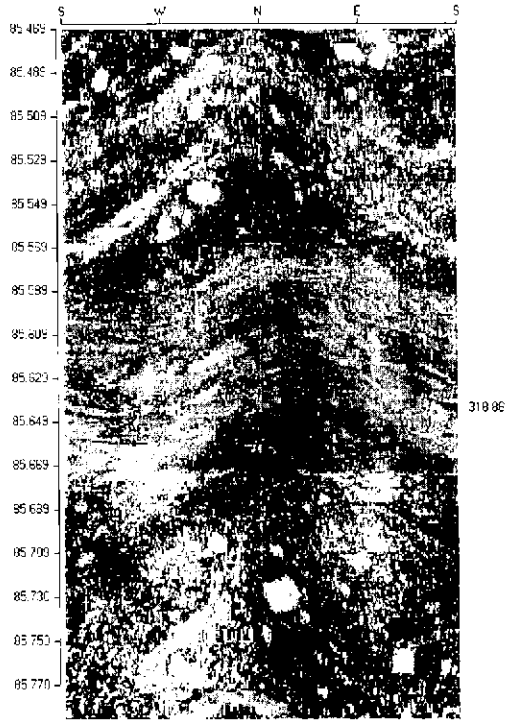

KI0023B
L = 85.6 m (318/89)

Structure #19

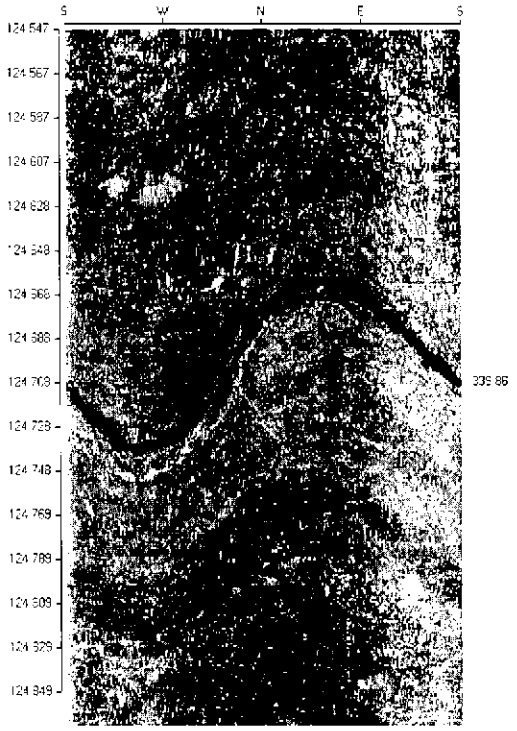

KI0025F03
L = 124.7 m (339/86)

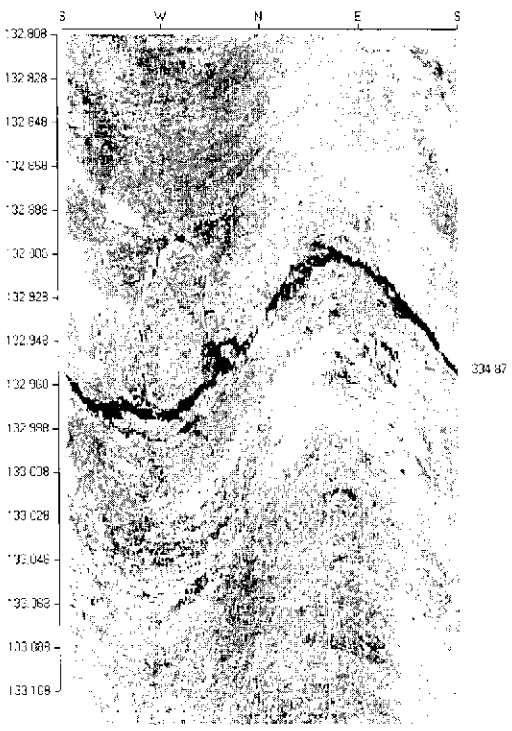

KI0025F02
L = 133.0 m (334/87)

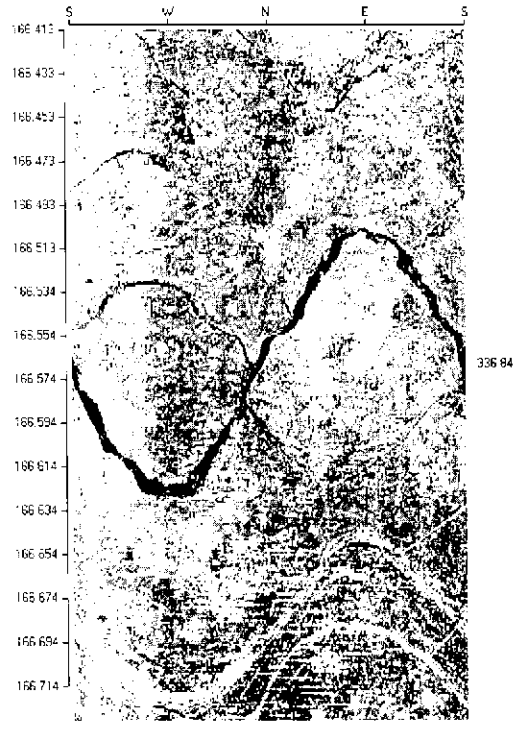

KI0025F
L = 166.4 m (336/84)

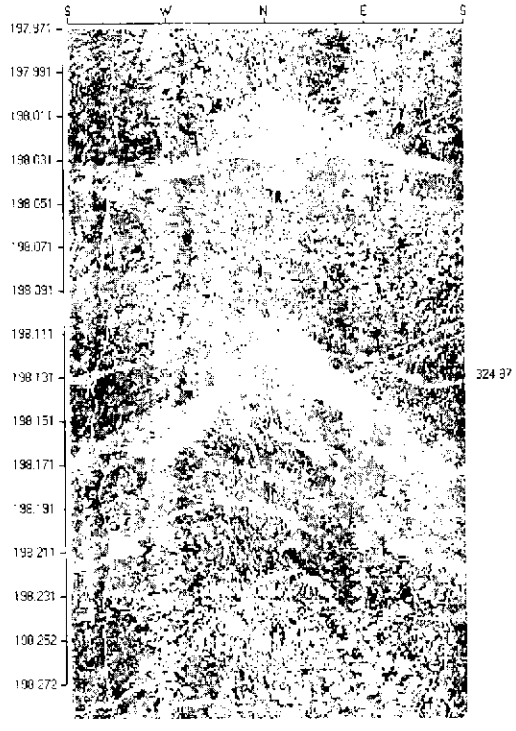

KA2511A
L = 198.2 m (324/87)

Structure #19

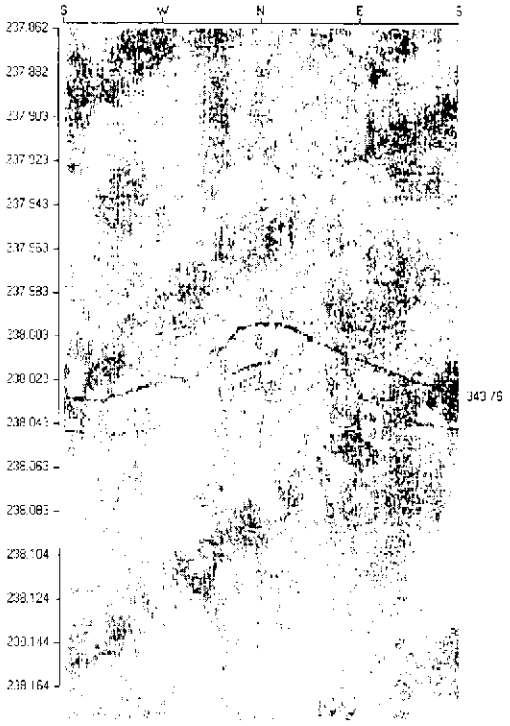

KA2563A
L = 237.9 m (343/76)

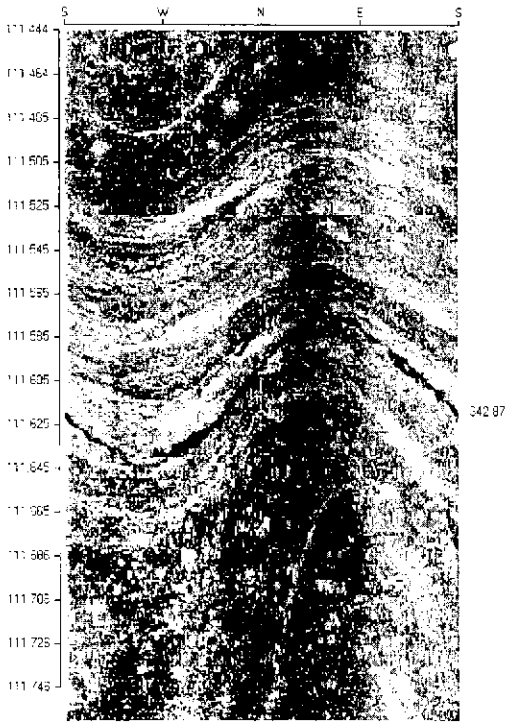

KI0023B
L = 111.6 m (342/87)

Structure #20

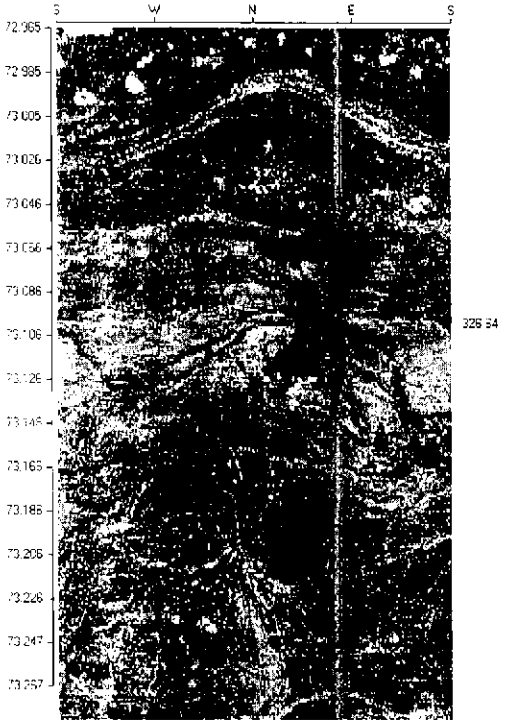

KI0025F03
L = 73.2 m (326/64)

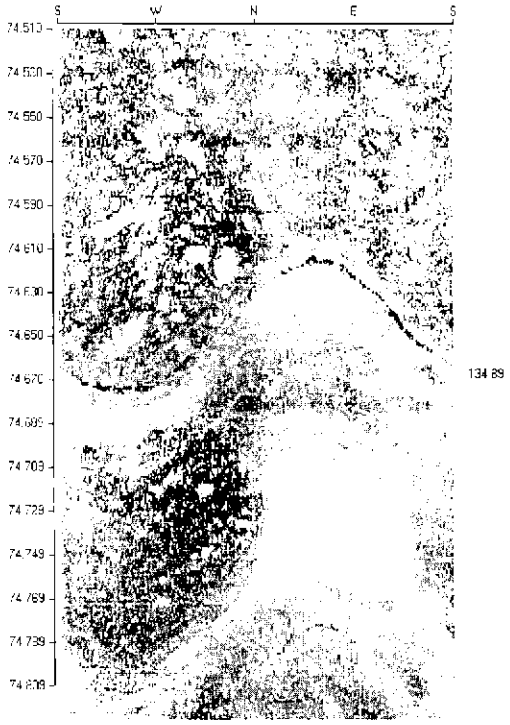

KI0025F02
L = 74.7 m (134/89)

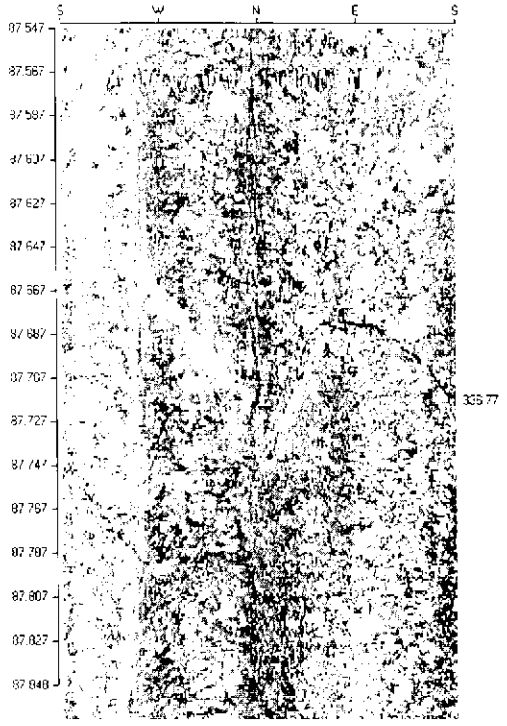

KI0025F
L = 87.7 m (336/77)

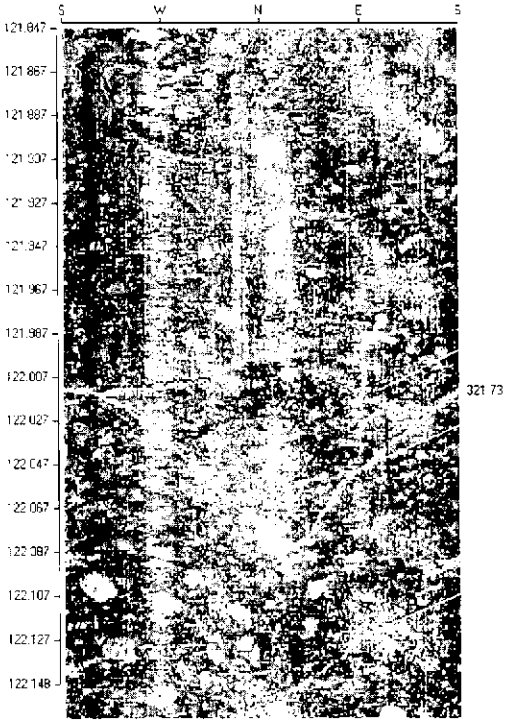

KA2511A
L = 122.0 m (321/73)

Structure #20

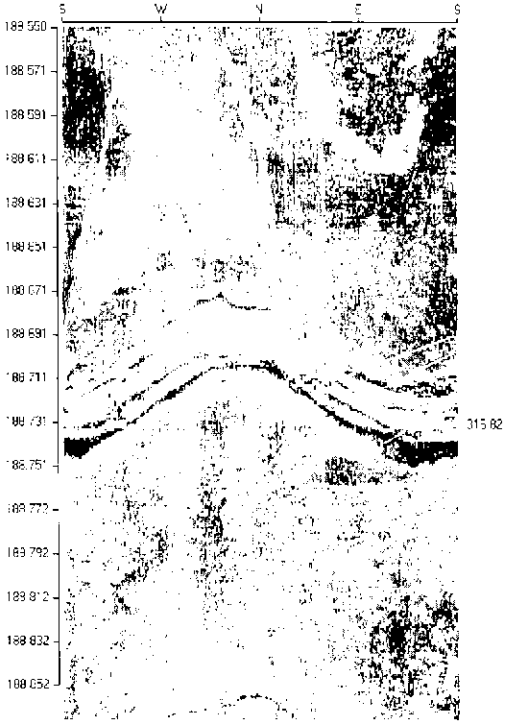

KA2563A
L = 188.7 m (316/82)

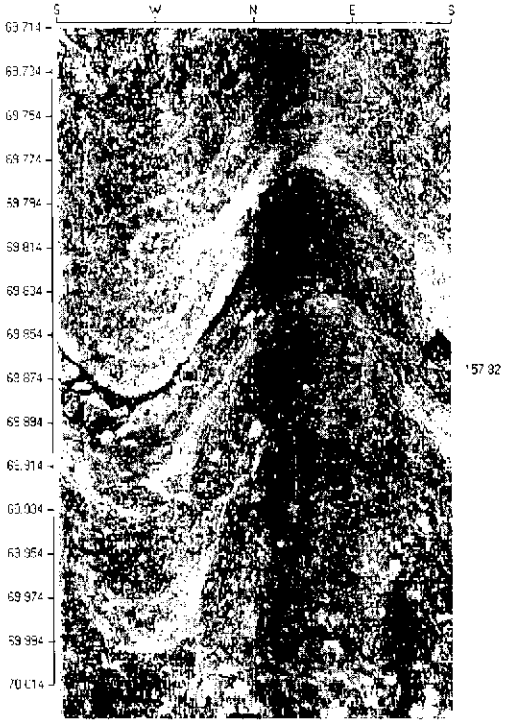

KI0023B
L = 69.8 m (157/82)

Structure #21

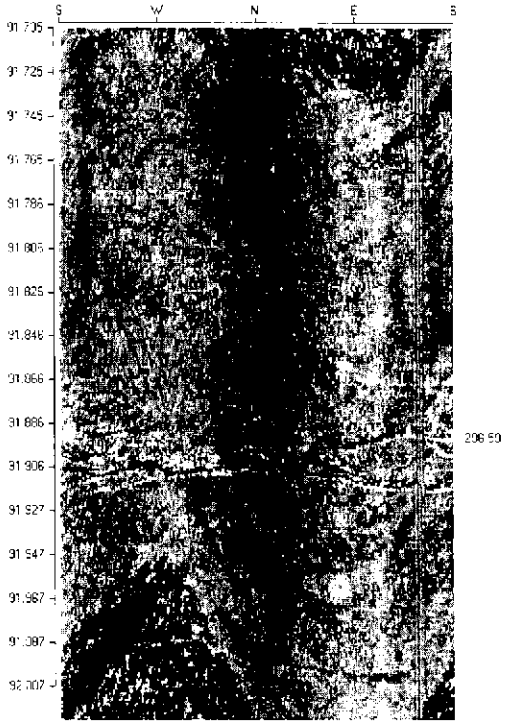

KI0025F03
L = 91.9 m (296/59)

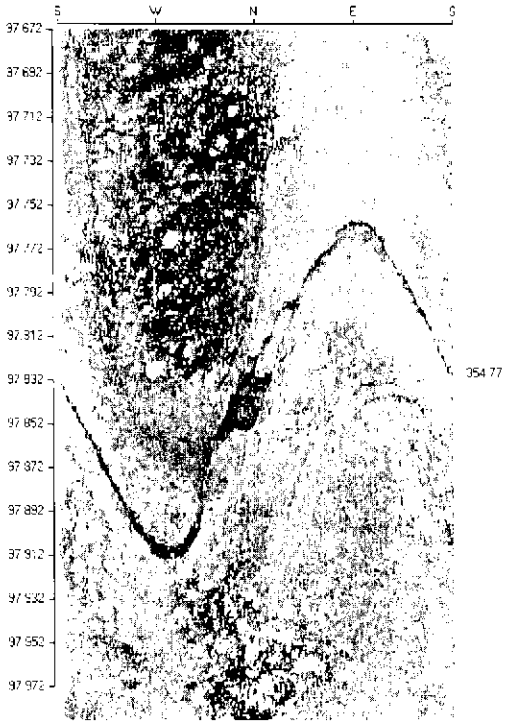

KI0025F02
L = 97.9 m (354/77)

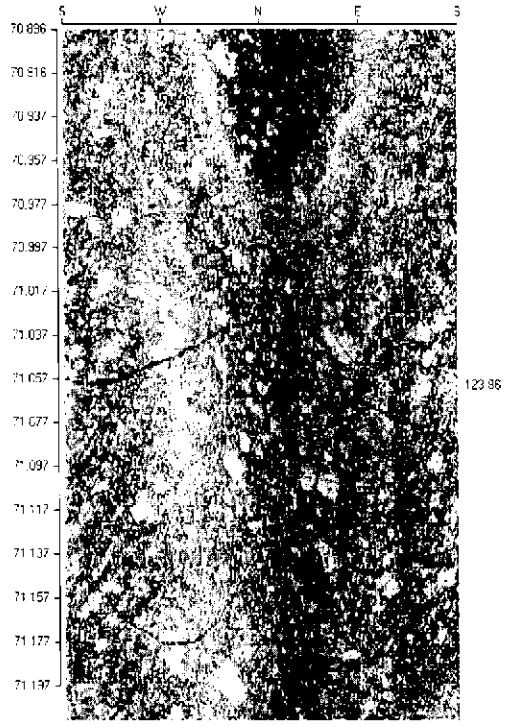

KI0023B
L = 71.1 m (123/86)

Structure #22

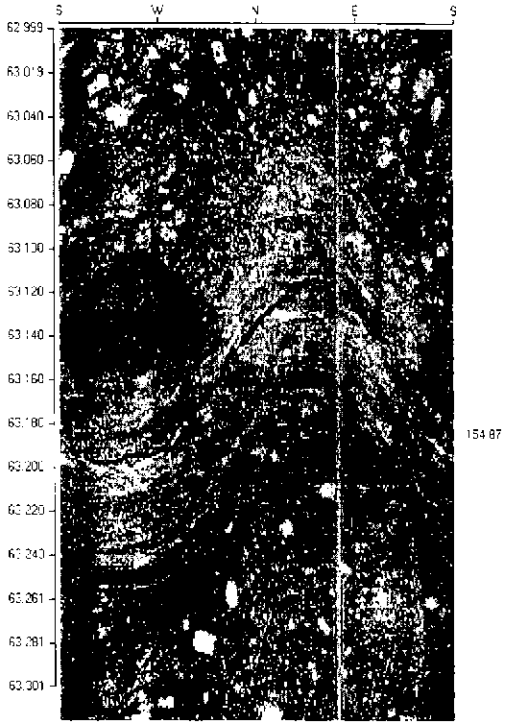

KI0025F03
L = 63.2 m (154/86)

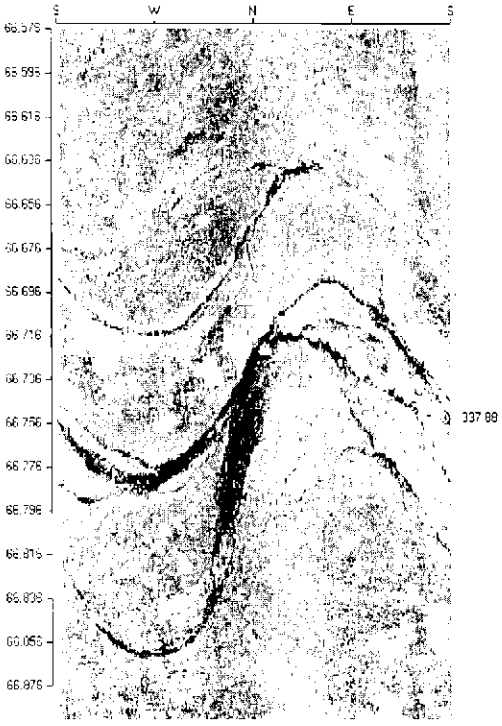

KI0025F02
L = 66.8 m (337/88)

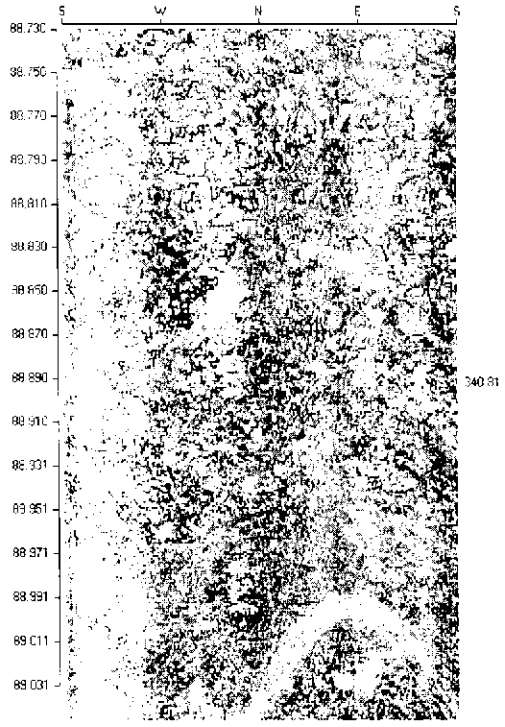

KI0025F
L = 88.8 m (340/81)

Structure in KI0023B

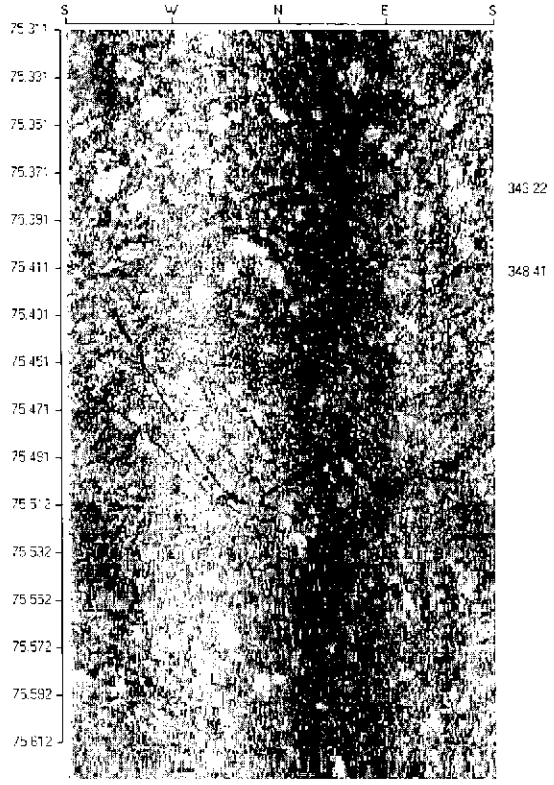

KI0023B
L = 75.5 m (348/41 alt 343/22)

Structure #23

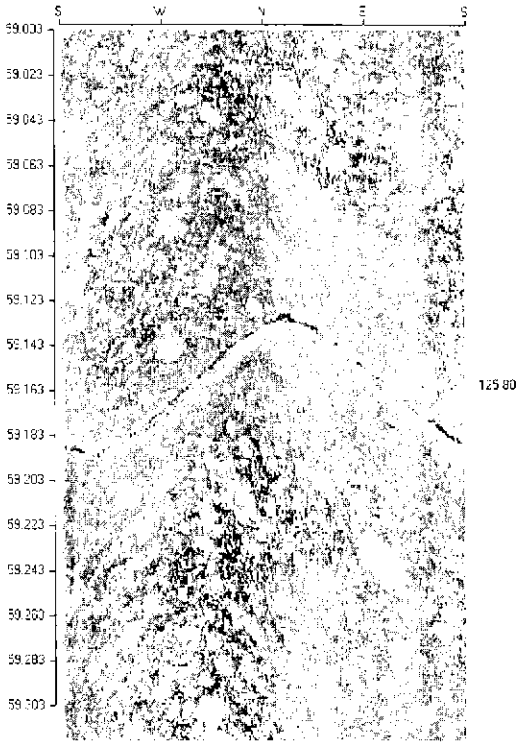

KI0025F02
L = 59.2 m (125/80)

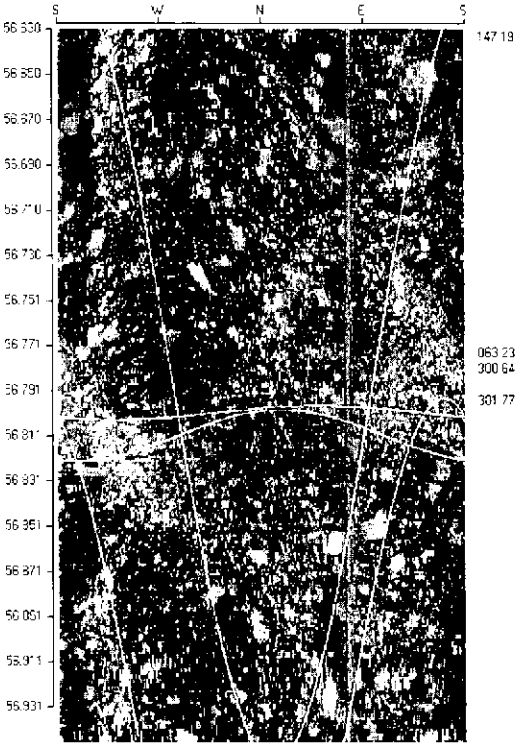

KI0025F03
L= 56.8 m (300/64 alt 301/77)

Structure #24

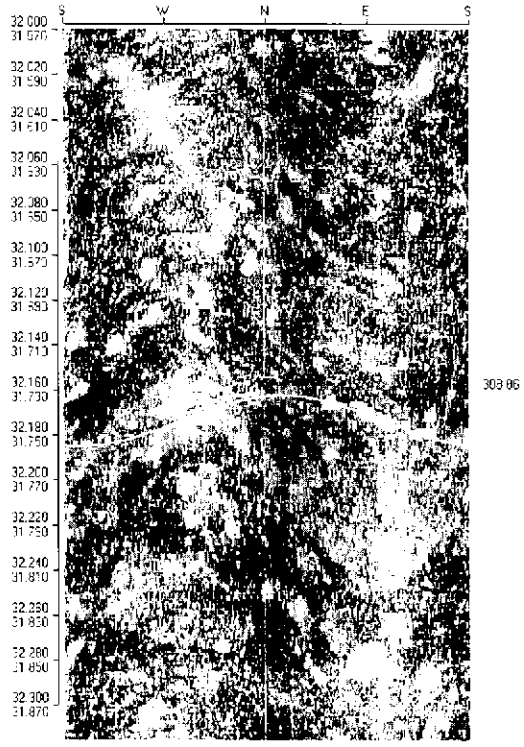

KI0023B
L = 31.75 m (308/76)

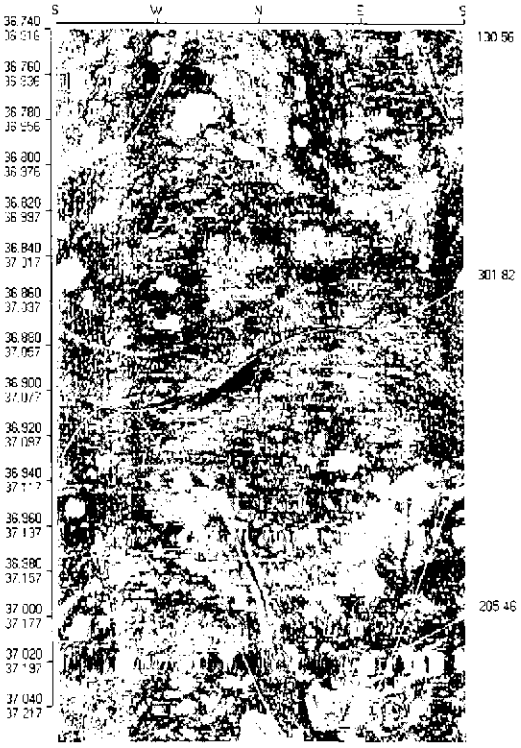

KI0025F
L = 37.1 m (301/82)

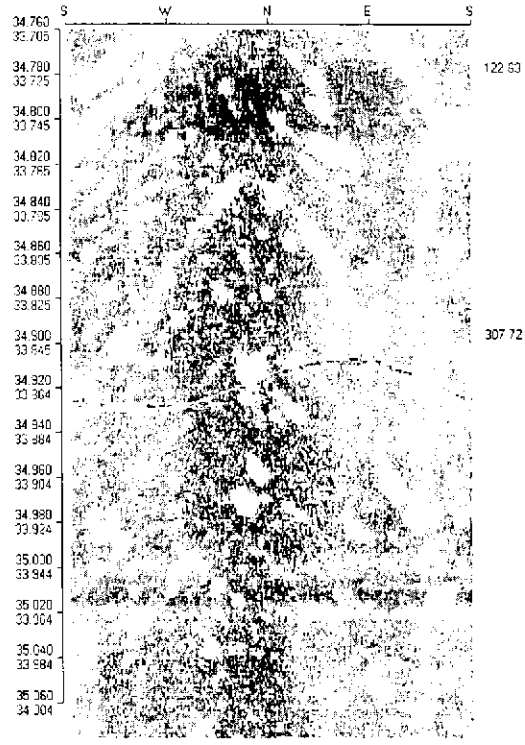

KI0025F02
L = 33.9 m (307/72)

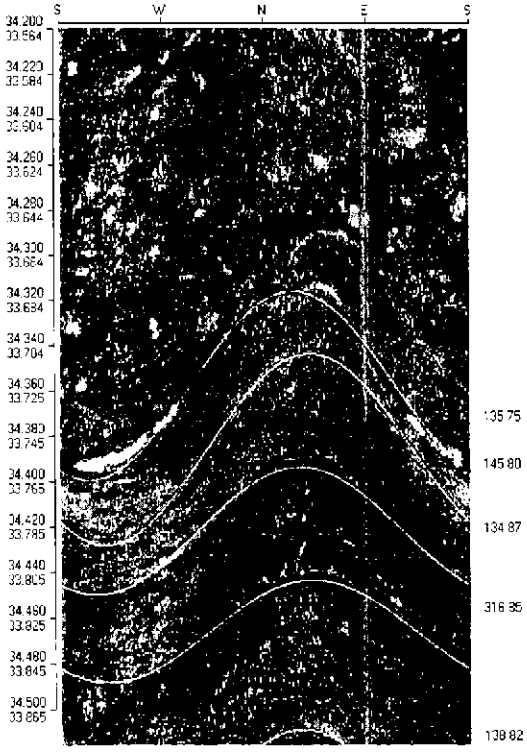

KI0025F03
L = 33.76 m (135/75)

Appendix C Supplementary Figures

Appendix C- 1 KA2563 pressure responses to KI0025F03 drilling

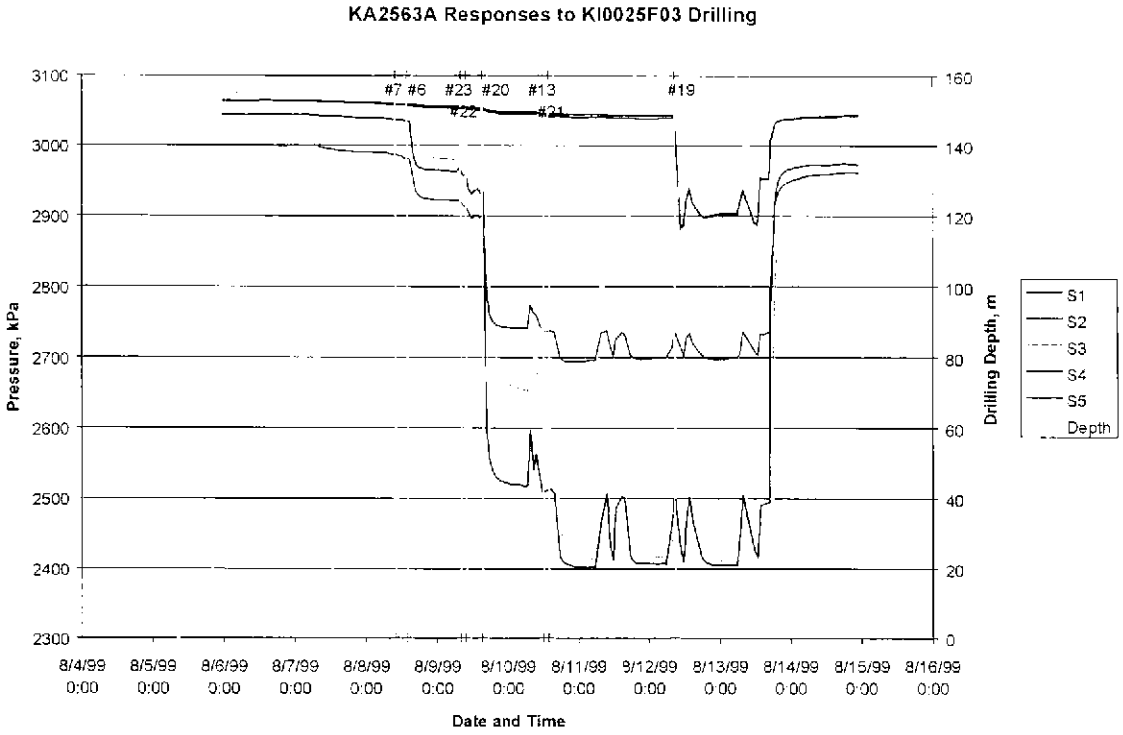

Appendix C- 2 KI0023B pressure responses to KI0025F03 drilling

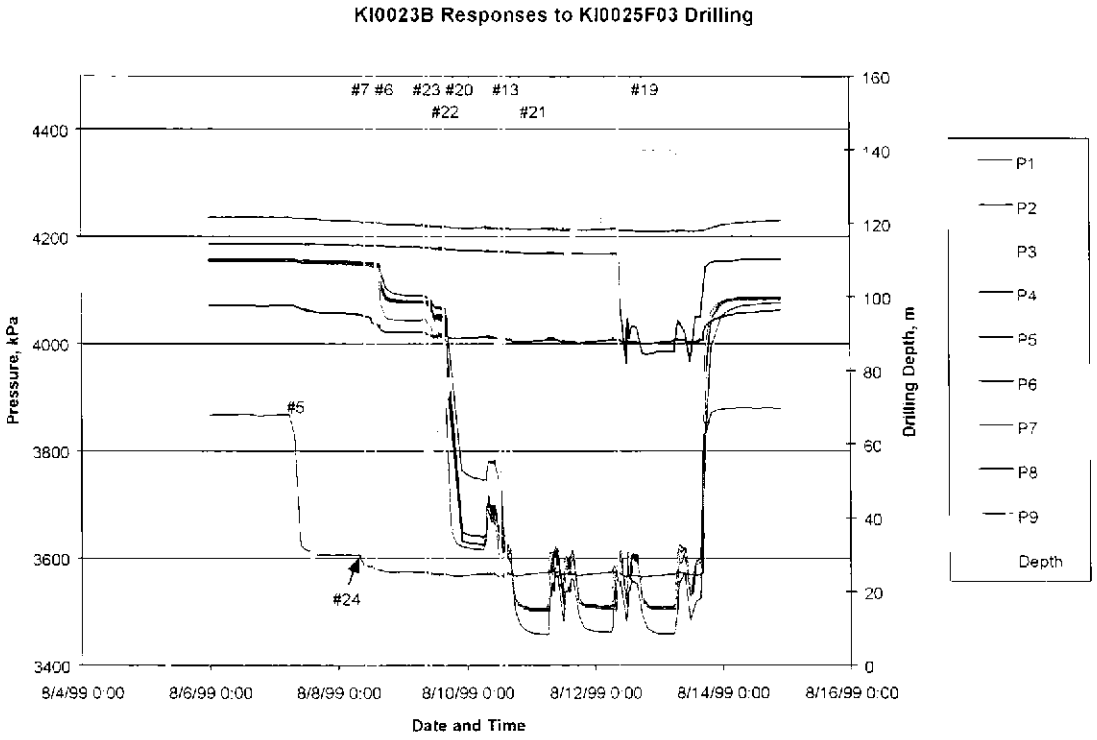

Appendix C- 3 KI0025F02 responses to KI0025F03 drilling

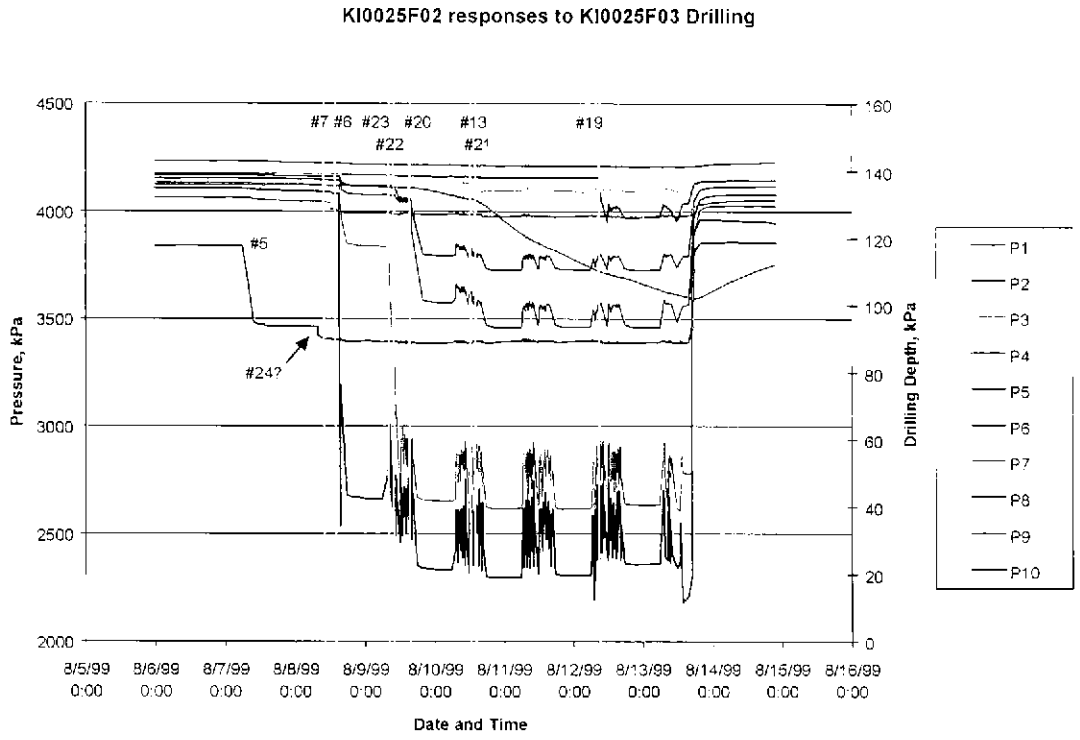

Appendix C- 4 KI0025F Responses to KI0025F03 drilling

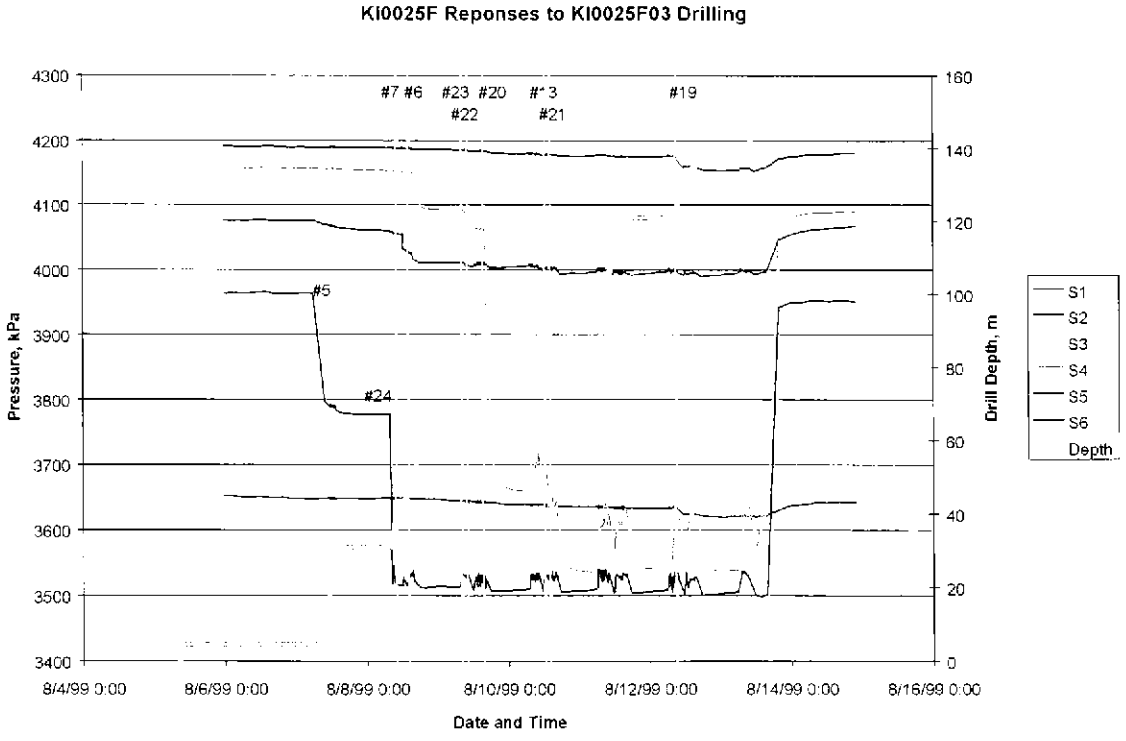

Appendix C- 5 Structure #6 in-plane map

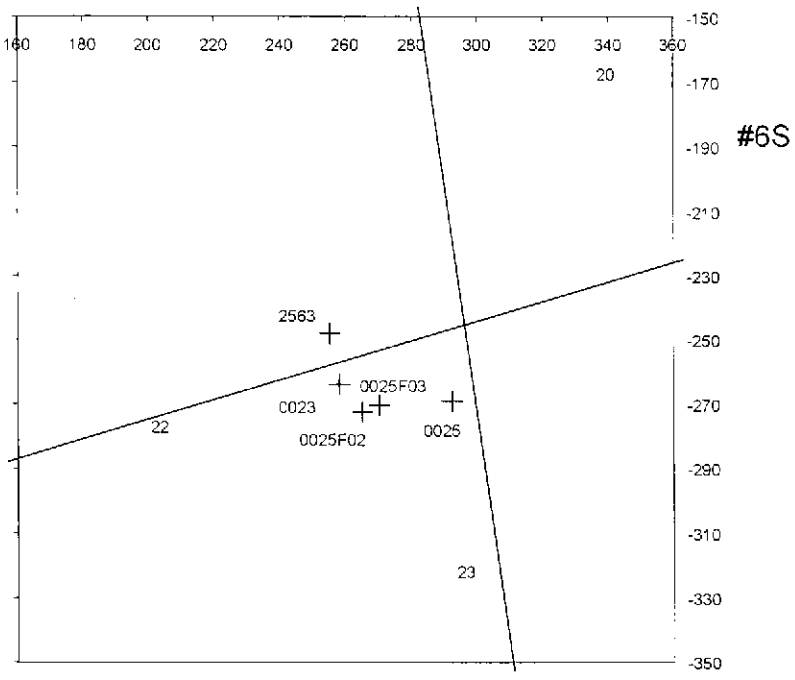

Appendix C- 6 Structure #23 in-plane map.

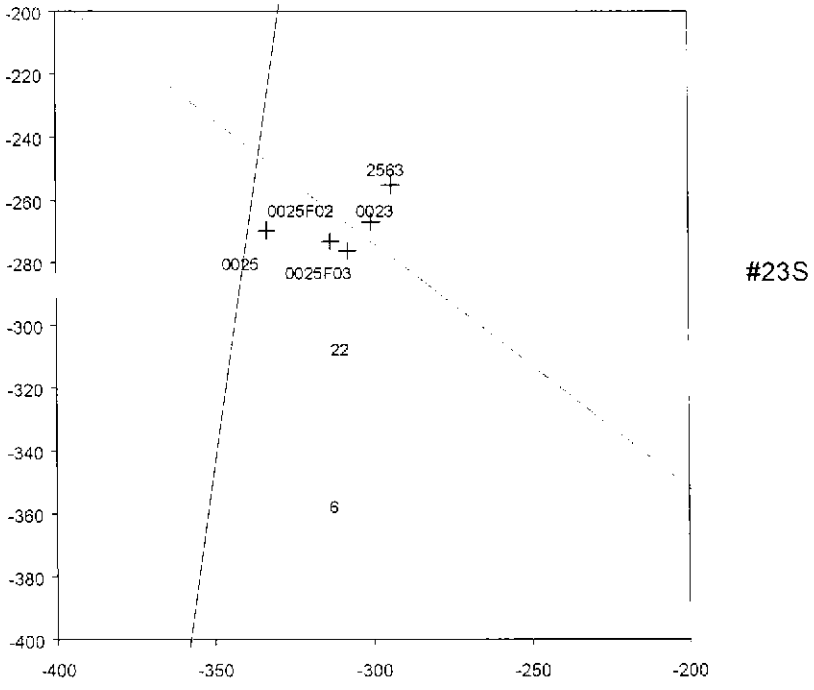

Appendix C- 7 Structure #22 in-plane map

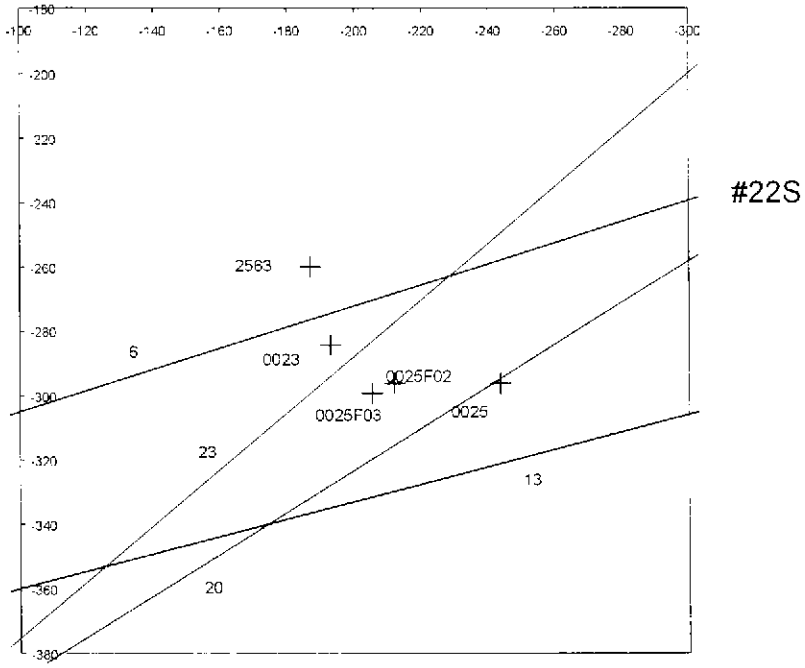

Appendix C- 8 Structure #20 in-plane map

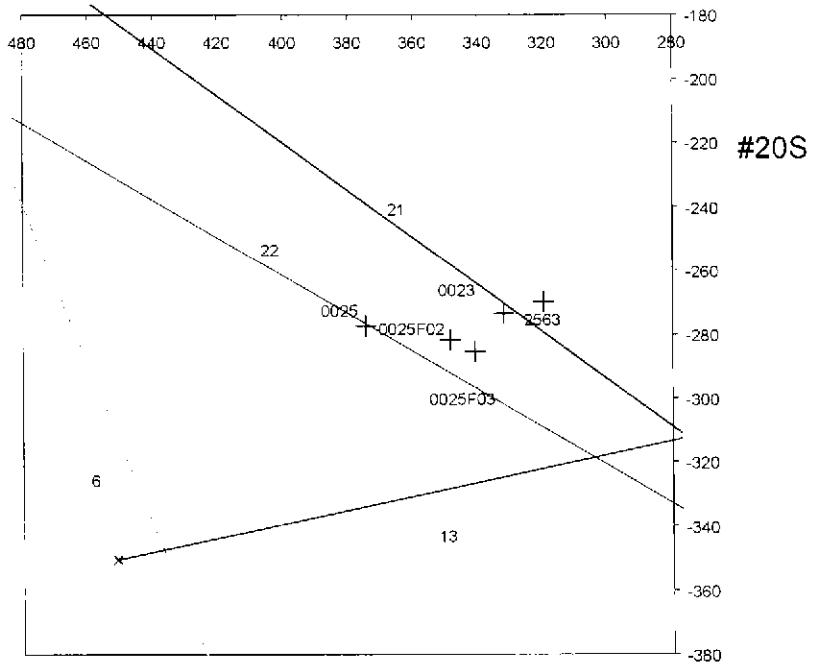

Appendix C- 9 Structure #13 in-plane map

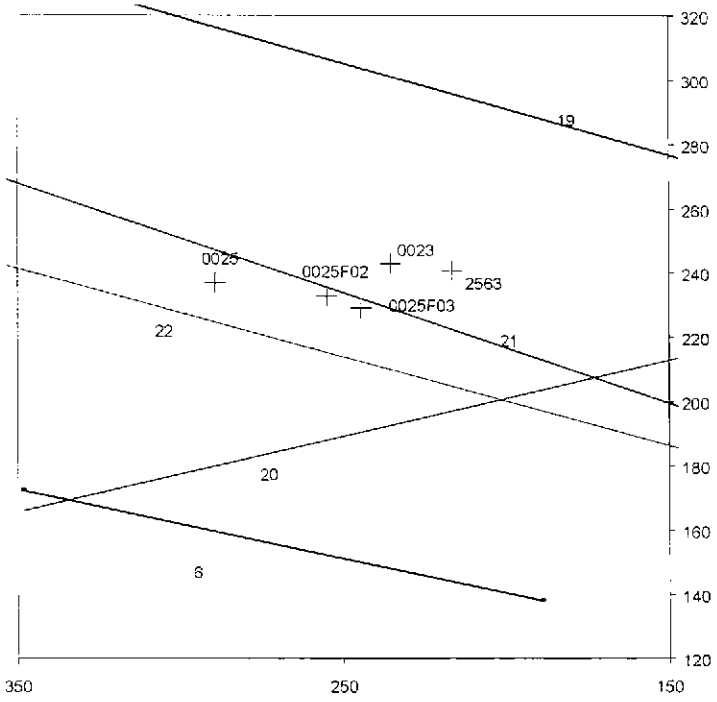

#13S

Appendix C- 10 Structure #21 in-plane map

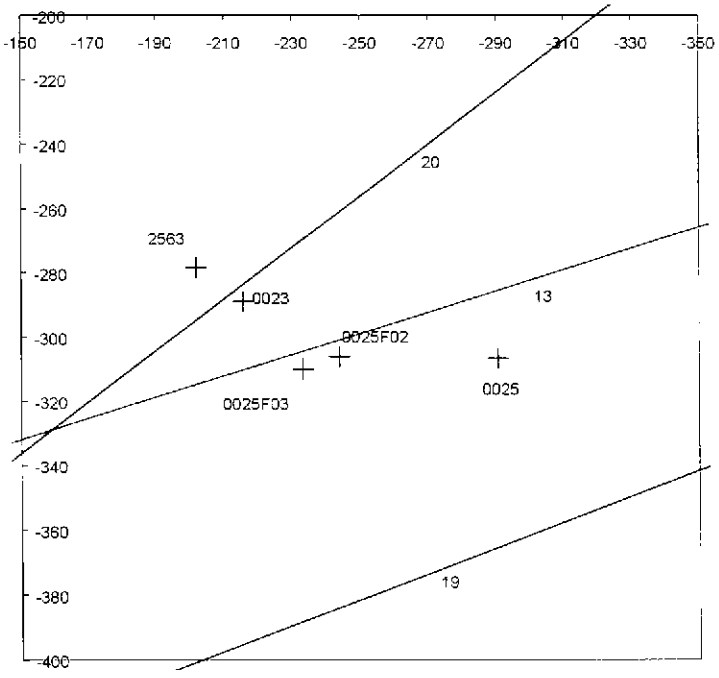

#21S

Appendix C- 11 Structure #19 in-plane map

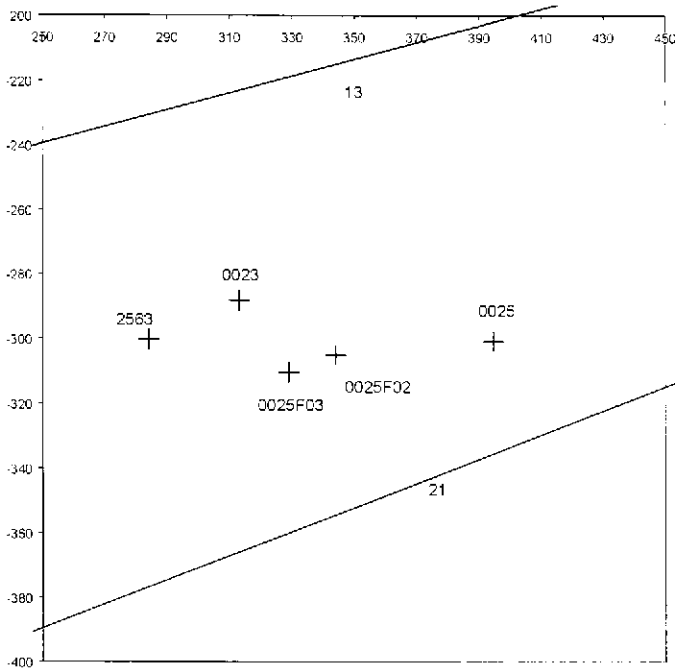

#19S

APPENDIX C

FRACMAN MODELING OF GEOCHEMICAL END-MEMBER TRANSPORT PATHWAYS ÄSPÖ HARD ROCK LABORATORY ÄSPÖ, SWEDEN, TASK 5

FRACMAN MODELLING OF GEOCHEMICAL END-MEMBER TRANSPORT PATHWAYS ÄSPÖ HARD ROCK LABORATORY, ÄSPÖ SWEDEN TASK 5

Dawn Shuttle, Golder
Bill Dershowitz, Golder
Masahiro Uchida, JNC
Richard Metcalfe, JNC-Tono
Mark Cave, BGS

November 2000

Keywords: Discrete Fracture Modelling, Groundwater Flow, Solute Transport, Coupled Hydrogeochemistry, Pathways Analysis, Äspö, Task 5

ABSTRACT

This report describes the participation of the JNC/Golder team in the coupled hydrogeological/geochemical pathway modeling of the construction of the Äspö Hard Rock Laboratory during the period 1990 through 1996. Modeling was carried out to the specifications of the Äspö Task Force on Modeling of Groundwater Flow and Transport of Solutes, Task 5.

The modeling was carried out using the discrete feature network/channel network approach (DFN/CN). In this approach, both major deterministic fracture zones and background fracturing was modeled explicitly as two-dimensional discrete features using FracMan/FracWorks. Deterministic fracture zones were based on the zone specifications of Rhén (1999), with the addition of a northwest trending feature to explain the step drawdown responses observed during shaft construction.

Flow and transport were modeled by transforming the fracture network to a topologically equivalent pipe network using FracMan/PAWorks.

The purpose of the modeling was to demonstrate the value of geochemical data for construction and validation of hydrogeological and pathway models. This investigation was undertaken in three separate stages.

- Stage 1: Calibrate and Predict Based on Hydrological Data Only (Results Presented 4/99);
- Stage 1.5: Improve the Calibration and Prediction for Stage 1 Based on Hydrological Data Only (10/99);
- Stage 2: Update based on Geochemical Data, Repeat Predictions (10/99); and
- Stage 3: Complementary Analysis to Address Uncertainty Issues (11/00).

The modeling approach was updated during the project. For Stages 1 and 2 hydrological and geochemical initial conditions for the model were provided by Rhén (1998). The transport calculations were made using transport pathways defined by graph theory searches through the channel network model. Flow velocities were adjusted to account for the effect of salinity on density and flow (Bear, 1972). The salinity-adjusted transport was expressed in terms of travel times and proportions of four geochemical end member water compositions: meteoric, glacial, marine, and brine. These compositions of end-members were calculated by SKB using the computer code Multivariate Mixing and Mass balance, referred to as M3 in this document (Rhén et al. 1997; Laaksoharju, 1999a; Laaksoharju et al. 1999b). These compositions and mixing proportions were presented in Data Delivery 19, released by SKB on 15th December 1999 (delivery reference

F65H). Oxygen-18 and chloride were back calculated from the geochemical end members. The modeled period was from 1990 through 1996.

For Stage 3 of the Task 5 modeling, two major changes were adopted. Firstly, the geochemical initial conditions for the model were adapted to enable consideration of all the chemical variability in the measured data. Several possible alternative combinations of input data were considered, in addition to the data used in the original M3 modeling. The second change was that the methodology for finding the source locations of the water types was changed from a graph theory search to a particle tracking approach. The latter provides a more accurate measure of the proportion of mass originating in a given location.

The stages of the modeling process achieved differing levels of success. The purely hydrogeological models constructed in Stages 1 and 1.5 were very successful in matching the head distribution, but did not provide optimum geochemical predictions. These data provided sufficient information to predict the likely existence of the additional "mystery" feature.

The Stage 2 geochemical calibration resulted in both lower head and geochemical error measures. These analyses, using the M3 chemistry and the original pathway algorithm, involved additional changes to the boundary conditions and connectivity. Many of these changes were subsequently seen to be the result of a poor geochemical conceptual model. The deficiencies of the pathway-tracking algorithm compounded the required changes.

However, the most interesting results from the modeling occurred during the Stage 3 analysis. This model used an improved chemistry model and pathways algorithm, but was only run using the hydrogeologically calibrated fracture model and boundary conditions. Fits between the measured and modeled chemistry were very good: the deficiencies primarily being related to travel velocities, not spatial location. The results from this set of simulations indicate that for a large modeled region the initial geochemical spatial variation used in the model is very important.

In conclusion, the authors believe that the specific objectives of Task 5 were met. The first objective, "to assess the consistency of groundwater flow models and hydrochemical mixing-reaction models through the integration and comparison of hydraulic and hydrochemical data obtained before, during and after tunnel construction" was addressed. The model derived from purely hydrogeological considerations was adequate for determining the major connectivity of the system. However, the geochemical response was strongly influenced by the geochemical interpretation and optimization required additional calibration. The use of geochemical data was also required to calibrate the model aperture and storage parameters.

The second Task 5 objective, "to develop a procedure for integration of hydrological and hydrochemical information which could be used for assessment of potential repository sites" is discussed in detail in

Sections 5-5 and 6. The approach is based on sequential use of hydrogeological and geochemical data. Based on the Task 5 modeling of the Äspö site this approach worked well. It was found that the calibration to measured heads provided a reasonable calibration to the general water sources, but that the travel velocity was poorly predicted. The chemistry data provided a data set from which to refine these velocities. Chemistry data also reduced the non-uniqueness of the system.

TABLE OF CONTENTS

LIST OF FIGURES

LIST OF TABLES

EXECUTIVE SUMMARY

This report describes the participation of the JNC/Golder team is coupled hydrogeological/geochemical pathway modeling of the construction of the Äspö Hard Rock Laboratory during the period 1990 through 1996. Modeling was carried out to the specifications of the Äspö Task Force on Modeling of Groundwater Flow and Transport of Solutes, Task 5. In order to demonstrate the value of geochemical data in hydrogeological modeling, models were calibrated separately to hydrogeological data and geochemical data. Both of these calibrated models were then used in predictive simulations.

Following these simulations an additional set of complimentary analyses were undertaken to address issues of uncertainty related to the geochemical methodology. Concurrently, the algorithm used to compute the source locations of the waters infiltrating into the tunnels was improved.

The modeling was carried out using the discrete feature network/channel network approach (DFN/CN). In this approach, both major deterministic fracture zones and background fracturing was modeled explicitly as two-dimensional discrete features using FracMan/FracWorks. Deterministic fracture zones were based on the zone specifications of Rhén (1999), with the addition of a northwest trending feature to explain the step drawdown responses observed during shaft construction.

Flow and transport were modeled by transforming the fracture network to a topologically equivalent pipe network using FracMan/PAWorks.

For the main simulations hydrological and geochemical initial conditions for the model were provided by SKB. All transport calculations were made using transport pathways defined by graph theory searches through the channel network model. The flow velocities were adjusted to account for the effect of salinity on density and flow (Bear, 1972). This density-corrected transport was expressed in terms of travel times and proportions of four geochemical end member water geochemistries: meteoric, glacial, marine, and brine. Oxygen-18 and chloride were back calculated from the geochemical end members. The modeled period was from 1990 through 1996.

For the additional complimentary Task 5 analyses, two major changes were adopted. Firstly, the geochemical initial conditions for the model were adapted to enable consideration of all the chemical variability in the measured data. Several possible alternative combinations of input data were considered. The second change was that the methodology for finding the source locations of the water types was changed from a graph theory search

to a particle tracking approach. The latter provides a more accurate measure of the proportion of mass originating in a given location.

The three stages of the modeling process achieved differing levels of success. The purely hydrogeological model constructed in Stage 1 was very successful in matching the head distribution, but did not provide optimum geochemical predictions.

The Stage 2 geochemical calibration, using the M3 chemistry and the original pathway algorithm, involved additional changes to the boundary conditions and connectivity. In particular the geochemical data provided information on model where the model required additional/lower connectivity. The addition of geochemical information resulted in both lower head and geochemical error measures.

However, the most interesting results from the modeling occurred during the Stage 3 analysis. This model used an improved chemistry model and pathways algorithm, but was only run using the hydrogeologically calibrated fracture model and boundary conditions. Fits between the measured and modeled chemistry were very good: the deficiencies primarily being related to travel velocities, not spatial location. The results from this set of simulations indicate that for a large modeled region the initial geochemical spatial variation used in the model is very important.

In conclusion, the authors believe that the specific objectives of Task 5 were met. The first objective, "to assess the consistency of groundwater flow models and hydrochemical mixing-reaction models through the integration and comparison of hydraulic and hydrochemical data obtained before, during and after tunnel construction" was addressed. The model derived from purely hydrogeological considerations was adequate for determining the major connectivity of the system. However, the geochemical response was strongly influenced by the geochemical interpretation and optimization required additional calibration. The use of a geochemical conceptual model improved the geochemical interpretation. The use of geochemical data was also required to calibrate the model aperture and storage parameters.

The second Task 5 objective, "to develop a procedure for integration of hydrological and hydrochemical information which could be used for assessment of potential repository sites" is discussed in detail in Section 5-5 and 6. The approach is based on sequential use of the hydrogeological and geochemical data. The phases could be summarized as:

- Develop a regional model of the site including only the large scale features
- Develop a conceptual model for the background fractures. For a DFN idealization this included the orientation, size, intensity, and transmissivity of the non-regional features.
- Develop boundary conditions for the modeled region.
- Create a finite element model including the major features, background features, and boundary conditions. Calibrate this model to the measured

head distribution by varying the fracture properties and boundary conditions.

- Use this calibrated model to predict chemistry distributions. Calibrate this model to the measured chemistry and head distribution by varying the fracture properties and boundary conditions.

Based on the Task 5 modeling of the Äspö site this approach worked well. It was found that the calibration to measured heads provided a reasonable calibration to the general water sources, but that the travel velocity was poorly predicted. The chemistry data provided a data set from which to refine these velocities. Chemistry data also reduced the non-uniqueness of the system.

It should be noted, however, that the goodness-of-fits achieved were also sensitive to the methodology used to compute the geochemical distribution across the site. The hydrogeology and the geology at the Äspö site are consistent with the major features dominating mixing and flows. Therefore it was necessary to distribute chemistry based on the major features, rather than assuming a continuum. The strong influence of the Baltic / Äspö Island boundary on the chemistry also markedly affected the interpretation. For a different site, this means that the modelers would need to ascertain the structures, geology and/or major processes affecting the chemistry prior to setting up the geochemical spatial distribution. Similarly, the interpretation scheme should also account for the hydrogeological conditions.

1. INTRODUCTION

This report describes the participation of the JNC/Golder team in coupled hydrogeological/geochemical pathway modeling of the construction of the Äspö Hard Rock Laboratory during the period 1990 through 1996. Modeling was carried out to the specifications of the Äspö Task Force on Modeling of Groundwater Flow and Transport of Solutes, Task 5 during the period June through October 1999.

The aim of Task 5 is to compare, and ultimately integrate, site scale hydrogeology and hydrochemistry by evaluating the large scale groundwater flow pathways activated by construction of the Äspö tunnels (Wikberg, 1998). This integration is expected to benefit underground radioactive waste repository performance assessment by providing a better understanding of transport pathways at the site scale.

JNC/Golder has defined an additional goal for this task, to demonstrate quantitatively the value of geochemical data for hydrogeological model development. In order to meet this goal, JNC/Golder carried out model calibration and prediction in three stages.

In the first stage, we developed and calibrated a model based solely on hydrogeological data, and used this model to predict end-member geochemical breakthroughs to predictive points defined by Rhén et al. (1998). In the second stage, this model was refined using geochemical data, and a second prediction was made. It is hoped that comparison of these two predictive stages will provide quantitative support to the increased use of geochemical data in hydrogeological modeling.

In the third stage additional complementary analyses were undertaken to address uncertainty issues. Uncertainty exists in the interpretation of the initial spatial variation of chemical compositions. Therefore the initial conditions for the geochemical model were adapted to enable consideration of all the chemical variability in the measured data. Additionally the methodology for finding the source locations of the water types was changed from a graph theory search to a particle tracking approach. The latter provides a more accurate measure of the proportion of mass originating in a given location.

These three stages are documented in the following reports:
- Approaches, Algorithms, and Demonstration Report Dated 12/98;
- Hydrological and Geochemical Calibrations and Predictions Report Dated 12/99;
- Complementary Analysis to Address Uncertainty Issues Report Dated 12/00 (current report).

This report is organized as follows: Chapter 2 describes the hydrogeological model used by the JNC/Golder team. Phase 1 (hydrogeological) model calibration and prediction are presented in Chapter 3. Chapter 4 presents Phase 2 (geochemical) model calibration and prediction. The modeling and analysis approaches used for Task 5 by the JNC/Golder team is described in a companion report, Dershowitz et al. (1998a). The additional complementary analyses undertaken to address uncertainty issues are described in Section 5.

2. HYDROGEOLOGICAL/PATHWAY MODEL

This section describes the initial hydrogeological model used for the calibrations and modeling presented in this report. Variants to this model for model calibration and prediction are described in Chapters 3 and 4. Additional variants related to Stage 3 uncertainty issues are described in Section 5.

2.1 DISCRETE FEATURES

The Task 5 modeling region is 2 km by 2 km, with a depth of 1 km (Figure 2-1). This scale was selected to include the Äspö tunnels and extend the boundaries as far as possible given computation time constraints. The structural model used for these analyses is based on the discrete fracture network (DFN) approach, in which all fluid storage, flow, and transport occurs through a limited subset of "conductive structures" represented by polygonal plates. The DFN approach assumes that there is no advective flow in the matrix. In the Task 5 implementation of the DFN approach the majority of fluid measured at the monitoring borehole locations was assumed to have originated in the fractures (not matrix). Hence any effect of matrix storage was accounted for implicitly in the fracture storativity values.

Task 5 is based on SKB's "SR-97" geological/structural model for Äspö Island. This model (Rhén et al., 1997) was distributed to modeling teams as a Task 5 data delivery. The Task 5 structural model is illustrated in Figure 2-2. Dershowitz et al. (1998) used an earlier version of this structural model, which may explain some of the differences between the results of the current and previous JNC/Golder Task 5 modeling. In addition, while Dershowitz et al. (1998) simulations generally used only the deterministic structural features, the current modeling includes a stochastic background fracture model. Background fracturing included in the current model is illustrated in Figure 2-3.

The model is summarized in Table 2-1.

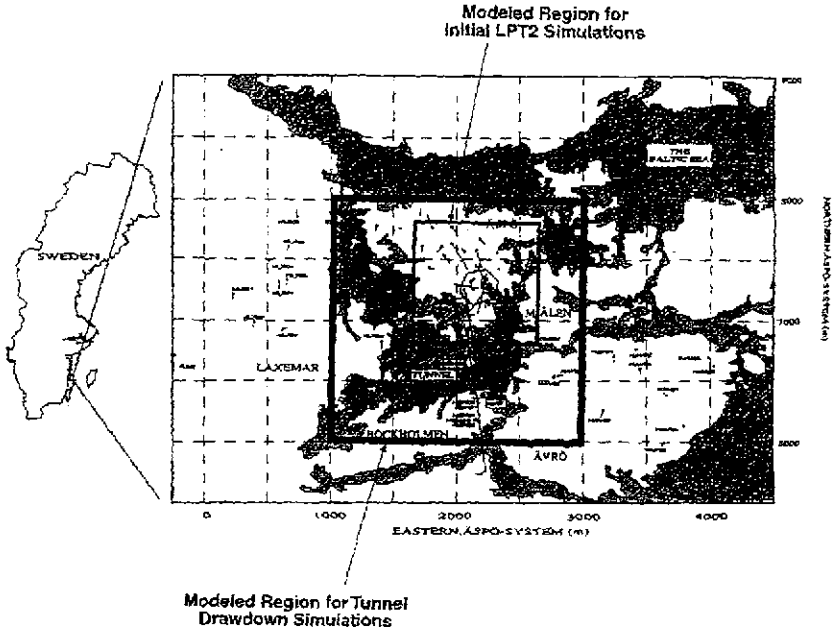

Figure 2-1 Äspö Task 5 Modeling Region

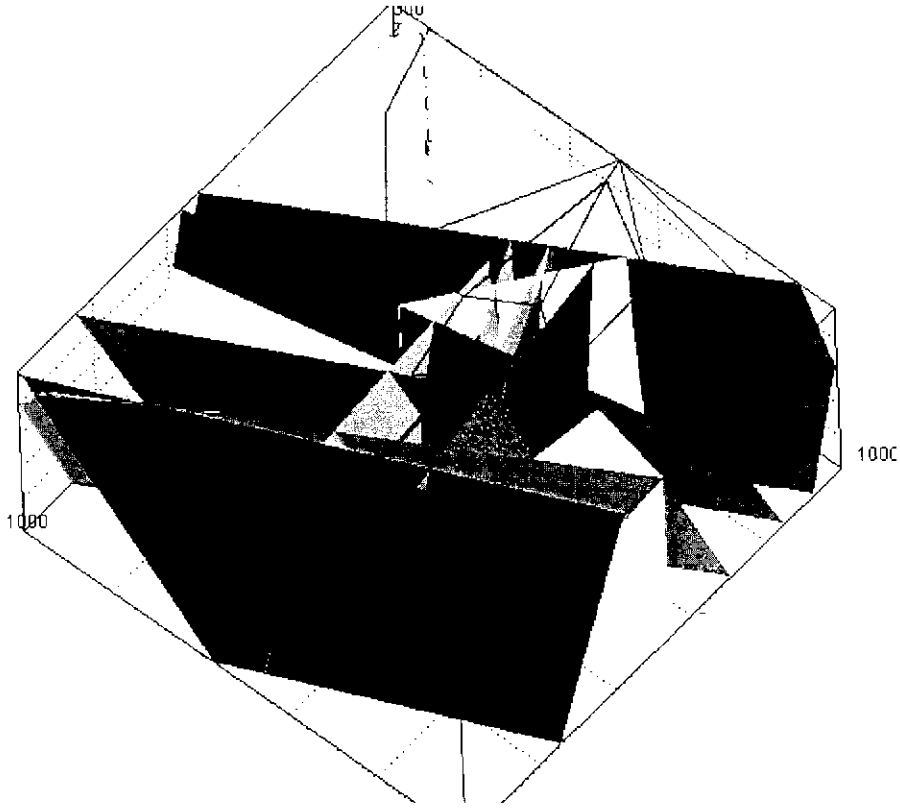

Figure 2-2 DFN Structural Model

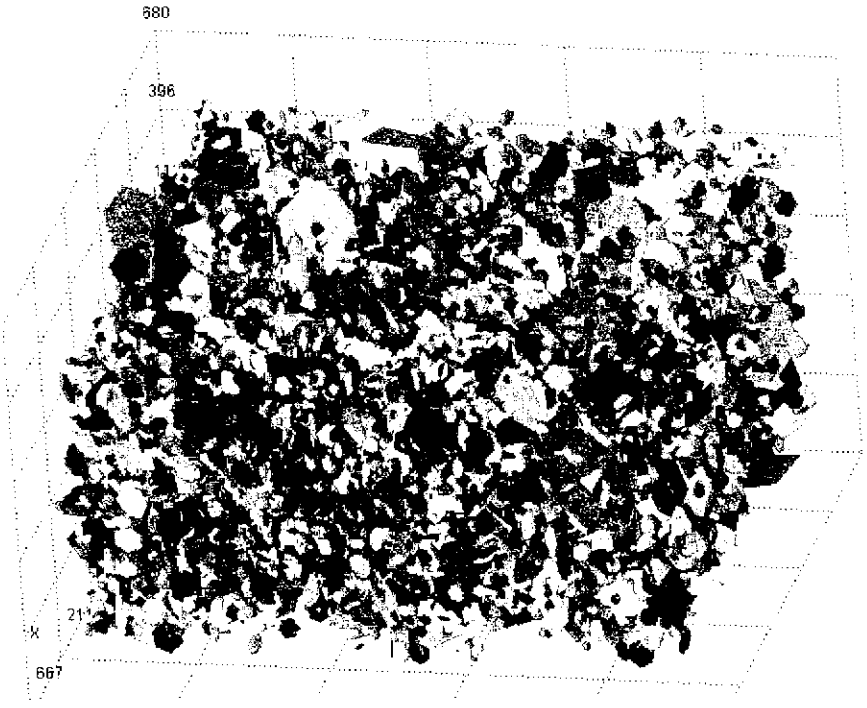

Figure 2-3 Background Fracturing

Table 2-1 Structural Model Parameters

Fracture Set	Deterministic Fracture Zones	Background Fracture Properties
Name	Fracture Zone Fractures	Background fractures
Location	22 Planar Homogeneous Zones (Rhén et al., 1997)	Baecher/Bart Model
Size	Surface Traces Mean = 1420 m	LogNormal (μ = 13.7 m, σ = 12.7 m)
Orientation	3 Point Solution	Bootstrap SKB, 1994 Fractures Mapped in Tunnels
Transmissivity	Rhén et al., 1997	LogNormal ($\mu = 9 \times 10^{-7}$ m^2/s, $\sigma = 5 \times 10^{-6}$ m^2/s)
Storativity	0.001 $T^{1/2}$	0.001 $T^{1/2}$
Intensity	Rhén et al., 1997	P_{32} = 0.020214 (m^2/m^3) (22704 fractures)
Transport Aperture	2 $T^{0.5}$	2 $T^{0.5}$

Since Task 5 requires calibration and evaluation of drawdown response to tunnel construction, conditioned discrete features were included in this model. These features were installed perpendicular to each of the monitoring intervals considered in boreholes KAS02 to KAS09, KAS12, and KAS14. The conditioned discrete features do not have the exact location or transmissivity of specific measured fractures within the boreholes, as this information was not available. The purpose of these features was purely to improve the connectivity between the borehole sections and the DFN, thereby increasing the number of locations in the DFN at which computed heads could be measured. These conditioned features are illustrated in Figure 2-4.

Uchida et al. (1997) carried out extensive simulations of drawdowns due to tunnel construction as part of Task 3 of the Äspö Task Force on Modeling of Groundwater Flow and Transport of Solutes. They identified step drawdown responses due to tunnel construction as one of the key factors contributing to difficulties in matching measured and observed drawdowns (Figure 2-5). Uchida et al. (1997) ascribed this to a discrete feature and was able to localize this feature by plotting the location of exceptionally fast, strong hydraulic responses to tunnel construction. These responses occur on a single plane, as illustrated in Figure 2-6. This previously undetected feature has been modeled as two fractures: the plane containing the step responses, and a small connecting feature to ensure connection to the shafts. The "Mystery Feature" is located between features NNW1and NNW7. The tunnel sections shown in green on Figure 2-7 are sections containing a step response (Uchida et. al, 1997). The shafts are depicted in red.

JNC/Golder are not asserting that an undiscovered fracture zone exists in this location, but only that discrete features providing the connectivity of the

features illustrated in Figure 2-7 are potentially useful to explain observed hydraulic responses to the shaft construction. This could be provided, for example, by particular "background" features which happen to intersect the shaft and monitoring sections at the location shown in Figure 2-7. The step drawdown responses observed, however, are indicative of isolated hydraulic connections rather than extensive background fracture connections.

2.2 BOUNDARY AND INITIAL CONDITIONS

For modeling purposes, Äspö Island and the Baltic were discretized into triangles as illustrated in Figure 2-8. Task 5 simulations required boundary and initial conditions for the head distribution and geochemistry.

2.2.1 Initial Head Conditions

Initial head boundary conditions are shown in Figure 2-9. The base of the model was assigned as a "no flow" boundary. The sides of the model were specified as constant head values interpolated from the values of Svensson (1999). The surface of Äspö Island was specified to have a constant infiltration rate of either 0.0 mm/year or 30.0 mm/year. Infiltration of 30 mm/year is equivalent to precipitation of approximately 650 mm/year assuming no runoff so that infiltration is equal to precipitation minus evapotranspiration). An infiltration of 0.0 mm/year was used for the hydrogeological calibrations. The Baltic seabed was modeled using a constant head boundary condition of 0.0 m. For some simulations, a 1 m thick skin was provided at the base of the Baltic to represent the influence of sea-bottom sediments (see Section 4).

Task 5 simulations were run over the time period from October 1, 1990 through November 28, 1996. October 1, 1990 through January 24, 1994 was used for calibrations to 2900 m tunnel face, and January 25, 1994 through November 28, 1996 were used for predictive simulations. Äspö tunnels were treated as time varying group flux boundary conditions. Therefore, for any individual section of tunnel, prior to its construction had a net flux of zero: after construction its flux was equal to the measured flow into that tunnel section from weir data. Weir data was provided by SKB for tunnel construction to 3600 m tunnel face. The weir flux boundary condition is illustrated in Figure 2-10.

The alternative tunnel boundary condition would have been an "internal" (i.e. no effect) boundary condition at early times, changing to a constant head condition once the tunnel was constructed. The most obvious head assumption at the tunnel wall, that of atmospheric pressure in the tunnel, is problematic however. This is because significant head loss will occur in the few meters behind the tunnel wall due to combined effect of grouting behind the tunnel lining and the tunnel lining itself. Any other head assumption is essentially a calibration parameter, not a constraint.

2.2.2 Initial Geochemical Conditions

Initial geochemical conditions were provided at 98 locations, in Appendix 14 of Data Delivery 7, as illustrated in Figure 2-11. These initial conditions utilized end-member definitions and proportions calculated using the program M^3 (Laaksoharju et. al., 1999b). These values were extrapolated by SKB (Rhén, 1998) using Kriging to a grid of 1000 locations (Figure 2-12). The extrapolation used a simple data-smoothing algorithm, and did not consider structural geologic issues, even through the majority of the measurement points are in fracture zones, at locations. Metcalfe (1999) has addressed the data quality issues and modeling implications associated with these initial geochemical conditions.

The JNC/Golder FracMan/PAWorks modeling for Stages 1 and 2 used a distance-weighted interpolation of the 1000 point grided initial geochemical conditions to define the initial conditions in each fracture in the DFN model.

At each point in the model, P_I (x, y, z), the percentage geochemical end member "I" was calculated by a distance-weighted interpolation in the x, y, and z directions as follows:

$$P_I(x,y,z) = RelY1 + z*(RelY2-RelY1)$$

where RelY1 and RelY2 reflect interpolation in the Y direction,

$$RelY1 = RelX1 + y * (RelX3-RelX1)$$
$$RelY2 = RelX2 + y * (RelX4-RelX2)$$

and RelX1 through RelX4 reflect interpolation in the X direction,

$$RelX1 = P(X_i,Y_i,Z_i) + x * (P(X_{i-1},Y_i,Z_i)- P(X_i,Y_i,Z_i))$$
$$RelX2 = P(X_i,Y_i,Z_{i+1}) + x * (P(X_{i-1},Y_i,Z_{i+1})-P(X_i,Y_i,Z_{i-1}))$$
$$RelX3 = P(X_i,Y_{i+1},Z_i) + x * (P(X_{i-1},Y_{i+1},Z_i)-P(X_i,Y_{i-1},Z_i))$$
$$RelX4 = P(X_i,Y_{i+1},Z_{i+1})+ x*(P(X_{i+1},Y_{i+1},Z_{i+1})-P(X_i,Y_{i+1},Z_{i+1}))$$

Initial geochemical conditions at the edges of the model were assigned based on those at the closest grid point.

The updated approach used for the Stage 3 complimentary analyses are described in Section 5.

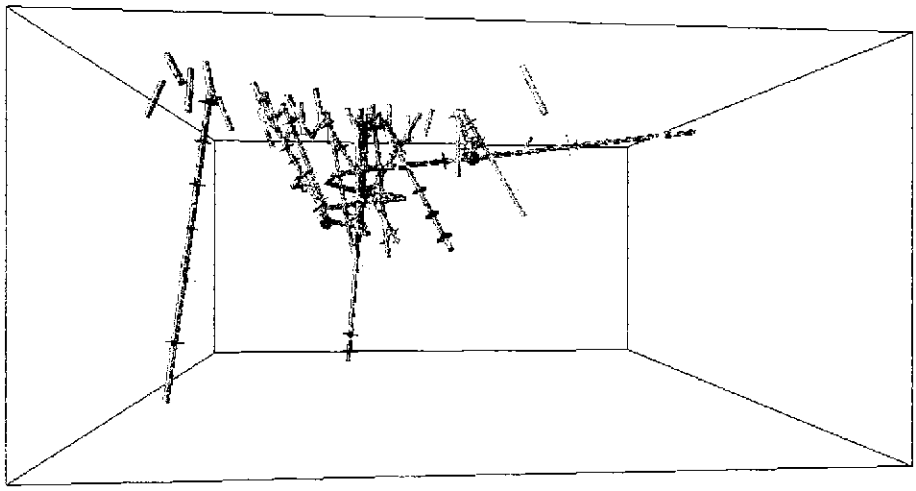

Figure 2-4 Conditioned Fracturing

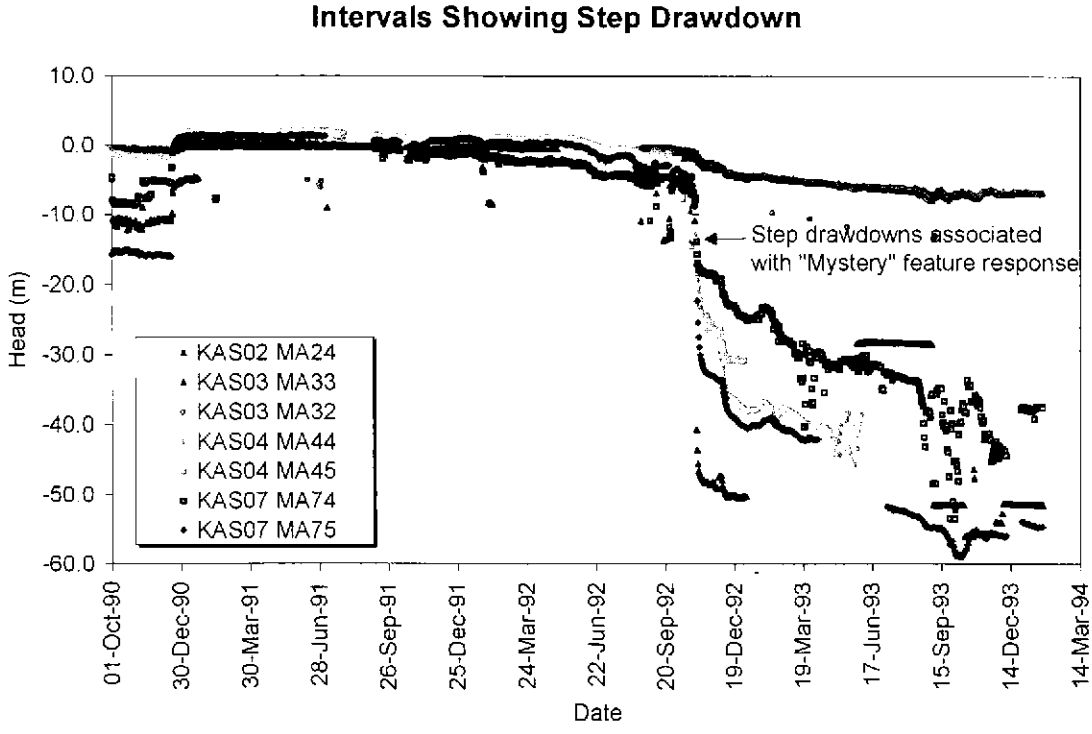

Figure 2-5 Mystery Feature Responses

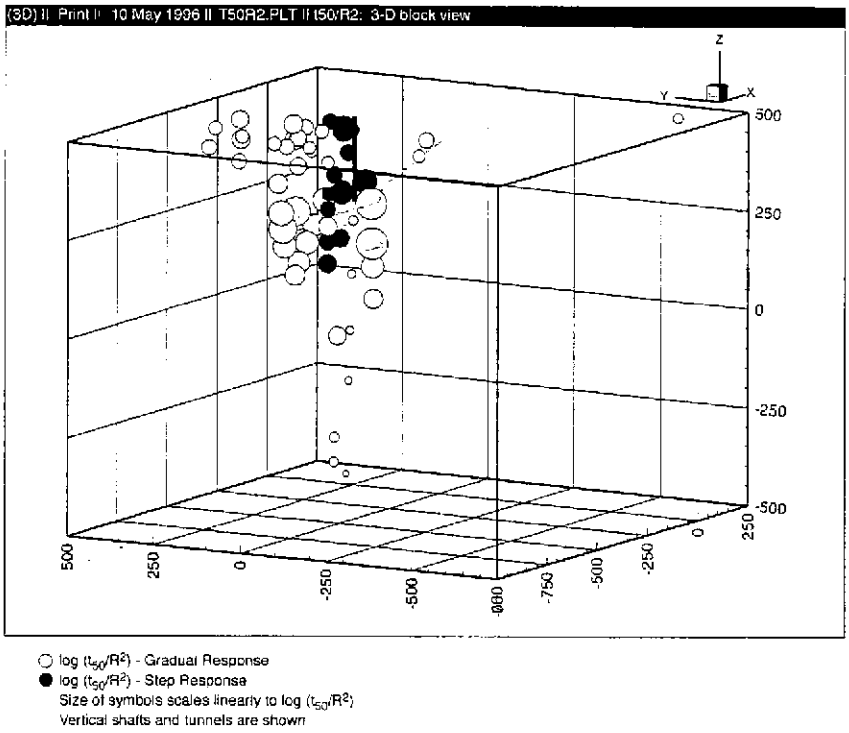

Figure 2-6 Mystery Feature Location

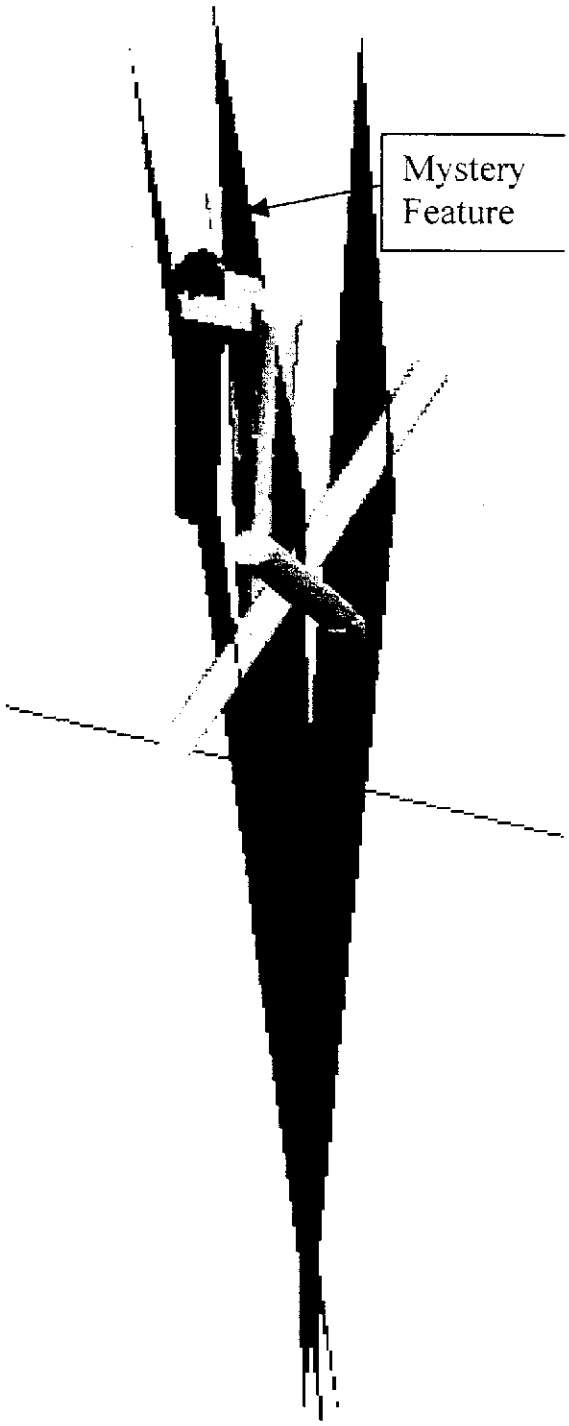

Figure 2-7 Mystery Feature comparison to SR-97 Structural Model

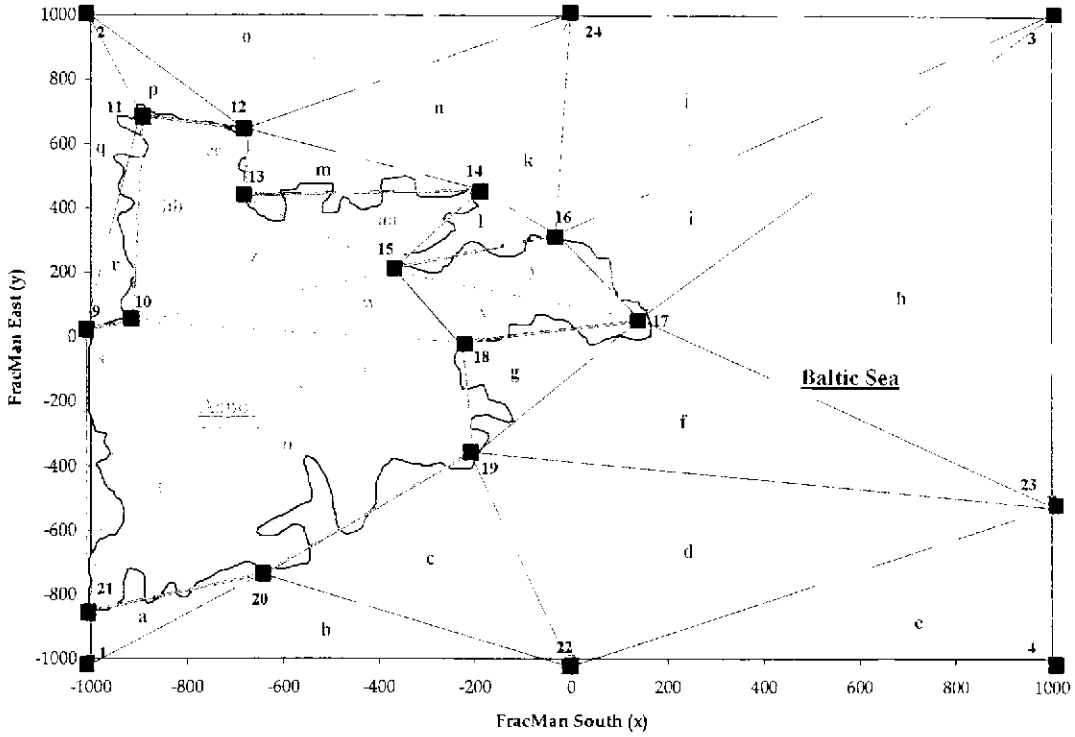

Figure 2-8 Model Boundary Discretization

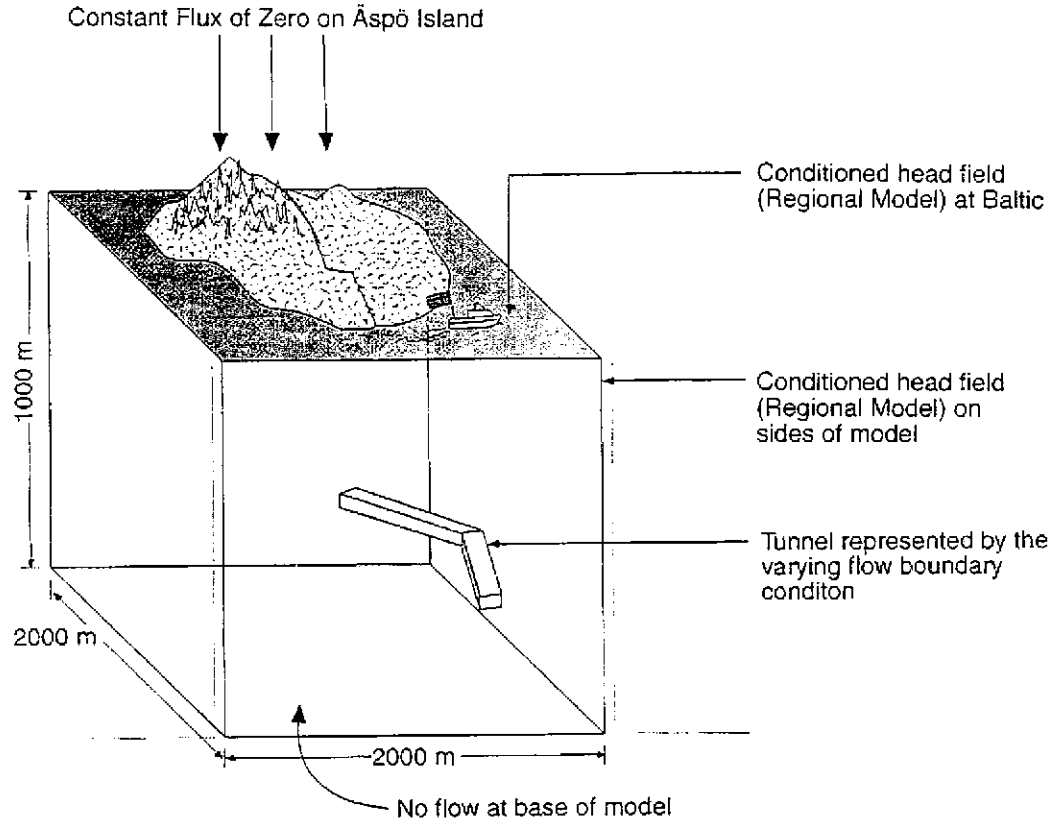

Figure 2-9 Boundary Conditions

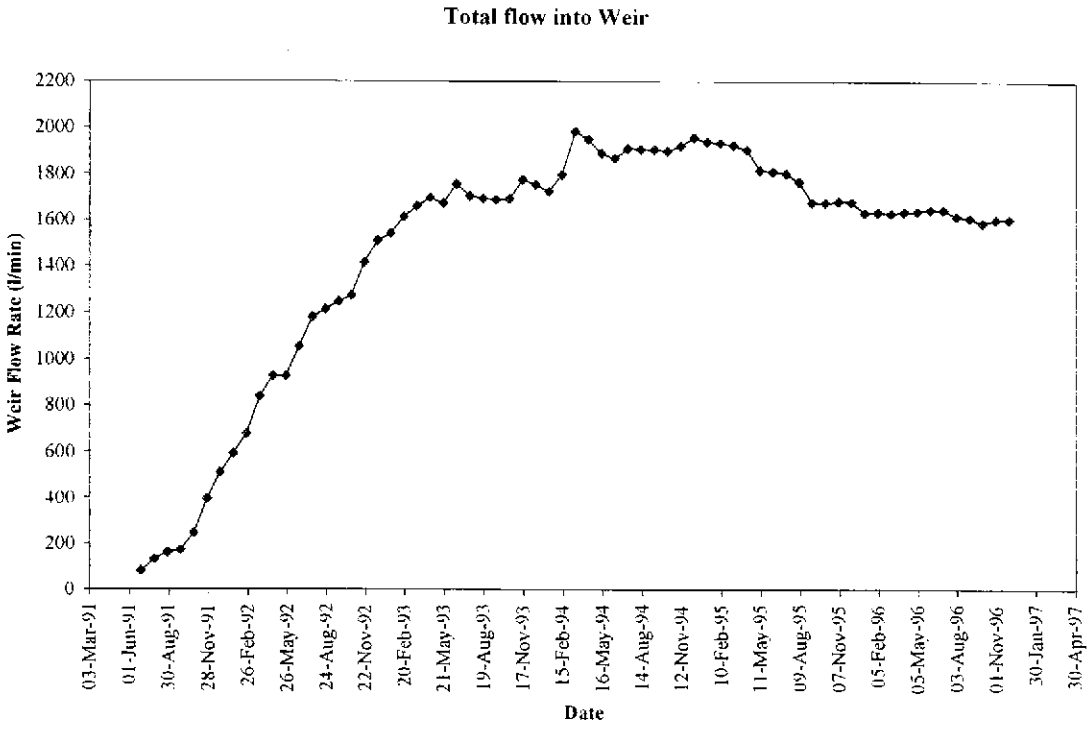

Figure 2-10 Weir Fluxes to June 4, 1996

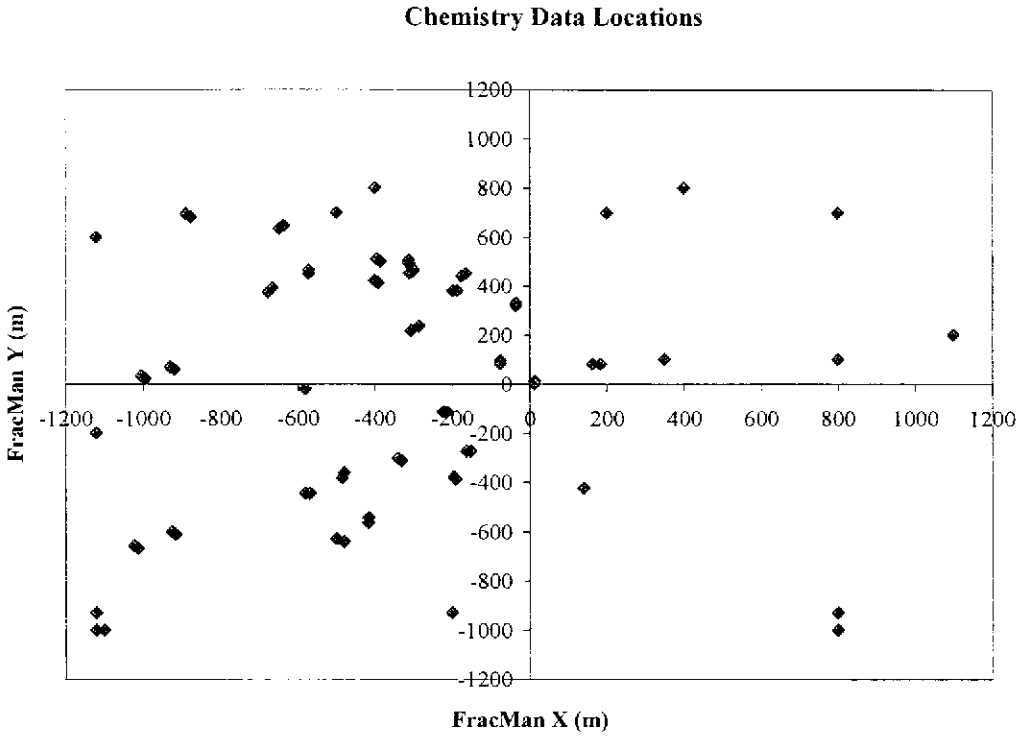

Figure 2-11 Geochemical End-Member Data Points

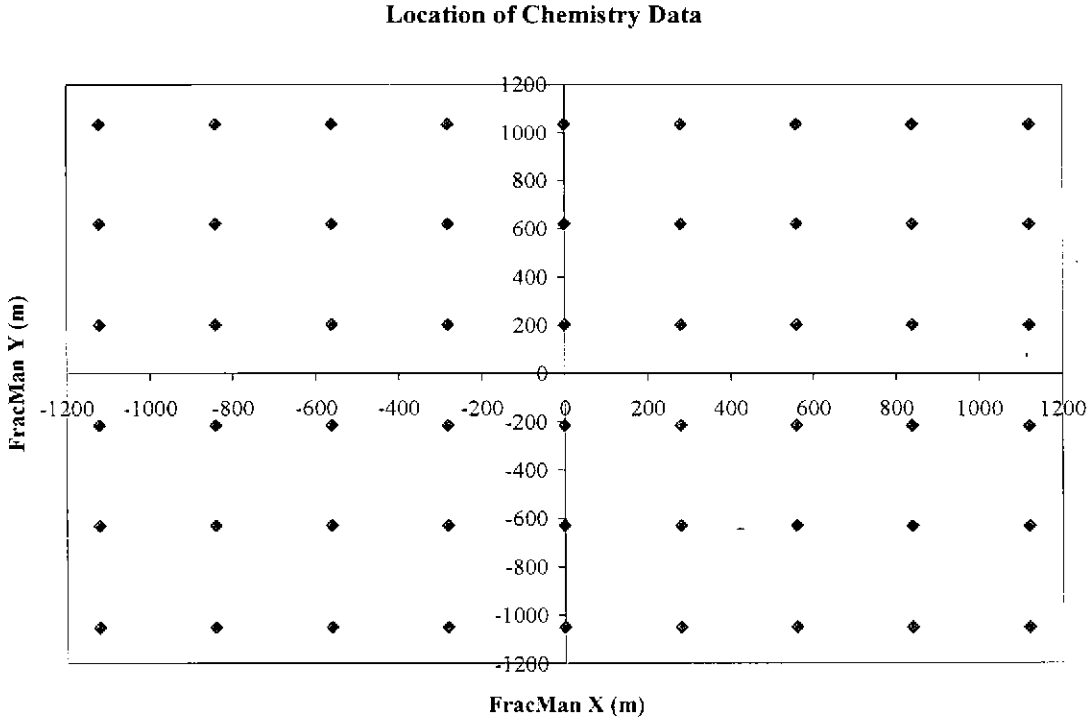

Figure 2-12 Geochemical End-Member Data Grid

2.3 MEASURES OF ERROR

In order to determine which hydrogeological DFN model provides the best idealization of the true groundwater system at Äspö the following error terms were used (Rhén et al., 1998).

Mean Error, dh

$$dh = \frac{\sum_{i=1}^{n} (h_i^m - h_i^c)}{n}$$

$$dh(abs) = \frac{\sum_{i=1}^{n} | h_i^m - h_i^c |}{n}$$

Accuracy

$$Dh = \sqrt{\frac{\sum_{i=1}^{n} (h_i^m - h_i^c - dh)^2}{n - 1}}$$

where

- n is the number of borehole intervals at which a head is measured. For the modeling results this is typically equal to the number of borehole intervals connected to the fracture network.
- h: Piezometric level (freshwater head) in meters above sea level (masl).
- m index to represent measured values
- c index to represent calculated values

For time dependent simulations the time-averaged value of mean error is used as an assessment of the error bias. This is the defined as Σ(dh)/(number of time measurements).

A similar error measure was used to provide an indication of the bias of the geochemical fit, the "geochemical absolute average error". The number is given as a percentage. The value is defined as:

$$dg(abs) = \frac{\sum_{i=1}^{n} | g_i^m - g_i^c |}{n}$$

where g are the percentages of measured (m) and calculated (c) Brine, Glacial, Meteoric and Baltic. The number of measured values is limited therefore all the measured values are used. Therefore the "n" is the total number of measurements.

2.4 SOFTWARE

The FracMan discrete feature network model was used for this analysis. In particular, FracMan/FracWorks was used for generation of background discrete fractures, FracMan/MAFIC was used for steady state and transient flow simulations, and FracMan/PAWorks pathway analysis was used to define pathways. FracMan is described in Appendix A of SKB 97-03 (Uchida et al, 1997) and in more detail in the FracMan manual (Dershowitz et al., 1998a), MAFIC manual (Miller et al., 1998) and PAWorks manual (Dershowitz et al., 1998b).

FracMan/PAWorks is a suite of analysis codes that represent fracture networks as a 3-D pipe network, with nodes defined by fracture intersection traces. The advantage of using pipe elements, as opposed to plate elements, is that there is a vast saving in memory and computation time requirements. In PAWorks, the pipes are generated to maintain the connectivity structure of the 3-D discrete fracture network, with approximately equivalent conductances and surface areas (Figure 2-13).

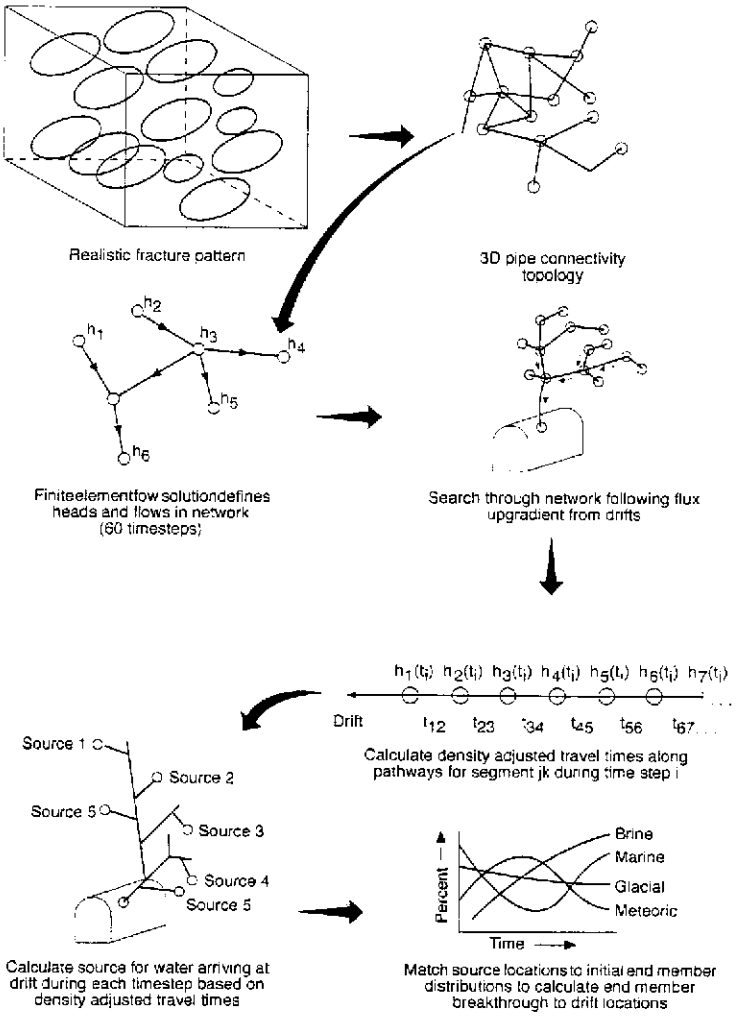

Figure 2-13 PAWorks Pipe Networks from Fractures

3. STAGE 1: HYDROGEOLOGICAL MODELING

JNC/Golder carried out the first modeling phase considering only hydraulic data for our calibrations. The hydrogeological calibration exercise took approximately one month. Calibration considered only the head values in the monitoring sections, and did not make use of any geochemical information.

Since one of JNC/Golder's goals for this task was to increase modeling transparency, the following section provides a record of the process of hydrogeological model calibration. The following section summarizes the results of the calibrated Stage 1 model. Detailed Stage 1 model results are provided as Appendix A.

3.1 HYDROGEOLOGICAL CALIBRATION

The hydrogeological model calibration for Task 5 started with the initial Task 3 model (Uchida et al., 1997), and was extended during preliminary Task 5 modeling in 1998 (Dershowitz et al., 1999) and in modeling for the Äspö Task Force meeting in April, 1999. The formal modeling for Task 5 was initiated in September 1999. The progress of hydrogeological calibration for the Task 5 simulations is illustrated in Figure 3-1. The hydrogeological model simulations are summarized in Table 3-1. In Table 3-1 the number of borehole sections being intersected varies with simulation. This number is defined as the minimum of the number of borehole sections connected to the DFN and the number of in situ measurements taken. It is defined at a specific time because the number of borehole sections at which in situ measurements were taken varied over time.

Initial modeling was carried out based on fracture zones alone (H-1). This model is very fast, and produced very good results, with an average error of only about 5 m. The success of this initial model can be attributed in part to the fact that this model benefits from the previous "Task 5" model of Uchida et al. (1997), which determined the appropriate skin value for the soils under the Baltic to be 0.01x.

The majority of the error in head predictions for the H-1 model arose from the lack of fit for the extreme drawdown responses to shaft construction (Figure 3-2). Therefore, the first change to the hydrogeologic model was to add the "mystery feature" to explain this response. As described in Section 2.1 above, these features were placed to connect the shaft to the locations at which anomalous large, steep drawdowns had been observed.

The mystery feature does not necessarily correspond to a single fracture zone, but may instead comprise a set of individual conductive features.

Table 3-1: Hydrogeological Calibration

Sim	Stage I: Head Calibration	Features	# of BH Sections 1st Oct 1990	Time Average dh	dh on 13th Jan 1994
H-1 20-Sep	Zones Only	Pipe network created from DFN model of 22 deterministic fracture zones. Baltic Sea skin applied to reduce T in upper 10m to a multiple of 0.01 times the original value.	14	4.94	6.31
H-2 23-Sep	add Mystery Feature	Two fractures added to explain mystery response	14	5.30	6.61
H-3 8-Oct	Zones and Background	First iteration with 22704 background fractures	14	4.20	
H-4 10-Oct	Background Fracs, Mystery Feature	Model includes two fractures to explain mystery response	14	2.74	
H-5 11-Oct	Background Fracs and Conditioned Features	161 deterministic fractures with T=10^-6 added at head calibration sections in order to ensure that all calibration sections are connected	45	9.45	25.66
H-6 14-Oct	Background Fractures, Mystery Feature, Conditioned Fractures	Model includes two fractures to explain mystery response	45	10.18	26.03
H-7 21-Oct	Adjust Conditioned Fractures	Number of deterministic fractures at head calibration sections reduced to 69 and transmissivity of remaining fractures decreased to 10^-8 to reduce excessive drawdowns	45	10.05	25.28
H-8 22-Oct	Remove Baltic Skin	Baltic Sea skin removed in order to reduce excessive drawdowns	45	5.13	13.46

The first model including the "mystery feature" is H-2. This model did in fact improve the drawdown response to shaft construction (Figure 3-3). However, it did not have a significant influence on the average error. In addition, the model still only provides connection with 14 monitoring sections. Models H-3 and H-4 add background fractures to models H-1 and H-2 respectively. However, these stochastic background fractures did not increase the number of monitored sections, although they do decrease the average error.

Conditioned features intersecting each of the monitoring sections were added to models H-3 and H-4, respectively in simulations H-5 and H-6. (Figure 2-4). These models significantly worsened the average error, since they produced drawdown in many sections which were not in fact hydrogeologically connected (Figure 3-4). The match was improved in model H-7, which removed conditioned fractures from non-responding sections, and reduced the transmissivity of the conditioned fractures from 10^{-6} to 10^{-8} m^2/s. This only made minor improvement to the average

drawdown measure dh, and the average drawdown in the model remained too high. Therefore, to reduce the average drawdown in the model, the low permeability skin was removed from the Baltic for model H-8.

Table 3-2 Summary of Model H-8

Property	Description
Fracture Model	
Major Discrete Features	22 Planar Homogeneous Zones (Rhén et al., 1997). See Table 2-1 for details.
Background Fractures	22704 features described in Table 2-1.
Mystery Feature	Addition an additional feature located between features NNW1and NNW7. Constructed from two fractures as shown in Figure 2-7.
Conditioned fractures intersecting tunnel sections.	Deterministic fractures added at 69 head calibration sections. Transmissivity of these deterministic fractures set at 10^-8 m^2/s to reduce excessive drawdowns.
Transport Aperture	Aperture = 2 * Transmissivity$^{0.5}$
Boundary Conditions	
North, South, East & West sides	Conditioned to the values reported in Svensson (1999).
Base	No flow boundary assigned to each node.
Baltic Sea	Head of 0.0 m.
Äspö Island	No flow boundary assigned to each node.
Geochemistry	
Chemical Composition	End-member definitions and proportions calculated using the program M^3 (Laaksoharju, M., 1999).
Interpolation Scheme	Linear interpolation from a grid of 1000 locations provided in Data Delivery No.4

It is interesting to note that a skin was required for model H-1, but gave excessive drawdowns in model H-7. The likely reason for this effect is that the addition of background fractures and conditioned features affects the connectivity of the DFN. This effect is magnified by the use of group flow boundary conditions for the tunnel sections: the number of tunnel sections connected into the DFN increases as the background fractures and conditioned features are added, and at each connected tunnel section water is removed from the finite element model.

This effect has implications for DFN model calibration. To provide a calibration that is insensitive to stochastic changes for a DFN model that

contains non-zero flow boundary conditions, or in which the total flow through the model is critical to the understanding, the majority of flowing features must be included. For the Äspö site, although the major features may dominate the flow regime, the background fractures are a necessary part of the model connecting the tunnel sections to the major zones or the outer boundary.

The last model in this series, model H-8, was used as the "hydrogeologic only" head and geochemical response prediction. The parameters defining the H-8 model are summarized in Table 3-2. However, the calibration of this model was somewhat limited by a decision to not change the assigned values of fracture zone transmissivity provided by SKB. The SKB transmissivity values were typically based on a small number of hydrogeological tests with wide variability. Therefore, to improve the calibration the major feature transmissivities were changed as part of the Stage 2 geochemical calibration.

3.2 PREDICTIVE SIMULATIONS

Hydrogeological performance measures for the hydrological prediction Model H-8 are presented in Appendix A. Figure 3-5 through Figure 3-8 present example hydrogeological results for model H-8.

As discussed earlier in the document, the predictions H-1 through H-8 were undertaken using only head data. The final prediction, H-8, provided the smallest time average head error and was selected as a baseline model for the geochemical calibrations, and a geochemical simulation was carried out.

Figure 3-9 though Figure 3-13 shows a comparison between the geochemical calibration control points and simulated results using Model H-8. This model resulted in a geochemical absolute average error of 14.4%. The poor quality of the fit to the measured head data and particularly the inaccurate geochemical results indicate that significant improvements could be made to the numerical model.

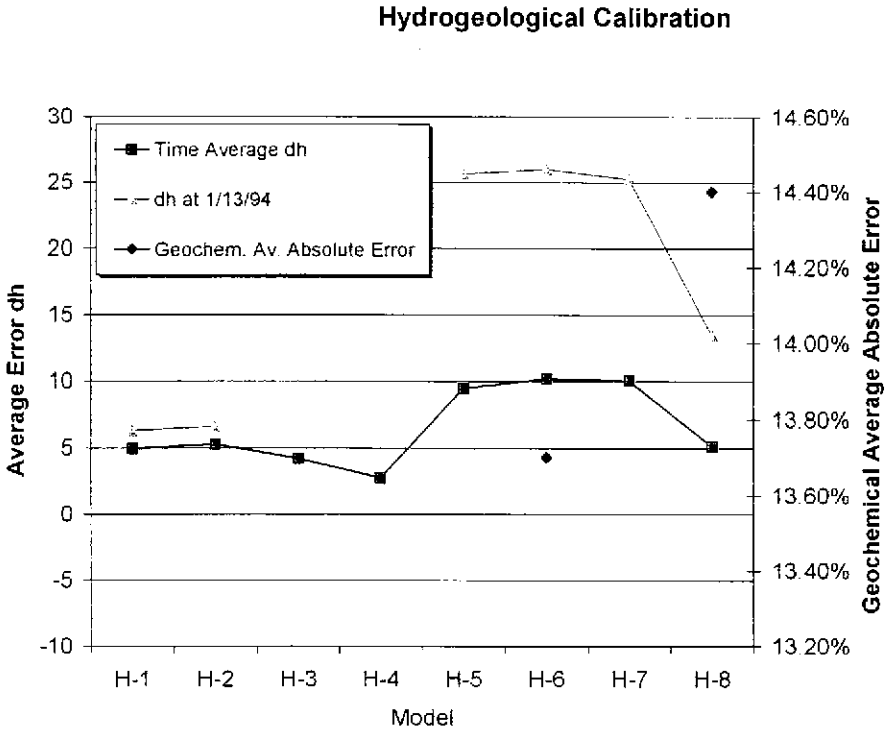

Figure 3-1 Error Associated with Hydrogeological Calibration

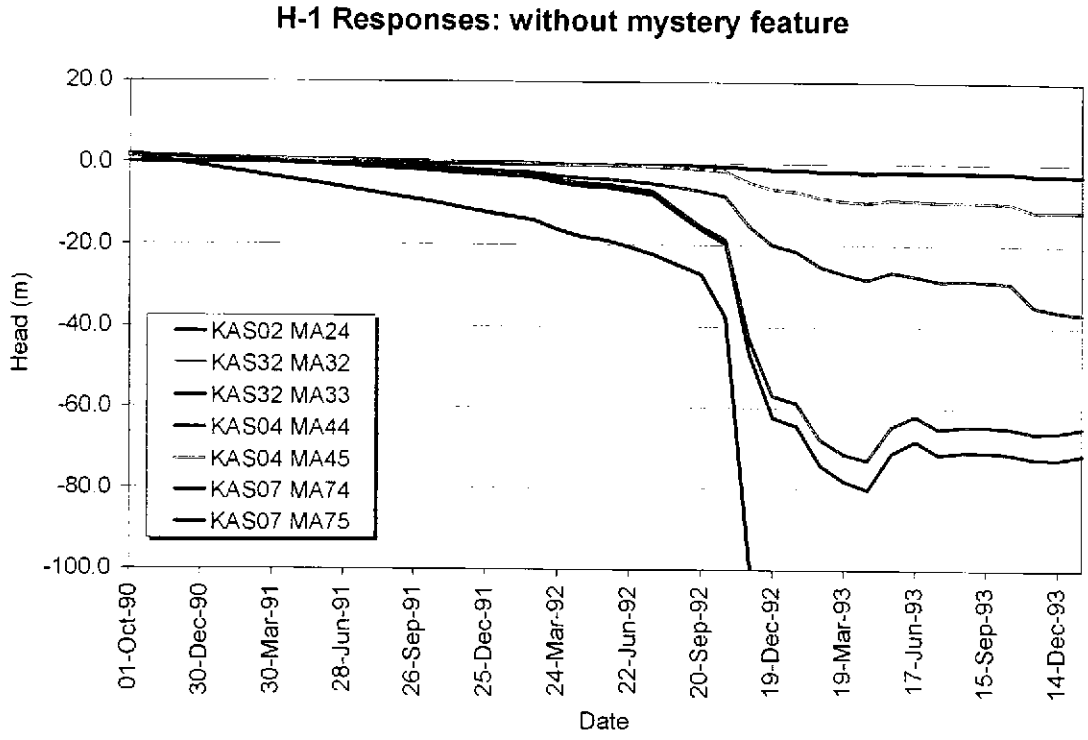

Figure 3-2 Responses to Shaft Construction in Model H-1

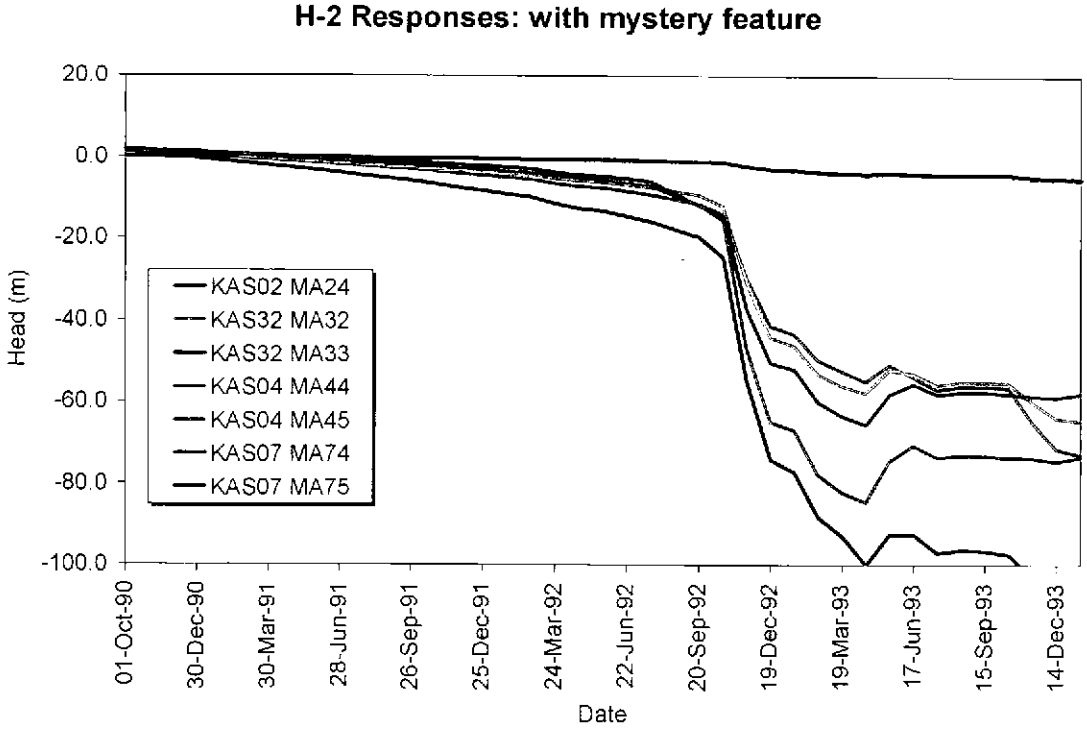

Figure 3-3 Zone-only Model H-2 including "Mystery Feature"

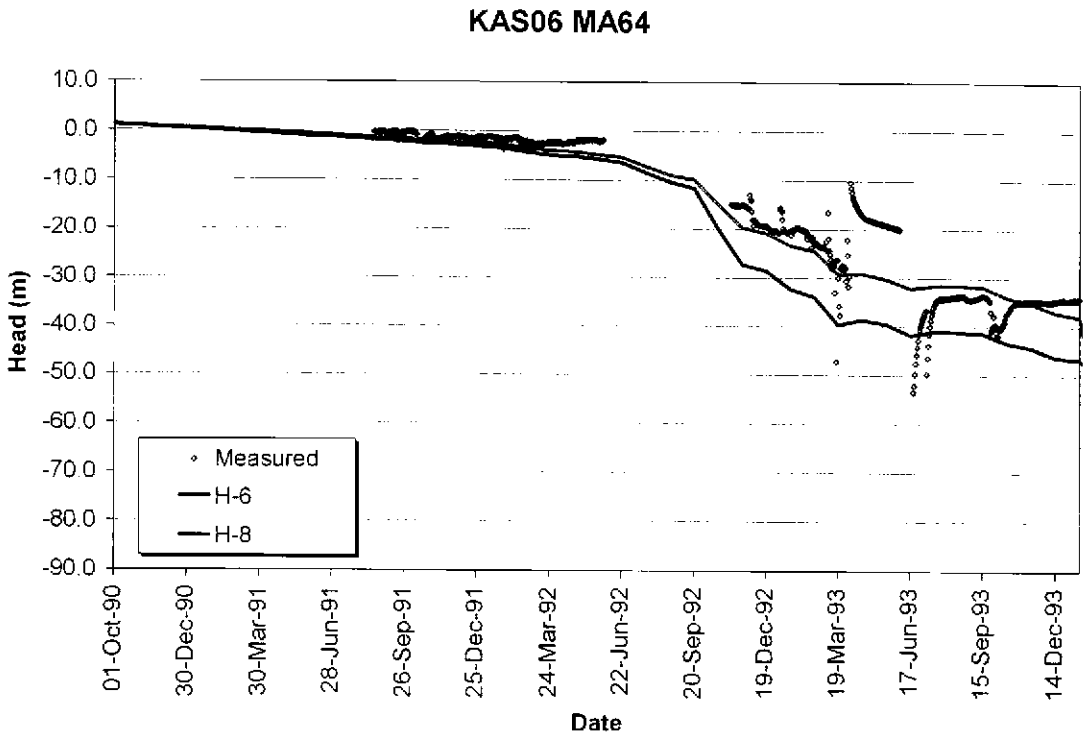

Figure 3-4 Example Drawdown, KAS06 MA64 in Model H-6

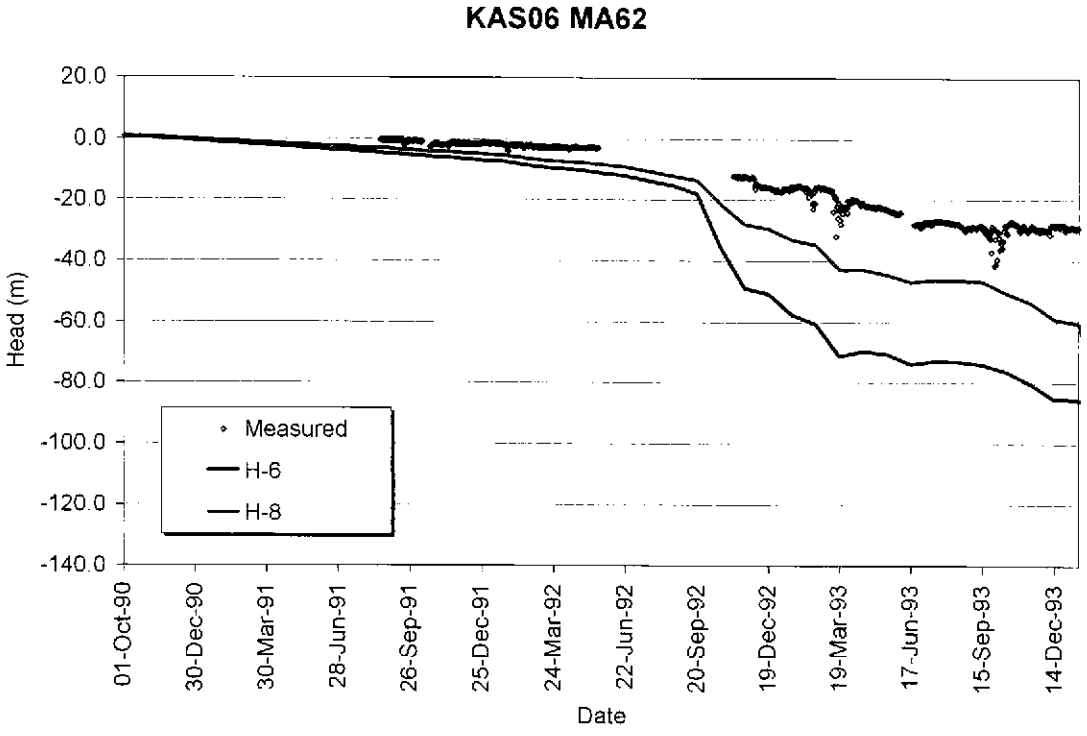

Figure 3-5 Drawdown Response of KAS06 MA62 in Model H-8

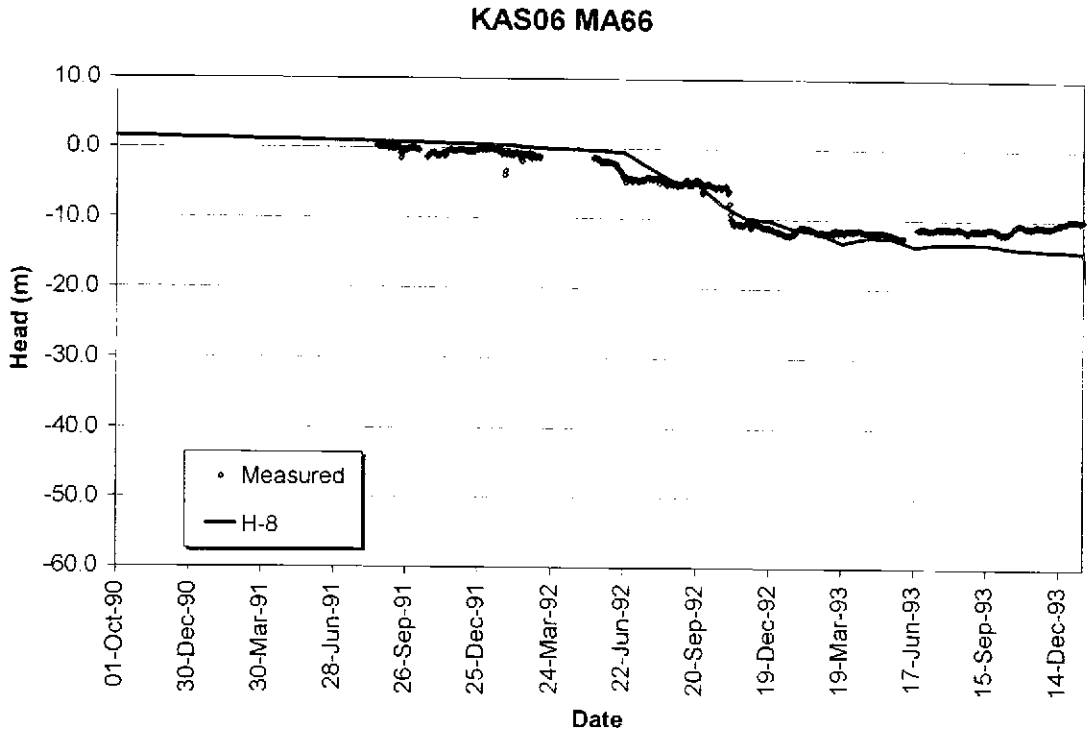

Figure 3-6 Drawdown Response of KAS06 MA66 in Model H-8

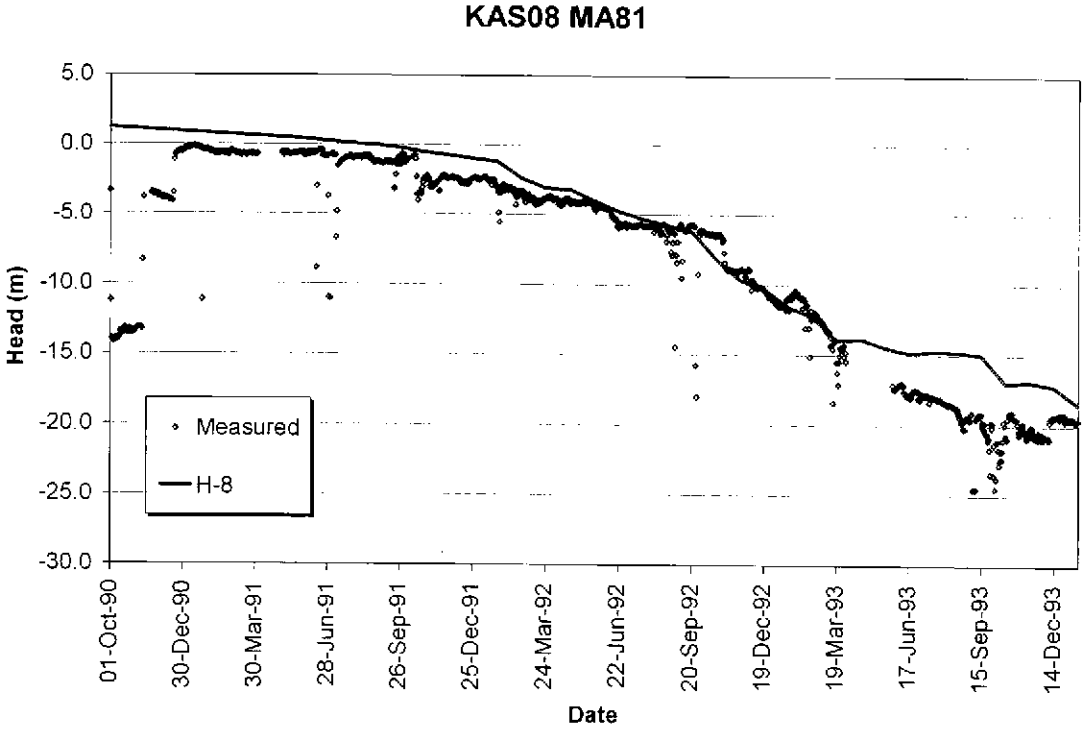

Figure 3-7 Drawdown Response of KAS08 MA81 in Model H-8

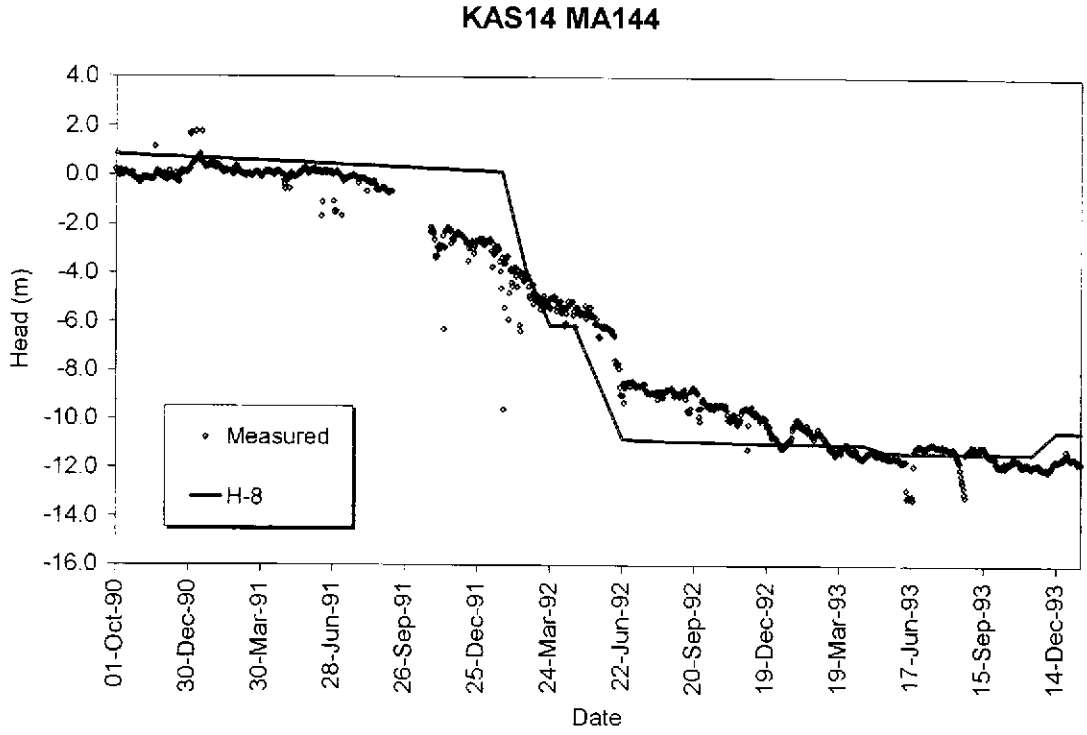

Figure 3-8 Drawdown Response of KAS14 MA144 in Model H-8

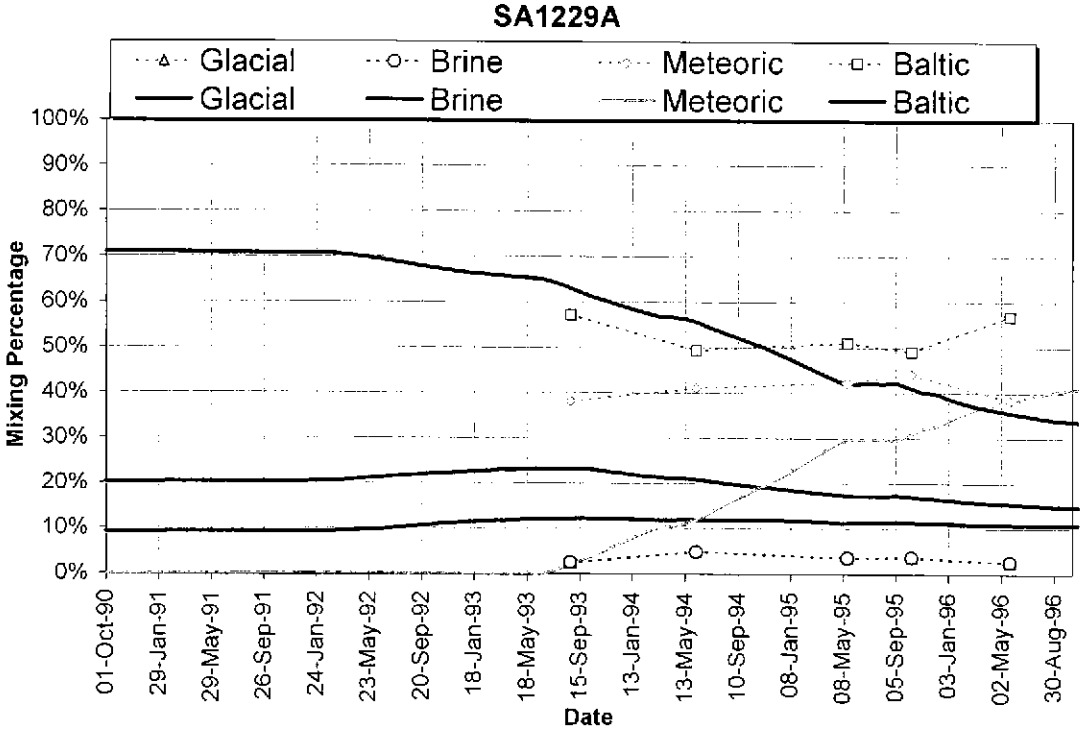

Figure 3-9 Geochemical Response of SA1229A in Model H-8

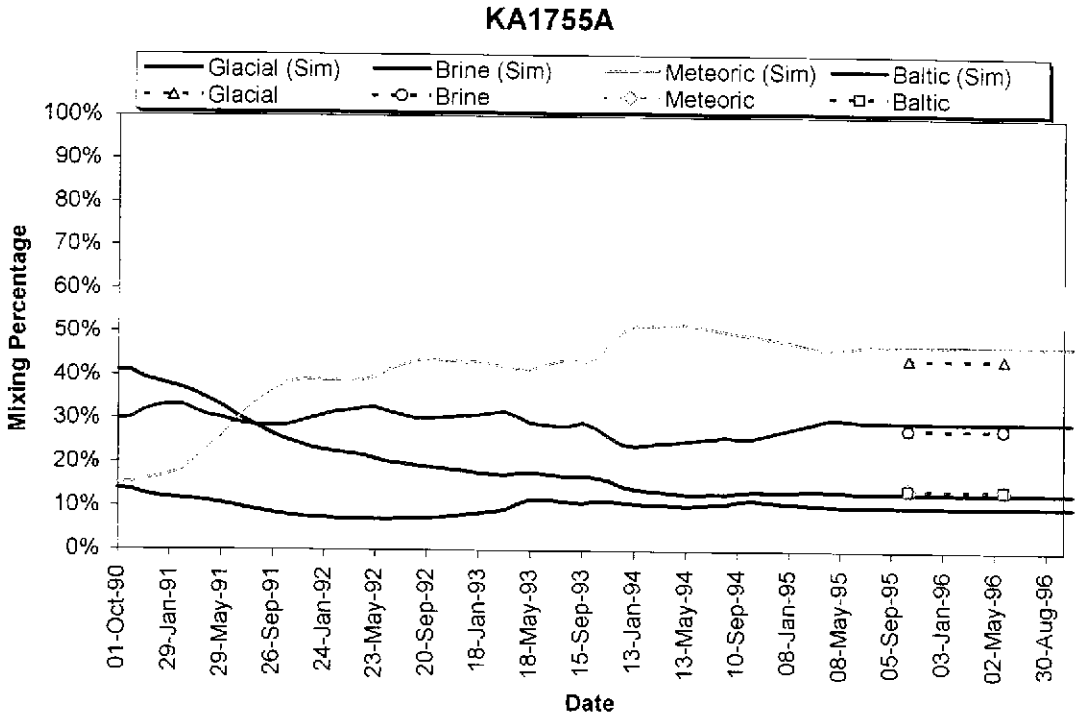

Figure 3-10 Geochemical Response of KA1775A in Model H-8

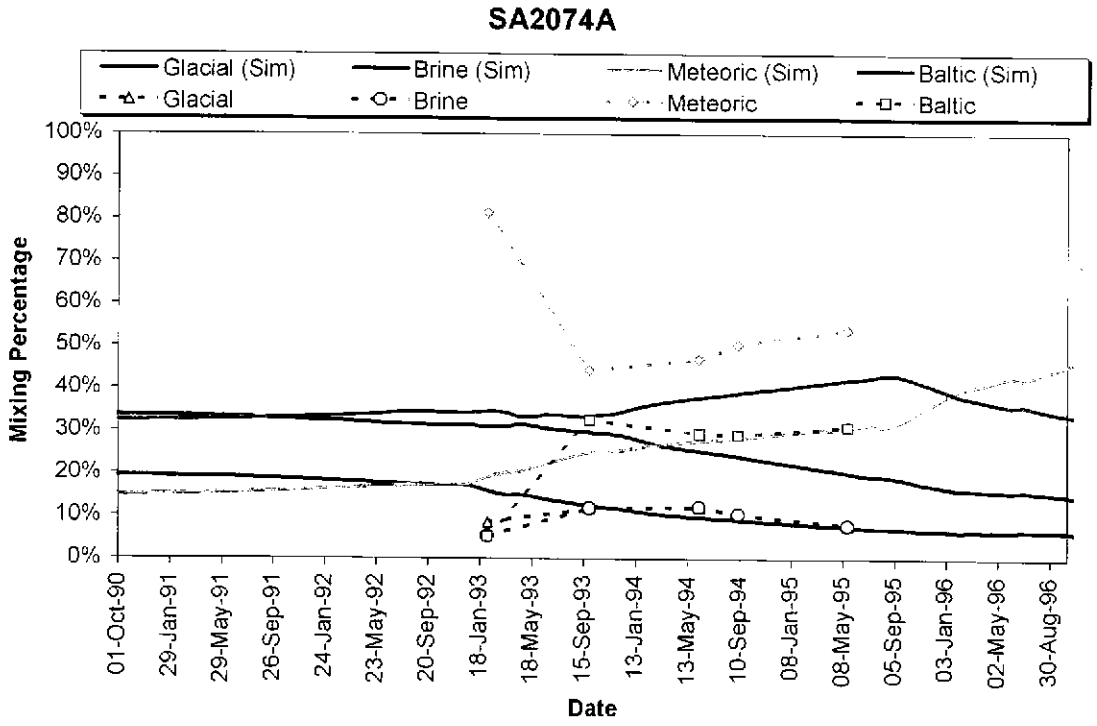

Figure 3-11 Geochemical Response of SA2074A in Model H-8

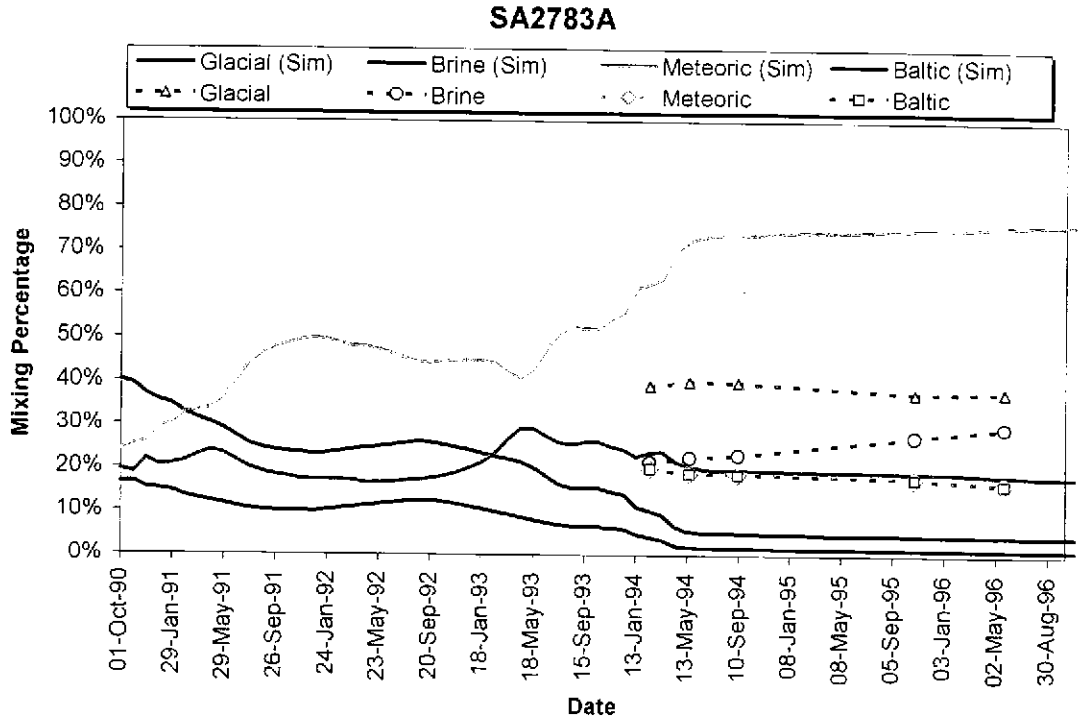

Figure 3-12 Geochemical Response of SA2783A in Model H-8

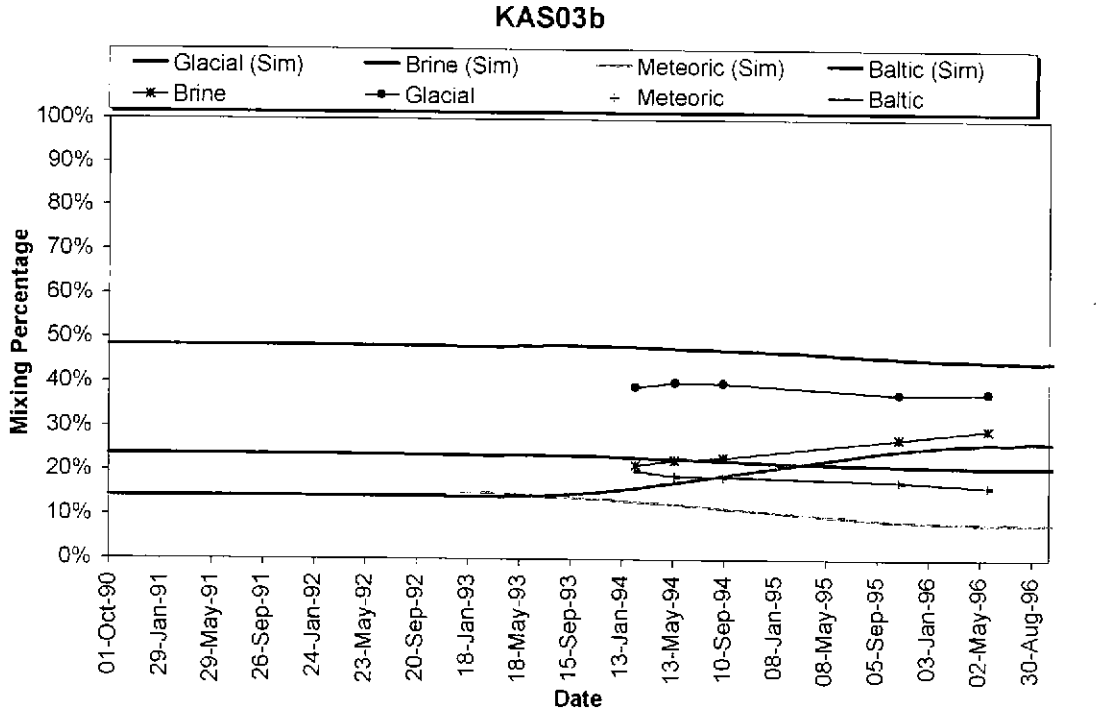

Figure 3-13 Geochemical Response of KAS03b in Model H-8

4. STAGE 2: GEOCHEMICAL CALIBRATION

In the second modeling phase JNC/Golder adjusted the Task 5 hydrogeological model to match the geochemical observations. The modeling was primarily focused on improving the calibration to geochemical end members collected at the control points. Of particular interest was the glacial component, which was lacking in the modeling from the hydrogeological calibration.

The following section provides a record of the process of geochemical model calibration and summarizes the results of the calibrated Stage 2 model. Detailed Stage 2 model results are provided as Appendix B.

4.1 GEOCHEMICAL CALIBRATION

The geochemical model calibration for Task 5 started from model H-8 developed in the previous section. The geochemical model calibration simulations are summarized in Table 4-1 and the progress of geochemical calibration is illustrated in Figure 4-1.

The first step for the geochemical calibration was to compare the geochemical results from the hydrogeological calibration H-8 to measured values. Although the average absolute error in the end-member fit was not bad, many deep control points have large measured influxes of glacial water end-members (Figure 4-2).

Since there are no connections to significant glacial water reserves (Figure 4-3), it was necessary to add fracture connections to the north to provide those connections. The structural connection added to the north is illustrated in Figure 4-4. The resulting transport pathways are shown in Figure 4-5.

Another problem with the model H-8 was that it did not provide sufficient meteoric water, as illustrated in Figure 4-6. To solve this problem, the surface boundary condition was changed from no-flow on Äspö Island to a constant infiltration.

The resulting model, G-1, provided a better match for glacial water and meteoric water. Model G-1 constituted the geochemical model prediction as presented to the Task Force in November 1999.

Comparison of end-member breakthrough at control points shows that Model G-1 still had too much Baltic seawater, as shown in Figure 4-7. To solve this, it was necessary to add the Baltic Sea skin back into the model. This skin had been removed to decrease the average drawdown and improve the hydrogeological model for simulation H-8. However, the geochemical

evidence indicates that the Baltic Sea skin effect is real. Therefore, to compensate for the increased drawdown due to reinstatement of the Baltic Sea skin, the transmissivity of all fractures, including the deterministic fracture zones, was increased by a factor of 3. Example results from this model are shown in Figure 4-8.

Results from Model G-2 indicated that the introduction of a 3-fold increase in fracture transmissivity was too much, as the model drawdowns are very sensitive to the fracture transmissivity due to the flow boundary conditions. The change in head is approximately linearly related to the change in transmissivity; therefore the transmissivity was decreased by a factor of 1.6 for Model G-3. Model G-3 showed a much better balance of glacial, meteoric, and Baltic water. However, the Baltic seawater boundary still arrives to the tunnel much to fast. Therefore, the effective transport aperture for model G-4 was increased by a factor of 5. Example results from model G-4 are provided in Figure 4-9 and Figure 4-10.

Table 4-1 Geochemical Calibration Simulations

Sim	Stage II: Geochem Calibration	Features	# of Sections at first time	Time Average dh	dh at 1/13/94	Geochem Fit Average ABS
H-8	No geochemical calibration	Final hydrogeological model.	45	5.13	13.46	14.4%
G-1 28-Oct	chem2: H-8 model with connection added to north, modify boundary condition on Äspö Island	Connection to north added in order to draw in more Glacial-rich water to deeper control points. Äspö Island boundary condition changed from no flow to 30 mm/year infiltration. No low transmissivity skin over Baltic.	45	3.75	9.74	15.6%
G-2 1-Nov	chem3: Baltic skin, change zone transmissivity	Baltic Skin of T=0.01x reintroduced, All fractures (incl. deterministic frac. zones) T= 3x	45	-4.11	-9.13	13.1%
G-3 2-Nov	chem3-2 s1	G-2, with all fractures (incl. deterministic frac. zones)T=1.6x	45	-0.49	0.25	13.3%
G-4 3-Nov	chem3-2 s5	G-3, with transport aperture increased to 5x to increase travel time	45	-0.49	0.25	12.7%

Table 4-2 Summary of Model G-4

Property	Description
Fracture Model	
Major Discrete Features	22 Planar Homogeneous Zones (Rhén et al., 1997). See Table 2-1 for details. Fracture transmissivities increased by a factor of 1.6.
Background Fractures	22704 features described in Table 2-1. Fracture transmissivities increased by a factor of 1.6.
Mystery Feature	Addition an additional feature located between features NNW1and NNW7. Constructed from two fractures as shown in Figure 2-7.
Conditioned fractures intersecting tunnel sections.	Deterministic fractures added at 69 head calibration sections. Transmissivity of these deterministic fractures set at 1.6×10^{-8} m^2/s to reduce excessive drawdowns.
Connection to North	Connection to north added in order to draw in more Glacial-rich water to deeper control points.
Transport Aperture	Aperture = 10 * Transmissivity$^{0.5}$
Boundary Conditions	
North, South, East & West sides	Conditioned to the values reported in Svensson (1999).
Base	No flow boundary assigned to each node.
Baltic Sea	Head of 0.0 m. Skin of $0.01*T_{original}$ added to upper 10m.
Äspö Island	Group flow boundary condition added equivalent to net infiltration of 30 mm/year.
Geochemistry	
Chemical Composition	End-member definitions and proportions calculated using the program M^3 (Laaksoharju, M., 1999).
Interpolation Scheme	Linear interpolation from a grid of 1000 locations provided in Data Delivery No. 4

4.2 PREDICTIVE SIMULATIONS

The G-3 geochemical model was then used as the basis for the Stage 2, geochemical model predictions. The model predictions are reported in Appendix B.

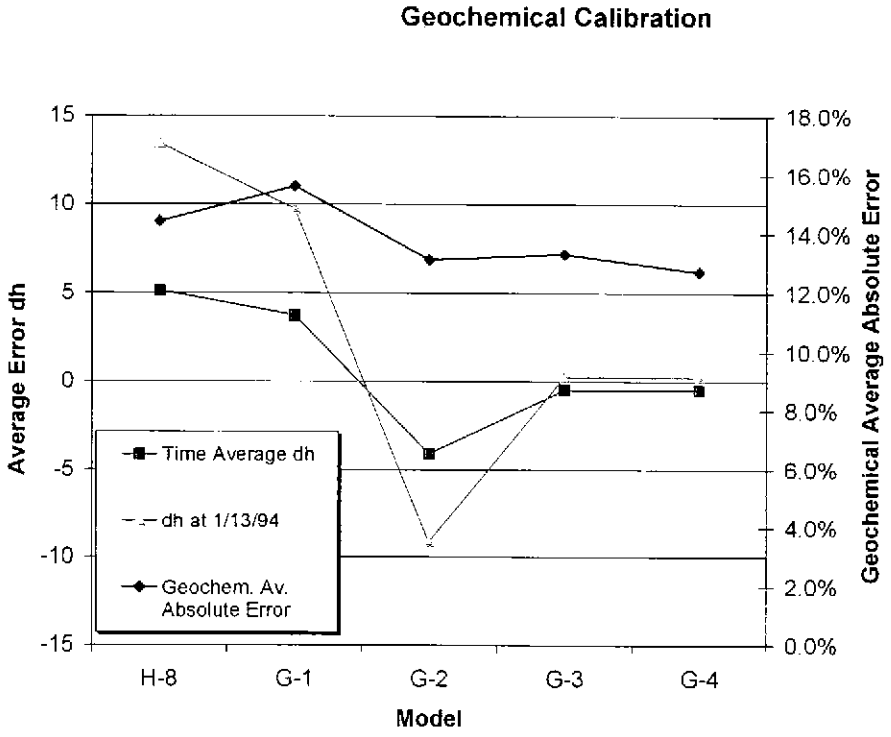

Figure 4-1 Progress of Geochemical Calibration

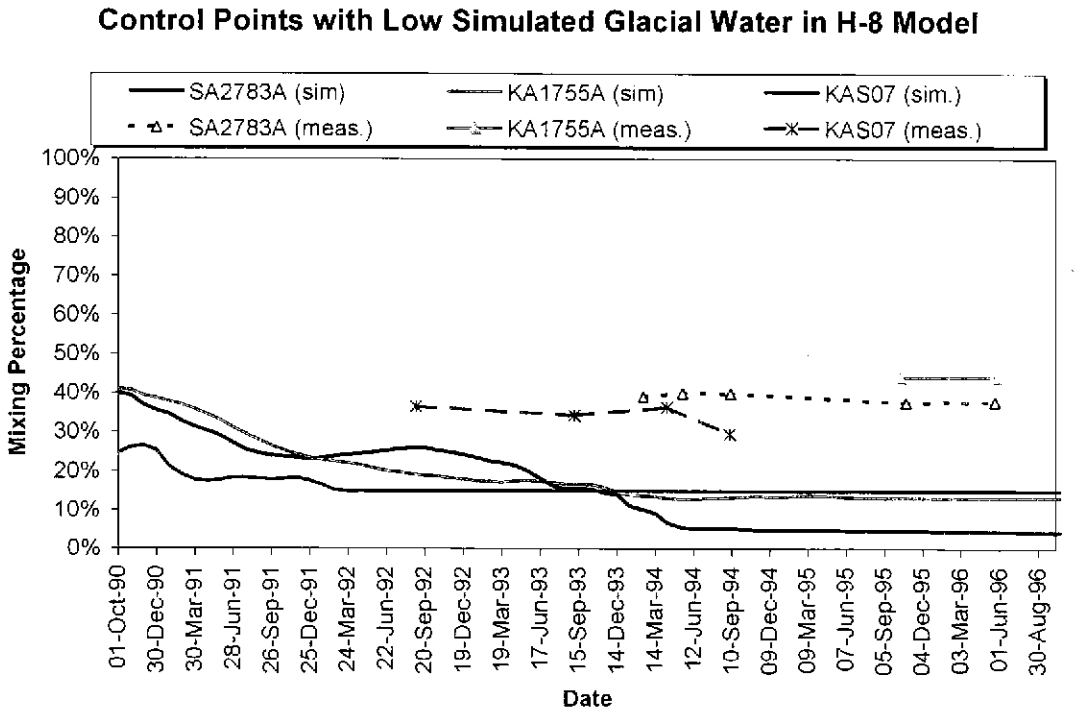

Figure 4-2 Glacial Water in Model H-8

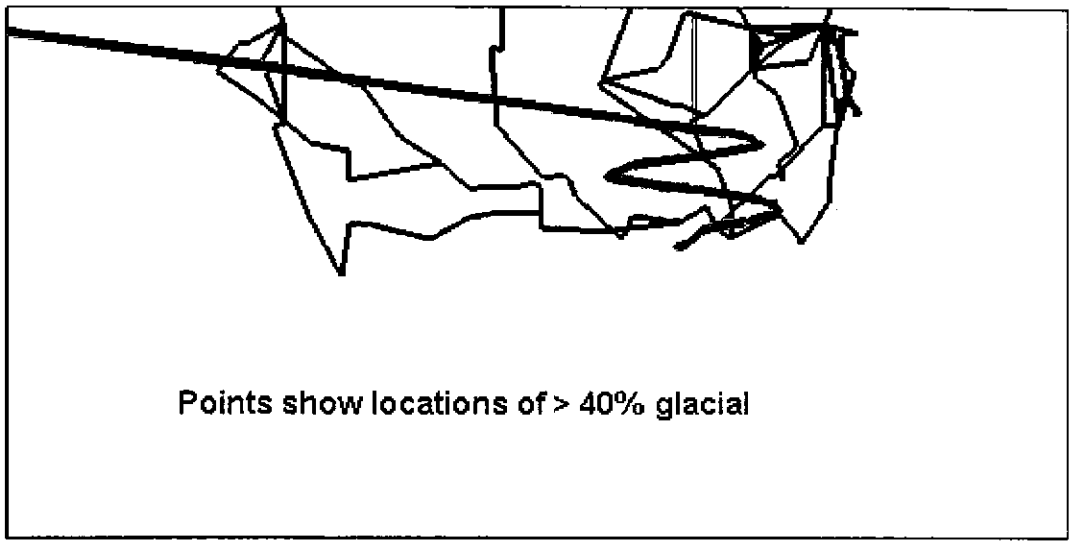

Figure 4-3 Pathways to Glacial Water in Model H-8

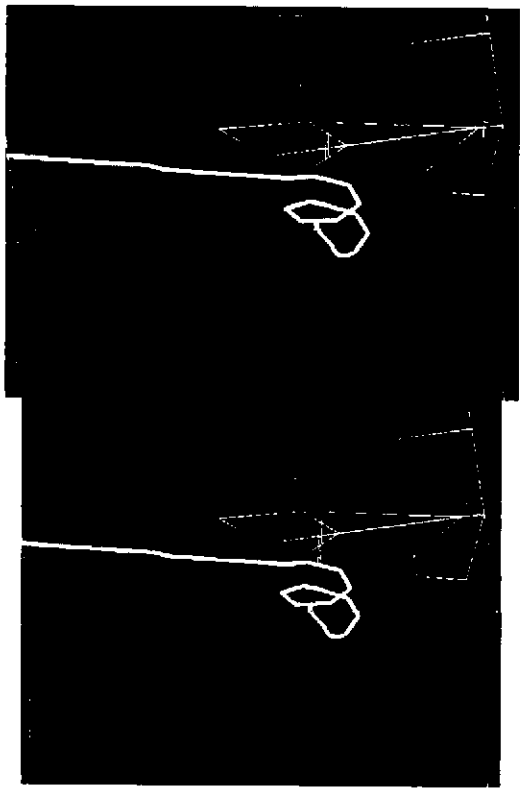

Figure 4-4 Modification to Structural Model for Geochemical CalibrationFigure on top shows original structural model with NNW-5 truncating near the latitude of the tunnel. Figure on the bottom shows the extension of this feature north, into the glacially rich groundwater zone.

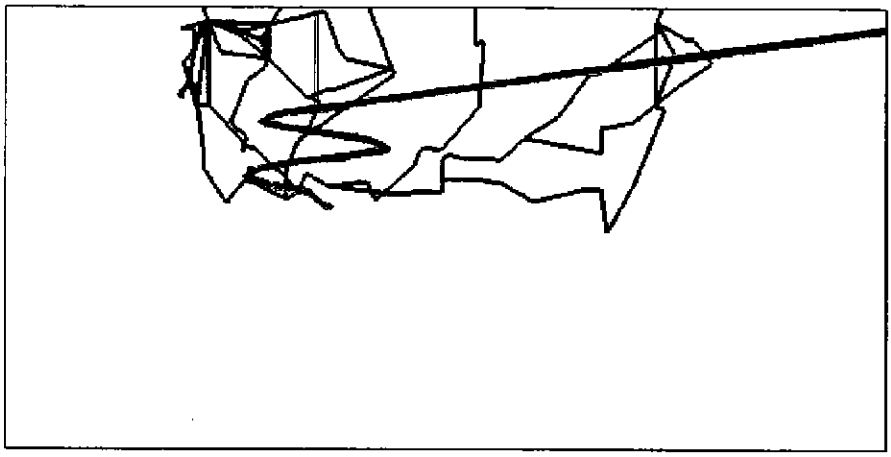

(a) Model G-1: No pathway to Glacial water

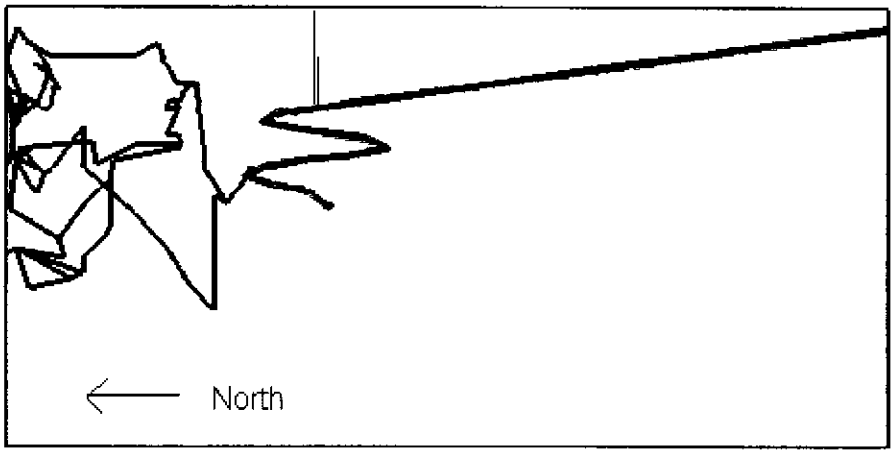

(b) Model G-3: Pathways to Glacial water at north

Figure 4-5 Pathways to Glacial Water in Model G-1

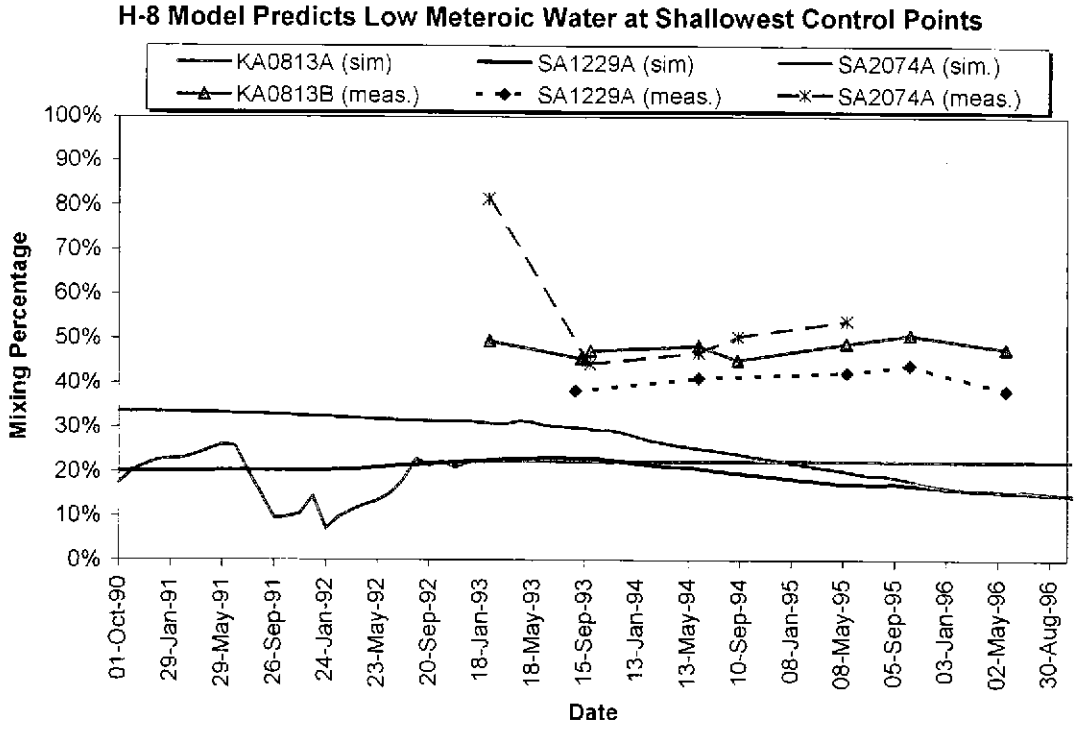

Figure 4-6 Meteoric Water in Model H-8

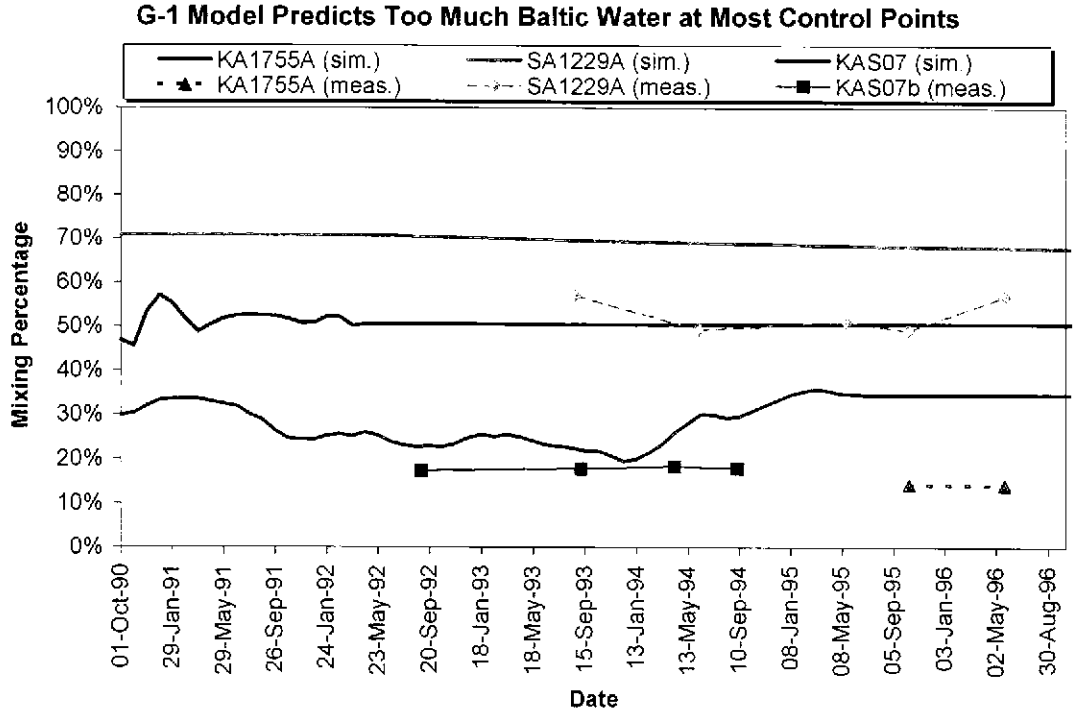

Figure 4-7 Baltic Sea Water in Model G-1

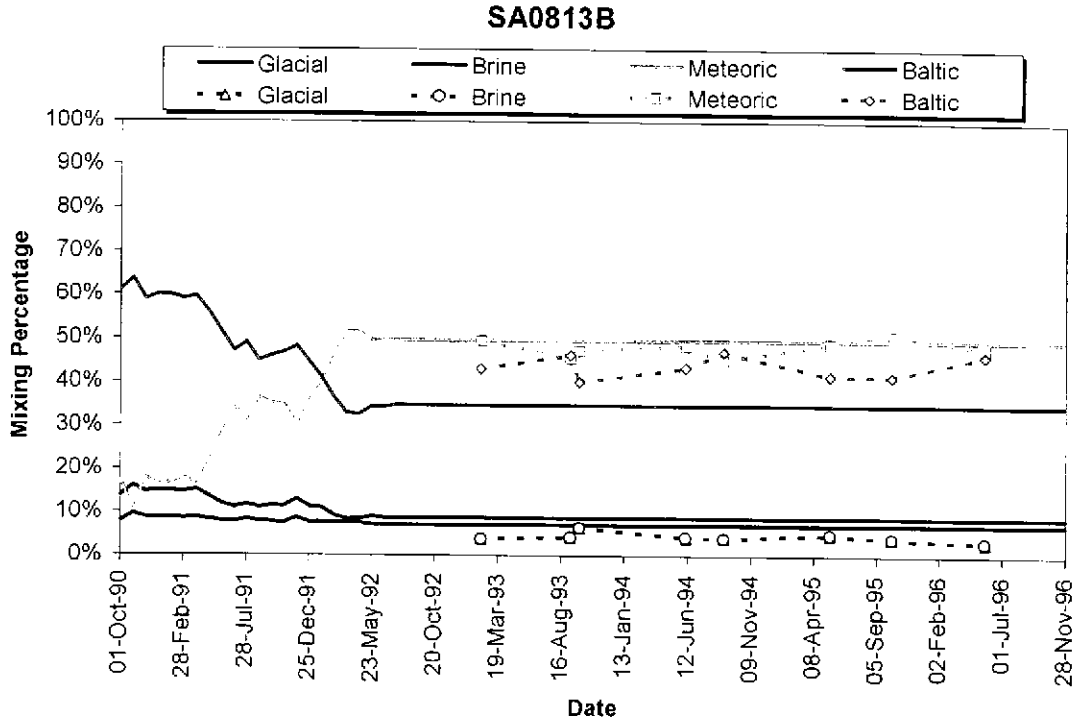

Figure 4-8 Geochemical Calibration, SA0813B of Model G-2

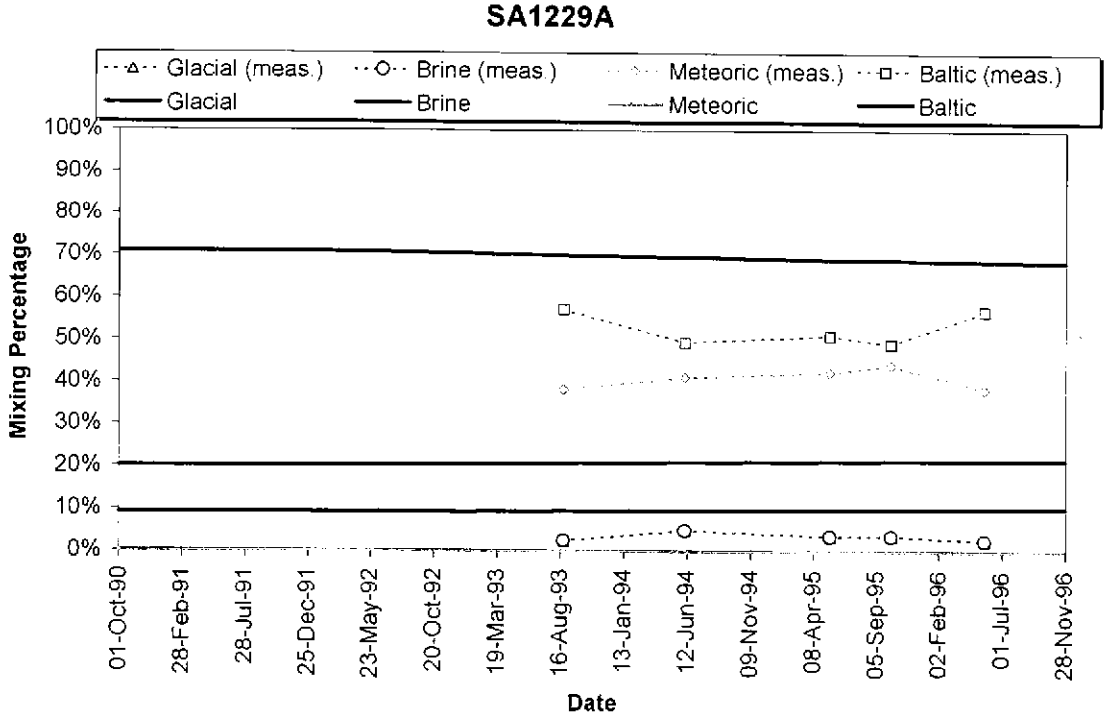

Figure 4-9 Geochemical Prediction, SA1229A of Model G-4

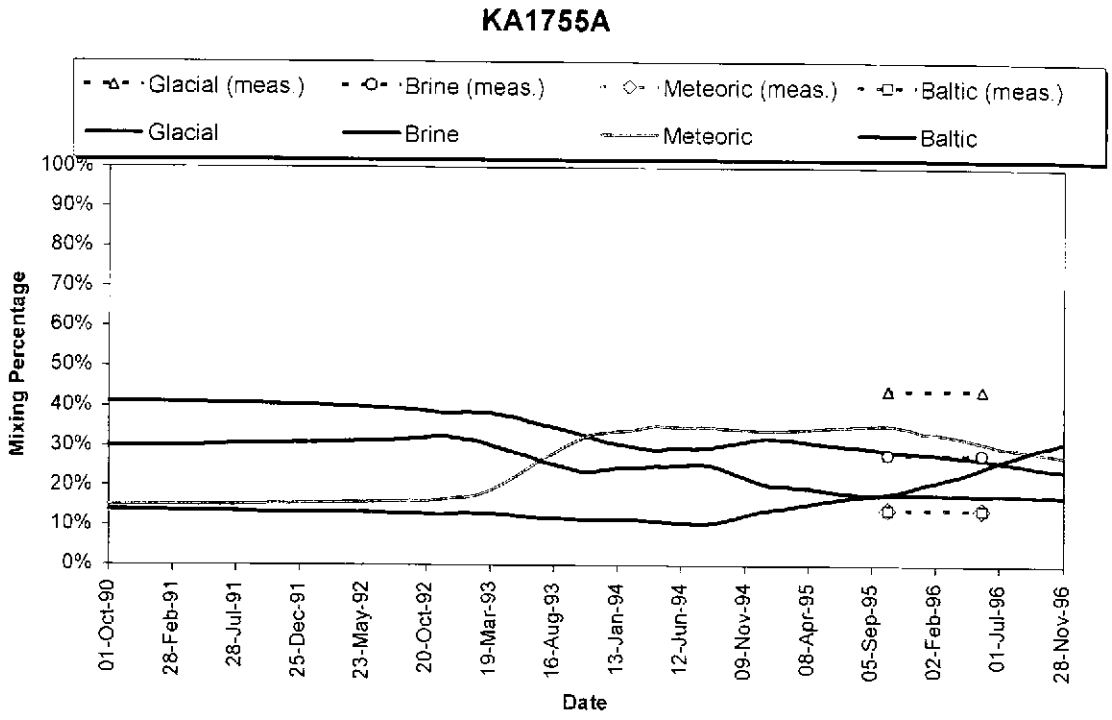

Figure 4-10 Geochemical Prediction, KA1755A of Model G-4

5. EVALUATION

A demonstration of consistency between physical hydrogeological models and hydrogeochemical models is a key goal of Task 5. Such a demonstration builds general confidence in the models. The smaller the uncertainties in models that are shown to be consistent, the greater will be the improvement in this confidence.

In the modeling approach adopted by JNC/Golder two main groups of hydrogeochemical uncertainties are important:

- Uncertainties in the initial spatial distributions of chemically distinct groundwaters;
- Uncertainties in the chemistry and mixing proportions of different end-members.

This section is concerned with the second group of hydrogeochemical uncertainties.

To represent this uncertainty additional numerical analysis was undertaken considering three issues:

Issue 1: Uncertainty introduced to the analysis by the use of the four M3 geochemical end members.
This was addressed by using a multivariate analysis for end members with lower residual error.

Issue 2: Pathway analysis limitations related to using a graph theory algorithm.
This was addressed by replacing the graph theory pathway analysis with a new particle backtracking algorithm to improve pathway identification

Issue 3: Spatial interpolation of initial conditions.
This was addressed by using an interpolation scheme that was weighted to reflect fracture zone geochemistry patterns, and to distinguish between waters under Äspö island from those beneath the Baltic.

The details of this analysis are presented in Sections 5-1 to 5-5.

5.1 GEOCHEMICAL ISSUES

5.1.1 Importance of Uncertainties in End-Member Compositions and Mixing Proportions

A demonstration of consistency between physical hydrogeological models and hydrogeochemical models is a key goal of Task 5. Such a

demonstration builds general confidence in the models. The smaller the uncertainties in models that are shown to be consistent, the greater will be the improvement in this confidence.

In the modeling approach adopted by JNC/Golder two main groups of hydrogeochemical uncertainties are important:

- Uncertainties in the initial spatial distributions of chemically distinct groundwaters;
- Uncertainties in the chemistry and mixing proportions of different end-members.

This section is concerned with the second group of hydrogeochemical uncertainties.

5.1.2 Definitions

Three definitions in particular are important in the following discussion:

- **End-member:** In the present context, this term simply means a water at the extreme of a compositional range (c.f. Bates and Jackson, 1980). Thus, the definition of an end-member depends upon the precise compositional range of interest and does not necessarily imply anything about the origin of the water; an "end-member" may be a mixture of other waters, which have simply not been identified.
- **Principal Component:** This term refers to a mathematical component derived during Principal Component Analysis (PCA). Each principal component is an eigenvector of a variance-covariance or correlation matrix and represents an independent contribution to the variability of the system being analyzed (e.g. Davis, 1986).
- **Chemical component:** This term refers to any chemical entity used to describe the chemistry of a system. Unlike phases (gas, liquid etc) or species (Fe^{2+}, Cl^- etc), which are real entities, chemical components are abstract quantities that may be defined in any convenient manner (Nordstrom and Munoz, 1994). For example, the formation of water, H_2O can be described in terms of the components H and O ($2H + O = H_2O$), or in terms of the components H2 and O2 ($H_2 + 0.5O_2 = H_2O$). While chemical components are often selected to be *real* chemical entities within a system (e.g. H_2O), this is not always the case.

Thus, in the present report a principal component derived from a set of chemical data always corresponds to a chemical component. However, the reverse is not true and there is not always a principal component that corresponds to a chemical component.

5.1.3 Justification for End-Member Modeling

Task 5 aims to predict the chemistry of water flowing into the Äspö tunnel, using knowledge of the initial spatial distributions of chemically distinct

groundwaters and simulations of mixing based upon an understanding of physical hydrogeology. Therefore, it is required to:

- Distinguish variations in chemical components that reflect only mixing over the time-scale of the investigations at Äspö (i.e. to neglect the effects of variations caused by water/rock interactions); and
- Reduce the number of alternative interpretations of mixing (ideally a unique interpretation of mixing is sought, though in practice this may not be possible).

By modeling based upon PCA it is possible in principle to meet both goals. This approach can distinguish correlations between several chemical components that reflect only mixing. Then, by identifying these correlations with variations in the proportions of end-members, it is possible to interpret groundwater mixing based upon a range of chemical components. This interpretation is likely to be less ambiguous than one based upon only a single chemical component, such as chloride (for example).

5.1.4 Approach to Evaluation

The initial modeling conducted by JNC/Golder used the compositions of end-members and mixing proportions of these end-members calculated by SKB using the computer code Multivariate Mixing and Mass balance (M3; Rhén et al. 1997; Laaksoharju, 1999a; Laaksoharju et al. 1999b). These compositions and mixing proportions were presented in Data Delivery 19, released by SKB on 15th December 1999 (delivery reference F65H).

The initial evaluation involved reviewing the M3 methodology; to identify and evaluate uncertainties of particular relevance to JNC/Golder's modeling approach. As part of this review, a series of questions were written concerning M3 and submitted to SKB. These questions were answered in Laaksoharju (2000).

From this initial evaluation it was apparent that the M3 approach did not consider all the variability in the chemical data (see below). Additionally, it was not clear to what extent the method would be generally applicable to groundwater systems other than systems like the one at Äspö, within which saline waters and brines occur. Therefore, a new statistical model was commissioned by JNC from Golder Associates, who sub-contracted the work to the British Geological Survey (BGS). This new model considered all the chemical variability in the data. Several possible alternative combinations of input data were considered, besides the data used in the original M3 modeling.

Finally, a comparison was made between the results of the new modeling and the original M3 modeling.

5.1.5 Summary of M3 Modeling

Statistical processing of analyses of these waters was undertaken by SKB's contractors using the computer code Multivariate Mixing and Mass balance (M3). This modeling has been described in detail elsewhere (Rhén et al. 1997; Laaksoharju, 1999a; Laaksoharju et al. 1999b) and only a brief overview is given here, to allow the following discussion of uncertainties to be understood. The basic approach is illustrated in Figure 5-1.

The M3 code was used to perform PCA, enabling groups of chemically similar waters to be identified. This modeling did not use analytical data for all the groundwaters' constituents, but only data for Na, K, Ca, Mg, HCO_3, Cl, SO_4, D, Tr, and ^{18}O. Most of the chemical variability in the waters (c. 70%) was attributed to just two principal components. These two components were considered to reflect mixing, rather than other potential contributors to chemical variability, such as water/rock reactions, contamination during sampling or, in the case of tritium, radioactive decay. These other possible contributors to chemical variability were represented by the other principal components. For example, the third principal component was considered to reflect the decay of tritium.

The groundwaters were plotted on a cross-plot, with axes representing the two principal components that represented most of the variability. The plotting position of each water was determined by the corresponding eigen values. When plotted in this way, the groundwaters define a field that can be surrounded by a polygon, having the most extreme groundwater compositions as its apices. Some of these compositions were chosen as "reference" compositions. The proportions of these compositions that would be required to mix to form each of the groundwaters within the polygon were then calculated, by assuming that the reference compositions mix conservatively (that is, without any chemical reactions occurring). A center point within the polygon was used to allow the proportions of more than three reference samples to be calculated. The proportion of any reference water in any other water of interest was assumed to be inversely proportional to the distance between the reference water and the water of interest on this bivariate plot. For each water, the mixing proportions calculated in this way were used together with the actual compositions of the reference waters to calculate theoretical concentrations of the chemical constituents on the water. The resultant theoretical composition was then compared with the actual composition of the water. Deviations from the actual compositions were assumed to be due to chemical reactions between the waters and the rocks.

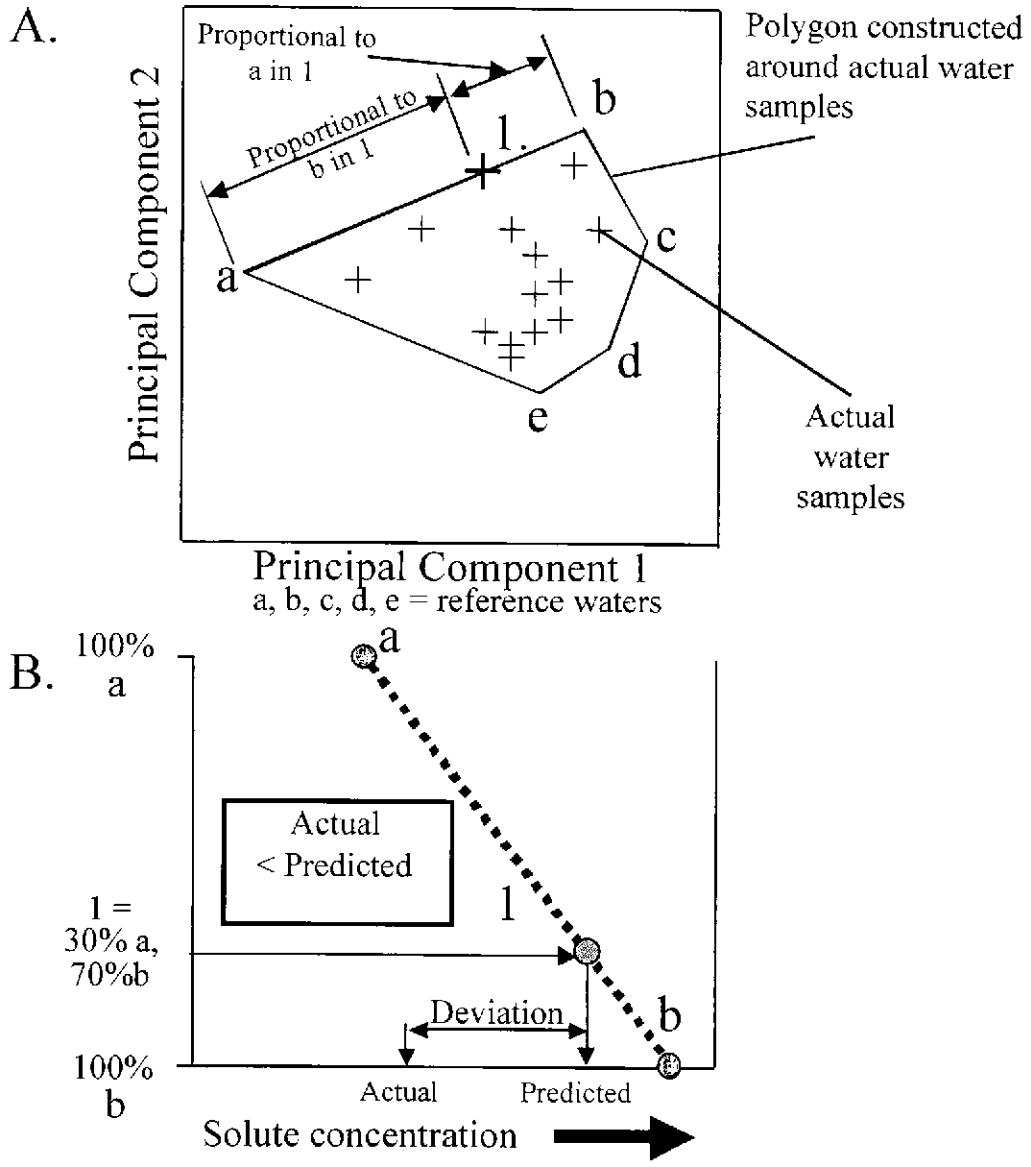

Using the eigen values, waters are plotted on the two most important principal components identified by PCA. The points are enclosed by a polygon with apices representing reference waters that are assumed to mix to form the actual waters. The proportions of the reference waters in each other water are derived geometrically. B. Theoretical concentrations of solutes in each water are calculated from these proportions and compared with actual concentrations. Differences between the values are generally attributed to water/rock interactions, in the case of potentially reactive constituents, like Na. Deviations in relatively non-reactive solutes, like Cl, may imply that that the assumption of mixing between the chosen reference waters is invalid.

Figure 5-1 Schematic illustration of the M3 approach

During the Task 5 work, the waters were all reported to be mixtures of the following end-members:

- Brine;
- Glacial water;
- Meteoric water; and
- Baltic Sea water.

5.1.6 Key Assumptions and Uncertainties in the M3 Modeling

The most significant causes of uncertainties in the end-member compositions and mixing proportions calculated by M3 (Laaksoharju, 2000) are:

- Sampling errors due to effects such as borehole drilling, pumping, contamination etc;
- Errors caused due to the analytical methods;
- Conceptual errors, such as the following assumptions being incorrect:

  - the assumption that the number of end-members have been correctly identified;
  - the assumption that all waters are mixtures of all end-members;
- Methodological errors, notably caused by:

  - the model being over-simplified or biased, for example by neglecting trace constituents of the groundwaters from the PCA and assuming that the end-members can be defined adequately by a sub-set of the constituents;
  - the simplifying assumption that the two most important principal components reflect groundwater mixing and that groundwater mixing effects are not represented significantly by any of the other components.

Sampling and analytical errors are unavoidable in any groundwater chemical investigation. These errors will affect not only the M3 modeling, but also any other modeling that uses the same chemical data. The effects of sampling errors were allowed for by evaluating the circumstances of sampling (e.g. rejecting samples collected during hydraulic tests that experienced difficulties). Contamination effects were minimized by using tracers in the drilling fluid and using samples for which contamination from this source was indicated to be less than 1% (Laaksoharju, 2000). The uncertainty from sampling errors was estimated/modeled to be in most cases around ± 10% from the undisturbed, *in-situ* values. Analytical errors for different elements vary but inter-laboratory comparisons indicate generally a deviation of 1-5% in the values (Laaksoharju et al., 1999a, b; Laaksoharju, 2000).

The choice of end-members is inevitably subjective. However, to minimize the chances of inappropriate end-members being chosen, these end-

members were selected to be consistent with both distributions of samples on the plot of the two principle components and an independent hydrogeochemical conceptual model. This latter suggested which type of water might have entered the bedrock and employed additional geological information and data from fracture minerals. The model was consistent with the choice of reference waters (glacial meltwater, seawater, meteoric waters) being appropriate for describing mixing in the groundwater system used to guide the minimum number and type of end-members needed to explain the observations.

Alternative mixing proportions were calculated using alternative possible end-members. These alternative end-members were chosen to be consistent with both the independent hydrogeochemical model and the ranges of groundwater compositions on the bivariate plot of the first two principal components (Laaksoharju, 2000). This approach suggested that the error in mixing proportions due to an incorrect selection of end-members was on the order of 10%.

The third principal component accounts for around 10% of the groundwaters' chemical variability. This is small compared with the first and second principal components which contain account for about 70% of the variability; the remaining principal components encompass the other 20% of the variability (Laaksoharju, 2000).

The location of a sample on the plot of the first and second principal components can be inappropriate because of all the errors mentioned above. Laaksoharju et al. (1999a,b) and Laaksoharju (2000) allowed form this by stating the uncertainty in the method to be ± 0.1 mixing proportion units and the detection limit for the method as <10% of a mixing portion.

5.1.7 Summary of Revised Modeling

There are several limitations to applying the M3 modeling in JNC/Golder's approach, notably:

- One goal of JNC/Golder is to evaluate how the basic Task 5 method might be applied in Japan. However, the M3 method was developed for application at Äspö where saline groundwaters and brines are major features of the groundwater system. The method may not be generally applicable. In particular, the reliance of the method on the first two principal components may not be appropriate in fresh groundwater systems. In such cases the first two principle components are more likely to reflect factors other than groundwater mixing. For example, water/rock interactions are likely to be a more significant cause of chemical variation in fresh groundwater systems than in saline groundwater systems. In such cases, it will be necessary to consider other principal components besides the two most important ones, in order to deduce information about groundwater mixing.

- By not considering principal components other than the first two, M3 potentially disregards important information that might be used to evaluate more precisely the validity of the underlying assumptions, such as the assumption that all end-members are present in all waters.
- While sensitivity calculations were conducted by SKB and its contractors to evaluate underlying uncertainties in the M3 method (Laaksoharju, 2000), the results of these calculations have not been reported in detail. Therefore, the precise significance of these uncertainties for JNC/Golder's modeling approach is not clear.
- Even though the end-members used in the M3 modeling were chosen with reference to a hydrogeochemical model for the site, there is still considerable subjectivity in their selection. The chosen end-members, while having extreme compositions near the limits the range of sampled waters compositions, are themselves mixtures of other waters. Additionally, some chemically similar waters have probably been introduced into the groundwater system at Äspö several times during the site's history. For example, sub-glacial water has presumably been recharged several times during the repeated glaciation of the site within the Quaternary period.

For these reasons, it was decided to carry out revised modeling, using a chemometric algorithm (Cave and Harmon 1997, Cave and Wragg 1997), which makes no initial assumptions about the nature of the end-members present, and which considered all the contributions to chemical variability in the groundwaters.

The basic approach is illustrated in Figure 5-2 and Figure 5-3. Here matrix **A** is the supplied groundwater data matrix and matrices **B** and **C** need to be found. The process for finding matrices **B** and **C** was carried out in a four-stage process:

- PCA and eigenvalue analyses were initially used in a similar fashion to the M3 method.
- The varimax rotated loadings matrix from the PCA of matrix **A**, containing the initial groundwater compositions, were used to produce a first approximation of matrix **B**, which contains the mixing proportions.
- The "pseudoinverse" method for non-square matrices was then applied to matrices **A** and **B**, to produce a first approximation of matrix **C**, which contains chemical components that contribute to the chemical variability in the groundwaters, some of which should correspond approximately to end-members.
- Matrices **B** and **C** were refined iteratively using the "pseudoinverse" method until both matrices contained estimates of mixing proportions and chemical component compositions that are consistent with the groundwater compositions in the original matrix **A.**

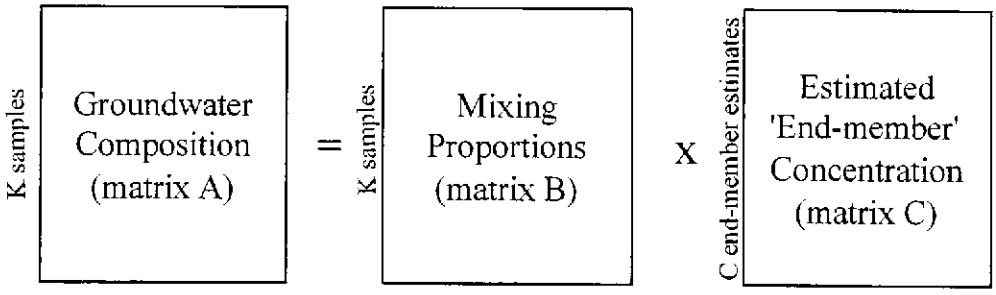

Figure 5-2 Relationships between matrices used in the revised modeling

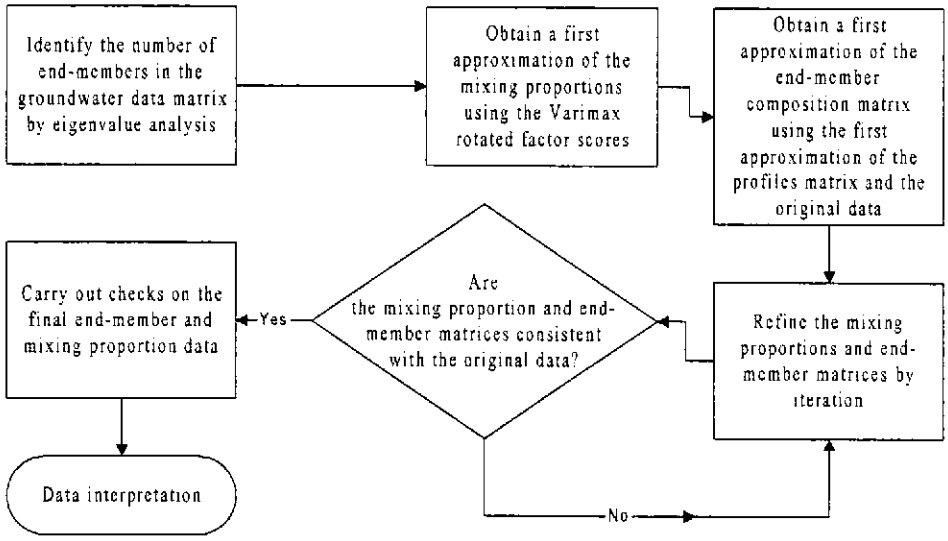

Figure 5-3 Summary of the procedure adopted in the revised modeling

It is important to note that the chemical components obtained from the new modeling are not principal components, but are derived from the principal components. Neither are the chemical components "end-members" in the sense of the M3 end-members. However, it is expected that there should be some similarities between compositions of the new chemical components and the M3 components.

To compare the results of the new modeling and the results of the M3 end-member modeling, the new mixing proportions were also expressed in terms of proportions of the original M3 end-members. This was done by a least-square approach, using the proportions of the new chemical components in each of the original M3 end-members and in each of the other waters as follows.

Several alternative cases were evaluated during the new modeling (Table 5-1). Some of these cases used exactly the same data as was used to produce the M3 model results in Data Delivery 9. This approach was to allow comparison of the results between the two methods. Other cases used a sub-set of this data, to explore the significance of departures from this approach.

Table 5-1 Summary of the cases considered in the revised modeling

Case	Determinands Considered	Water Compositions Used	Other Model Details
Model 1	Na, K, Ca, Mg, HCO_3, Cl, SO_4	All waters in Data Delivery 19, except for (Brine, Baltic Sea Water, Glacial Water and Meteoric Water, which were employed as end-members in the M3 modeling, and Sea Water, which was not employed in the latest M3 modeling)	Three separate models, using the different combination of water samples shown at the left Modeling was not carried out separately for high TDS samples as there were insufficient data in this group (6 samples)
		Samples in Data Delivery 19 with medium Total Dissolved Solid (TDS) contents (Cluster 1) (Brine, Baltic Sea Water, Glacial Water Meteoric Water, and Sea Water excluded from consideration)	
		Samples in Data Delivery 19 with low TDS contents (Cluster 2) (Brine, Baltic Sea Water, Glacial Water Meteoric Water, and Sea Water excluded from consideration)	
Model 2	Na, K, Ca, Mg, HCO_3, Cl, SO_4, D, Tr, $\delta^{18}O$	All waters in Data Delivery 19, except for (Brine, Baltic Sea Water, Glacial Water and Meteoric Water, which were employed as end-members in the M3 modeling, and Sea Water, which was not employed in the latest M3 modeling)	δD and $\delta O18$ values were multiplied by –1 to make them positive numbers.

Case	Determinands Considered	Water Compositions Used	Other Model Details
Model 2 (v3)	Na, K, Ca, Mg, HCO_3, Cl, SO_4, δD, Tr, $\delta^{18}O$	All waters in Data Delivery 19, except for (Brine, Baltic Sea Water, Glacial Water and Meteoric Water, which were employed as end-members in the M3 modeling, and Sea Water, which was not employed in the latest M3 modeling)	Tritium data were used as reported. δD and $\delta^{18}O$ data were converted from per mil values to D/H and $^{18}O/^{16}O$ ratios for the purposes of the modeling and converted back to per mil values at the end
Model 2 (v5)	Na, K, Ca, Mg, HCO_3, Cl, SO_4, δD, Tr, $\delta^{18}O$ [8]	All waters in Data Delivery 19, INCLUDING Brine, Baltic Sea Water, Glacial Water and Meteoric Water, which were employed as end-members in the M3 modeling. Sea Water, which was not employed in the latest M3 modeling, was not included)	
Model 3	Na, K, Ca, Mg, HCO_3, Cl, SO_4, δD, $\delta^{18}O$	All waters in Data Delivery 19, except for (Brine, Baltic Sea Water, Glacial Water and Meteoric Water, which were employed as end-members in the M3 modeling, and Sea Water, which was not employed in the latest M3 modeling)	The model differs from Model 2(v3) only in that Tritium data were excluded

5.1.8 Key Assumptions and Uncertainties in the Revised Modeling

Unlike the original M3 modeling, the new model makes no prior assumptions about the numbers or compositions of chemical components (analogous to end-members in the M3 modeling). However, other assumptions are made, notably:

- the compositions of at least some of the chemical components derived statistically will approximate real groundwater compositions;
- the assumption that δ–values for ^{18}O and D are additive over the range considered is valid; and
- that all the chemical variability in the groundwaters is expressed by the chemical constituents (Na, Ca, Cl etc) used in the modeling, which form a subset of the actual constituents.

These last two assumptions were also made in the M3 modeling.

5.1.9 Results of the new modeling

All the results of the new modeling are tabulated in Appendix C. The compositions of the chemical components obtained from each model are compared with the compositions of the groundwater end-members used in the M3 modeling in Table 5-2. It is important to note that the chemical components are not placed in order of significance for the overall chemical variations; they are not principal components, though they are derived from principal components. Additionally, chemical components designated by

the same number, but produced by different models are not necessarily equivalent.

None of the models in Table 5-2 produced components with the same compositions as the "end-members" used in M3. This result is expected since:

- The new approach makes no *a priori* assumptions about the compositions of waters that mix to form the sampled waters.
- The new approach is aims to identify chemical components of the groundwaters, which reflect underlying *processes* rather than actual groundwaters.
- Even if some of the components do represent possible natural waters, it is not unexpected that they differ from the M3 end-members. These latter are simply waters of extreme composition chosen by the user of M3; some of these M3 end-members are themselves mixtures of other waters. It is these "other waters" that could potentially be identified by the new approach.

Several underlying features are common to the results of all models:

- There are usually three or four chemical components that are close to charge balance. Potentially, these could represent the compositions of actual waters.
- The charge-balanced chemical components in any model are broadly similar to the charge-balanced chemical components produced by the other models (though as noted previously, the numbers used to designate a particular chemical component may change from model to model).
- There are always components that do not charge balance. These chemical components cannot represent actual waters, but instead possibly represent other processes such as water/rock interactions.
- In all the models, there is at least one component that contains HCO_3 and little else. It is possible that this component reflects microbial activity, notably the oxidation of organic matter. Microbial processes were also suggested to be important, based on the M3 modeling (Laaksoharju et al. 1999b).

By comparison between the results of different models, several general conclusions can be drawn:

- Model 1 showed that a single consistent model for the solutes in the water could not be produced without the inclusion of stable oxygen and hydrogen isotope data and tritium data. When these data were not included, the waters had to be divided into three groups to ensure a self-consistent result.
- The inclusion or omission of tritium from the model does make a significant difference to the compositions of all the chemical

components, except the most saline component (comparison of Models 2 (v3) and Model 3).

- Addition of a small number of waters of extreme composition to a data set could have a small but significant effect on the compositions (and hence proportions) of the chemical components (comparison of Model 2 and Model 2(v5)).

The relatively large effect of tritium on the results is important, because this isotope is radioactive with a half-life of only 12.43 years. Therefore, considerable decay of tritium must have occurred during the investigations at Äspö, which have lasted more than 10 years. Variations in the reported tritium values will generally not reflect only groundwater mixing. Thus, tritium cannot be considered a conservative tracer for groundwater flow. The fact that the inclusion or omission of tritium significantly affects most of the chemical components in the present model means that errors due to its radioactive decay cannot be allowed for just by neglecting a single component. Thus, it would strictly be more appropriate to exclude tritium from consideration altogether.

Notwithstanding this potential drawback, the results of Model 2 (which includes tritium) were used with the groundwater flow model to predict the compositions of inflows to the tunnel. The reason for using these results was that Model 2 employed the same data as the original M3 modeling (which included tritium). Thus, the predictions based on the revised statistical modeling could be compared more easily with the original M3 modeling results.

Table 5-2 Compositions of end-members used in M3 modeling, reported previously by Laaksoharju et al. (1999b) and the results of JNC/Golder's modeling

Compositions of end-members reported previously (From M3 modeling, reported in SKB's data Delivery 19)											
	Na	K	Ca	Mg	HCO3	Cl	SO4	O18	D	Tr	Bal
Brine ref. w	8500	45.5	19300	2.1	14.1	47200	906	-8.9	-44.9	4.2	-0.6
Baltic Sea ref. w.	1960	95	93.7	234	90	3760	325	-5.9	-53.3	42	-1.2
Glacial ref. w	0.2	0.4	0.2	0.1	0.12	0.5	0.5	-21	-158	0	13.6
Meteoric ref. w.	0.4	0.3	0.2	0.1	12.2	0.2	1.4	-10.5	-80	100	-67.9
Model 1											
Chemical Component	Na	K	Ca	Mg	HCO3	Cl	SO4	O18	D	Tr	Bal
All Data											
1	641	23.8	0.00	270	507	0.00	0.00	N.I.	N.I.	N.I.	71.8
2	5663	0.00	10607	0.00	0.00	27529	742	N.I.	N.I.	N.I.	-1.0
3	2342	76.5	1227	214	0.00	6434	448	N.I.	N.I.	N.I.	-2.2
4	0.0	0.0	0.0	0.0	476	0.0	0.0	N.I.	N.I.	N.I.	-100.0
5	767	16.8	0.0	57.5	103	484	466	N.I.	N.I.	N.I.	21.2
Cluster 1 – Medium TDS Samples											
1	3896	0.0	4631	0.0	3367	12845	0.0	N.I.	N.I.	N.I.	-2.1
2	3168	242	0.0	593	242	6241	293	N.I.	N.I.	N.I.	1.8
3	2765	7.5	3759	9.9	0.0	10946	547	N.I.	N.I.	N.I.	-1.8
4	825	0.0	0.0	0.0	0.0	578	747	N.I.	N.I.	N.I.	6.0
5	1225	0.2	0.0	214	131	1615	0.0	N.I.	N.I.	N.I.	19.6
Cluster 2 – High TDS samples											
1	1730	8.5	1089	27.8	0.0	4864	149	N.I.	N.I.	N.I.	-3.0
2	0.00	0.0	0.0	0.0	335	0.0	1.2	N.I.	N.I.	N.I.	-100.0
3	889	2.0	448	0.0	534	1718	422	N.I.	N.I.	N.I.	-3.9
4	70.7	10.7	0.0	27.7	0.0	259	0.0	N.I.	N.I.	N.I.	-13.0
5	179	2.1	0.0	147	682	0.0	0.0	N.I.	N.I.	N.I.	28.2
Model 2											
Chemical Component	Na	K	Ca	Mg	HCO3	Cl	SO4	O18	D	Tr	Bal
1	8508.6	5.1	17235.0	0.0	47.1	44001.5	800.3	-11.8	-75.7	14.6	-1.1
2	2066.3	0.0	1379.1	169.1	225.4	6163.5	0.0	-8.8	-68.5	0.0	-1.4
3	456.9	5.5	258.4	16.7	0.0	1207.9	79.8	-12.4	-94.2	0.0	-2.1
4	0.0	1256.2	0.0	2020.1	505.6	0.0	0.0	0.0	0.0	492.0	92.0
5	0.0	0.0	0.0	0.0	22039.5	0.0	0.0	0.0	0.0	0.0	-100.0
6	0.0	0.0	0.0	0.0	298.8	0.0	0.0	0.0	0.0	391.5	-100.0
7	2021.3	17.8	205.4	8.0	0.0	3230.3	1284.4	-14.3	-107.9	0.0	-8.6

N.I. = Not included. Values that appear to be zero are actually very small numbers.

Table 5-2 Continued

Model 2 V3											
Chemical Component	Na	K	Ca	Mg	HCO3	Cl	SO4	O18	D	Tr	Bal
1	11782.6	26.8	23756.3	0.0	0.0	60832.1	1119.8	-14.5	-92.4	0.0	-1.2
2	5107.0	43.7	0.0	729.7	247.5	7971.5	51.6	1.3	-6.0	0.0	10.4
3	3285.6	227.3	1689.9	371.9	53.1	9018.2	923.6	1.3	3.9	66.5	-2.0
4	20187.6	287.5	44808.2	0.0	58890.3	81067.1	66.0	128.7	1167.0	477.0	-2.1
5	4.0	0.0	0.0	0.0	112.4	0.0	0.0	-11.0	-82.6	8.7	-82.7
6	3135.7	0.0	0.0	185.5	0.0	0.0	1911.2	-15.2	-119.7	0.0	58.4
7	1664.1	24.3	4004.8	131.2	462.3	9300.7	385.0	17.0	114.4	1017.0	1.0
Model 2 V5											
Chemical Component	Na	K	Ca	Mg	HCO3	Cl	SO4	O18	D	Tr	Bal
1	9045.0	33.9	18802.0	0.8	42.0	47544.9	891.7	-10.7	-64.1	0.0	-1.0
2	1975.8	0.0	1228.7	169.6	231.8	5738.2	0.0	-8.5	-66.7	6.1	-1.4
3	433.4	6.0	243.4	15.7	0.0	1140.5	75.3	-12.7	-95.9	0.0	-2.0
4	0.0	0.0	0.0	0.0	9841.4	0.0	0.0	0.0	0.0	0.0	-100.0
5	3841.4	910.2	0.0	1683.6	315.1	0.0	327.6	0.0	0.0	0.0	93.0
6	1949.8	7.1	407.0	0.0	0.0	3528.3	1147.4	-14.3	-107.9	4.2	-7.9
7	0.0	0.0	0.0	0.0	213.1	0.0	0.0	0.0	0.0	436.4	-100.0
Model 3											
Chemical Component	Na	K	Ca	Mg	HCO3	Cl	SO4	O18	D	Tr	Bal
1	11825.3	28.1	23723.5	0.0	0.0	60865.2	1121.2	-13.8	-87.9	N.I.	-1.2
2	3225.9	25.5	0.0	449.5	108.5	5046.4	47.6	-4.1	-40.5	N.I.	10.2
3	3483.6	246.3	2020.5	403.3	107.8	9950.1	960.1	3.9	22.4	N.I.	-1.8
4	39462.1	454.2	30364.5	3113.6	70548.1	90027.7	0.0	208.7	1732.3	N.I.	-2.7
5	2071.4	0.0	0.0	78.2	0.0	0.0	1595.1	-15.9	-122.3	N.I.	48.8
6	1.7	0.5	0.0	0.0	125.3	0.0	0.0	-10.6	-80.1	N.I.	-91.9

N.I. = Not included. Values that appear to be zero are actually very small numbers.

In Model 2, all the chemical variability could be attributed to 7 principal components (Figure 5-4). This suggested that 7 chemical components could be used to model the groundwater chemistry. When the 7 original principal components were adjusted by iteration, as described in Section 6.1.7, the resulting fit between the reconstructed compositions of the waters (i.e. calculated from matrices B and C above) and the actual compositions was very good for all components except for stable oxygen and hydrogen isotopes (*The difference between the line and the data points is a measure of the error. Perfectly correlated results would have coincidence of data and line.*

Figure 5-5). This approach demonstrates a high degree of internal consistency in the model. However, the model did not give a good fit for light (relatively heavy-isotope-depleted) water compositions (*The difference between the line and the data points is a measure of the error. Perfectly correlated results would have coincidence of data and line.*

Figure 5-5: note that the isotopic compositions were converted to positive values for the PCA). One possible explanation is that the waters may not all

be mixtures of the same end-members. However, additional processing would be required to evaluate this more fully.

The main features of the chemical components that were calculated by Model 2 are:

- The components in Model 2 do bear some similarity to real waters or to water/rock interactions/contamination effects:
- Chemical component 1 is broadly similar to the brine end-member identified by Laaksoharju et al.;
- Chemical component 2 is broadly similar to the seawater and/or Litorina sea water identified previously by Laaksoharju et al. (1999b);
- Chemical component 3 is broadly similar to a glacial reference water reported previously by Laaksoharju et al. (1999b);
- Chemical components 5 and 6 could potentially represent water/rock interactions and/or microbially mediated reactions;
- Chemical component 7 has some similarities to a sediment pore water identified by Laaksoharju et al. (1999b) previously.
- In support of the hypothesis that microbial action might explain component 5 is that fact that this component tends to be more abundant in waters from the redox zone monitoring boreholes, than in other boreholes. In the redox monitoring boreholes the mean is 1.2445×10^{-2}, std dev 0.0049, whereas in the other boreholes the mean is 3.9475×10^{-3}. std dev 0.0056. Microbial processes have been well documented from the redox zone.
- Component 4, produced by Model 2, is the most difficult to ascribe to a real process. This is because it is not charge-balanced and appears to contain very high concentrations of K and Mg (much higher concentrations than are in fact observed in any actual water). Possibly, component 4 could represent a water/rock interaction, such as cation exchange of Ca and Na for Mg and K. In fact, component 4 composes a maximum of only 1.77% of any actual water (and usually much lower than this). Since water/rock interactions of this kind would be expected to have a relatively small effect on the overall compositions of the predominantly saline waters, this small value is consistent with component 4 representing water/rock interactions.

The general similarity of some of the chemical components and some of the M3 end-members can be approximated by comparing Figure 5-6 and Figure 5-8. There are generally similar patterns in the depth dependence of the new chemical components and the M3 end-members.

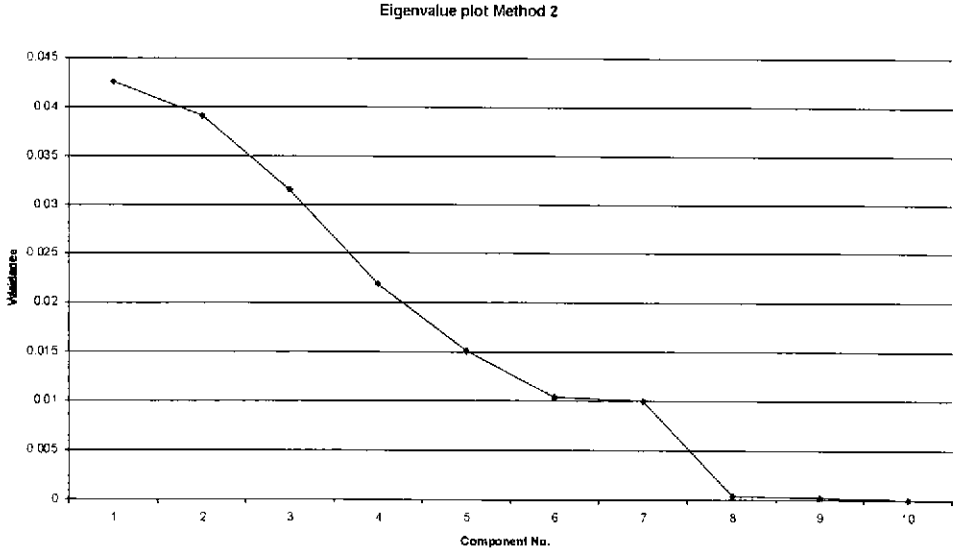

Figure 5-4 Plot showing eigenvalues, reflecting the contribution of each principal component to the overall chemical variance

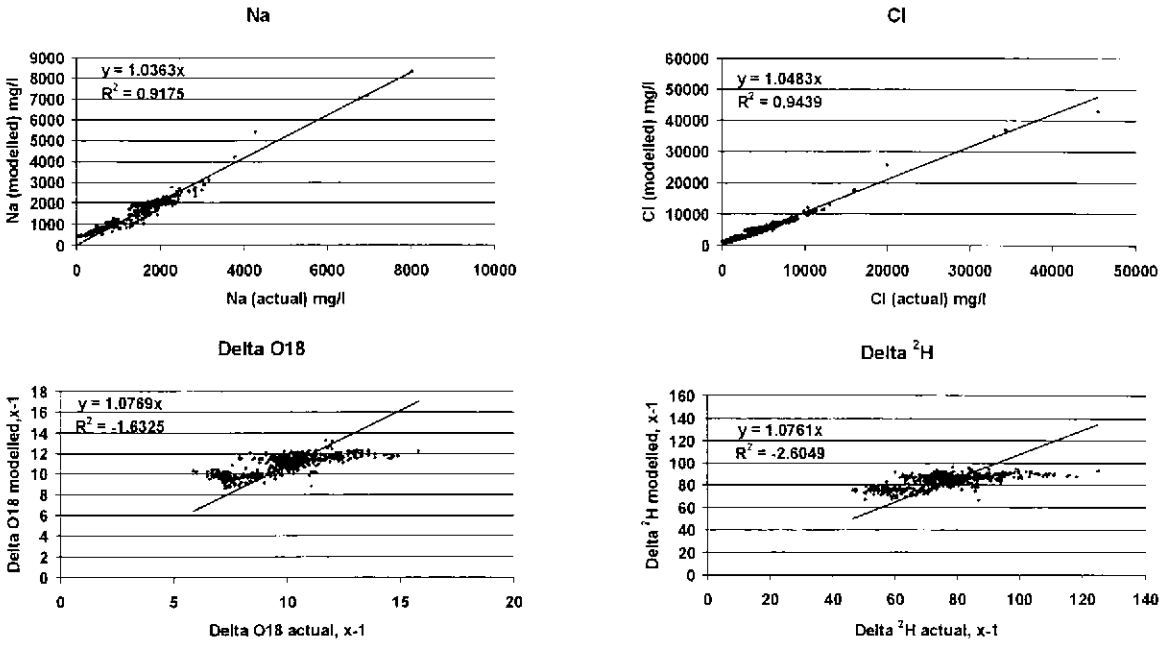

The difference between the line and the data points is a measure of the error. Perfectly correlated results would have coincidence of data and line.

Figure 5-5 Comparison between concentrations of a relatively reactive solute (Na) and relatively unreactive solutes (Cl, $\delta^{18}O$ and δH) reconstructed from the statistically derived chemical components, and the actual concentrations. Similar plots were produced for all the constituents.

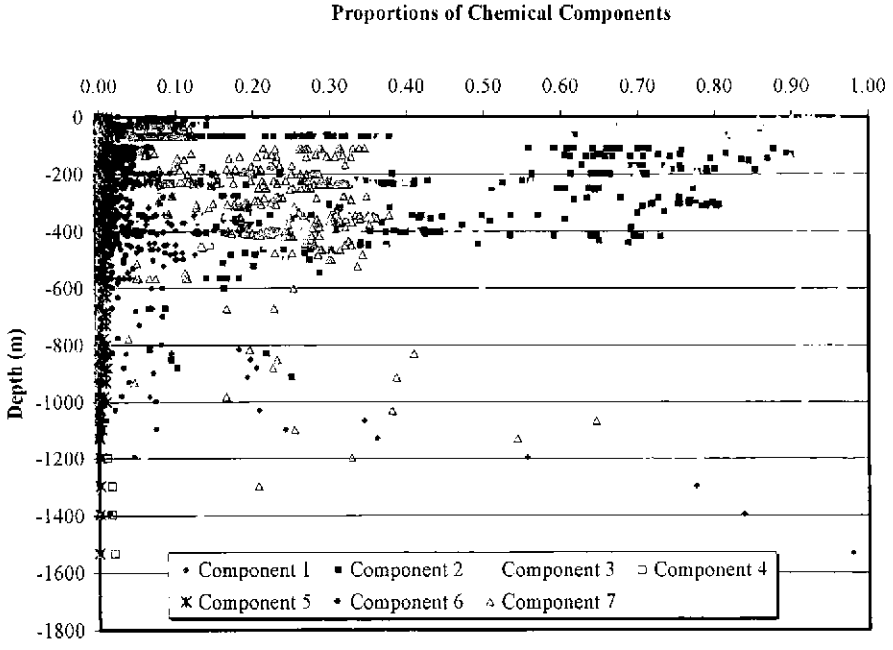

Figure 5-6 Plot showing variations in proportions of chemical components, calculated using Model 2, with respect to depth.

5.1.10 Comparison Between Results Of M3 And New Modeling

The results of the new Model 2 are expressed as proportions of the original M3 end-members and plotted versus depth in Figure 5-7. For comparison, Figure 5-8 is similar, but shows the proportions of the same end-members, as calculated in the original M3 modeling and reported by SKB in Data Delivery 19. From these figures, it is apparent that:

- There is generally a positive correlation between proportions of end-members calculated by Model 2 and the proportions calculated by M3 (Figure 5-9).
- There is a particularly good positive correlation between the proportions of brine calculated from Model 2 and the proportions of brine calculated by M3 (Figure 5-9).
- Compared to the M3 modeling, the new modeling calculated generally higher proportions of Baltic sea water at shallower depths (above around 400 m) and generally lower proportions of meteoric water at greater depths (between around 400 m and 1000 m). However, the general depth distribution is similar (Figure 5-7).
- The maximum proportion of the Baltic seawater end-member calculated from Model 2 is around 0.8, whereas the maximum proportion calculated by M3 is close to 1 (Figure 5-9).

However, in contrast to the M3 modeling, the new modeling predicts *negative* proportions of meteoric water for samples of intermediate salinity (Figure 5-7, Figure 5-9 and Figure 5-10). These are clearly unrealistic and initially seem inconsistent with the M3 results. However, a detailed comparison reveals a high degree of underlying consistency, notably:

- The negative proportions given by the new model are almost all given by samples for which M3 also calculated a large deviation between theoretical Cl concentrations (assuming all samples are mixtures of all end-members) and actual Cl concentrations (Figure 5-11).
- The proportions of end-members given by the new calculations can also be used to calculate "deviations" between theoretical and actual concentrations of determinands (Figure 6-1, Section 5.1.5). There is a negative correlation between Cl deviations obtained from the new results and Cl deviations calculated from the M3 results (Figure 5-12).
- The Cl deviations, as a percentage of the total, are largest for waters of low salinity in both the latest modeling and the original modeling.

The reasons why the new model results and the original M3 modeling is consistent are:

- The M3 approach uses calculated mixing proportions and end-member compositions to derive theoretical water compositions, for

comparison with actual water compositions. The M3 modeling assumes that all waters contain all end-members. For some waters, this assumption results in calculated Cl concentrations that are lower than the actual concentrations. Since Cl is relatively unreactive in groundwaters, the most logical explanation is that in these, the estimates of meteoric water concentration, based on the assumption of conservative mixing, are too high.

- In contrast, the new modeling adopted the opposite approach. The actual compositions of the waters and the end-members to calculate the mixing proportions. Therefore, the calculation of negative proportions of meteoric water effectively amount to the same thing as the negative deviations for Cl calculated by M3.

A plausible explanation for these discrepancies is that the actual waters are not actually all mixtures of all end-members.

This possibility was also pointed out by Laaksoharju (2000). However, based on the M3 modeling, it was considered that the uncertainty due to this could be encompassed by a ±10% error on the proportion of each component.

The new modeling produced negative proportions of meteoric water as low as around –0.3 (Figure 5-7). An implication is that the uncertainty for individual components could be much greater than the ±10% suggested by Laaksoharju et al (2000).

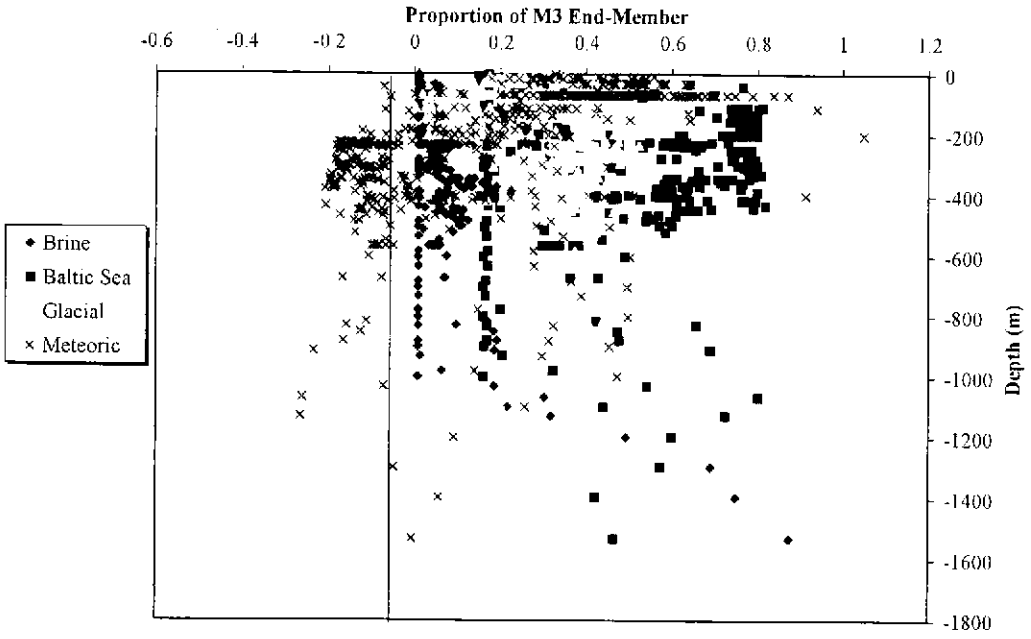

Figure 5-7 Variations in proportions of end-members used in M3 modeling, calculated from results of the new Model 2, using all 7 chemical components.

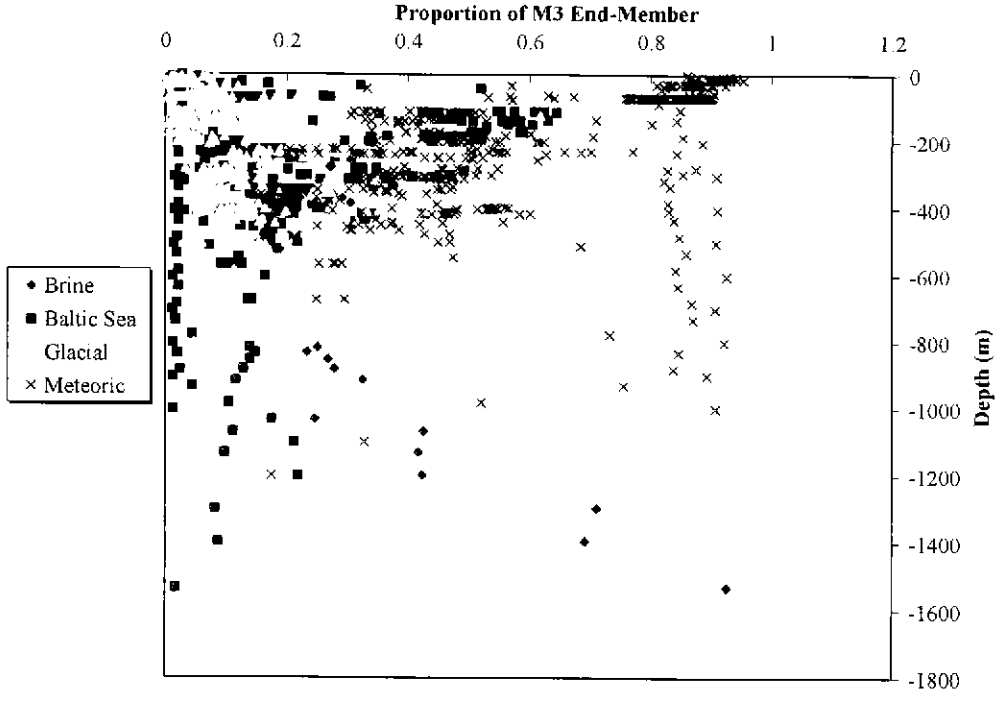

Figure 5-8 Variations in proportions of end-members used in M3 modeling, as calculated by M3 and reported by SKB in Data Delivery 19

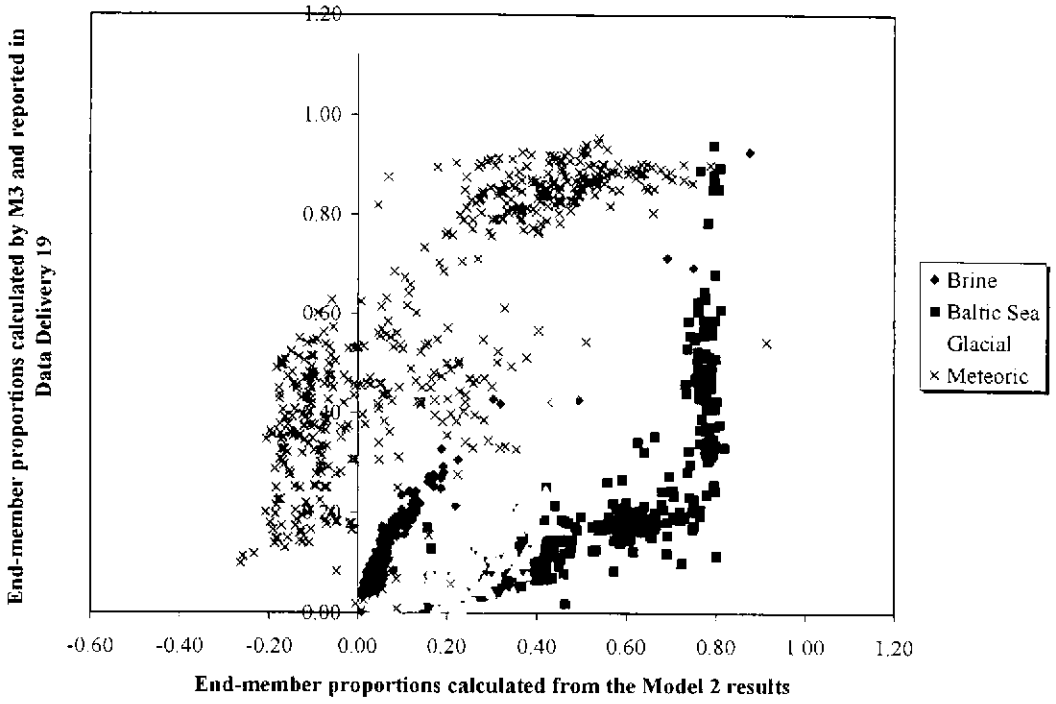

Figure 5-9 Comparisons between proportions of end-members calculated by M3 and released by SKB in Data Delivery 19, and proportions of the same end-members calculated using the revised Model 2.

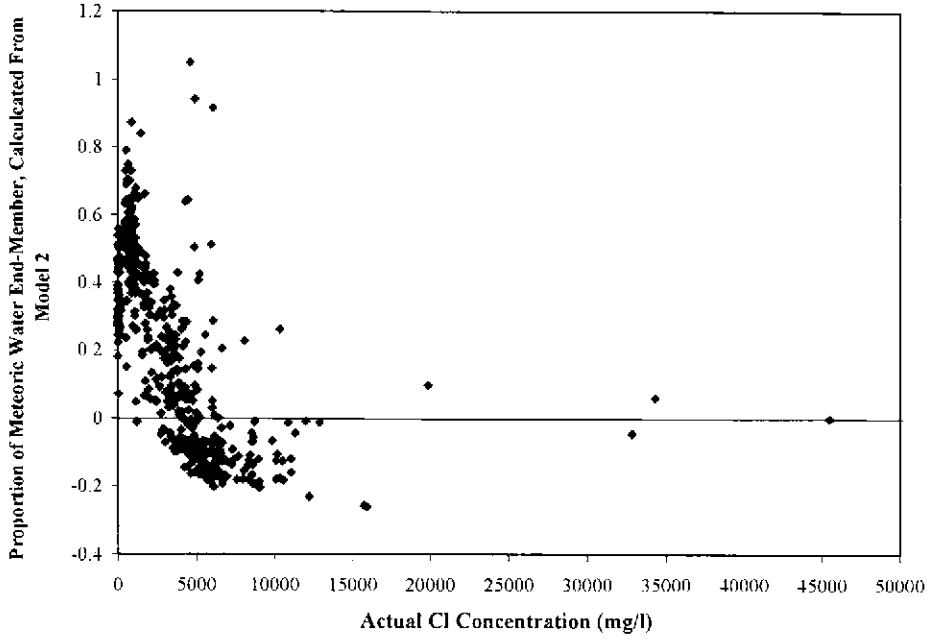

Figure 5-10 Comparison between the proportion of the meteoric water end-member in each sample, calculated from the Model 2 results, and the actual Cl concentration in each sample.

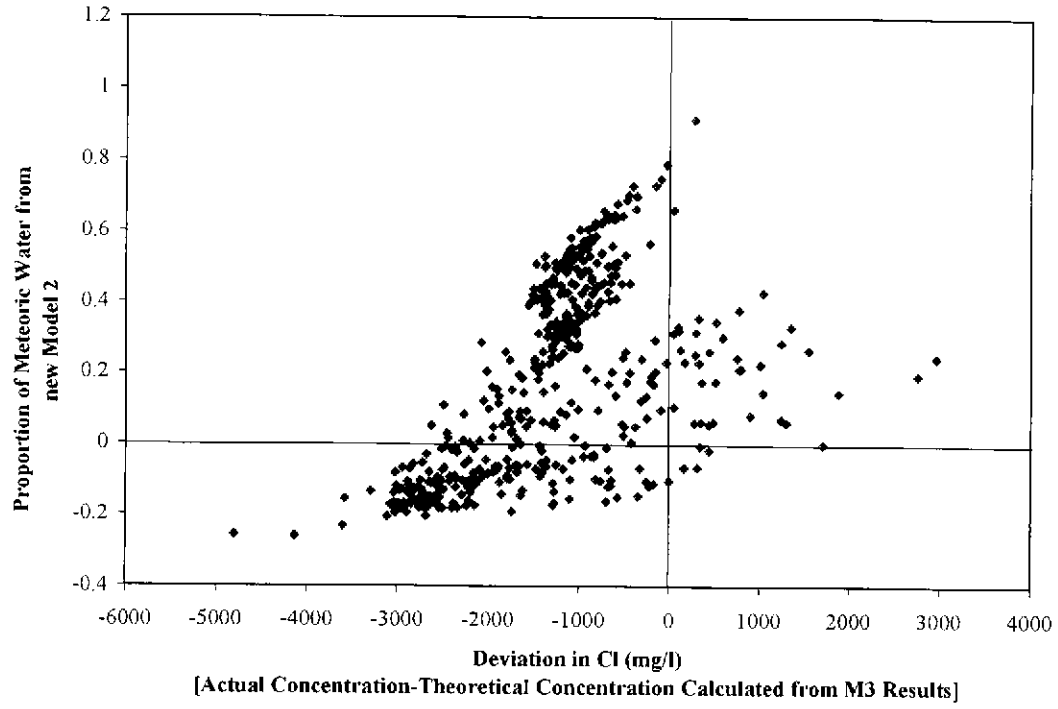

Figure 5-11 Comparisons between the proportions of the meteoric water end-member, calculated from the new Model 2, and the deviation between theoretical and actual Cl concentrations in each water, from the M3 results.

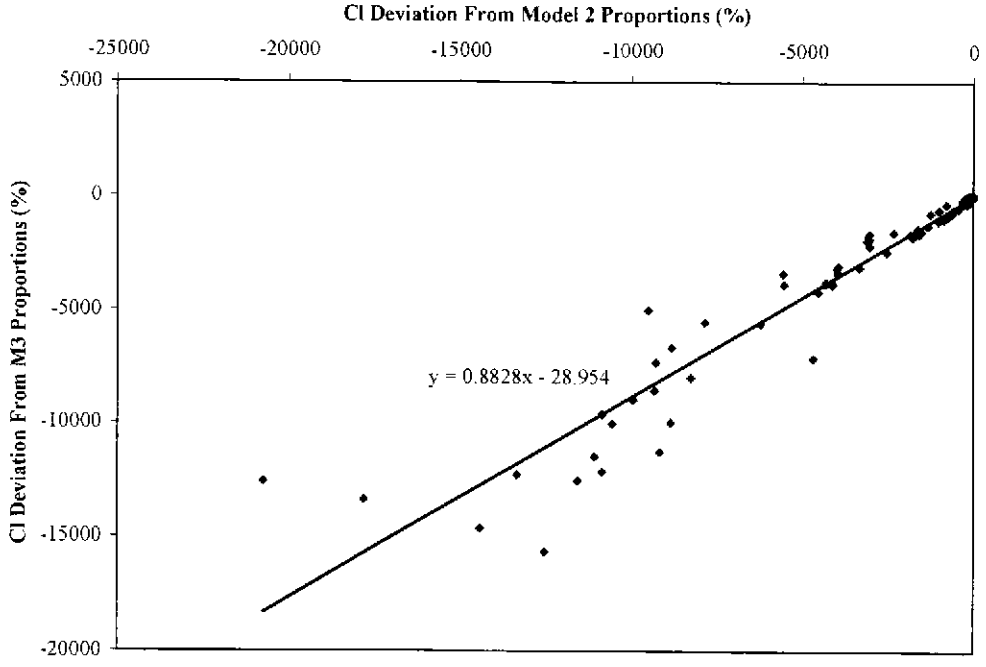

Figure 5-12 Comparisons between deviations in Cl (calculated - actual), calculated from Model 2 proportions, and deviations in Cl (calculated - actual), calculated from the original M3 proportions.

5.1.11 Conclusions From The New Modeling

- The new approach should be more generally applicable than the M3 approach, since it takes into account all the chemical variability in the groundwaters.
- The new method allows chemical variability that is due to mixing to be distinguished from components of chemical variability that is due to water/rock interaction. Chemical components that are not attributable to water/rock interactions or other effects can be considered "conservative" tracers for groundwater flow.
- An internally consistent model of all the solute data cannot be obtained if stable oxygen and hydrogen isotope data are not used.
- When stable oxygen and hydrogen isotopic data are included in the model, the internal consistency of the model for solutes is very good. However, the model is not consistent for waters that are relatively depleted in the heavy isotopes. Though the reasons for this could not be evaluated fully, it may be due to the waters not all being mixtures of the same end-members.
- It is possible to express the results of the new method in terms of real groundwaters if so desired, allowing mixing relationships among real groundwaters to be distinguished. In the present study this was done for the original M3 end-members.
- Inclusion or exclusion of groundwater constituents and/or additional waters of extreme composition has a significant effect on the outcome of the method.
- Seven principal components are needed to explain all the chemical variability in the data, when the same data as those used by M3 are employed.
- The M3 results and the new modeling are broadly consistent.
- The proportions brine in any water are most likely to be reliable.
- It is probable that not all the M3 end-members are actually present in the Äspö groundwaters. In particular, meteoric water is probably not present in many groundwaters from intermediate depths.
- Better consistency and more precise mixing proportions could probably be obtained by splitting the data set into several parts and applying the model to each part. In general, an iterative procedure would be needed, involving repeated splitting of the data set and modeling of each part, until the most consistent set of results is obtained. This procedure was outside the scope of the present project.

5.2 PATHWAYS ANALYSIS/MIXING ISSUES

The analyses presented in the preceding sections used a two-stage approach to generating the source locations of the waters flowing into the monitoring sections (JNC, 1999):

1) determine the spatial location of the pathways
2) determine the distance traveled along each pathway each month using the head solution along each path. This head solution was updated every 30 days based on the transient finite element solution.

The individual pathways were defined by graph theory searches through the channel network model using a monitoring section as the source location of each search. The standard PAWorks graph theory search was amended to look for pathways upgradient of the source, hence allowing the sources of the waters infiltrating the monitoring sections to be determined. The graph theory searches used flow weighting, and the search procedure can be summarized by the rules in Figure 5-13. More details of the searching algorithm are provided in the PAWorks Manual (Dershowitz et. al., 1998b).

The pathways found through this graph theory search provide a good representation of the different pathways with the highest flows. However, while the method provides a good measure of the range of locations from which the waters are originating, there is no accurate way to determine the proportion of the waters along a specific pathway. The reason this difficulty arises is that while pathway length and travel time are additive values, the flow along a pathway is not. Weighting of the individual pipe flow may be used to estimate the net flow contribution from a pathway, but this methodology is by necessity approximate. Alternatively, the flow infiltrating a monitoring location may be assumed to be proportional to the flow rate in the pipe from which the water originated. This method was used in the Stage 1 and 2 modeling, but is also approximate.

The other major limitation of the original approach is that although the distance traveled along each pathway is a function of the monthly flow solution, the spatial coordinates of each of the pathways are defined by a single flow solution. A flow solution near the end of the modeled period was used. If the location of the inflows changes with time, due to a marked change in the head solution, these changes in flow direction and true source water coordinates (and water source location) could be significant.

The two major disadvantages of the original pathway analysis, lack of an accurate computation of the proportion of flow coming from each location and specifying pathway coordinates based on a single flow solution, are addressed in the improved approach that uses the newly introduced PAWorks particle tracking algorithm.

For each source (monitoring) location determine the flow in each of the attached pipes.

Select the pipe with the highest inflow into the source (Source Pipe A).
From Source Pipe A:

a) Record the flows in all the upgradient pipes attached to this pipe.
b) Add these inflows to the list of inflows recorded.
c) Select the pipe with the highest inflow.
d) Repeat a) to c) until the specified sink location is reached.
e) Repeat a) through d) until the user specified pathways per source is reached.

For Task 5 modeling, the external head boundaries of the model region were specified as sink locations.

Select the pipe with the second highest inflow into the source (Source Pipe B).
Repeat a) through e) for Source Pipe B until the user specified pathways per source is reached.

Continue for Source Pipes with the next highest inflows until the total number of user specified pathways is reached.

Figure 5-13 Rules for PAWorks Graph Theory Search used for Task 5 modeling

The algorithm continues to use the monitoring locations as the sources, the outer head boundaries of the finite element region as the sinks, and searches upgradient to determine where the water originated. At each intersection an individual particle is assigned to the upgradient pipes stochastically, the weighting of each pipe being in proportion to the flow.

For example, if the flows in the three upgradient pipes were:

Pipe	Flow Rate	Weight	Assignment Range
Pipe A	$5. \times 10^{-5}$ m^3/s	0.5	0.0 – 0.5
Pipe B	$3. \times 10^{-5}$ m^3/s	0.3	>0.5 – 0.8
Pipe C	$2. \times 10^{-5}$ m^3/s	0.2	>0.8 – 1.0

A random number between 0.0 and 1.0 is generated and depending on its value the particle is moved into the upgradient pipe depending on an "assignment range" that is proportional to the flow rate. The more particles used in the analyses, the more closely this algorithm matches a flow-weighted solution. The Task 5 analyses used 1000 particles at each source.

The new particle-tracking algorithm was expanded to allow the code to write particle locations after a user-specified time had elapsed, and to read the initial particle locations from file. Hence, a script file can be used to step through each of the 76 head solutions with the particles moving for 30 days per file. This enables the transient effects of the flow solution to be replicated in time-varying particle pathways.

Example pathways using the original graph theory algorithm and the particle tracking algorithm that is more appropriate to this problem, are presented in 3-D in Figure 5-15 and as a 2-D representation in Figure 5-14 for monitoring section SA2074A. The difference in the derived pathways is marked. The particle-tracking algorithm results in more clustered pathways and more pathways towards the east. This occurs because the flow is preferentially along the large-scale features and hence most of the particles follow these paths. Conversely, although the particle-tracking algorithm shares many of the same paths as the particle-tracking algorithm, it also includes some of the less likely pathways. The pathways also show the effect of the changing head distribution with time, which can be incorporated into the particle tracking results.

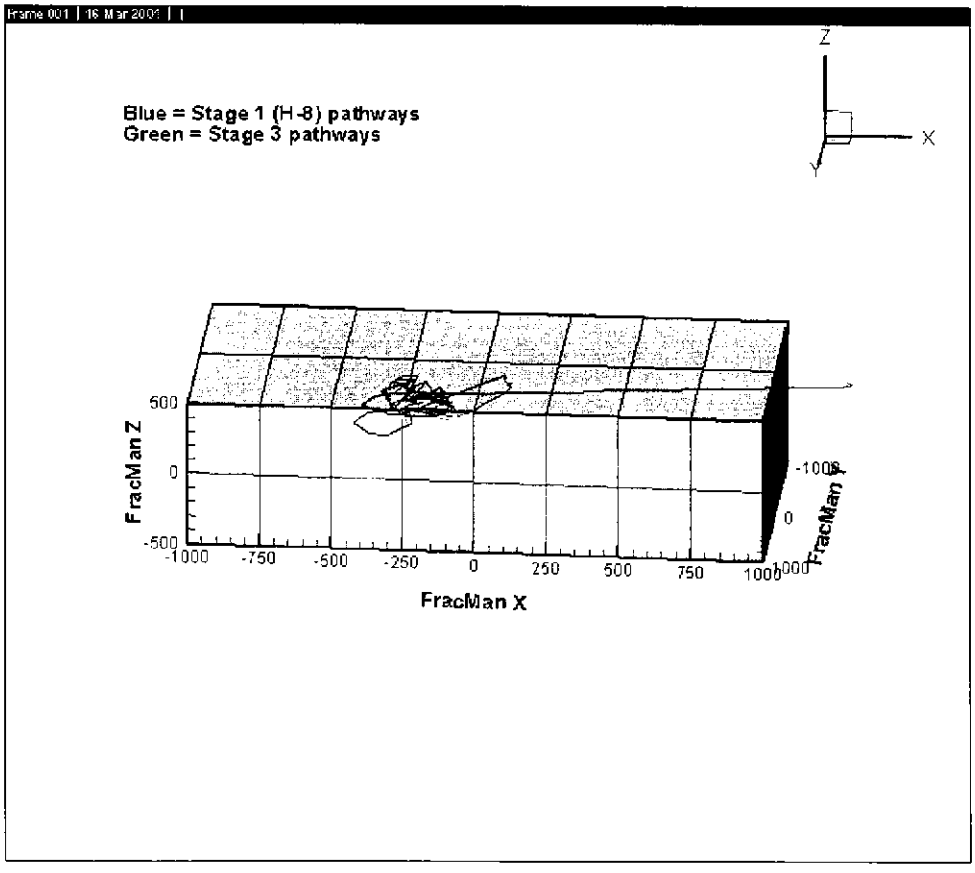

Figure 5-14 Monitoring section SA2074A graph theory algorithm and particle tracking algorithm pathways (3-D)

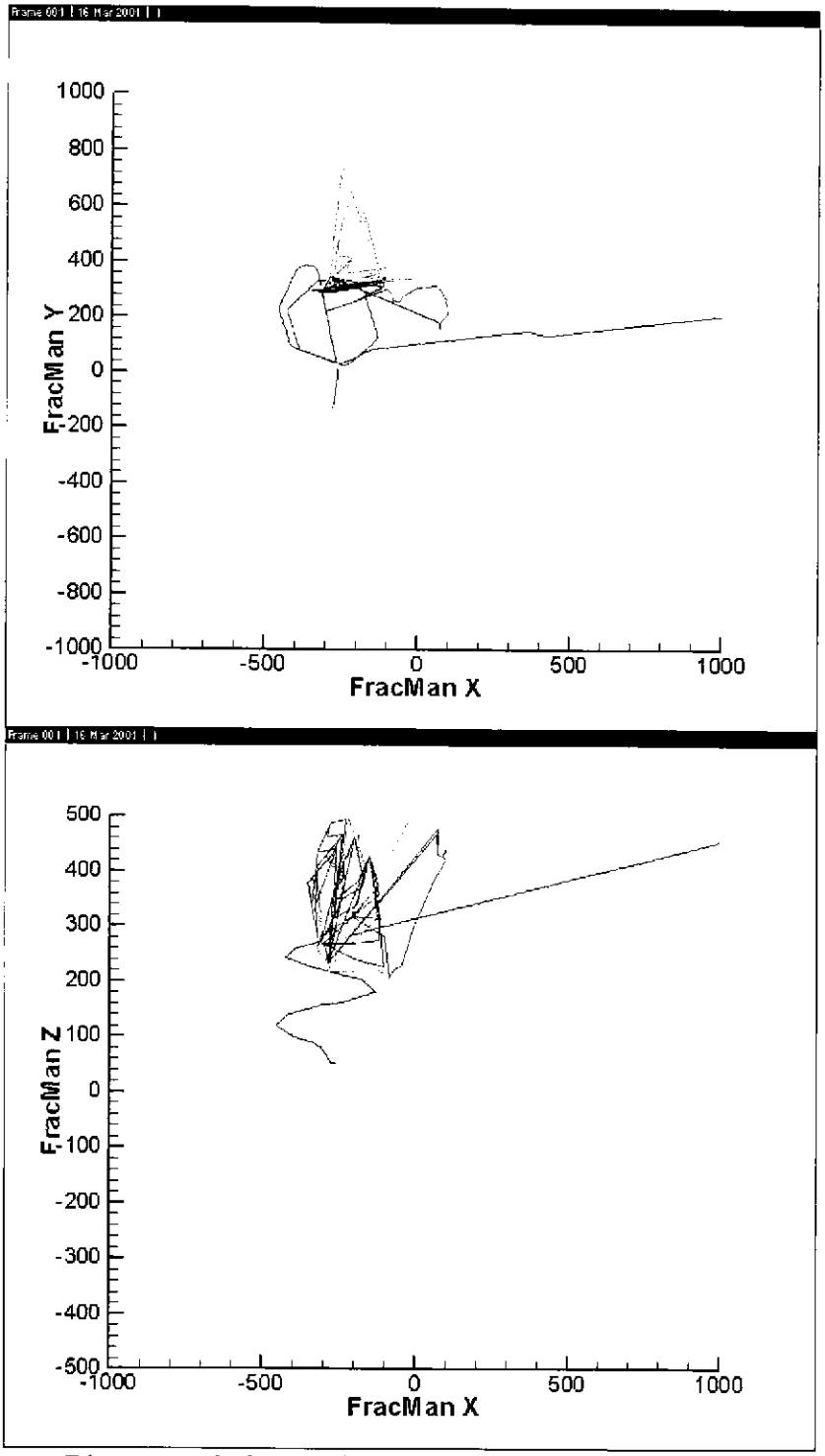

Blue = graph theory algorithm
Green = particle tracking algorithm

Figure 5-15 Monitoring section SA2074A graph theory algorithm and particle tracking algorithm pathways (2-D)

5.3 INITIAL CONDITION/INTERPOLATION ISSUES

As part of the geochemical analyses it is necessary to make assumptions about how the measured chemistry should be extrapolated to other locations in the vicinity of the Äspö tunnel. The methodology used for the Stage 3 modeling differed from that used for the previous simulations.

For the Stage 2 geochemical analyses the initial geochemical distribution in the vicinity of the Äspö tunnel was based on the spatial grid from the limited borehole sample locations, as developed by SKB and provided as data delivery No. 4. The chemistry at the sample locations was computed using the M3 approach, and the points extrapolated to the grid using a Kriging methodology. The chemistry between the grid points was linearly interpolated between the four surrounding points.

An inherent assumption of this Stage 2 approach was that the chemical composition is unrelated to the hydrogeology in the vicinity. For example, if a fracture is equidistant between a major fracture zone and a background fracture, this approach assumes that the chemistry will be equally affected by the background fracture and the major fracture zone. In effect an average chemical composition should be assumed.

Similarly, any effect of the Baltic Sea on the chemistry is assumed to be completely addressed by the chemistry of the grid points.

The updated analysis uses different assumptions.

- The chemistry at the borehole sampling points is computed using the principal component model described in Section 5.1.
- The chemistry at a specific location is assumed to be dominated by the chemistry on the closest main fracture zone. This assumption is based on the premise that as these features are conductive over a large distance, mixing preferentially occurs between the main features and the background fractures.
- Chemistry is strongly influenced by the vicinity of the Baltic Sea. Therefore whether a location is beneath Äspö Island or the Baltic Sea should be considered as part of the chemical extrapolation process.

In order to use the chemistry on the main fractures as the basis of an interpolation algorithm, the chemistry on these main features needed to be computed. Each main fracture needed sampling points at the four corners of the feature, at the two edges of the feature at a FracMan elevation of 0.0 m, and at the Äspö Island/ Baltic Sea interface, as a minimum. Additional chemistry points were also used where the chemistry showed a distinct non-linear variation with depth.

Determining the main feature chemistry was done in stages. First, any borehole sampling points within 50m of a main fracture zone was projected onto that fracture. Where this did not provide sufficient data points, depth dependent trend lines were computed for each chemistry under/not under Äspö Island and used to compute the chemistry. This approach is limited

due to the small number of borehole sampling locations. However, it makes optimum use of available data and still allows for the observed chemical dependence of the water to the vicinity of the Baltic.

Having computed the chemistry on the main features, the following approach was used to determine the time varying chemical composition of the waters in the prediction locations.

Step 1: Obtain location of particle using the PAWorks particle backtracking algorithm

Step 2: If particle is not already within a main fracture zone, project particle to the nearest zone

Step 3: Interpolate chemistry from the chemistry on these fracture zones

The chemistry within a fracture zone was derived using a linear interpolation scheme between the three closest surrounding points.

This interpolation scheme was subsequently found to work well. This implies that the main fracture zones may dominate the chemical compositions of the waters. Additionally, the more general approach to the chemical components enabled the accuracy of the assumptions of pure mixing to be assessed.

5.4 UPDATED MODEL CALIBRATION

This section of the report summarizes the model and results obtained for two related chemistry models:

- Model 2, the 7 chemical component model described in Section 5.1.9 and Table 5-2.
- The end-members (Brine, Baltic, Glacial and Meteoric) computed from the 7 chemical component model.

The model used for both these cases is summarized in Table 5-3.

Table 5-3 Summary of Model for Sensitivity Study

Property	Description
Fracture Model	
Major Discrete Features	22 Planar Homogeneous Zones (Rhén et al., 1997). See Table 2-1 for details.
Background Fractures	22704 features described in Table 2-1.
Mystery Feature	Addition an additional feature located between features NNW1and NNW7. Constructed from two fractures as shown in Figure 2-7.
Conditioned fractures intersecting tunnel sections.	Deterministic fractures added at 69 head calibration sections. Transmissivity of these deterministic fractures set at 10^-8 m^2/s to reduce excessive drawdowns.

Property	Description
Transport Aperture	Aperture = 2 * Transmissivity$^{0.5}$
Boundary Conditions	
North, South, East & West sides	Conditioned to the values reported in Svensson (1999).
Base	No flow boundary assigned to each node.
Baltic Sea	Head of 0.0 m.
Äspö Island	No flow boundary assigned to each node.
Geochemistry	
Chemical Composition	Seven chemical components. See Section 5.1 for details.
Interpolation Scheme	Updated interpolation scheme described in Section 5.3

The time varying fit between the measured and numerically modeled 7 chemical component model provides a measure of how well the approach worked. The end member fits are also provided to enable direct comparison to the published SKB solutions.

The best fit hydrogeological model, model H8, described in Section 3.1 and Table 3-1 was used for the analyses. This model was developed using only hydrogeological data. The hydrogeological model was chosen as the base case, in preference to the geochemically fitted models, because it allowed a clearer interpretation of the effect of the addressed uncertainty issues on the derived chemistry. The methodology used for the pathways analysis and the chemistry initial condition/interpolation are given in sections 5.2 and 5.3 respectively.

The time-varying chemistries are presented as computed: no additional calibration has been undertaken.

5.4.1 Results of Seven Component Model Simulations

The calibration borehole section results for the seven component model are presented in Figure 5-16 to Figure 5-24. The two (of three) meshed prediction borehole locations are presented in Figure 5-25 to Figure 5-26.

The calibration sections KR0012B, SA0850B, SA1327B, and the prediction section KA3110A, are not included because these sections were not connected to the general fracture network in the stochastic background fracture realization.

The fits for borehole sections SA2074A, KAS03a, KAS03b and KA3005A were very good. The first three of these sections showed time dependent

behavior, indicating the simulation correctly replicated the flow velocities as well as the flow location.

SA0813B showed a good fit for chemical component 2, but component 3 is incorrectly shown as component 3. However, the time dependence of the components is correctly replicated.

SA1229 also indicates time dependent behavior. The fit for component 7 is excellent. The deficiency in the analysis is that component 2 is overestimated due to the absence of component 3 in the simulated results.

The three poorest fits were SA2783A, KAS07, KA1775A and KA3385A. KA1775A indicates very different chemical compositions for the two measured data points, and are therefore possibly inaccurate. The three remaining borehole sections show time dependent responses that would be better modeled if the flow velocities in the finite element model were slower. Slowing the velocity by increasing fracture aperture was not attempted due the good fits to the other sections.

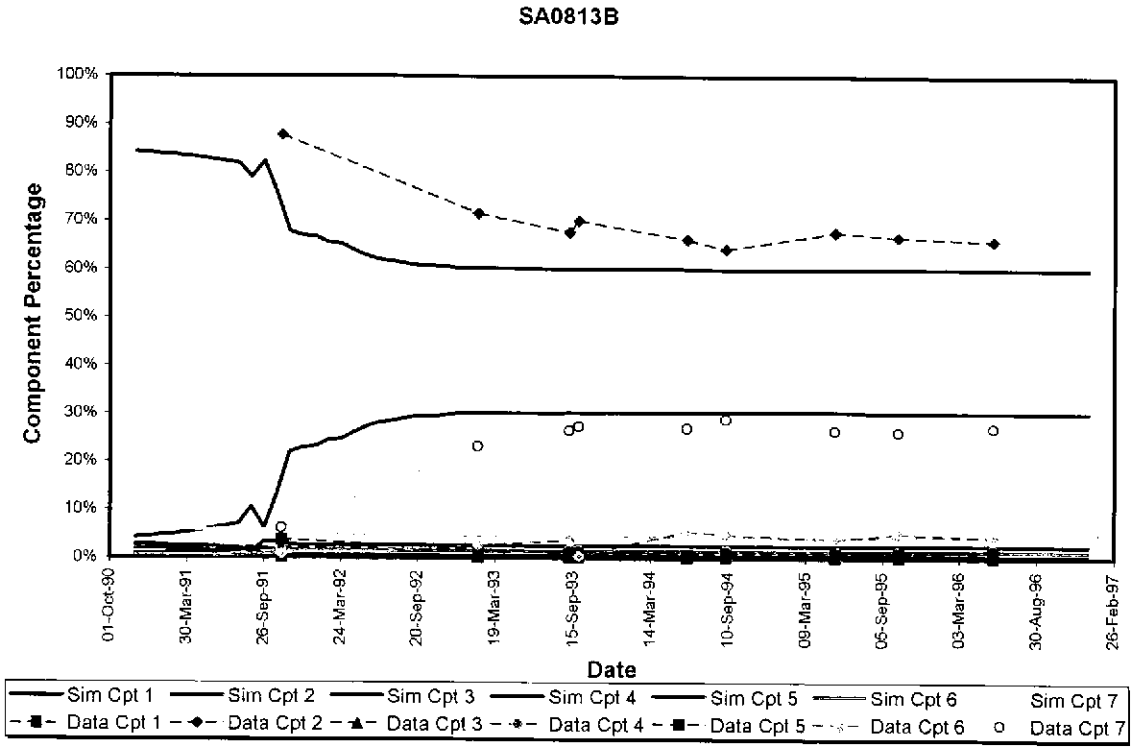

Figure 5-16 SA0813B geochemical inflows for 7 component model

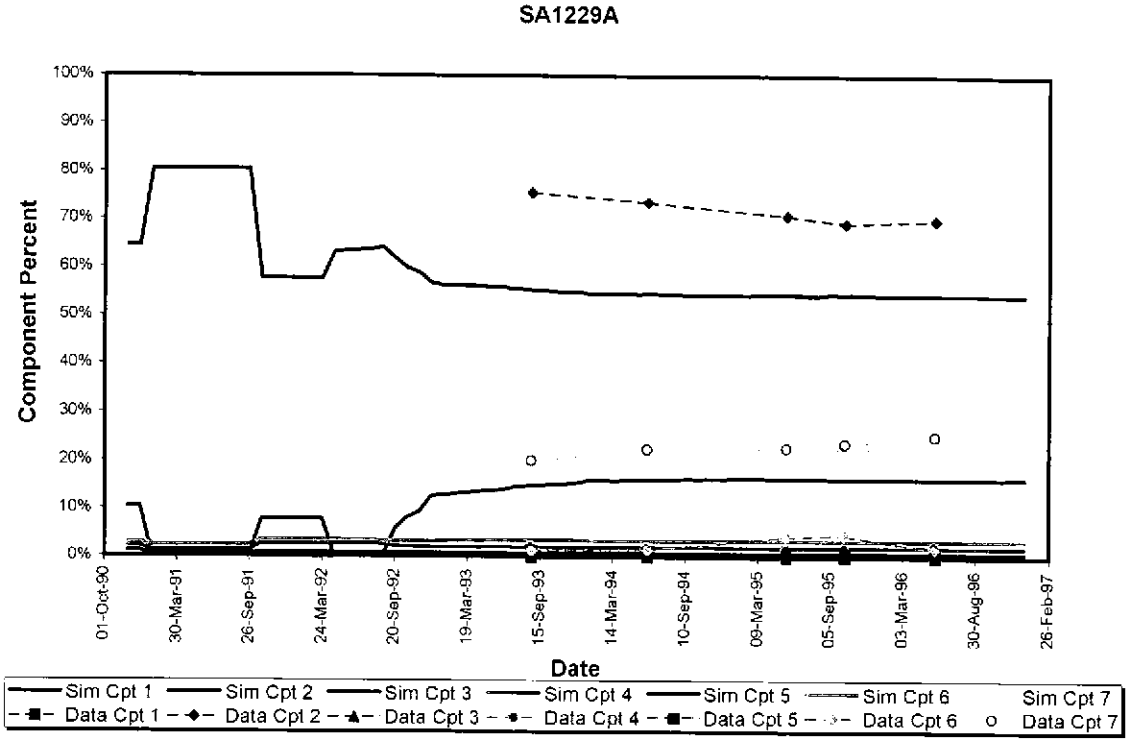

Figure 5-17 SA1229A geochemical inflows for 7 component model

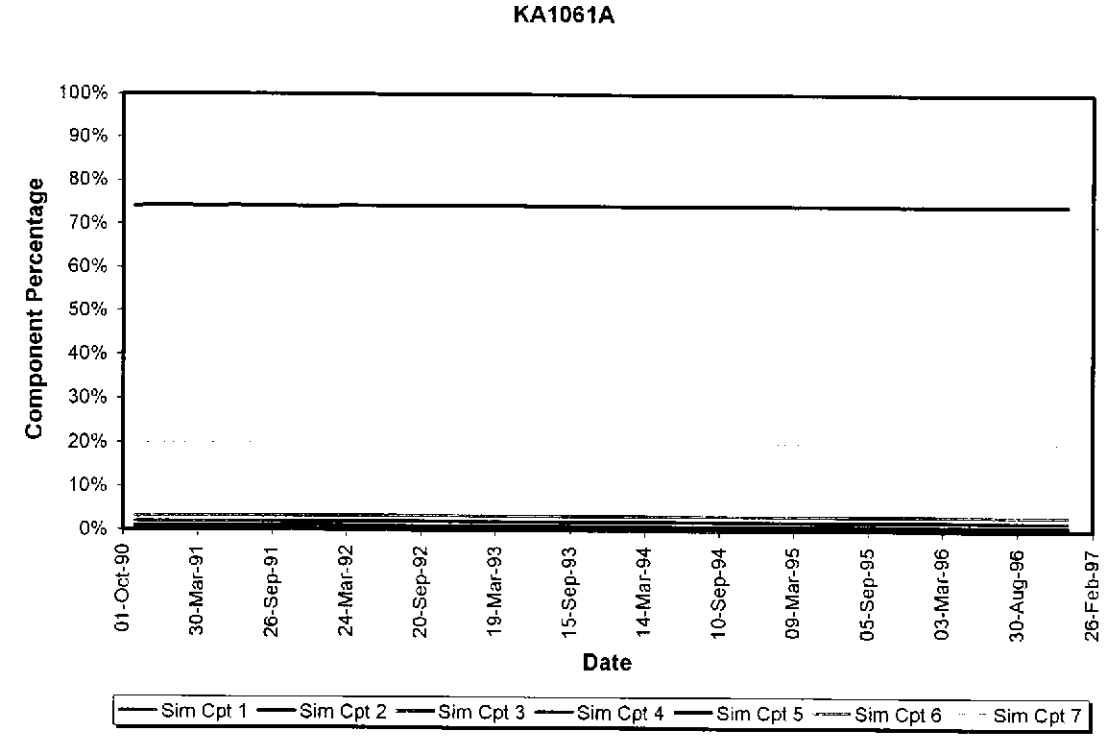

Figure 5-18 KA1061A geochemical inflows for 7 component model

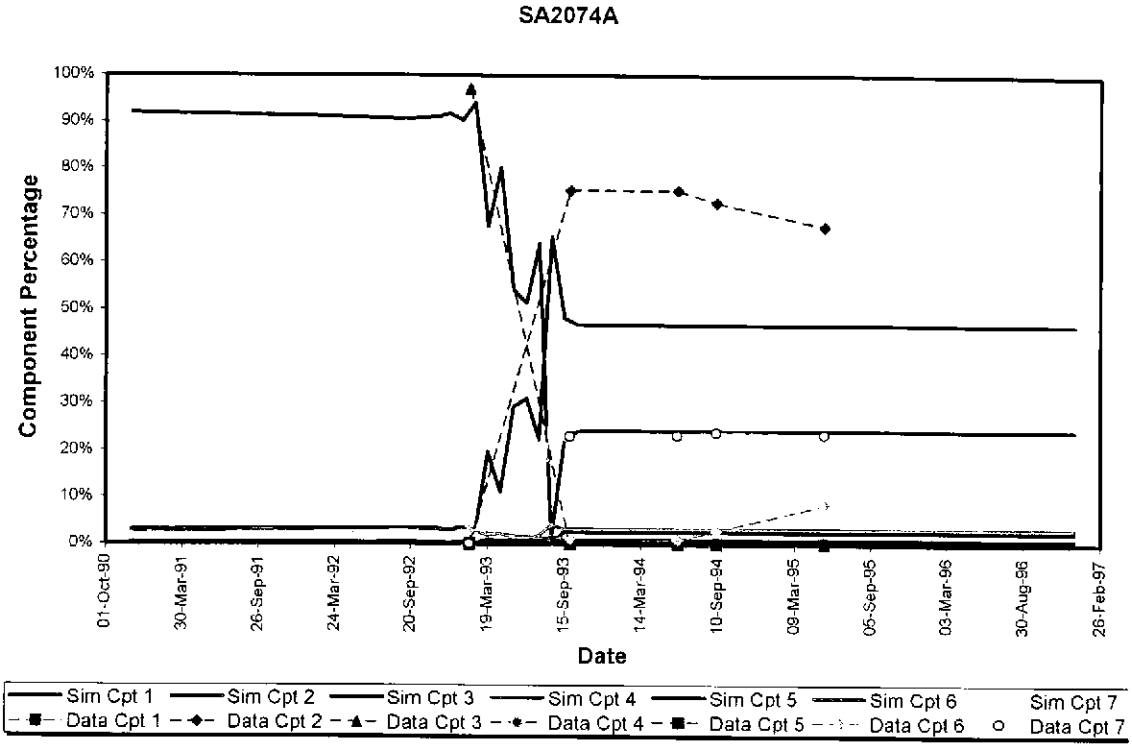

Figure 5-19 SA2074A geochemical inflows for 7 component model

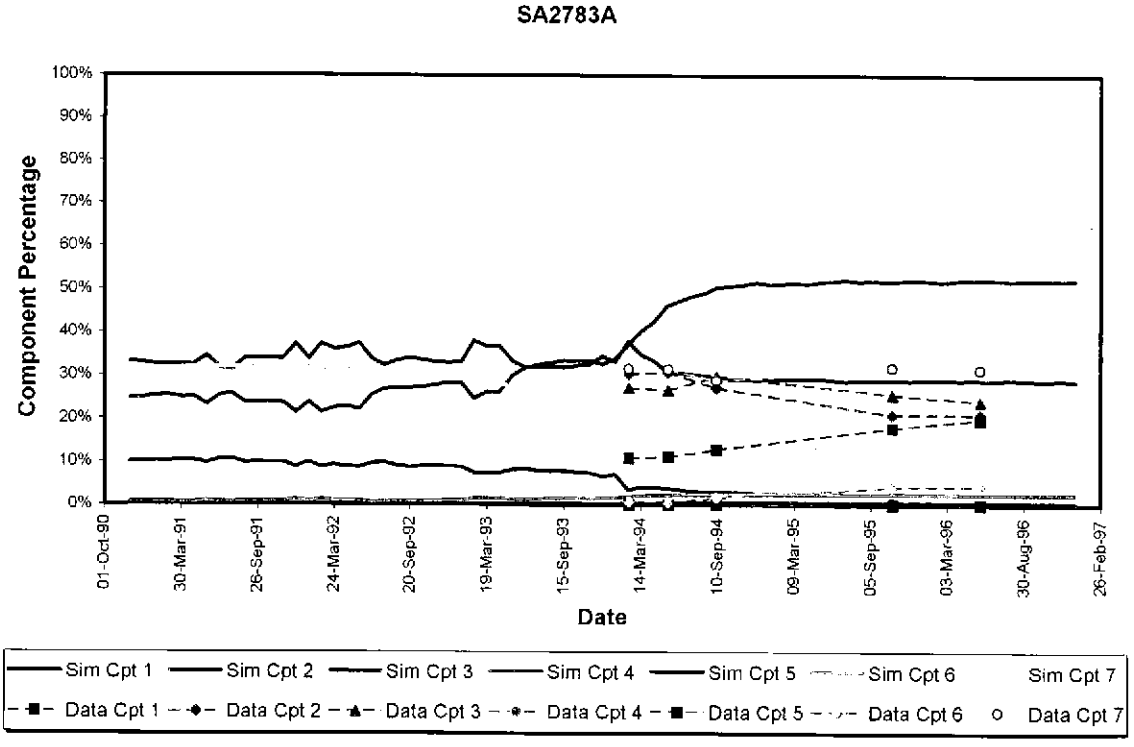

Figure 5-20 SA2783A geochemical inflows for 7 component model

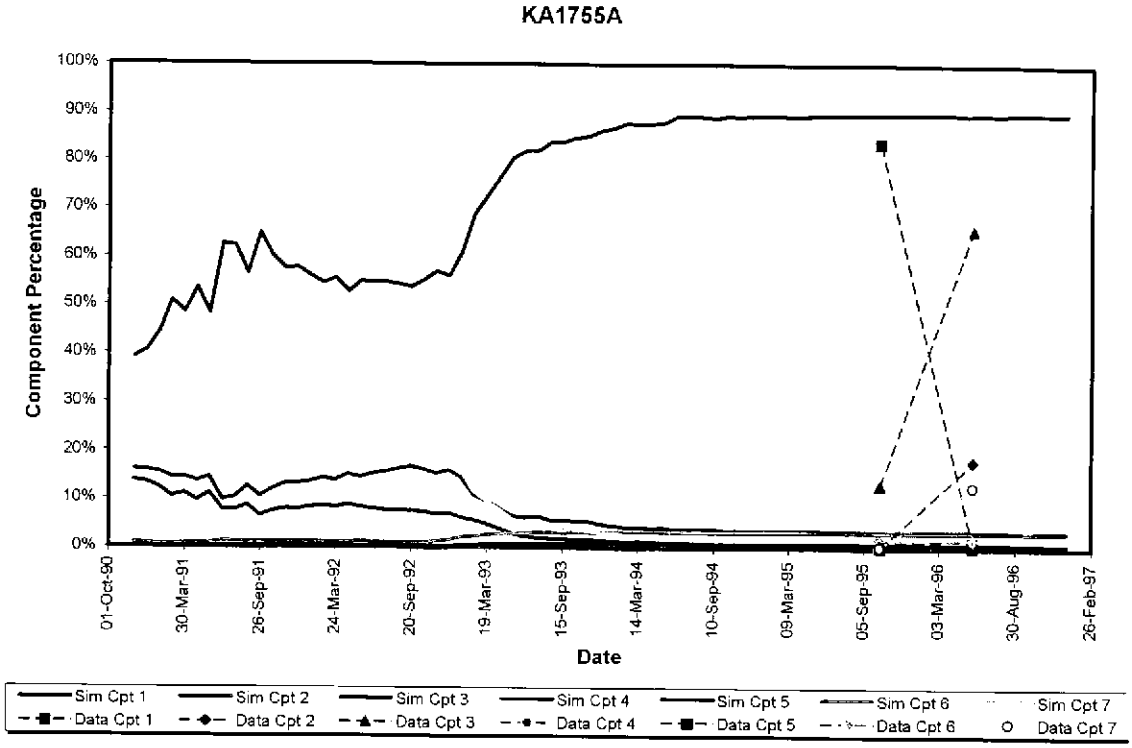

Figure 5-21 KA1775A geochemical inflows for 7 component model

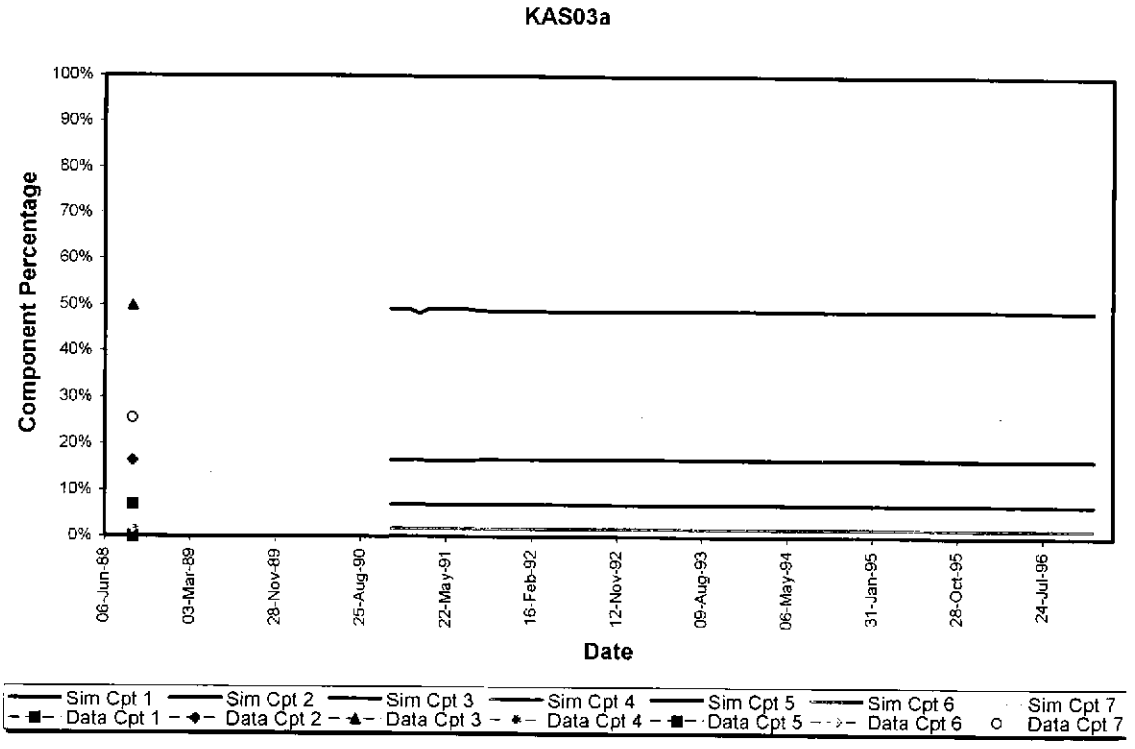

Figure 5-22 KAS03a geochemical inflows for 7 component model

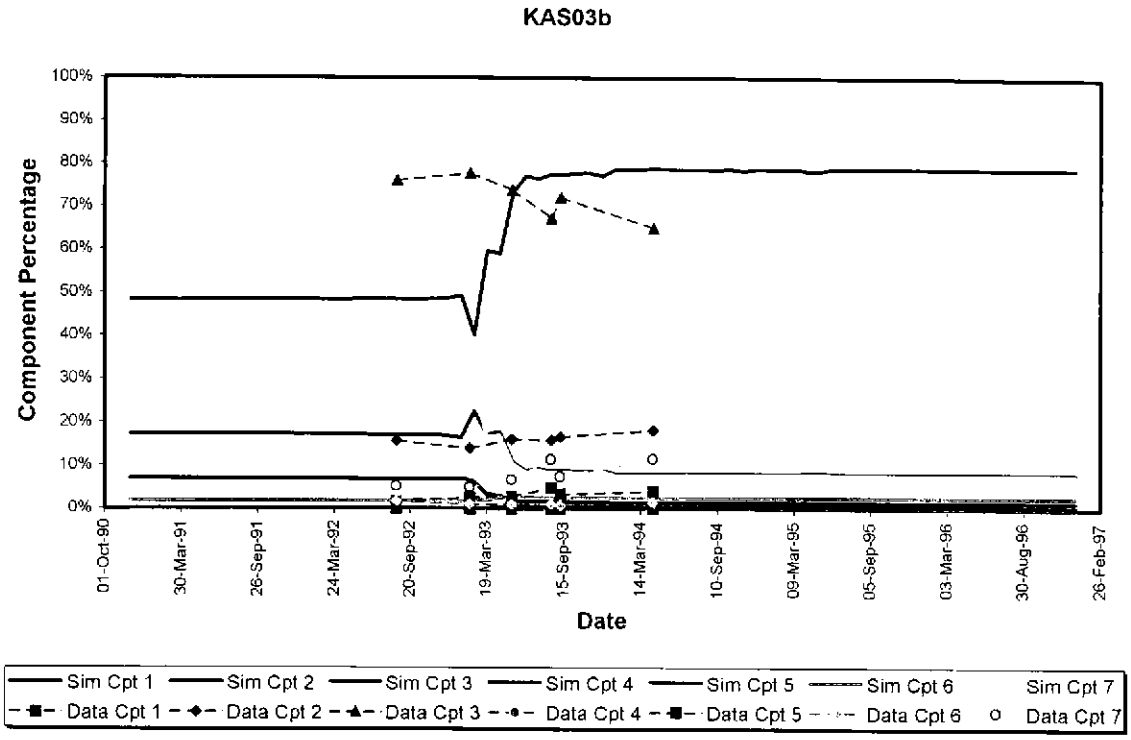

Figure 5-23 KAS03b geochemical inflows for 7 component model

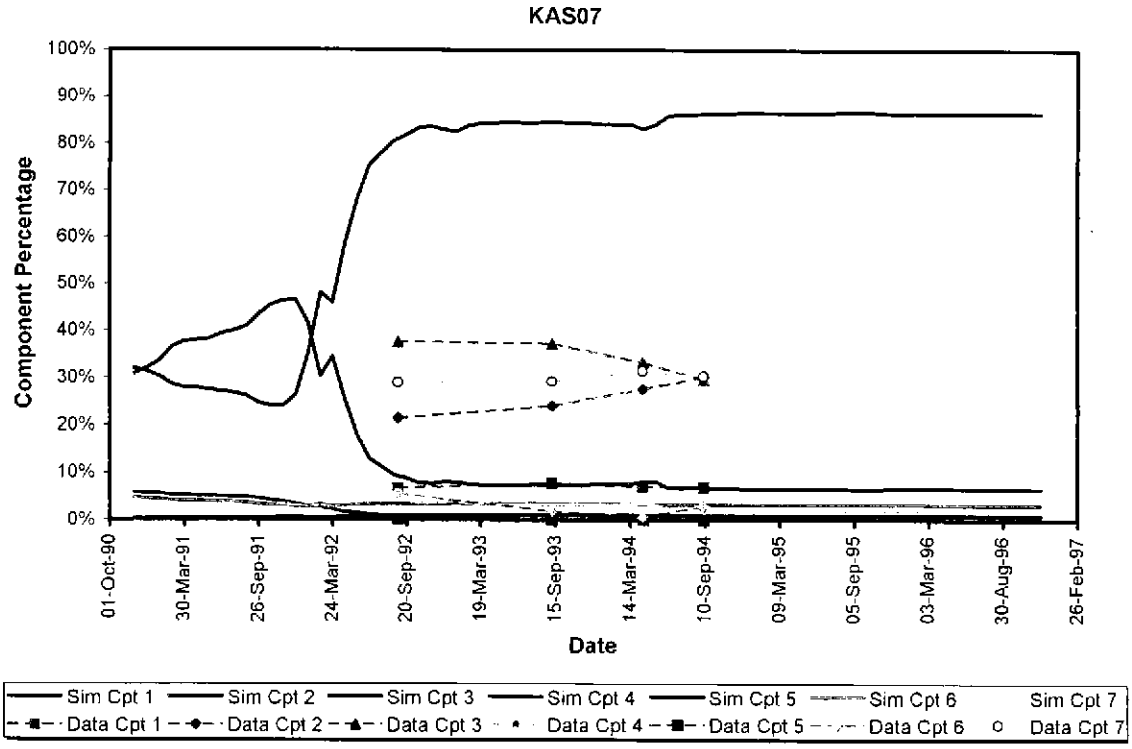

Figure 5-24 KAS07 geochemical inflows for 7 component model

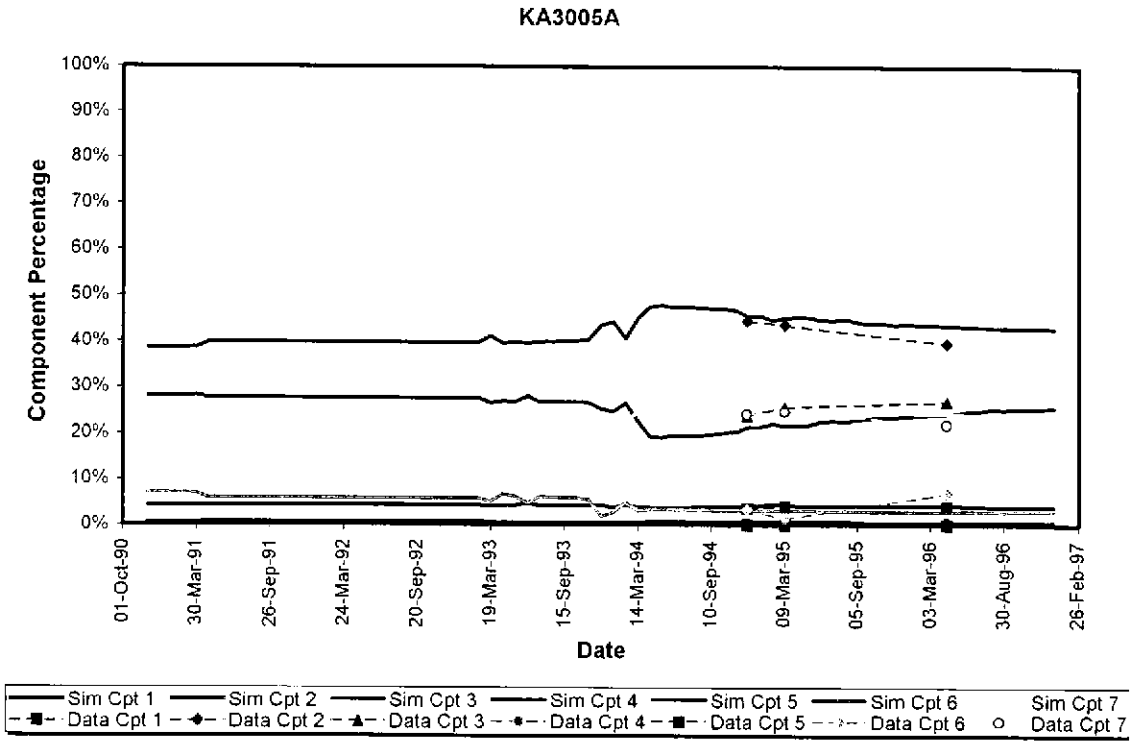

Figure 5-25 KA3005A geochemical inflows for 7 component model

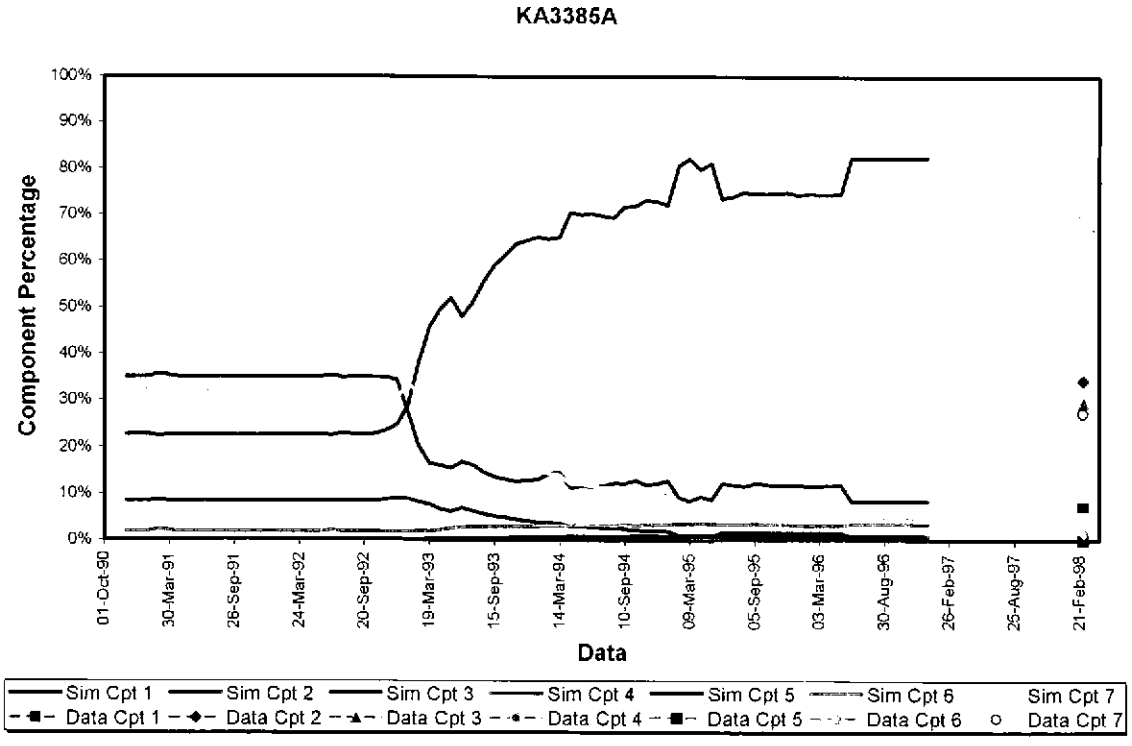

Figure 5-26 KA3385A geochemical inflows for 7 component model

5.4.2 Results of End Member Simulations

Endmember simulation results based on the seven component model are presented in Figure 5-27 to Figure 5-35. The two meshed prediction borehole locations are presented in Figure 5-36 and Figure 5-37.

As explained above, the calibration sections KR0012B, SA0850B, SA1327B, and the prediction section KA3110A, are not included because these sections were not meshed in the finite element simulation.

Table 5-4 New Chemistry Error Estimates

Sim	Stage II: Geochem Calibration	Features	# of Sections at first time	Time Average dh	dh at 1/13/94	Geochem Fit Average ABS
NC-1	New Chemistry model.	Based on the H-8 hydrogeological model with revised chemistry definition.	45	5.13[1]	13.46[1]	12.3%

[1] Identical to H-8 model

It should be noted that the sum of the four end-members does not necessarily add to 1.0. This is a function of the method in which the proportions were computed. The 7 defined chemical components in each of the original end-members (Brine, Baltic, Glacial and Meteoric water) and in each of the other waters is known. By a least-squares method, the coefficients for each of the end-members (brine, Baltic, glacial and meteoric) was calculated such that, when the compositions of these end-members are multiplied by the coefficients, and the results summed, the unknown water composition is obtained.

i.e.

		New Chemical Component						
	End-member	1	2	3	4	5	6	7
a	Brine	Br1	Br2	Br3	Br4	Br5	Br6	Br7
b	Baltic	Ba1	Ba2	Ba3	Ba4	Ba5	Ba6	Ba7
c	Glacial	Gl1	Gl2	Gl3	Bl4	Gl5	Gl6	Gl7
d	Meteoric	Me1	Me2	Me3	Me4	Me5	Me6	Me7
	Other Water	OW1	OW2	OW3	OW4	OW5	OW6	OW7

Where Br1, Br2,....Br7 represents the proportions of the new chemical component 1, 2, ...7 in the brine end-member; Ba1, Gl1, Me1 and OW1 represent the proportions of component 1 Baltic sea end-member, glacial end-member and other water, respectively.

By a least-squares method, values for a, b, c and d were calculated, representing proportions such that a x Br1 + b x Ba1 + c x Gl1 + d x Me1 = OW1, and similarly for the other components 1, 2, 3, 4.

The numbers representing the proportions of the end-members are the coefficients a, b, c, d in the table represented above. In theory, they should add up to 1.0.

The reason that they do not is due to the fact that they were derived from least-squares fitting and, quite likely the fact that the underlying assumption that the waters are all mixtures of the 4 end-members is incorrect. For this latter reason, the numbers were not normalized to 1.0.

This conclusion is in fact consistent with the original M3 modeling. The M3 modeling effectively neglects mass from the system, by basing the mixing proportions on geometrical relationships on a plot of eigenvalues corresponding to only the first two principal components. When the M3 proportions calculated in this way are used to calculate concentrations of unreactive groundwater constituents, like Cl, it is found that the numbers calculated do not always correspond to the concentrations in the actual waters. What is striking is that the discrepancies tend to correspond to waters for which negative proportions of meteoric water were calculated by the new modeling.

The results presented in Figure 5-27 to Figure 5-37 appear better than those for the seven individual chemical components. The results for SA2074A, KA3005A, KAS03A and KAS03B are very good. This is consistent with the results of the seven individual chemical components. The match between the measured and modeled end-members for SA1229 is also extremely good. This fit is better that achieved for the individual chemical components.

SA0813B provides a reasonable match between measurement and model. The measurement values include the largest negative fraction of glacial waters. This is obviously unrealistic, and indicates a poorly constrained problem.

The fit to borehole section SA2783 is good, but would be improved if the velocities were reduced. Similarly the fits to KA1755A, KA3385A, and KAS07 would be improved if lower velocities (i.e. larger aperture values) were used in the model. This observation is consistent with that observed for the seven individual chemical components.

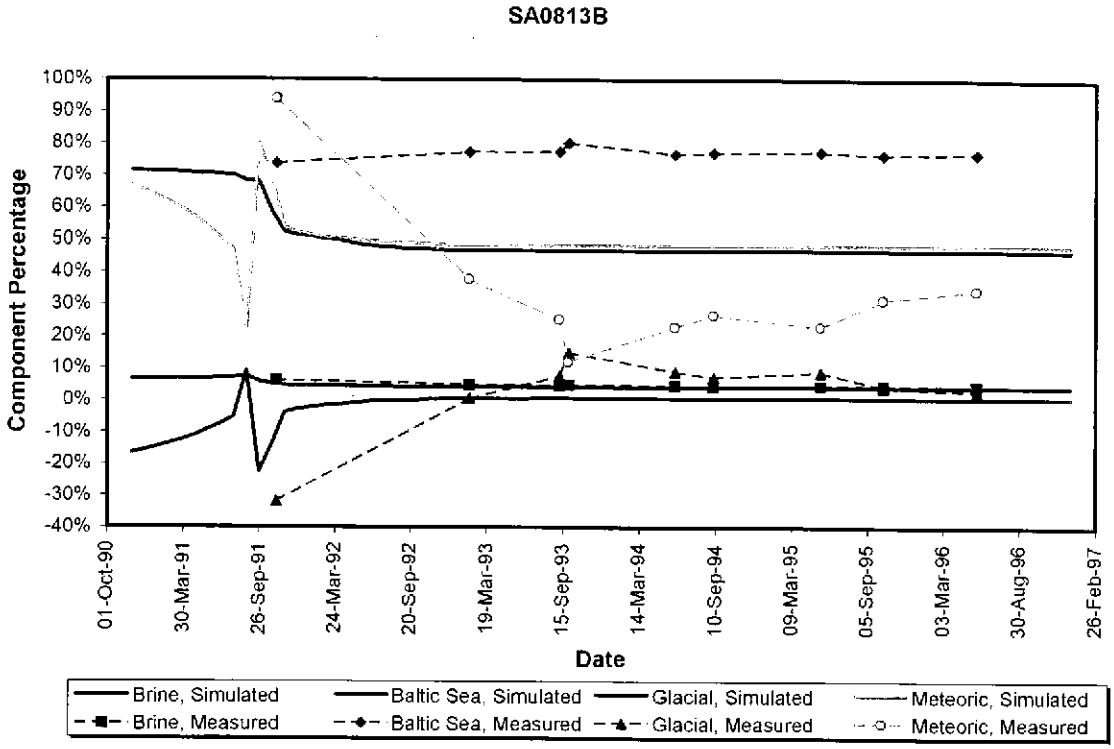

Figure 5-27 SA0813B geochemical inflows for 4 endmembers

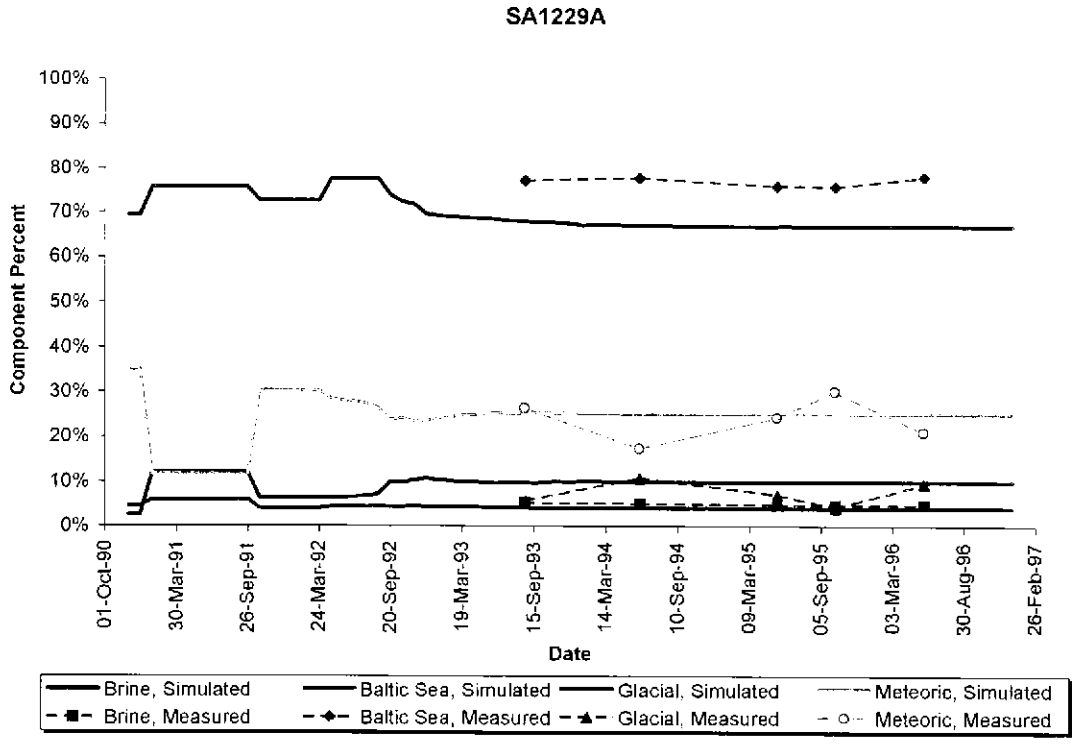

Figure 5-28 SA1229A geochemical inflows for 4 endmembers

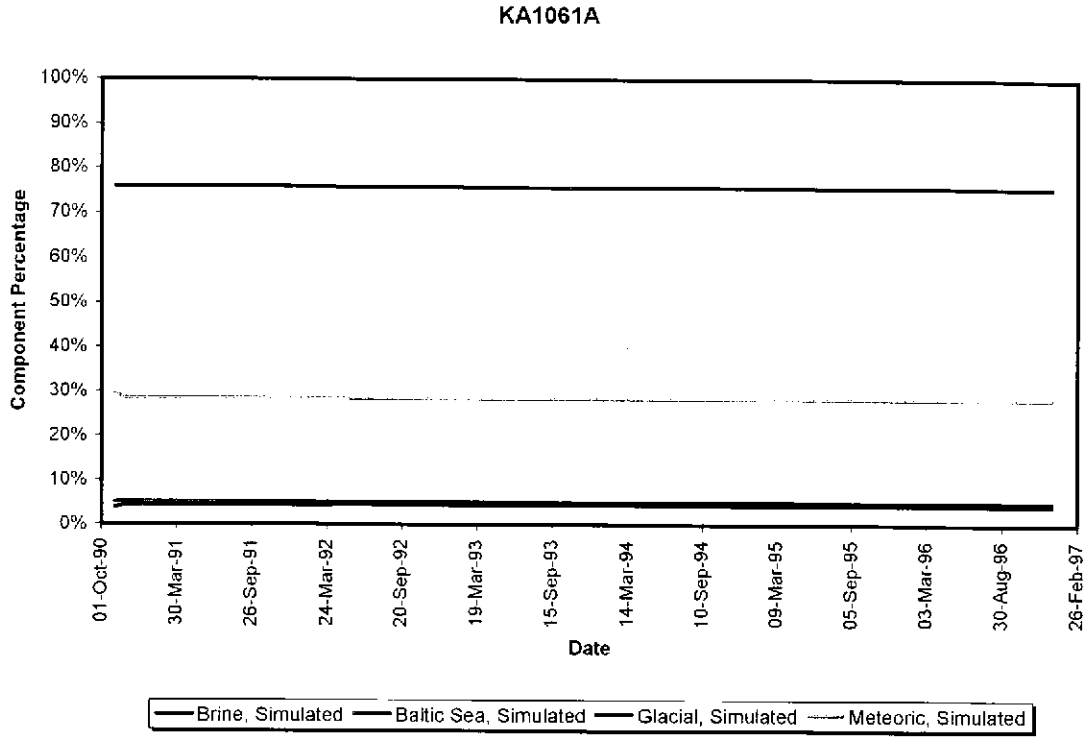

Figure 5-29 KA1061A geochemical inflows for 4 endmembers

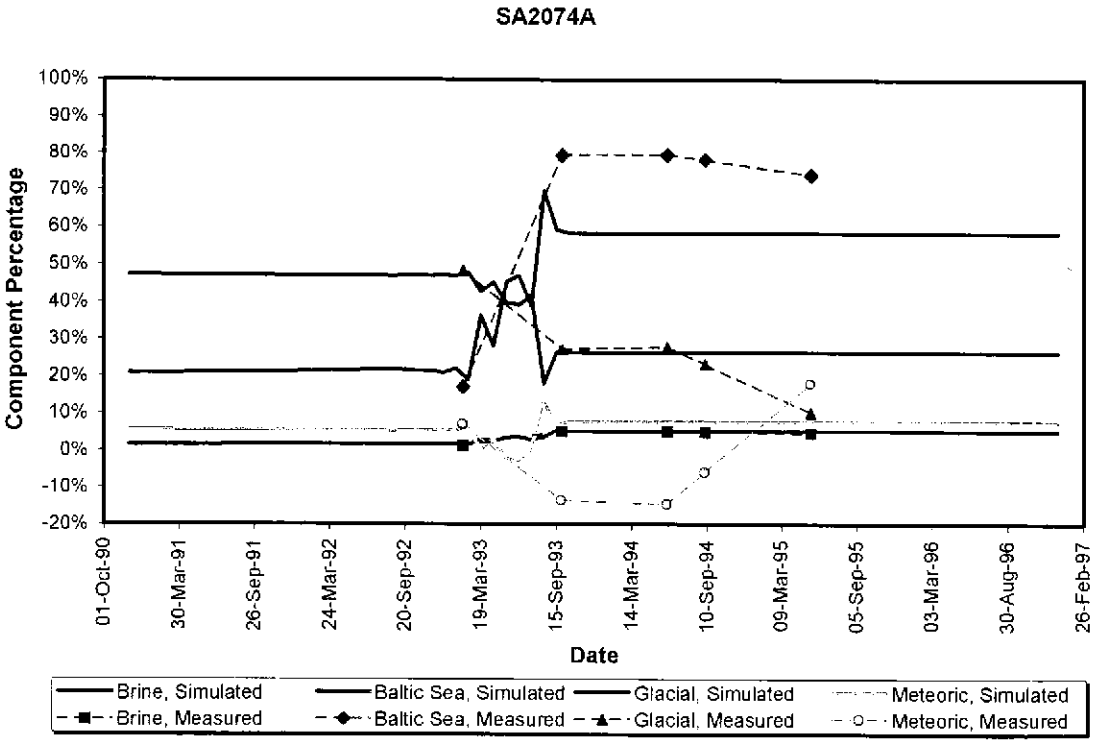

Figure 5-30 SA2074A geochemical inflows for 4 endmembers

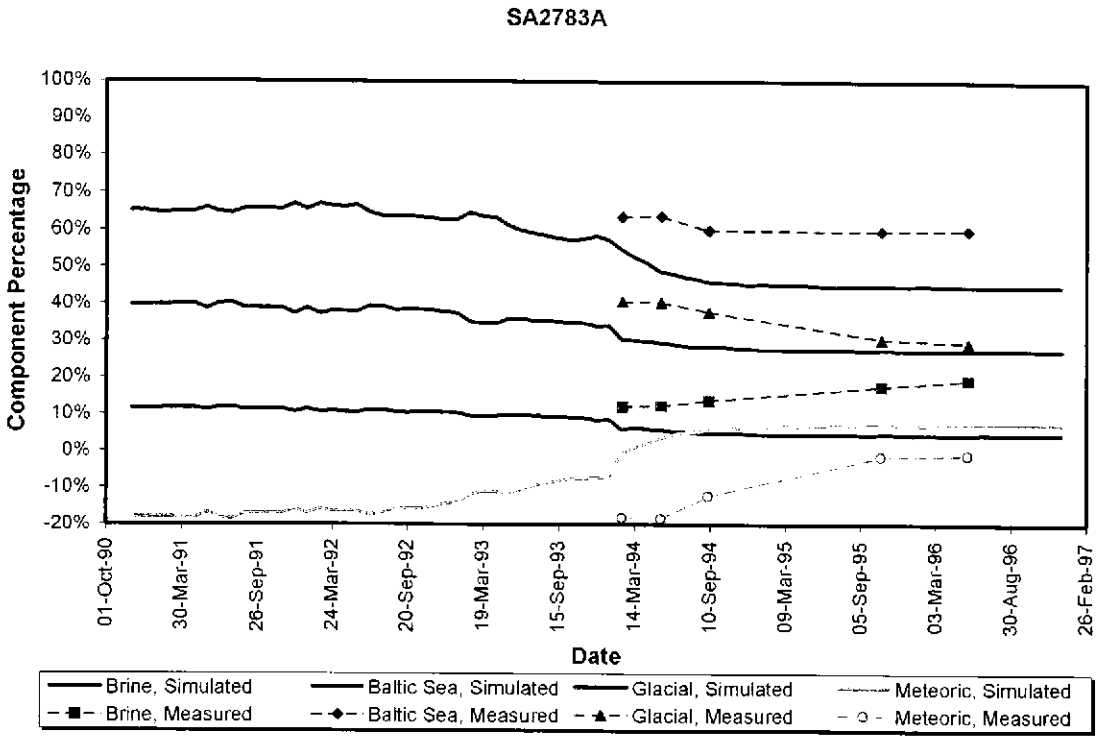

Figure 5-31 SA2783A geochemical inflows for 4 endmembers

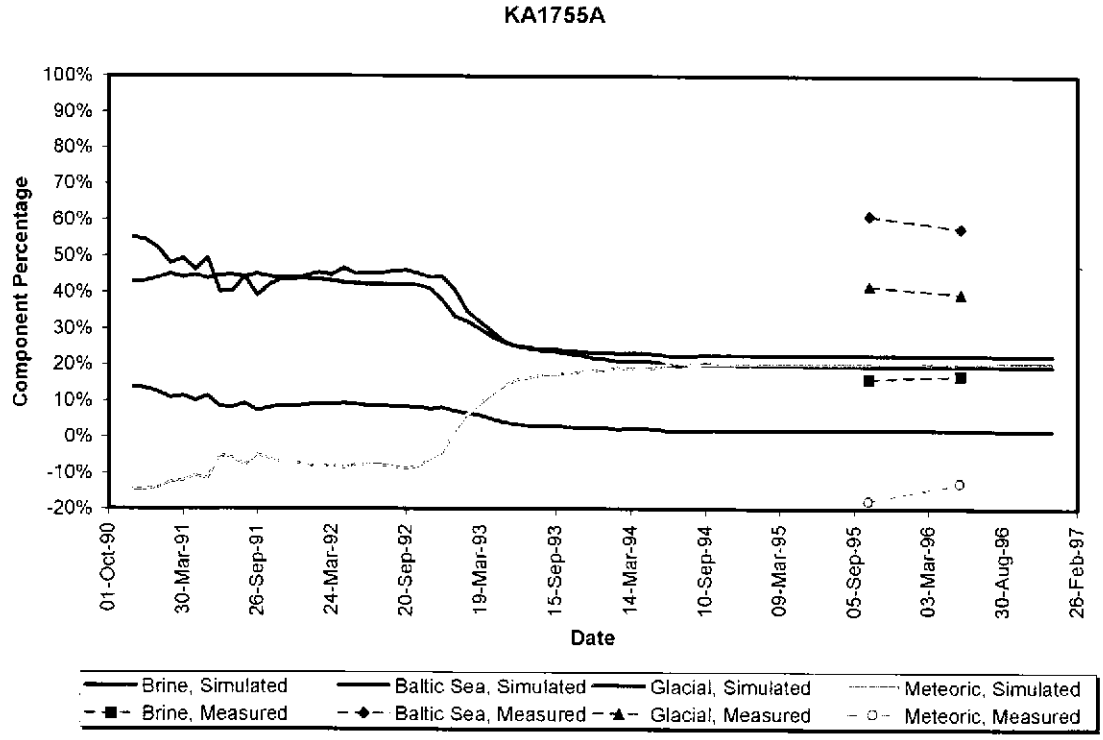

Figure 5-32 KA1775A geochemical inflows for 4 endmembers

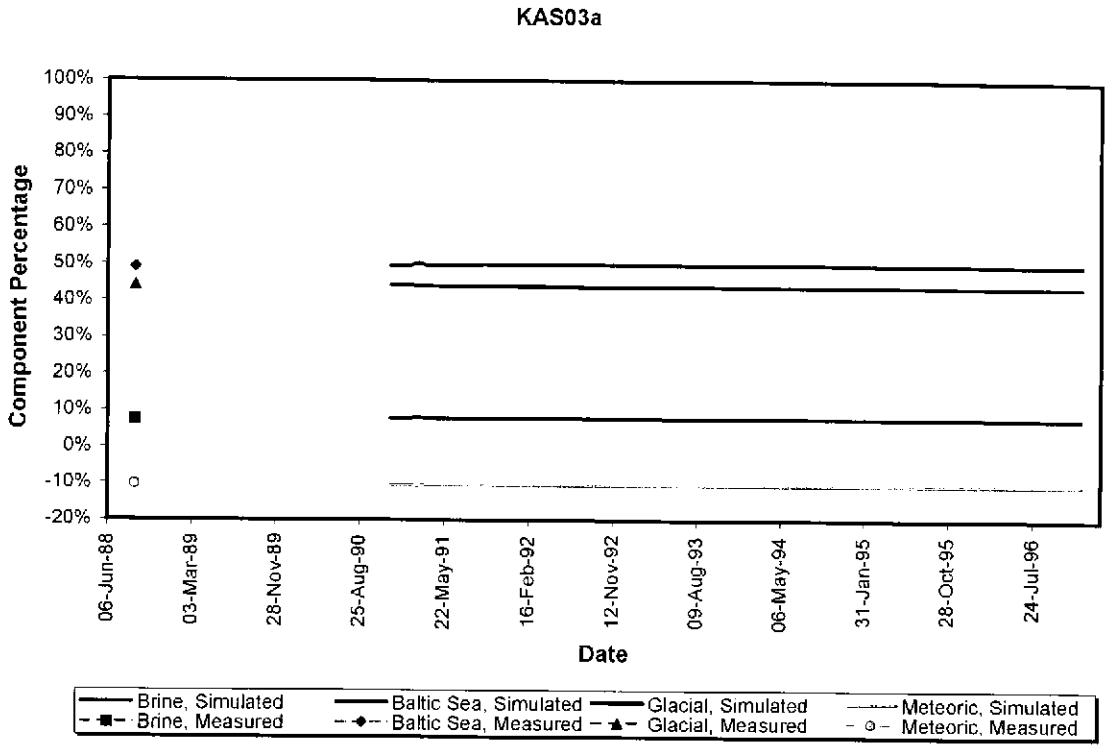

Figure 5-33 KAS03a geochemical inflows for 4 endmembers

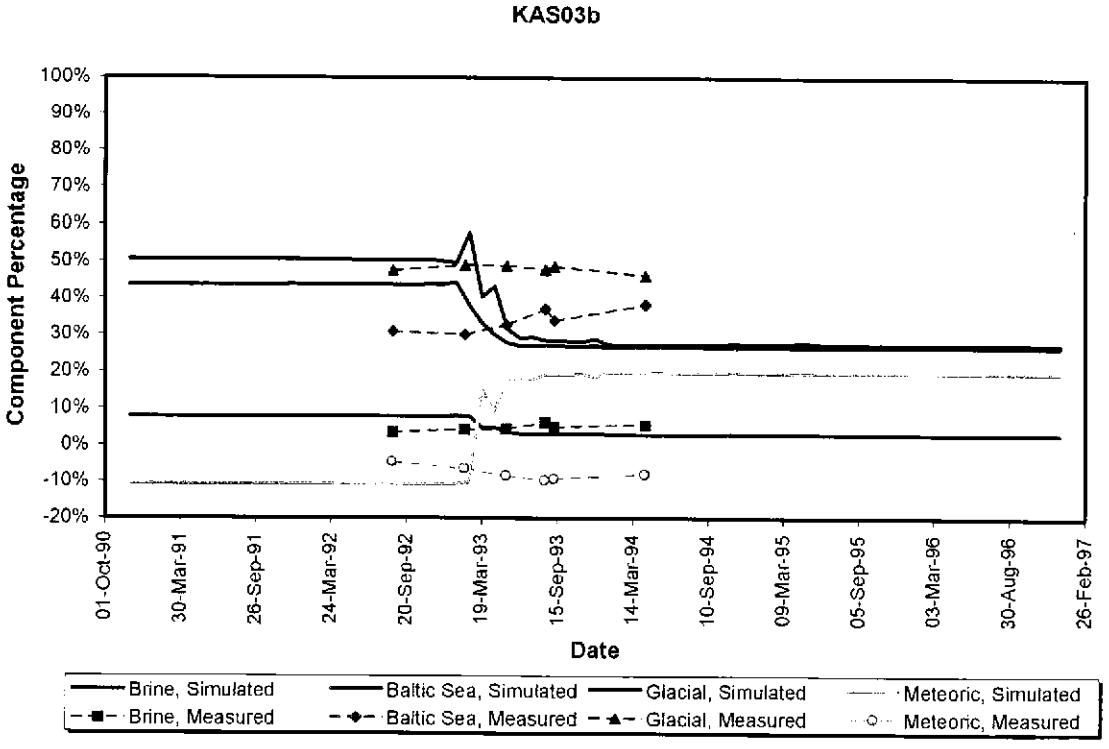

Figure 5-34 KAS03b geochemical inflows for 4 endmembers

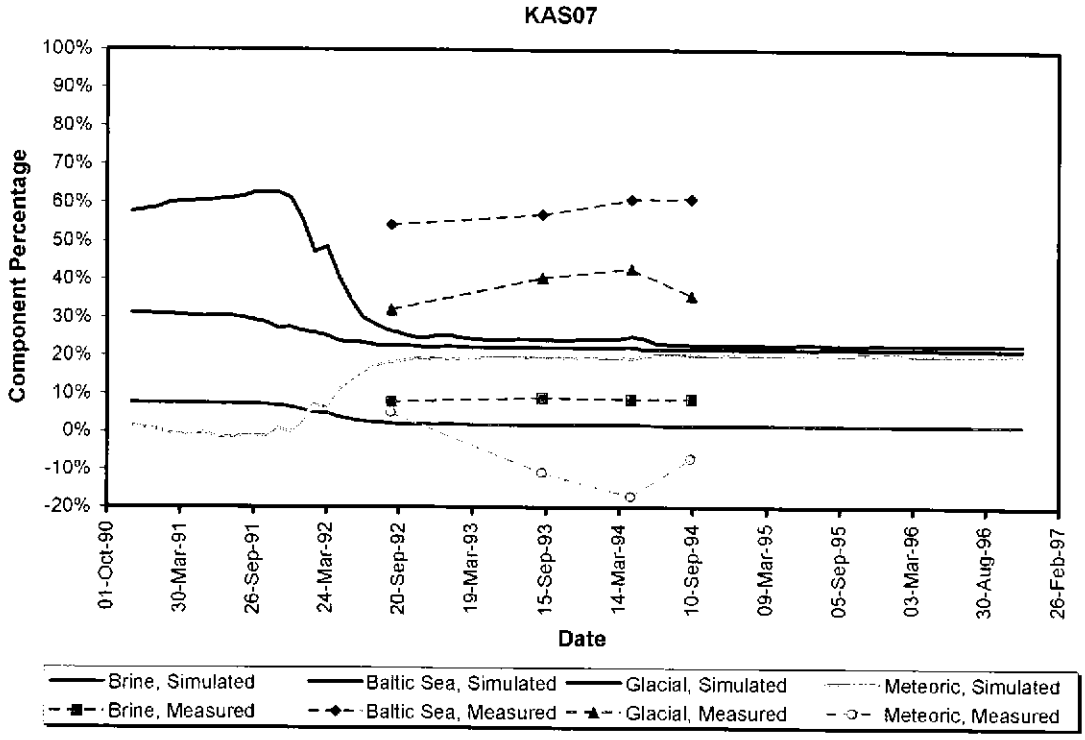

Figure 5-35 KAS07 geochemical inflows for 4 endmembers

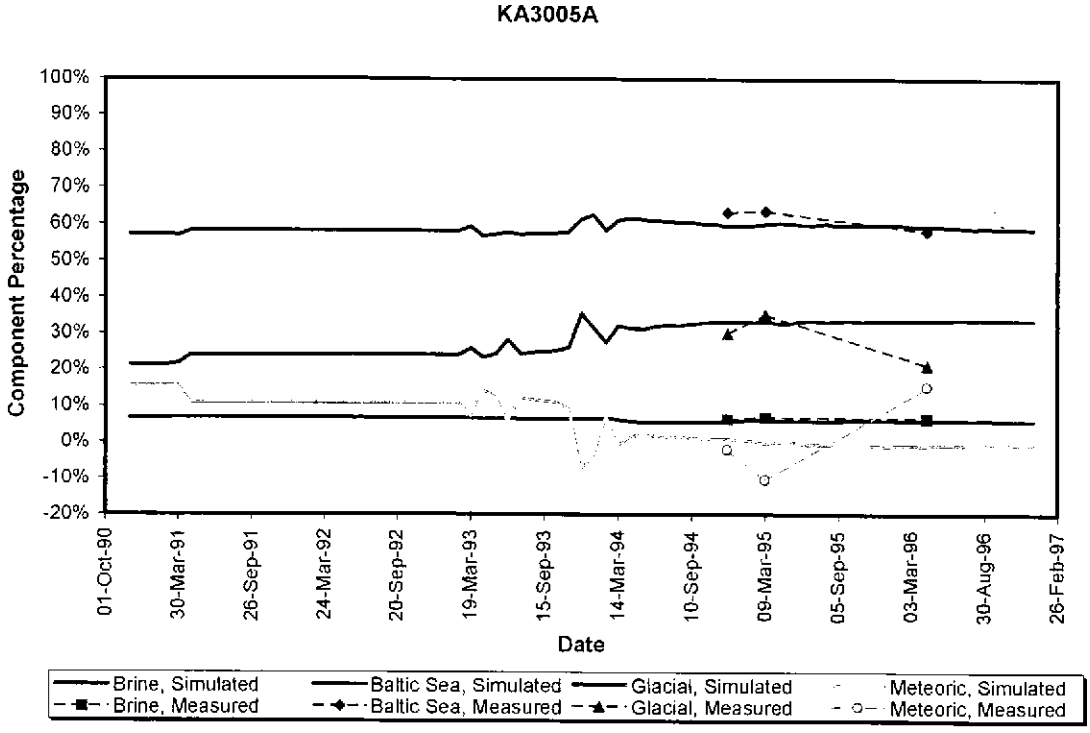

Figure 5-36 KA3005A geochemical inflows for 4 endmembers

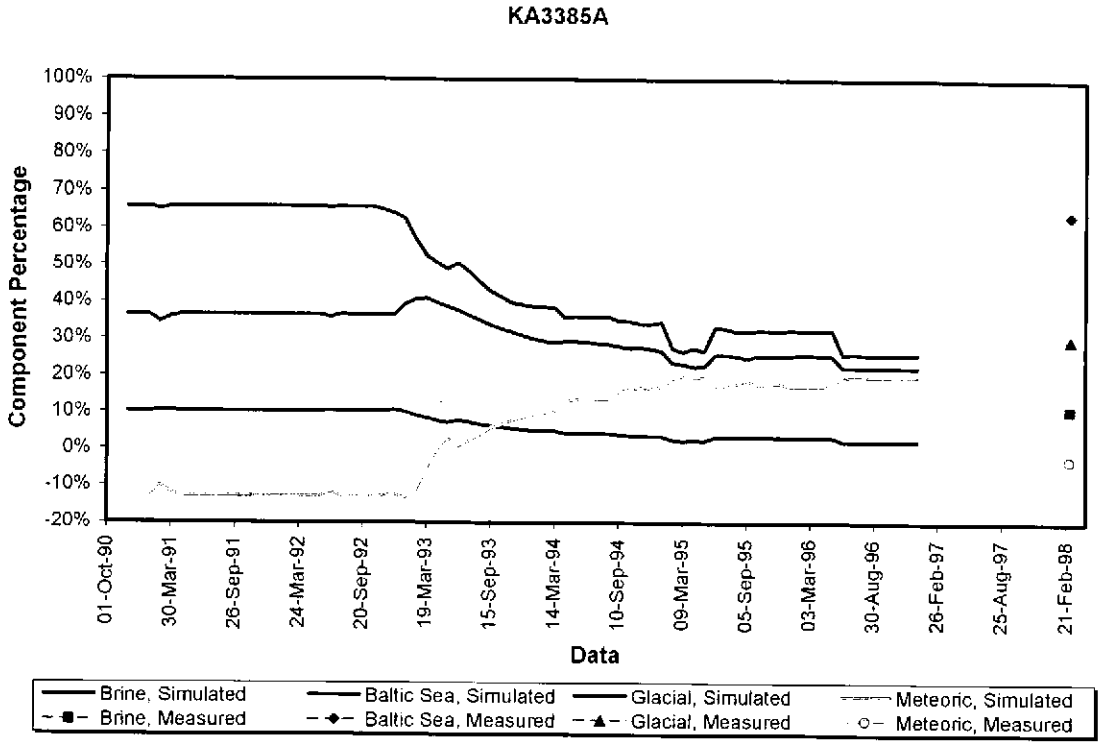

Figure 5-37 KA3385A geochemical inflows for 4 endmembers

5.5 VALUE OF TASK 5 FOR JNC

One goal of JNC's participation in the Task 5 project is to evaluate how the methodology used at Äspö might be applied to potential repository sites in Japan. In order to assess the usefulness of the Äspö approach, the methodology was separated into five topics.

1) general conceptual approach
2) applicability of M3 and principal component approaches to geochemistry interpretation
3) spatial chemistry interpretation
4) hydrogeological and hydrochemical constraints on the model
5) site characterization requirements for geology, hydrogeology and geochemistry data

These topics are covered in the following five sub-sections. Concluding remarks are provided in Section 5.5.6.

5.5.1 General Conceptual Approach

The general approach used in the Äspö Task 5 modeling, by the JNC/Golder team and generally by the other Task 5 team members, was sequential. The phases could be summarized as:

- Develop a regional model of the site including only the large scale features
- Develop a conceptual model for the background fractures. For a DFN idealization this included the orientation, size, intensity, and transmissivity of the non-regional features. For porous medium models this would be the equivalent block transmissivities.
- Develop boundary conditions for the modeled region.
- Create a finite element model including the major features, background features, and boundary conditions. Calibrate this model to the measured head distribution by varying the fracture properties and boundary conditions.
- Use this calibrated model to predict chemistry distributions. Calibrate this model to the measured chemistry and head distribution by varying the fracture properties and boundary conditions.

Based on the Task 5 modeling of the Äspö site this approach worked well. It was found that the calibration to measured heads provided a reasonable calibration to the general water sources, but that the travel velocity was poorly predicted. The chemistry data provided a data set from which to refine these velocities. Chemistry data also reduced the non-uniqueness of the system.

It should be noted, however, that the goodness-of-fits achieved were also sensitive to the methodology used to compute the geochemical distribution across the site. The hydrogeology and the geology at the Äspö site are consistent with the major features dominating mixing and flows. Therefore it was necessary to distribute chemistry based on the major features, rather than assuming a continuum. The strong influence of the Baltic / Äspö Island boundary on the chemistry also markedly affected the interpretation. For a different site, this means that the modelers would need to ascertain the structures, geology and/or major processes affecting the chemistry prior to setting up the geochemical spatial distribution. Similarly, the interpretation scheme should also account for the hydrogeological conditions.

5.5.2 Applicability of M3 and Principal Component Approaches

The M3 method was used for the Stage 1 and Stage 2 modeling. The numerically interpreted Principal Components were used to assign chemical properties for the Stage 3 sensitivity modeling. The two approaches have differing advantages and disadvantages.

The M3 method was developed for application at Äspö where saline groundwaters and brines are major features of the groundwater system. The method as applied for Task 5 had the advantage that the four end-members chosen were physically meaningful. However, the M3 method may not be generally applicable. In particular, the reliance of the method on the first two principal components may not be appropriate in fresh groundwater systems. In such cases the first two principle components are more likely to reflect factors other than groundwater mixing. For example, water/rock interactions are likely to be a more significant cause of chemical variation in

fresh groundwater systems than in saline groundwater systems. In such cases, it will be necessary to consider other principal components besides the two most important ones, in order to deduce information about groundwater mixing.

In Model 2, seven chemical component model used for the Stage 3 sensitivity analyses makes no prior assumptions about the numbers or compositions of chemical components (analogous to end-members in the M3 modeling). The advantage of this approach is that the chemical components are based purely on analysis and provide a measure of the applicability of mixing (and by implication chemical reaction) to the groundwater regime. This is extremely important, as if chemical reaction is an important component of the variation in groundwater composition, the geochemical mixing approach used to calibrate the DFN model is invalid. The disadvantage of this approach is that the chemical compositions, and the end-members created from them, are not necessarily physically realistic.

5.5.3 Spatial Chemistry Interpretation

The Task 5 modeling both highlighted the difficulty of extrapolating measured chemistry at a few distinct locations throughout a much larger region, and showed that this could be successfully achieved. Unless the density of measurement locations is sufficiently high, providing good resolution at all chemistry interfaces, a meaningful interpretation requires that the hydrogeology of the area be considered as part of the extrapolation process. Without this interpretation, the number of locations at which chemistry has been measured is typically too small to define chemical boundaries. In particular, the effect of saline interfaces (e.g. the Baltic/Äspö Island boundary), and chemistry depth dependence should be considered.

The dominance of the regional features on the chemistry should also be addressed when choosing an interpolation scheme.

5.5.4 Hydrogeological and Hydrochemical Constraints on the Model

The major constraint on the model should be a good conceptual model for the site prior to modeling. The hydrogeological and hydrochemical data provide invaluable information, but on their own can not be expected to generate anything approaching a unique solution.

The head and geochemical data provides differing constraints on the model. Head data is critical, and ought to be used to calibrate the model prior to geochemical input. The reasons for using the head data first are that this information is less ambiguous. The time-dependent head information is dominated by local connectivity and transmissivities as the tunnel section is being constructed, and by the regional connectivity and boundary conditions later on. Therefore, if the original fracture model accurately reflects the major connectivity, missing connectivity (e.g. the Mystery Feature) and boundary conditions can be calibrated fairly successfully.

The geochemical information provides the only real constraint (or validation) on the source location of waters predicted by a model. This calibration provides information, like the head data, on whether a major connection is missing. However, like the head calibration, it relies on having a good underlying DFN model that already replicates most of the major hydraulic structures.

Additionally, geochemical data can be used to calibrate transport apertures and storage affects. These effects are difficult to calibrate using solely time dependent heads measures at tunnel sections.

5.5.5 Site Characterization Requirements for Geology, Hydrogeology and Geochemistry Data

The site characterization requirements for geology, hydrogeology and geochemistry may be summarized as follows. Note that all three topics are inter-dependent and should be considered together where possible.

Geology:

- Location and size of all major features.
- Orientation, size and intensity of background fracturing.
- Topography, location of streams, etc. required to provide boundary conditions for the edges of the modeled region. Ideally the boundaries should be distant so that the model is not sensitive to the assumptions, and the boundaries should be located where the boundary condition is not sensitive to the model used to generate them. For example, infiltration boundaries based on porous medium results should generally not be assigned to fracture network models.
- Aperture information.

Hydrogeology:

- Hydrogeological properties of the major features. The variation in properties across a feature may be important. Similarly, the effect of the feature on adjacent fractures (e.g. impermeable or permeable zone at edge of fault zone).
- Hydrogeological properties of the background fracturing.
- Time-dependent heads required to provide differing scale of properties
- Both density-corrected and raw information should be collected and reported.
- Measurement locations should be distributed both in main fracture zones and in the background network to allow verification of the relative permeabilities of the DFN. Geology only provides the orientation and size information, intensity and transmissivity should be derived from hydraulic testing.

Geochemistry:

- Time dependent geochemistry both within the major features and the background fracturing.

- Interpretation to provide geochemical overview of the site. This should include the in situ controls on the chemistry variations (e.g. saline – freshwater interface, long term chemical reactions, age of waters, etc.).

5.5.6 Conclusions

The conclusions of the additional Stage 3 analysis are:

- The Stage 3 analysis simulations provided significant improvements in breakthrough calibration.
- The change to an improved interpolation scheme for spatial distribution of end-members was the key to improving the Task 5 predictions
- Seven principal component end-members provide a better match to the actual chemistry and a clearer measure of whether the mixing assumption is appropriate. However, the seven principal components, based solely on numerical analysis, lack physical meaning
- The improved particle-tracking algorithm also contributed to a more accurate breakthrough calculation. This algorithm, which is consistent with the solute allocation in transport codes such as LTG (Dershowitz et al., 1998c), PICNIC (Barten, 1996), etc., is potentially useful for Performance Assessment calculations.

6. CONCLUSIONS

This report presented hydrogeological and pathways modeling of Äspö Island as part of "Task 5" of the Äspö Task Force on Modeling of Groundwater Flow and Transport of Solutes. The report describes model evolution, and the use of hydrogeological and geochemical information to develop predictive models. The head and geochemistry results at three representative times are provided in Appendix D.

The modeling was undertaken in three stages. In Stage 1 the finite element model of the DFN was calibrated to hydrogeological data. Stage 2 used geochemical measurements to improve the calibration. These results were presented as Task 5 predictions. The final stage, Stage 3, documents an additional sensitivity analysis developed to investigate the sensitivity of the results to the interpreted chemical components and particularly the interpolation scheme used to compute the source chemistry within the modeled domain.

Calibration to heads, using a well-defined geological model as the starting point, provided a reasonable estimate of the local connectivity of the system. However, the time dependence of the flows into the tunnel was generally not well modeled.

The inclusion of geochemical data allowed a much better fit to the time dependence of the model. The data also highlighted where additional connections were required to increase the connectivity to a specific area of the model. Inclusion of such features improved the head calibration, as well as the chemistry fit. However, the results proved to be highly sensitive to the methodology used to spatially locate the initial end-members, and to a lesser extent to the choice of chemical components. The Äspö site is dominated by the large-scale features. It was necessary to use the large-scale features as the dominant influence on the chemistry. The Kriged grid of chemistry locations, combined with a linear interpolation scheme to compute the chemistry between the grid points, did a poor job of calculating the chemistry of the inflows. It is believed that the reason for this poor calibration was that the Kriging and interpolation scheme did not incorporate the geology of the model into the interpretation.

The Stage 3 model could have been improved further using the geochemical information. This was not attempted, as the purpose of this modeling stage was to highlight the sensitivity of the results to the data extrapolation/interpretation.

During this Task 5 modeling two main objectives were set:

1) to assess the consistency of groundwater flow models and hydrochemical mixing-reaction models through the integration and

comparison of hydraulic and hydrochemical data obtained before, during and after tunnel construction;

2) to develop a procedure for integration of hydrological and hydrochemical information which could be used for assessment of potential repository sites.

The groundwater flow and hydrochemical mixing-reaction models were found to provide consistent results for the Äspö site. This is in part due to the staged approach, with the geological, hydrogeological and chemical data providing differing information. However, the M3 method was developed for application at Äspö where saline groundwater and brines are major features of the groundwater system. The method as applied for Task 5 had the advantage that the four end-members chosen were physically meaningful. However, the M3 method may not be generally applicable. In particular, the reliance of the method on the first two principal components may not be appropriate in fresh groundwater systems. In such cases the first two principle components are more likely to reflect factors other than groundwater mixing. For example, water/rock interactions are likely to be a more significant cause of chemical variation in fresh groundwater systems than in saline groundwater systems. In such cases, it will be necessary to consider other principal components besides the two most important ones, in order to deduce information about groundwater mixing.

The general procedure for integration of hydrological and hydrochemical information in the Äspö Task 5 modeling was staged. The stages could be summarized as:

- Develop a regional model of the site including only the large scale features
- Develop a conceptual model for the background fractures. For a DFN idealization this included the orientation, size, intensity, and transmissivity of the non-regional features. For porous medium models this would be the equivalent block transmissivities.
- Develop boundary conditions for the modeled region.
- Create a finite element model including the major features, background features, and boundary conditions. Calibrate this model to the measured head distribution by varying the fracture properties and boundary conditions.
- Use this calibrated model to predict chemistry distributions. Calibrate this model to the measured chemistry and head distribution by varying the fracture properties and boundary conditions.

This staged approach is very general, and is therefore applicable to other potential repository sites. The staging was advantageous, because it necessitated constructing a good geology based DFN model of the site prior to calibration. Without such a structure for the DFN, the problem is poorly constrained and the calibration non-unique. A unique calibration likely cannot be obtained in practice, but the staged approach should enable the dominant features to be well replicated.

The head and geochemical data provides differing constraints on the model. Head data is critical, and ought to be used to calibrate the model prior to geochemical input. The reasons for using the head data first are that this information is less ambiguous. The time dependent head information is dominated by local connectivity and transmissivities as the tunnel section is being constructed, and by the regional connectivity and boundary conditions later on. Therefore, if the original fracture model accurately reflects the major connectivity, missing connectivity (e.g. the Mystery Feature) and boundary conditions can be calibrated fairly successfully.

The geochemical information provides the only real constraint (or validation) on the source location of waters predicted by a model. This calibration provides information, like the head data, on whether a major connection is missing. However, like the head calibration, it relies on having a good underlying DFN model that already replicates most of the major hydraulic structures.

Additionally, geochemical data can be used to calibrate transport apertures and storage affects. These effects are difficult to calibrate using solely time dependent heads measures at tunnel sections.

The Äspö Task 5 modeling had access to a wide range of data and generally the quality of these data was very high. The authors feel that the staged approach was advantageous to allowing a systematic assessment of the modeling success. The area where the data could possibly be improved for future performance assessment of repository sites is related to the choice of locations. Generally, the aim of the model validation is to indicate whether the model correctly replicates the overall response of the groundwater system, while still reproducing more local effects. At Äspö the tunnel was a major influence of the groundwater system. Therefore it is important to ensure that any model used for PA correctly replicates these affects. However, the groundwater and pressure regime immediately adjacent to the tunnel is also influenced by the effect of grouting behind the tunnel lining (e.g. reduced inflows into tunnel and head drop across the tunnel lining). For a regional scale model these effects are difficult to include and do not improve understanding of the overall system response. Therefore, where possible, data and calibration locations should be beyond the zone of influence of these activities.

Chemistry measurements prior to tunnel excavation are a more accurate representation of the in situ chemistry distribution, as the tunnel construction was seen to markedly affect the flow regime. Therefore, more early time measurements are advantageous (although difficult to obtain in practice). For the calibration process, chemistry measurements distributed approximately evenly through time would have enabled the flow velocities to be more accurately calibrated. The use of measurement boreholes both within the main fracture zones, and within the background network, are useful in determining the proportion of flow occurring in the different fracture types.

The current modeling was focused on the heads and chemistry measured over several years. For performance assessment the time scale is much longer, typically thousands of years. The usefulness of this modeling to longer time scales should be considered. Tunnel construction likely involves the largest head changes to occur throughout a repository construction and operation. Hence, a good fit to head and chemistry responses gives confidence in the connectivity and transmissivity of the DFN. Prediction of long-term head distributions is more difficult, as the boundary conditions that should be applied to the model are poorly defined over longer time frames. However, this is a deficiency of future knowledge, rather than a deficiency of the DFN model. Potentially, the greater deficiency is the lack of information on the chemistry during tunnel/repository resaturation. It is important to collect chemistry information over a sufficient area to account for longer-term inflows from more remote locations. These inflows, if of differing density and chemistry, may affect the steady state pressure distribution, and possibly chemical reactions within the rock mass adjacent to the tunnels.

Overall, the authors believe the Äspö Task 5 modeling to have been successful, achieving a good fit to both heads and chemistry. The lessons learned are generally applicable to other potential repository sites.

7. REFERENCES

Barten, W., 1996. PICNIC-I test cases: Fracture Case, Paul Scherrer Institut

Bates, R.L. and Jackson, J.A. (eds) 1980. Glossary of Geology. American Geological Institute. Falls Church, Virginia, 1980.

Bear, J., 1972. Dynamics of Fluids in Porous Media. American Elsevier Publishing Co., New York.

Cave, M.R. and Wragg, J, 1997. Measurement of Trace Element Distributions in Soils and Sediments Using Sequential Leach Data and a Non-specific Extraction System With Chemometric Data Processing. *Analyst*, 122, 1211-1221.

Cave, M.R. and Harmon, K, 1997. Determination of Trace Metal Distributions in the Iron Oxide Phases of Red Bed Sandstones by Chemometric Analysis of Whole Rock and Selective Leachate Data. *Analyst*, 122, 501-502.

Davis, J.C. 1986. Statistics and data analysis in geology, 2nd edition. John Wiley and Sons, New York.

Dershowitz, W., D. Shuttle, M. Uchida, and A. Fox, 1998a. Preliminary 2 km Scale Modeling of Geochemical Pathways Äspö Hard Rock Laboratory, Äspö Sweden (Task 5). SKB International Cooperation Report IC-99-XX. SKB, Stockholm.

Dershowitz, W., G. Lee, P. LaPointe, and J. Geier, 1998b. FracMan Interactive Discrete Fracture Data Analysis, Geometric Modeling, and Exploration Simulation. User Documentation, Version 2.6. Golder Associates Inc., Seattle.

Dershowitz, W., T. Foxford, E. Sudicky, D. Shuttle, and Th. Eiben, 1998c. PAWorks Pathway Analysis for Discrete Fracture Networks with LTG Solute Transport. User Documentation, Version 1.5. Golder Associates Inc, Seattle.

Laaksoharju, M., Tullborg, E-L., Wikberg, P., Wallin, B. and Smellie, J. 1999a. Hydrogeochemical conditions and evolution at the Äspö HRL, Sweden. Applied Geochemistry, 14, 835-859.

Laaksoharju, M., Skårman, C. and Skårman, E. 1999b. Multivariate Mixing and Mass Balance (M^3) Calculations. A New Tool for Decoding Hydrogeochemical Information. Applied Geochemistry. Vol. 14., p 861-871.

Laaksoharju, M. 2000. M3 calculations and their interpretation within task#5. INTERA Report for Task 5 Participants.

Metcalfe, R., 1999. Geochemical Uncertainty Influences on Äspö Task 5. In preparation. JNC, Tono, Japan.

Miller, I., G. Lee, and W. Dershowitz, 1998. MAFIC Matrix/Fracture Interaction Code with Heat and Solute Transport. User Documentation, Version 1.6. Golder Associates Inc., Seattle.

Nordstrom, D.K. and Munoz, J.L. 1994. Geochemical thermodyanamics 2nd Edition. Blackwell Scientific Publications, Oxford, England. 493pp.

Rhén, I., 1999. Data Distribution. Reference Äspö Structural Model for Task 5. SKB, Stockholm.

Rhen, I., 1998. Data Distribution 4, Boundary Conditions and Initial Conditions. SKB, Stockholm.

Rhén I (ed), Gustafson G, Stanfors R, Wikberg P, 1997a. Äspö HRL - Geoscientific evaluation 1997/5. Models based on site characterization 1986-1995. SKB Technical Report TR-97-06. SKB, Stockholm.

Rhén, I., Gustafson, G. Stanfors, R. and Wikberg, P. 1997b. Äspö HRL – Geoscientific evaluation 1997/1995: Models based on site characterization 1986-1995. SKB Technical Report 97-06.

Rhén, I., J. Smellie, and P. Smellie, 1998. Äspö HRL Task Force on modeling of groundwater flow and transport of solutes. Task 5, Performance Measures, Version 1. SKB, Stockholm.

Svensson, U., 1999. Äspö HRL Task Force on Modeling of Groundwater Flow and Transport of Solutes, Data delivery No 11. Pressure and salinity boundary conditions. Task No 5 - Integration of hydrology and chemistry.

Uchida, M., W. Dershowitz, A. Sawada, P. Wallmann, and A. Thomas, 1997. FracMan Discrete Fracture Modeling for the Äspö Tunnel Drawdown Experiment. SKB Äspö Project International Cooperation Report ICR-9703. SKB, Stockholm.

Wikberg, P., 1998. Äspö HRL Task Force on modeling of groundwater flow and transport of solutes. Plan for modeling task # 5: Impact of the tunnel construction on the groundwater system at Äspö. A hydrological-hydrochemical model assessment exercise. SKB Report HRL 98-07. SKB, Stockholm.

APPENDIX D

EVALUATION OF UNCERTAINTY PRELIMINARY MIU HYDROGEOLOGICAL MODELING AND GROUNDWATER FLOW SIMULATION

Evaluation of Uncertainty Preliminary MIU Hydrogeological Modelling and Groundwater Flow Simulation

Dawn Shuttle
Golder Associates Inc.
January, 2001

1. INTRODUCTION

This document provides recommendations for the proposed approach for the DFN modelling and groundwater simulation of the MIU project. Recommendations include a suggested methodology for constructing the discrete fracture network (DFN) model, and running the sensitivity analyses.

The main focus of the document is to highlight the areas of the data analysis and model construction which have a strong effect on the modelling results, and to discuss, and make recommendations on, the approaches that may be used to achieve a useful model of the MIU site.

The following are addressed:

- Issues associated with the technical specification
- Data analysis – methodology and associated problems
- Size of DFN model and truncation
- Structures in .SAB file
- Boundary Conditions
- LTG and "particle tracking"
- Calibration of model
- Pathways analysis
- Sensitivity analysis
- Choice of finite element

1.1 Issues

The technical specification states that "one of the main goals of the MIU project and the Regional Hydrogeological Study is to establish comprehensive techniques for investigating the geological environment. An important part of these projects is to develop methodologies for hydrogeological modelling and groundwater flow simulation".

The technical specification also states that "In this study, in situ data analysis, hydrogeological modelling and groundwater flow simulation will be done by using several modelling and simulation methodologies in order to evaluate the influences of uncertainty in in situ data analysis, hydrogeological modelling and groundwater flow simulation..... ".

Therefore the purpose of this study is twofold:

1. to provide a methodology for the construction of a DFN and subsequent groundwater modelling
2. to evaluate the influences of uncertainty introduced by data analysis and groundwater modelling implementation

In order to "evaluate uncertainty range of parameters", the meaning of "uncertainty range of parameters" needs to be defined. Since FracMan is a stochastic model the parameters are typically input as distributions.

An alternative is to compare the mean and standard deviation of the data with the mean and standard deviation of the fitted parameter distribution. However, standard deviation is affected by the number of data points, so the comparison is not theoretically correct.

For the purposes of the data analysis the chi^2 and Smirnov statistics will be used as the measure of uncertainty in the data parameter distribution

The proposed scope does not clearly differentiate between parameter uncertainty (due to uncertainties in the true fracture property parameter distributions) and stochastic spatial uncertainty (due to not knowing exactly where a fracture is located).

The specified sensitivity analysis should only consider parameter variation. Spatial uncertainty needs to be considered in order to measure the uncertainties in the modelling and simulation methodologies. Therefore, multiple realizations will be required for the pathways analysis (section 5 of the technical specification).

The technical specification does not clarify the difference between the "steady state" and "present" groundwater states. It is unclear whether the "present" state is a transient analysis.

2. ISSUES TO BE CONSIDERED PRIOR TO DATA ANALYSIS

2.1 Groundwater Head

Prior to simulating the groundwater regime, it is also necessary to decide which aspects of the head distribution it is important to replicate. For example, a sparse DFN comprised of large vertical transmissive features are likely to contain low gradient head distributions along vertical boreholes. However, if these fractures are all generated stochastically the distribution of low head gradients will be represented, but locally these variations are unlikely to match those measured. This affect is magnified if the boundary is close to the borehole interval location, as the number of fractures between a boundary and the borehole interval is small.

2.2 Stochastic Realizations Needed

The effect of the stochastically generated fracturing needs to be considered carefully. This should be taken into account after a DFN model has been selected from the sensitivity analyses. If possible, it would be preferable to either

- Use a lower level of calibration for the groundwater table, water head distribution in boreholes, etc. but use multiple DFNs, or
- Generate many (e.g. 100) realizations of the final uncalibrated fracture network, and choose the 10 that most closely represent the measured head field (uncalibrated) to undertake particle-tracking simulations.

The use of a single DFN simulation for regional simulations is not able to capture the true uncertainty in our understanding of the flow regime. To model small-scale tests where the fractures intersecting the boreholes are a major component of the flow regime, such as interference tests; a single DFN could be sufficient. But to represent a network where the primary flow pathways are primarily totally stochastic, multiple realizations are required.

2.3 Geological Issues

The DFN model should be based on the "soft" information of available geological interpretations as much as the "hard" statistical data. To achieve this MIU geologists should be involved directly in the DFN model preparation.

Working with geologists should be very useful for creating your conceptual model. However, as we are only interested in flowing transmissive features, and geologists measure every feature, geologists and hydrogeologists/modellers usually have a different way of looking at things.

The geology provides information on where boundaries between different fracture properties (e.g. orientation, fracture intensity, size, etc.) are likely to exist.

The geological model can also provide insight into whether the regional features (faults) should be modelled as single discrete features, or as a zone of fracturing. The issues affecting this decision are the permeability variation over the fault zone (e.g. is complete connectivity over the fault expected) and whether the feature is a flow conductor or a flow barrier.

2.4 Location of Monitoring Points for Groundwater Flow Simulation

Section 5 of the technical specification, "Summarized results of GW flow simulation", provides a summary of the type of measurements that will be required from the flow modelling. It is understood that JNC do not wish to release an exact specification of the result locations, etc. at this time. However, the typical approach to DFN modelling of large regions is to use a higher level of truncation (i.e. a sparser fracture network) for less important portions of the modelled region. If the measurement points are all distant and spatially heterogeneous from the repository, then the measurement resolution will need to be on a fairly large grid and differing levels of truncation may not be appropriate. It would therefore be useful to know whether the distribution of flux and the monitoring points are located close to the repository or to the model boundary.

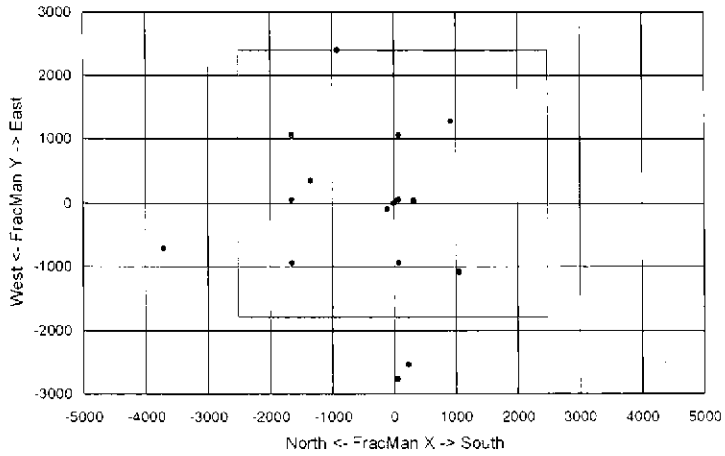

The figure above shows borehole locations in FracMan coordinates.

The red source locations are spaced well apart in X and Y, but a lot closer in the Z direction. With this spacing it is possible that the addition of fractures with a lower level of truncation (i.e. more fractures) at these locations could influence your pathways by allowing more vertical connections. A more accurate model may be obtained if you limit the higher intensity fracturing (lower truncation level) to a very small region local to the release locations (of the order of 30m cubes). The same effect could also be obtained by adding explicit features to connect your release locations to the network.

The measurement locations can be treated the same way.

2.5 Size of Model (truncation issues)

The study area is 4 km by 6 km, with a vertical extent from ground level to 3 km below sea level. This model volume is large for most workstations. Therefore an important component of the DFN implementation will be how the DFN model is truncated to achieve the important aspects of the flow regime. For most large nuclear repository models a "Russian doll" (nested) approach is used. The DFN model close to the waste canisters contains a greater fraction of the entire fracture network than the far field DFN network. This is necessary because close to the canisters local connectivity is extremely important. If no fracture intersects a canister, then no nuclides are able to leave. Conversely, a small, low transmissivity, feature in the far field likely has negligible effect.

The major consideration in deciding the extent of truncation is the maximum size of model that can be simulated on your computer system and the number of realizations required. For running a single realization a restart file size of about 100 MB can be used. For running multiple stochastic realizations a restart file size of 40-50 MB is about the largest that should be attempted. Smaller, e.g. 20 MB, is preferable. The larger files are much slower to view using visualization software, and will not view in Windows editors.

Although more time consuming, large files may be viewed (e.g. in FracViz AVS) by subdividing the restart files using the EDMESH/EDPIPE code. This methodology has been successfully used on other projects.

We subdivided the files by resetting the transmissivities of all finite elements outside the region we are interested in (using the box region, outside option) to a very low value (e.g. 1.e-15), and then deleting all fractures below a slightly larger minimum transmissivity.

The number of fractures that can be modelled is related to whether the pipe or plate option is used to create the finite element mesh, the connectivity of the network, and for plate elements the degree of predivision used. Typically a fracture file containing of the order of 15,000 fractures creates a 20 MB restart file using plate elements. A 20 MB pipe element restart file typically contains on the order of 27,000 fractures. However, for both options the model size is also dependent upon the options used for the mesh generation: element subdivision for plates, and generation options for pipes. The choice of element type is discussed in section 8.

The two fracture properties that are commonly used to truncate DFN models used for hydrogeological flow modelling are fracture transmissivity and fracture size. These properties may be used in combination. However, the combined effect of both truncations must not reduce the block permeability of the system to below the percolation limit. If this occurs, a smaller model region is required.

Note that if a nested "Russian doll" approach is used, care needs to be exercised with differing truncation cut-offs. The flow regime can be influenced by the fracturing intensity, and preferentially biasing the location of fractures using a different truncation limit also affects the flow regime.

An alternative approach to improving local connectivity is to explicitly add deterministic fractures where connections are required (e.g. connecting canisters and/or monitoring borehole sections to the background fracture network). This approach is efficient if the fractures are small and do not affect the global connectivity of the network.

Note that the Excel file "coordinate of boreholes.xls" dated December 1, 2000 shows a model region of 5000m(N-S) by 4188m (E-W).

3. DATA ANALYSIS

The fracture properties that are typically derived from measured data are the spatial model for the fractures, the fracture orientation, fracture size, fracture transmissivity, and intensity of fracturing. Aperture distribution (used for transient analyses) is also derived from measured data and is generally correlated to transmissivity. Storativity (also used for transient analysis) is computed using transient hydrogeological tests.

The output from a FracMan data analysis is a distribution of the analysed fracture property. The distribution, if it provides a good fit to the measured data, will allow for low probability high/low values. The fitted data distributions should be chosen to provide a good fit over the entire data range. If it is not possible to obtain a good fit,

different parameter distributions may be used, and sensitivity analyses used to determine the model sensitivity.

3.1 Spatial Model

The DFN is likely constructed from the following four types of fractures:

1. Deterministic fracture zones

   Deterministic fracture zones should be included in the DFN to replicate the mapped fault zones. These features may be represented as discrete features, or as zones of fracturing. The choice of a single feature, or zone of fracturing, should be related to the geological interpretation, and the variation in measured transmissivity and connectivity over the fault area.

   The inclusion of low transmissivity fault zones (i.e. aquitards) may be incorporated into the DFN model using EDMESH. This code contains an option to reduce the transmissivity of all fractures, or portions of fractures, between two parallel fractures by a user-specified amount. The output of this analysis is a revised fracture file (the source file is not modified).

   It is recommended that these features are located in a separate fracture file, and that this file is the first fracture file to be meshed.

   If no data are available on the geology of the LSFs, using the simplest option of a single feature with a uniform high transmissivity is usually the most sensible. The assumption can be modified to a flow barrier, multiple transmissivities over the LSF area, zone of fracturing, etc, if the modelling indicates this is required to replicate the measured data.

   The orientation of the regional features is likely sub-vertical (but not vertical).

2. Stochastic fracture zones

   Stochastic fracture zones are used to model higher intensity fracturing, but which is not associated with mapped fault zones or other mapped features.

   These fractures should be kept as a separate fracture (.fab) file.

   At the scale of the regional model, these features may be treated as intermediate scale fractures (rather than zones of fractures). The lineament data may be used to provide a length distribution. Connectivity between zones will be stochastic.

   In the absence of data to the contrary, we typically assume the larger features are the most transmissive. This may be incorporated into the DFN model by estimating the proportion of larger fractures plus fracture zones within the packer tests (using the lineament maps to compute relative P_{21}). If the transmissivity is correlated to size, the proportion of largest features will map to that proportion of the highest fracture transmissivities derived from Oxfilet.

3. Background fracturing

   The majority of fractures in the model will be stochastic background fractures. The distribution of properties for this type of fracturing is typically well sampled.

   These fractures should be kept as a separate fracture (.fab) file. This fracture file is typically meshed last because the number of fractures varies between realizations.

   The database probably cannot be explicitly divided into different scale features. However, if size and transmissivity are correlated (typically assumed if no contrary information) the following is possible:

   - Size distribution for the features is derived from the fractal size analyses.
   - Transmissivity and transmissive fracture spacing is derived from an Oxfilet analysis of the available packer test data. The data seems to fit a single log-normal distribution (not two distributions) therefore it would be reasonable to assume that if X% of the fractures are intermediate fractures and fracture zones, then the top X% of the fitted transmissivity distribution should be assigned as intermediate fractures and fracture zones. The bottom of the distribution would be assigned to the background fracturing.
   - The flow log data may be used as a cross check on the Oxfilet results. The spacing of the most transmissive features should approximately match the spacing of the flowing zones in the flow logs.
   - The faults and LSF are explicitly assigned transmissivities. These would be initially assumed to be close to the highest measured transmissivities.

4. Conditioning fractures

   The MIU project DFN model is likely to contain two types of conditioned fractures. The first are discrete fractures intersecting the borehole interval sections and canisters. The purpose of these fractures is to increase connectivity between the DFN background fractures and the borehole intervals/canisters. The fractures intersecting the borehole intervals should be of low transmissivity, to have minimal effect on the head distribution within the model. The conditioning fractures intersecting the canisters will be higher transmissivity, but small. The intent is again to connect a structure to the background fracture network, while not distorting the flow field.

   It is recommended that these features be kept in a separate fracture (.fab) file. Typically these fractures, if used, are meshed after the large-scale features because fractures remain constant between successive stochastic realizations as the same fracture file is always used.

   The second type fracture of conditioning is used for modelling transient hydraulic tests and in other situations where replicating the orientation and/or transmissivity of fractures intersecting a structure is important. This conditioning is done automatically within FracWorks, with FracWorks moving fractures and adjusting fracture transmissivities to produce the

correct orientation and/or transmissivity. The limitation on this method is that the fracture intensity in the conditioning data set and the fracture file must be similar.

The spatial model (e.g. Baecher, fractal, etc.) is derived from the spacing of the in situ fracturing. No trace maps were observed in the provided data, therefore the spatial model will likely be based on fracture intensities measured in boreholes. These data are contained in TGC_Geo_6 and TGC_Geo_10. The data in TGC_Geo_10 is pictorial only, and therefore difficult to use. TGC_Geo_6 contains the depth of the fractures measured using borehole TV in Excel format. The depth and number of fractures at a specific depth (usually 1.0) may be exported to ASCII .txt format, and then read into the Fractal code. For input into Fractal column 1 of the file contains the fracture depth, column 2 of the file contains the number of fractures at the depth.

The slope of the box dimension curve within Fractal provides a measure of the dimension of the fracture network. A straight line fit in log-log space with a dimension of 1.0 indicates a Baecher model. A straight line fit at any other slope indicates a Fractal spatial model.

Note that if trace map data is available, Fractal also reads input files in the FracMan .f2d format. An example of an analysis for trace map data is displayed below.

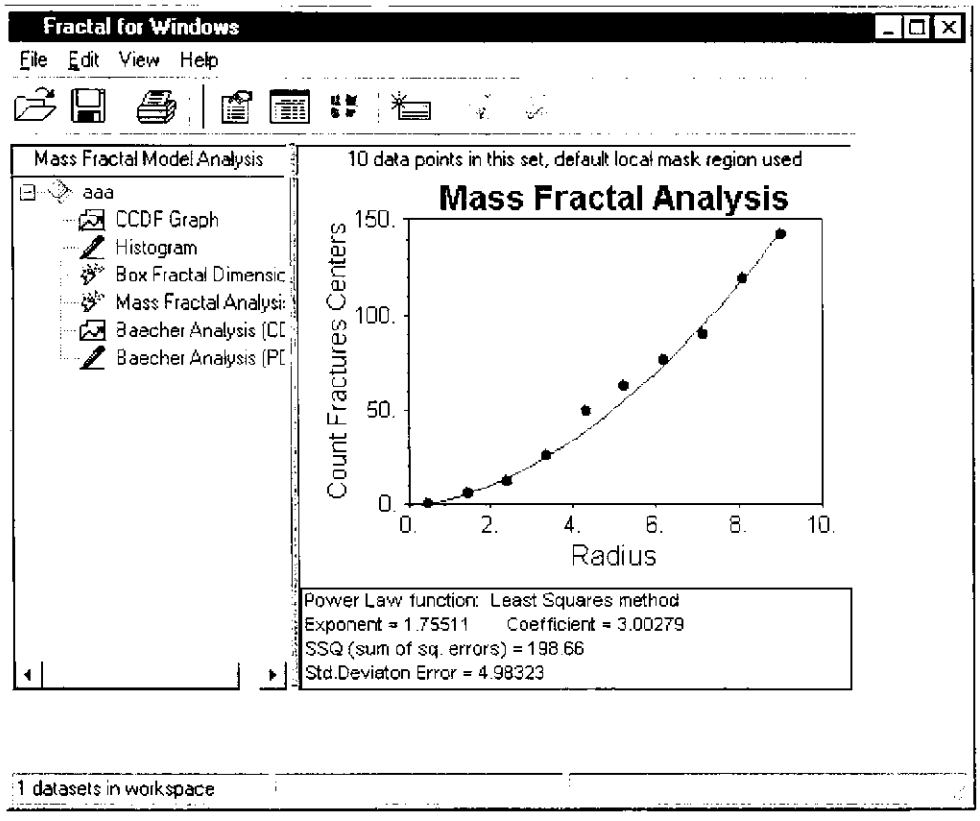

3.2 Orientation

The fracture orientations are also contained in the borehole television data. Again the most useful file is the Excel spreadsheet, TGC_Geo_6. Both the dip and the dip

direction (see far right of the spreadsheet) are provided in numerical format. This information may be converted to pole orientations for FracMan within Excel. The Excel file contains a large number of data points. This enables the following analyses to be undertaken:

- Orientation of the entire data set;
- Orientation by BH to see if there is horizontal spatial variability;
- Orientation by elevation or depth to see if there is vertical spatial variability;
- Orientation of "open crack" fractures; and
- Correlated orientation (using the .ISI or .ISP format).

Based on these analyses, the orientation data set should be divided into subsets for the DFN construction. Geological features, such as geology or the location of faults, should be reviewed to determine whether any variations in the fracture orientation are correlated to geology.

The analyses undertaken in early December and provided to Golder show an analysis of orientations measured in borehole MIU-3. The analysis includes the stereonet for the entire borehole, and stereonets for 100m intervals along the borehole. The stereonet for the entire borehole shows very dispersed sets. The variation of orientation with depth shows large differences between successive plots. Similar analyses on different boreholes would provide information on whether the differences are related to geology, depth, elevation, or are apparently random in space.

If the goodness of fit obtained using FracSys/ISIS is not good, visual comparison of the stereonets may be used to determine the spatial variability.

In addition, if the goodness of fit obtained using FracSys/ISIS is not good the large number of available data points allows the use of bootstrapping the orientations. For large data sets the use of bootstrapping has the advantage of making optimum use of all available data.

The measurement data will contain bias due to the orientation of the boreholes. A borehole is less likely to intersect a fracture nearly parallel to its axis that a fracture perpendicular to the borehole. This bias should be minimised using the Terzaghi correction implemented within ISIS. Note that this correction places additional fractures in the exact location of the fracture that was statistically undercounted. Hence, the Terzaghi correction does not change the raw stereonet plot, only the contoured version of this plot.

3.3 Size

No trace length data was apparent in the Data CDs. If no data exists, then "expert geological judgement" would be required to determine suitable length distributions. However, if possible, it is recommended that measured lengths be used. Length distribution estimates could be measured inside non-flooded sections of the mines, or at any rock outcrops.

Generally, it is usually more defensible to use a range of distributions based on fits to a small number of measured data, using "expert judgement" and sensitivity analyses to refine the fits and ranges where necessary.

If possible, providing length distributions by geology is recommended.

In the absence of measured data, the power law distributions from the H12 PA analyses are recommended.

In the MIU modelling, the length distribution will need to be truncated to make the model tractable. It is expected that the minimum fracture radius in the far field (i.e. distant from the canisters and the outer boundaries) will be of the order of 50m.

The likely length distribution will be exponential or power law. Therefore, the number of fractures in the DFN will be extremely sensitive to the minimum fracture radius included in the model. To truncate the size distribution, the theoretical proportion of the size distribution to be included in the DFN is computed, and the fracture intensity to be generated scaled accordingly. The fractures are then generated within FracWorks using the lower intensity, and explicitly defining the minimum size of fracture to be generated (i.e. a truncated distribution is used).

Common biases on trace length size include the minimum measured trace length, size of plane on which trace measurements are made, and orientation of the trace map plane. The first two biases are accounted for automatically within FracMan. The orientation of the trace map plane is only of concern when the measurement plane does not approximate horizontal or vertical.

Lineament data in 10-km scale and 30km scale as shown below:

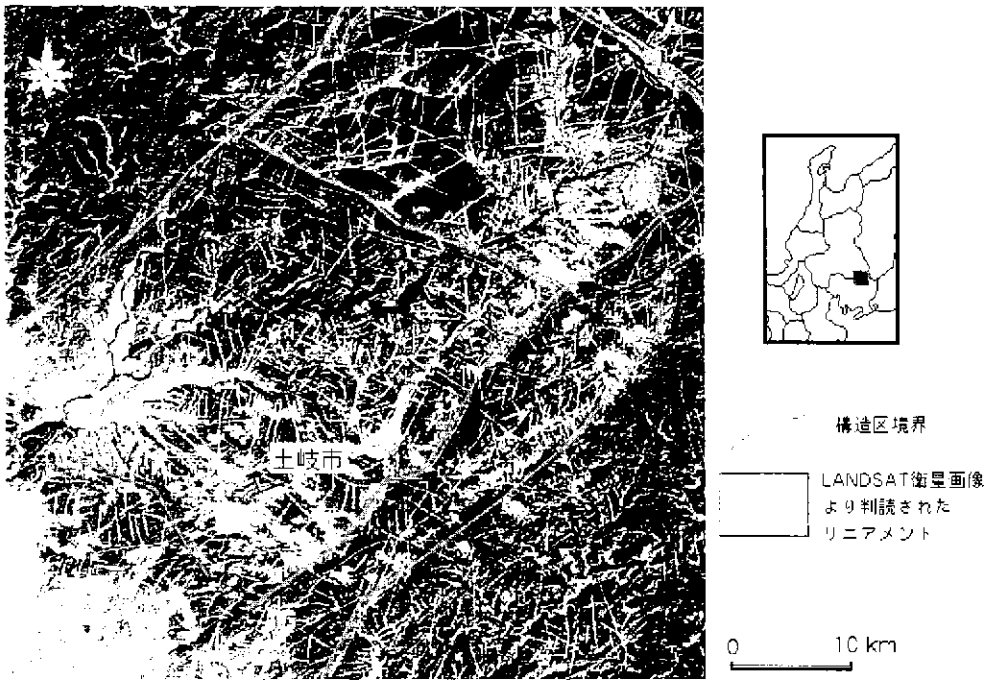

30-km scale

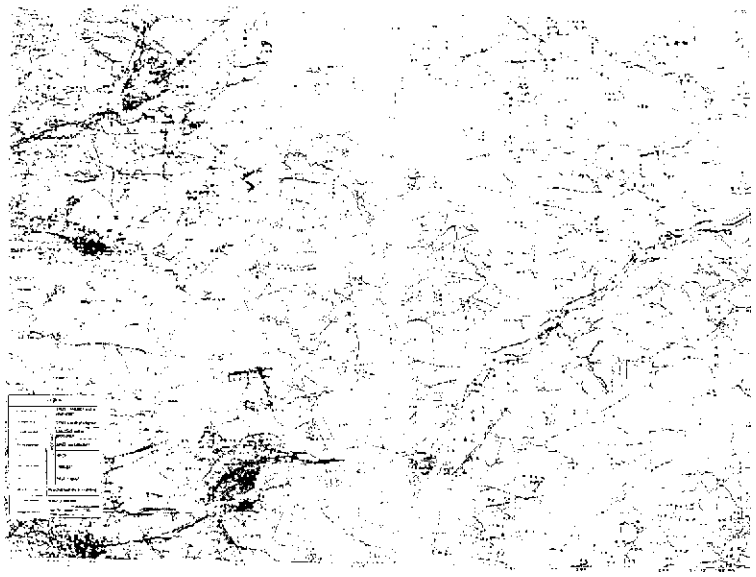

10km scale

The trace length of 10 km scale of lineament data distribute along straight line in log-log plot as shown below:

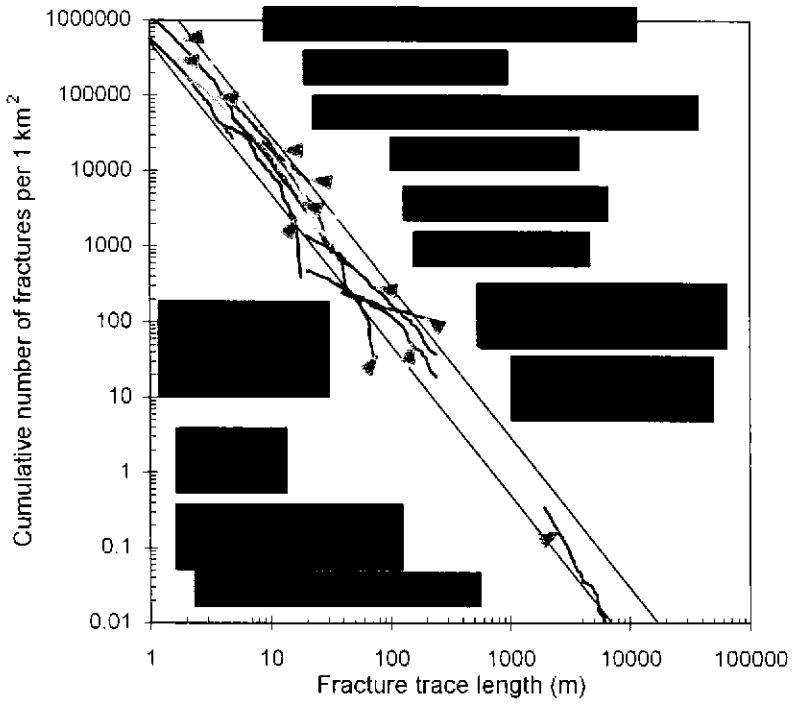

Fracture trace length distribution observed at any sites (after Sawada et al., 2000)

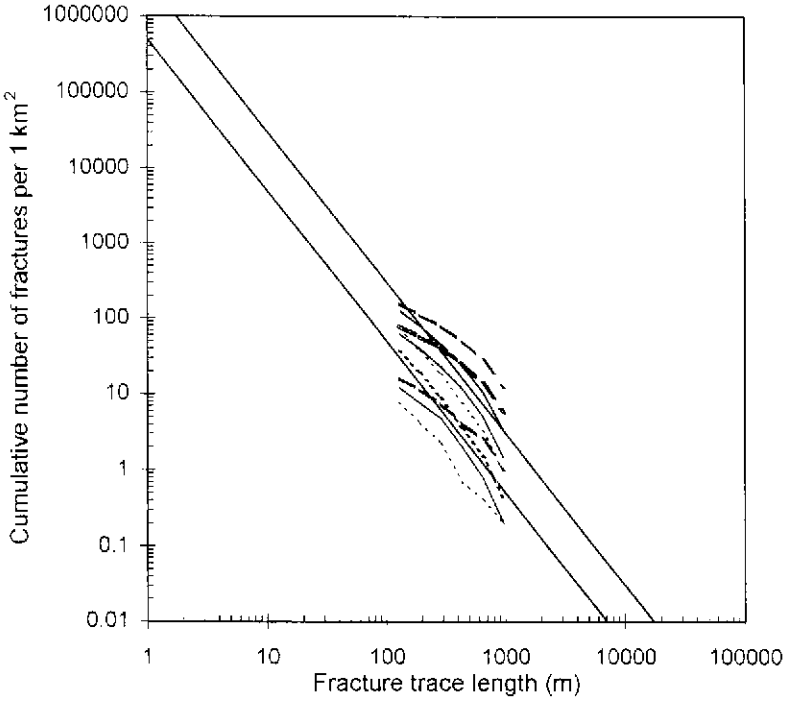

Simulated fracture trace length in 1000 x 1000 x 1000m region box with miu-3 orientation bootstrap, and changing P32 and power b; RED: P32=0.1, Green: P32=0.05, Blue: P32=0.01, broken line: b=2.5, solid line: b=3.0, dot: b=3.5

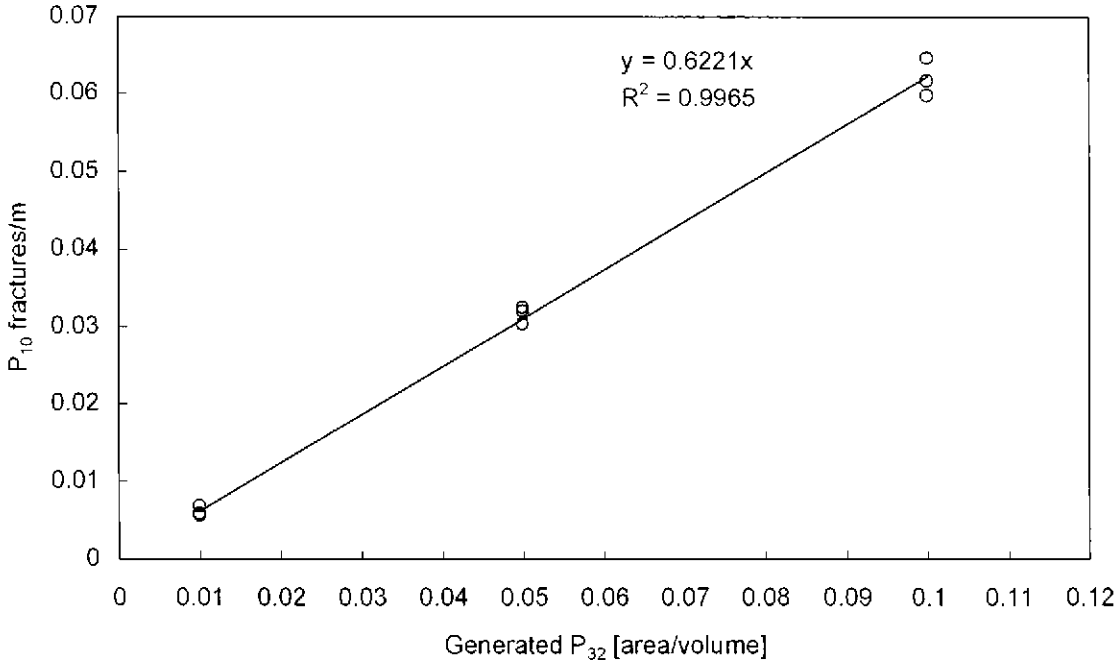

Relationship between simulating P32 and sampling P10

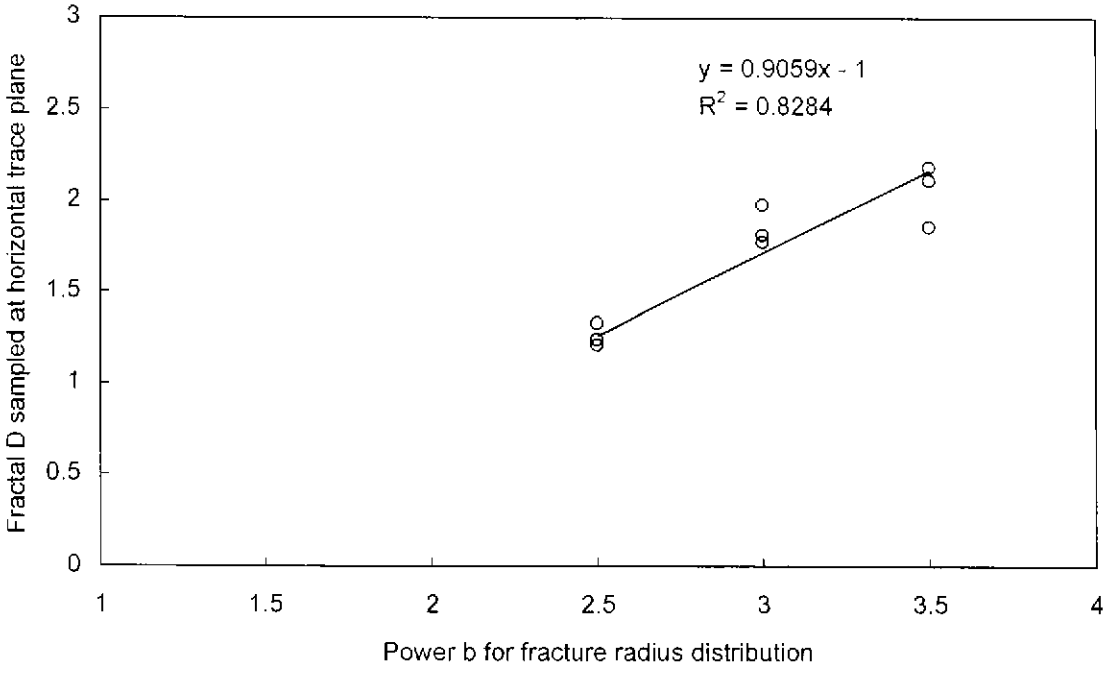

Relationship between power b and fractal D sampled at horizontal plane

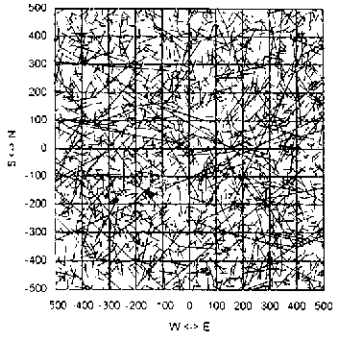

b=3.5, P32=0.1

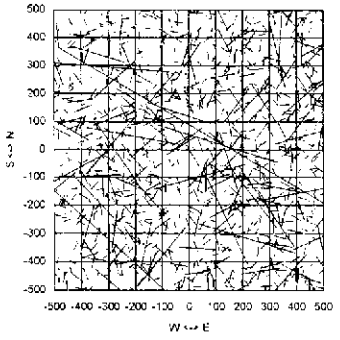

b=3.5, P=0.05

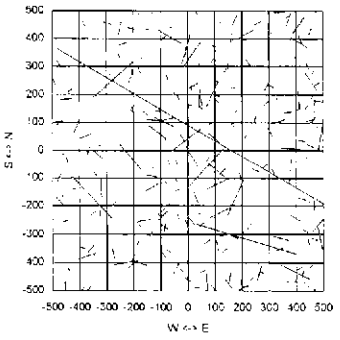

b=3.5, P=0.01

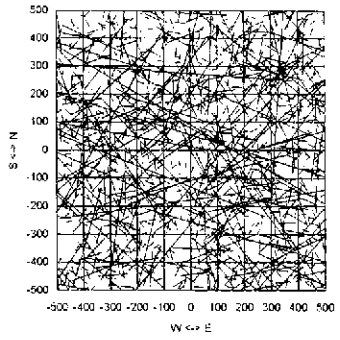

b=3.0, P32=0.1

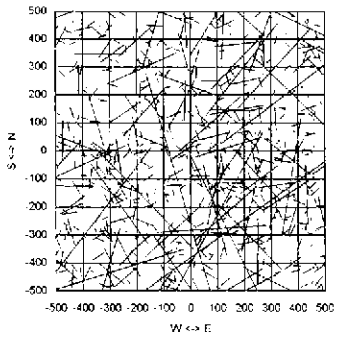

b=3.0, P=0.05

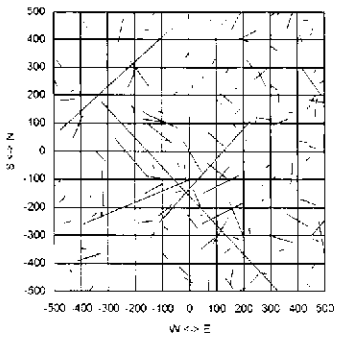

b=3.0, P=0.01

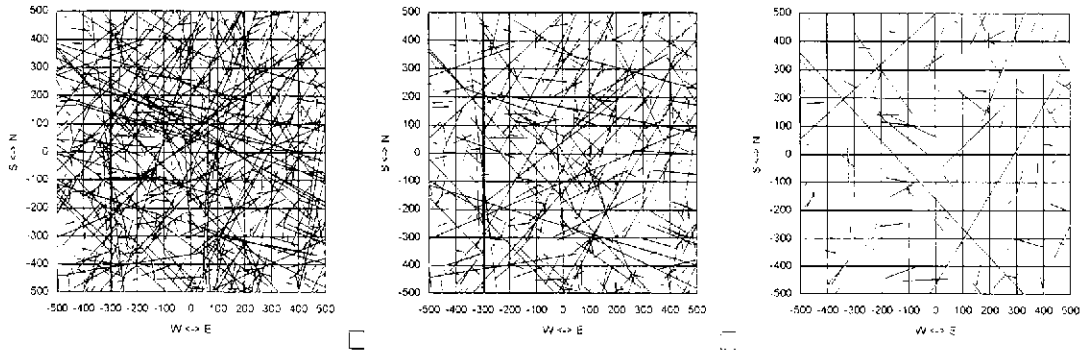

b=2.5, P32=0.1 b=2.5, P=0.05 b=2.5, P=0.01

Fracture trace at each case; an example of each realization

3.4 Transmissivity

The transmissivity data in Excel format is contained in TGC_Hydro_4 and TGC_Hydro_7. These spreadsheets contain the hydraulic conductivities for the DH and AN/MIU boreholes respectively. The provided hydraulic tests do not provide a continuous transmissivity distribution along the borehole.

The analyses undertaken in early December, and provided to Golder, include FracSys/Oxfilet analyses. Two analyses have been undertaken. The first uses the measured data directly, not accounting for the discontinuous data set. The second appears to include longer sections to account for the effect of the zero transmissivity sections.

The latter analysis, accounting for the non-transmissive sections, is more accurate. However, it would be better to include the low transmissivity sections as separate hydraulic tests with a transmissivity of 0.0 (i.e. below the transmissivity threshold). The advantage of this approach is that it provides a better estimate of the transmissive fracture spacing, as smaller intervals are used.

The transmissivity data provided has an inbuilt threshold value, equal to the minimum transmissivity measurable by the testing equipment. However, in this data set (provided the non-tested sections are included) the transmissivity threshold used in Oxfilet should be the threshold value to determine whether hydraulic testing was carried out.

Oxfilet is able to account for the minimum transmissivity automatically. However, care should be taken not to underestimate this number: a shorter than usual hydraulic test interval may result in a spuriously low minimum transmissivity where transmissivities are computed from hydraulic conductivity measurements.

Transmissivity data typically fits a lognormal distribution. The DFN for the MIU model will require truncation on transmissivity. As for the size distribution, to truncate the transmissivity distribution the theoretical proportion of the transmissivity distribution to be included in the DFN is computed, and the fracture intensity to be generated scaled accordingly. The fractures are then generated within

FracWorks using the lower intensity, and explicitly defining the minimum fracture transmissivity to be generated (i.e. a truncated distribution is used).

The transmissivity truncation needs to be determined taking into account the fitted fracture transmissivity distribution. However, for most situations, fractures with transmissivities lower than 10^{-9} m^2/s do not carry a significant proportion of the regional flow.

A lower transmissivity and/or smaller size cut-off will likely be required in the vicinity of the canisters and close to the modelled region boundaries.

3.5 Aperture and Storativity

Aperture and storativity are only required for transient analyses. From the scope it is not clear whether transient analyses are required. If they are not, this section is not relevant.

Aperture data exists, although truncated to differing degrees, in the TGC_Geo_6 Excel files. The unequal truncation will cause some unavoidable bias.

To compute an aperture distribution, two stages are suggested.

Firstly analyse the data in TGC_Geo_6 by taking the data and plotting as a cumulative distribution function. If it is assumed that the aperture is correlated to the transmissivity via a power law then the aperture, e, is related to the transmissivity by an equation of the form, $e = a.T^b$, where 'a' and 'b' are fitted parameters. Setting 'b' equal to 1/3 and 'a' equal to approximately 0.101 returns the parallel plate cubic law. Generally the cubic law gives a poor fit to real data and 'b' is at or above 0.5. We recommend 'a' = 0.1 and 'b' = 0.5 in the absence of tracer tests.

Using the measured aperture distribution in cumulative distribution format, and using a least fit computation within Excel, together with the best fit for the transmissivity distribution, values for 'a' and 'b' can be obtained. These values are a good starting estimate for the hydraulic aperture.

The storativity is also typically correlated to transmissivity using a power law. The relationship $S = 0.01\ T^{0.5}$ is a reasonable starting estimate. Note that higher storativity values may be required to replicate the effect of the truncated small and low transmissivity features.

Using the transient flow tests contained in TGC_Hydro_6, transient simulations should be undertaken and the storativity relationship adjusted to provide a good fit to the data.

3.6 Intensity

For a hydrogeological model, the only fractures that are of interest are fractures that carry flow. Only a subset of these features is typically identifiable using logging techniques. Therefore the fracture intensity is usually taken directly from the fitted transmissivity distribution (average fracture spacing is an output from this analysis).

To compute the P_{32} a modelling region large compared to the fracture size (to reduce boundary effects) is defined in FracWorks. Boreholes are added that are statistically similar to the boreholes in which the hydrogeological tests used for the transmissivity analyses were carried out. "Similar" means that the proportion of borehole length that is vertical is the same in the model and in the hydrogeological testing. Fractures are then generated in FracWorks with the same orientation as derived from the orientation analyses. The borehole "sample" option is then used to compute the P_{32} of the region and the number of fractures intersecting the boreholes. It is recommended that the number of intersections computed be a multiple of the number of intersections required, such that the projected P_{32} is insensitive to additional fractures being added to the system.

As discussed in Section 4, the modelled region (4 km by 6 km, with a vertical extent from ground level to 3 km below sea level) is very large. Therefore the model will require truncation, typically using transmissivity and/or size. Truncation is implemented by multiplying the P_{32} value by the proportion of fractures being included in the model. Note however, that the intensity of fracturing (i.e. the fracture spacing) derived from the transmissivity analyses already has a transmissivity truncation based on the minimum interval transmissivity.

3.7 Head distribution

The information on borehole heads provided on the CDs are presented in terms of pressure and derived water level. Therefore the presented values will require conversion into heads.

The MAFIC flow code is designed for constant density flow. Based on the depth of the boreholes, some effect of temperature and salinity on the density could be expected. Therefore it is recommended that the "environmental head" values (i.e. head values corrected for density and temperature) be used. The use of "environmental head" ensures that the correct vertical gradient along a vertical borehole is computed.

4. BOUNDARY CONDITIONS AND MODEL SET-UP

This section looks at the outer boundaries of the model region, and the treatment of the mines and boreholes.

For convenience of processing, it is recommended that the prism region or polyhedron region be the first structure in the .SAB control file, followed by all the monitoring boreholes, with the mines coming last. Separation of the differing structures minimizes confusion in data processing.

4.1 Base

The base of the model will be assigned a "no flow" boundary condition. The proposed elevation of the base of the model, at -3 km below sea level, should be sufficient to reduce edge effects.

4.2 Sides

The four vertical sides of the model (north, south, east and west faces) could be set as 'conditioned head' or 'no flow' boundaries. Golder does not have a copy of Figure 2 in the technical specifications, so the exact location of the model boundary is not known. But based on the description in the technical specification, the north, east and west sides are ridges. The south is a river.

It is recommended that two separate boundary conditions for the edges of the model be considered: "no flow" on all four sides or "conditioned head" on all four sides.

Based on the description of the edges of the model as ridges or a river, the topography may be consistent with the edges of the finite element model being flow boundaries (i.e. recharge and discharge interfaces, with no flow across the interface). If this is correct, then using "no flow" boundaries at the edges of the model would be a sensible approximation. The "no flow" boundaries are also simple to implement, and provide a useful reference case for calibrating the model.

If the topography at the edges of the finite element model are not consistent with "no flow", the alternate boundary condition is conditioning the heads. Conditioning heads in the absence of larger scale regional modelling is difficult. If the head distribution is available in boreholes close to the edge of the model, the head distribution inferred from these measurements should be used. Typically in a model of this scale, this provides insufficient information to build a conditioned head field. Therefore it is recommended that local to a borehole the measured heads be used to derive the conditioned heads. Remote from measurements it is recommended that a vertical head gradient of zero be used. The head at the surface is derived from the elevation of the groundwater if available, or the topography.

The reason for using a zero vertical gradient is that this is the opposite of a no flow boundary. It therefore provides a very good sensitivity test on how much the boundary condition assumptions at the edge of the model affect the heads at the interior boreholes.

The conditioned grid of head values should, if possible, be equally spaced in the plane of the boundary. The head conditioning algorithm uses the user defined N closest points. Unequal grids preferentially bias the conditioning.

If calibration of the heads is required for the final simulations, the boundary to be changed will require a conditioned head field. If the head distribution from the "no flow" boundary was a closer match than the zero gradient assumption, the "no flow" head values for that boundary group can be obtained from the restart.maf file and used to create a baseline conditioning file.

4.3 Top

It is recommended that the top of the model be assigned as a conditioned head field. The head field should be based on water table measurements where available, and topography elsewhere.

4.4 Mines

The mines will have a large effect on the head field in their vicinity, and need to be included in the modelling.

The layout of the mine is not known. The structure used to represent the mines will depend on the layout of the mine. It is recommended that the mines be modelled using a single prism region, or as few circular tunnels as can effectively represent the overall geometry.

Flows into the mines have been provided in the data set. However, it is recommended that a constant head (or time varying head) be used as the boundary condition. Use of the group flux boundary is very sensitive to individual fracture intersections. The head boundary condition typically gives more similar results between differing realizations.

The computed flows into the mine can be used as a measure of the validity and variability between DFN models. The modelled flows into the wells should be lower than, or equal to, the measured values.

Tono mine is excavated in overburden sedimentary rocks. Therefore, if the mines are to be modelled the overburdened sedimentary rocks should be explicitly included. As the overburden is much more permeable than the granite it is important to include the upper surface as a very permeable zone (or feature) if the phreatic surface is located in the overburden. This you have already done.

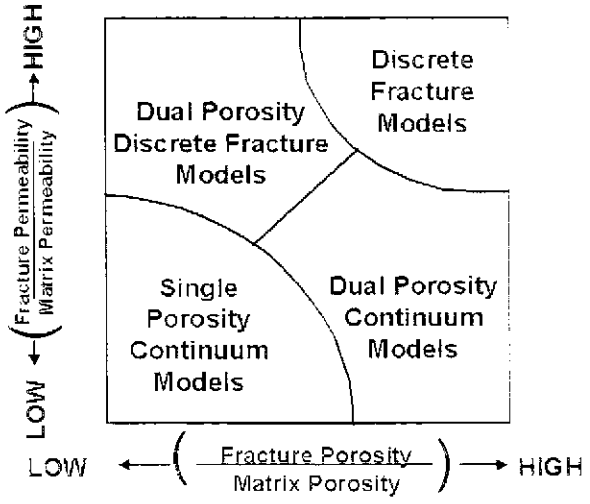

For modelling Tono mine, the model may need to be on a smaller, more local scale, in order to provide an accurate estimate of inflows and heads if the fracture intensity is higher. The other issue is whether the matrix porosity is important. Matrix porosity may be included using MAFIC (triangular elements).

4.5 Boreholes

The borehole intervals are used for head monitoring, pumping test hydraulic analyses, etc. For numerical convenience it is recommended that the boreholes be constructed in the MESH/GenPipes .sab file to replicate the interval lengths at the start of the modelling. This is convenient because it is allows the modeller to ensure the relevant sections have connected to the background fracture network.

The recommended boundary conditions are:

- "No flow" (i.e. flux = 0.0) for borehole sections that are cased and prevent flow through the section.
- "Group flux" of 0.0 for all monitoring sections.
- "Group flux" equal to the pumping rate for pumping tests.

4.6 Nested Models

As discussed in Section 2.5, most large nuclear repository models use a "Russian doll" (nested) approach, with a higher proportion of the total DFN fractures being included in critical areas. It is expected that such a nested approach will be required for the MIU project. The locations requiring a higher density of fracturing are the canisters (or source locations) and the monitoring locations. In these locations, although the majority of flow is still likely being transported through the larger and higher transmissivity fractures, local connectivity is very important.

Using this nested approach required that care be exercised implementing the differing truncation cut-offs. The flow regime can be influenced by the fracturing intensity, and preferentially biasing the location of fractures using a different truncation limit also affects the flow regime.

To reduce this it is recommended that:

- The volumes of higher density fracturing be kept as symmetrical as possible, to reduce bias in the flow regime.
- The monitoring locations are most likely to be located at, or near, the edge of the model. To implement this region of higher intensity fracturing, it is recommended that the thickness of the higher density zone be constant throughout the model. It is also recommended that the region be placed on all five sides of the model, excluding the base. The reason for this is to project the head field into the model using the same resolution on all sides.

4.7 Polyhedron versus Prism Region

The description of the model region suggests the surface of the model be implemented as a simple prism region or using the polyhedron outer boundary.

The prism region is the simplest finite element mesh implementation, but requires additional work to compute an approximate conditioned head field.

The alternate method, the polyhedron region, can be used to model an approximation of the topography explicitly, setting the head boundary condition to zero excess head. To set up a polyhedron region it is recommended that the topography be kept simple because the MESH/GenPipe codes cannot handle some convex regions. Additionally, it is recommended that triangles be used to construct the top surface of the model: the corners of a polyhedron element must lie on a plane and this is achieved automatically with a triangle. Use of large surface regions is also advantageous, as the meshing code must subdivide an element at the boundary of every polyhedron element.

Higher transmissivity flow in surface deposits may be represented using a high transmissivity surface fracture for both polyhedron and prism outer boundaries.

5. CALIBRATION

In order to address the influences of uncertainty addressed by stochastically generating fracture networks on the pathways analysis, it is recommended that a more than one DFN model be used for the results of the groundwater flow simulation. This will require some modification of the general approach.

5.1 Measurement of goodness of fit

A measure of the goodness of fit is required to determine whether the modelled head distribution is a good measure of the measured heads. Two measures are suggested. The first is the absolute difference in head, measured as abs(h_{MAFIC} - $h_{measured}$). For the total model the recommended measure is sqrt((h_{MAFIC} - $h_{measured}$)^2) / (number of head locations).

The second measure determines whether the head gradient along each borehole is replicated correctly. The measure is defined as, ($gradient_{MAFIC}$ / $gradient_{measured}$). For the total model the recommended measure is sqrt(($gradient_{MAFIC}$ / $gradient_{measured}$)^2) / (number of gradient locations).

The location of the heads to determine the gradients should be chosen such that distinct gradient changes are not masked.

For boreholes with very discontinuous head distributions along their length (i.e. variable gradients along the length of the borehole not correlated to geology), it may be more appropriate to consider the length averaged borehole head and the gradient measure.

5.2 Optimization

The three obvious changes to the model to optimize the head calibration are:

- Modification of boundary conditions;
- Modification of large scale discrete features (for example the properties, and location, of faults); and

- Addition of deterministic features.

The measured locations of large-scale features may not be changed. However, in some cases slight changes in the dip or dip direction of a fault cause it to intersect/ not intersect another feature, having a larger effect on the groundwater system. Similarly, the transmissivity of a large-scale feature may change over its extent.

The addition of deterministic features is only worthwhile if the measurement location is close to a head boundary or a major feature, and the head is clearly highly dependent on a direct connection to this location.

The calibration process can be time consuming. It is recommended that 10 realizations be used for the pathways and results analyses. Therefore a slightly modified approach is suggested.

- In order to reduce the calibration process, it is recommended that the best model computed during the sensitivity analyses is selected and additional realizations (50 to 100 total) simulated using a different seed number.
- The ten realizations that most closely match the measured head distribution should be selected and used for the calibration process.
- The modifications to the fracture file(s) and/or boundary conditions should be the same for all 10 realizations. Only one of the 10 stochastic realizations should be used for the calibration process.

Since multiple realizations are being used, the calibration process should be simplified as much as possible. It is recommended that prior to starting the calibration the variation in heads at each specific borehole interval be reviewed, and the mean and standard deviation of the head at each borehole interval computed. Since each stochastic realization was generated using the same parameter distributions, the mean computed head should be compared against the measured value. A high standard deviation indicates stochastic variation between realizations, and a good fit to all of the realizations will likely not be obtained.

The realization with the heads closest to the mean of the 10 simulations should be used for the calibration. This realization is most likely to improve the overall head match to all 10 realizations following calibration.

5.3 Tolerance on calibration

The tolerance on calibration will be affected by the variability in the measured head distribution. The more discontinuous the measured head distribution, the more difficult it will be to fit exactly. However, a fit to the head within 5% of the head distribution across the model should be achievable.

6. PATHWAYS ANALYSIS

The pathways analysis is required to produce information on the:

- Location of flow pathways;
- Length of flow pathways;
- Travel time of flow pathways;
- Velocities along flow pathways;
- Flow rates along the pathways;
- Distribution of head along the flow pathways; and
- Discharge locations.

This information may be obtained using the "particle tracking" option in the plate or pipe versions of MAFIC. The same information may also be obtained from LTG V2.0 (pipe version of LTG) or LTG_V3.0 (plate version of LTG).

Note that both the "particle tracking" and the pipe/plate LTG codes provide essentially the same solution, as both codes assign mass (or particles) in proportion to flow. However, LTG, although requiring more post-processing to extract the pipe properties along the pathways, also allows the effect of diffusion, chemical retardation, etc. to be incorporated. The only reason the LTG codes should not be used is if including the time dependence of the flow solution is important.

Due to time constraints, the recommended approach is staged. The staging ensures that the fastest approach is followed first, and results are obtained quickly.

If the plate network is being used:

1. Create the restart files.
2. Run MAFIC with particle tracking. The particle tracking algorithm will require 1000 particles to provide a good distribution of flow-weighted pathways.
3. Plot particle-tracking results.
4. Run a single advective only LTGplane simulation to show equivalence of LTG and particle tracking results. The input file to this simulation is the MAFIC restart file.
5. Run LTG with diffusion to illustrate effect on the results.

Note that the LTG_V3.0 code has yet to be tested on a large 3-D MAFIC network. Therefore the validation of equivalence between particle tracking and LTG_V3.0 should not be excluded from the analyses.

If the pipe network is being used the following approach is recommended:

1. Create the restart files

2. Run PAW to both create input files for LTG and carry out the particle-tracking algorithm. The particle tracking algorithm will require 1000 particles to provide a good distribution of flow-weighted pathways.
3. Plot particle tracking results
4. Run a single advective only LTG simulation to show equivalence of LTG and particle tracking results.
5. Run LTG with diffusion to illustrate effect on the results.

7. SENSITIVITY CASES

As discussed in the introduction, the DFN model should be constructed to be able to provide the information required by JNC at the highest possible resolution. Section 5, of the technical specification, "Summarized results of GW flow simulation" contains the summary of the type of measurements that will be required from the flow modelling. As discussed in Section 2.4 the exact specification of the result locations, etc. is not known at this time. Because the typical approach to DFN modelling of large regions is to use a lower level of truncation for less important portions of the modelled region, it would be useful to know whether the distribution monitoring points are located close to the repository or to the model boundary. If the measurement points are all distant and spatially heterogeneous from the repository, then the measurement resolution will need to be on a fairly large grid and differing levels of truncation may not be appropriate.

The sensitivity analyses should be structured to either:

1. Investigate specific parameter and/or boundary condition changes; and
2. Investigate a number of different conceptual models of the site.

The major difference between the two approaches is that the first only changes one parameter at a time relative to a base case, and the effect of that parameter is reported. This allows the sensitivity of the model to a single parameter to be quantified. The second approach does not attempt to quantify the effect of any one parameter, but instead compares completely different concepts. It is recommended that only one of these approaches be chosen.

The decision on which approach is preferable depends on the data analysis. Uncertainty over the choice of a spatial model would imply use of different conceptual models. Fracture size, different transmissivity distribution (and by dependence fracturing intensity), or depth dependence, could probably be investigated one parameter at a time. Uncertainty in orientation for this data set could be implemented using bootstrapping.

Note that it is worthwhile to run multiple realizations of the baseline fracture model and boundary conditions, and review the results, prior to carrying out any sensitivity analyses.

8. ELEMENT TYPE

The choice of element type will have a large influence on the MIU project implementation. The number of fractures modelled is strongly affected by the choice of element.

The choice between using plates and pipes should be based on:

- Will a plate model contain sufficient fractures to provide percolation, and sufficient connections between the background fracture network and the source/sink location;
- Are the plate finite element models small enough to manipulate in an efficient manner; and
- Will the plate model of the MIU mesh quickly enough to allow multiple stochastic simulations to be completed in an acceptable time frame.

If the size of model and simulation time is sufficiently fast for the use of plate elements, this element type is preferred. Plates have the advantage of being less sensitive to differing fracture intensities, because the element generation is less dependent on local fracture intersections.

However, the LTG and particle tracking algorithms are more efficient for pipes, and the model size significantly smaller. Therefore if pruning the DFN model could cause percolation problems, use of the pipe network is recommended.

The user also has the option of using either linear or quadratic elements. It is generally recommended that more linear elements be used in preference to fewer quadratic elements. This is based on good flow results being obtained with linear elements in most situations. Note however, that plate elements must be generated using element subdivision, or both very slow mesh generation, and poor flow solutions, will result.

The only situation where linear elements might not be the optimum solution is for the solute transport code LTG_V3.0. This code has not been fully tested.

Particle tracking in plate elements uses an element dispersion length to more closely replicate true behaviour and reduce the effect of the linear flow across a single element.

ATTACHMENT A

TABLE OF FRACTURE PROPERTIES
PROVIDED BY MIU DATA

TABLE OF FRACTURE PROPERTIES PROVIDED BY MIU DATA

Data	Description	Property	Comments
TCG_All_1.doc	Technical specification	n/a	In Japanese, but I think Golder has printed copy in English
TGC_All_2.tif	topographic map	boundary conditions spatial location of BHs	cannot see reference coordinates on map
TGC_All_3.tif	Borehole location map (MIU)	spatial location of BHs	cannot see reference coordinates on map
TGC_All_4.tif	Borehole location map (DH)	spatial location of BHs	cannot see reference coordinates on map
TGC_All_5.tif	Borehole location map (Tono Mine)	spatial location and elevation of BHs	cannot see reference coordinates on map
TGC_All_6.tif	Borehole location map (MC)	spatial location and elevation of BHs	cannot see reference coordinates on map
TGC_All_7.jpg	Photographic image (Spot)	aerial photo	
TGC_All_8.jpg	Photographic image (LANDSAT)	aerial photo	
TGC_All_9	DTM (20m mesh)	topography in numerical format	
TCG_Geo_1	Geological information, borehole logs and cross sections through boreholes	Fault locations, Geology, Transmissivity, Spatial model from fracture intensity heads for verification	Includes transmissivity data, interpreted head data and fracture intensity data (similar to info in TCG_Geo_10
TCG_Geo_2	Raw data set of geophysical logging	Could be used to correlate properties spatially.	Large amounts of data that could potentially be used to correlate with fracture properties required by FracMan.
TCG_Geo_3	Fault distribution map (only printed matter)	LSF locations	Golder does not have copy
TCG_Geo_4	Geological map (printed matter)	Geology	Golder does not have copy
TCG_Geo_5	Geological map (polygon digital data)	Geology	Golder does not have copy
TCG_Geo_6	Borehole television data	Fracture intensity for stability analyses Spatial model Fracture orientation Correlation orientation to fracture "type" Aperture distribution	Location and orientation of fractures in MUI and DH boreholes. Also aperture above variable tolerance value.
TCG_Geo_7	Fluid volumes lost data	Relative permeabilities / Spatial distribution of permeabilities	Drilling information on drilling fluid losses
TCG_Geo_8	Seismic exploration data	Geological model	

Data	Description	Property	Comments
TCG_Geo_9	The boundary of between basements and sedimentary rocks (unc50.dat) Estimated from the ground electromagnetic survey	Geological model	elec_jpn.doc is in Japanese 9999 is used for missing data
TCG_Geo_10	Borehole logs for MIU-1 to MIU-3	Fault locations, Geology, Spatial model from fracture intensity heads for verification	Includes transmissivity data, interpreted head data and fracture intensity data
TCG_Geo_11	Fault distribution map (only printed matter; revised)	Location of faults	Golder does not have copy
TCG_Geo_12	X-Y coordinates data of seismic survey lines	Interpretation	Location of seismic survey lines.
TGC_Hydro_1	Water pressure monitoring(MP) in MIU area	In situ head distribution in boreholes for DFN boundary condition verification	In situ head & pressure distribution in boreholes MIU-1, MIU-2, AN-1, AN-3
TGC_Hydro_2	Water pressure monitoring(MP)	In situ head distribution in boreholes for DFN boundary condition verification	Location of all boreholes included Not sure of units of measured pressure
TGC_Hydro_3	Water balance monitoring data	Flow boundary condition at outer boundaries of model	Mine locations
TGC_Hydro_4	Hydraulic test data inc. initial pressure	Transmissivity of fractures Storativity of fractures	Transmissivity, storage (MIU-1 and some DH boreholes only), and water level of borehole sections DH-1 to –9, AN-1, AN-3, MIU-1 to 3 boreholes
TGC_Hydro_5	Water table measurement data	Transient heads	Mainly in Japanese I think the files contain the water table measurements during and after drilling.
TGC_Hydro_6	Hydraulic test raw data (area for the analysis)	Transmissivity of borehole sections	Text partially in Japanese
TGC_Hydro_7	Hydraulic test data inc. initial pressure(revised MIU/AN)	Transmissivity of fractures Storativity of fractures	Transmissivity, storage (MIU-1 to –3) and water level of borehole sections AN-1, AN-3, MIU-1 to 3 boreholes
TGC_Hydro_8	Discharge rate from Tono Mine	Boundary conditions	Time dependent discharge rate